

UNIVERSITY OF CALIFORNIA

Santa Barbara

Loss Mechanisms in Solution-Processed Small Molecule Bulk Heterojunction Solar Cells

A dissertation submitted in partial satisfaction of the  
requirements for the degree Doctor of Philosophy  
in Materials

by

Christopher Michael Proctor

Committee in charge:

Professor Thuc-Quyen Nguyen, Co-Chair

Professor Guillermo Bazan, Co-Chair

Professor Michael Chabinyc

Professor Alan J. Heeger

Professor Edward Kramer, in memoriam

September 2015

The dissertation of Christopher Michael Proctor is approved.

---

Alan J. Heeger

---

Michael Chabinyc

---

Guillermo Bazan, Committee Co-Chair

---

Thuc-Quyen Nguyen, Committee Co-Chair

June 2015

Loss Mechanisms in Solution-Processed Small Molecule Bulk Heterojunction Solar Cells

Copyright © 2015

by

Christopher M. Proctor

## ACKNOWLEDGEMENTS

*I dedicate this work to my parents, Susan and Richard Proctor, whom have worked tirelessly to provide me with the wonderful opportunities I have had in life. Mom and Dad, I cannot thank you enough for always looking out for my best interest and for pushing me when I needed it while still giving me the space to find my own way. I cannot imagine two better role models and I certainly would not be who I am today without your unwavering love and support.*

In addition to my parents, there are several individuals that heavily influenced my decision to go to pursue a PhD. I thank my undergraduate research advisors Professor Rachel Goldman and Professor Tom Armstrong as well as my mentors Dr. Michael Lau and Dr. Leon Webster, all of the University of Michigan, for introducing me to thrills and challenges of scientific research. I would have never have considered pursuing a PhD if not for my favorable experiences as an undergraduate. I also thank Serita Sanders of the NRC for supporting me when I decided to leave the comforts of government work to go back to school.

My time at UCSB was enjoyable most of all because of all the people who I met along the way. First and foremost I want to thank my PhD advisor, Quyen Nguyen, for her guidance and support throughout my time at UCSB. Her funding raising efforts enabled me to have access to great facilities, novel materials and superb collaborators. Furthermore, she has excelled in fostering a very dynamic and enjoyable work environment by recruiting some of the finest students and post-docs I have ever had the privilege of working with. Indeed I want to thank all of the Nguyen group members who have each been teachers, collaborators and friends: Dr. Alex Sharenko, Dr. Jianhua Liu, Dr. Chunki Kim, Dr. Bright Walker, Dr. Corey Hoven, Dr. Xuan-Dung Dang, Dr. Viktor Brus, Dr Hui Li, Dr. Martijn Kuik, Dr. Cristiano Woellner, Dr. Peter Zalar, Dr. Binh Duong, Dr. Jenny Du, Dr. Oleksandr

Mikhnenko, Dr. Yuan Zhang, Dr. Michele Guide, Dr. Jason Lin, Kenny Liao, Daniel Kamkar and future Dr.'s Sam Collins, Zach Rengert, Niva Ran, Jack Love, Michael Hughes, Zhi Li, Brett Yurash, Hung Phan and Abhishek Kher. Speaking of friends, I also want to extend a heartfelt thank you to my good friend Prateek Choudhary for countless servings of delicious Indian food and chai that helped fuel me through the PhD marathon.

I thank Professor Dieter Neher for hosting me at the University of Potsdam for what turned out to be three of my most productive months during my graduate studies. Dieter's scientific input and good humor were much appreciated and helped shape much of the work in this dissertation. I also thank the entire Neher research group for their warm hospitality and notably Dr. Steve Albrecht and Jona Kurpiers for contributing to the research described here. I also thank Professor Harald Ade and Dr. Subh Mukherjee of North Carolina State University for fruitful collaborations that led to interesting insights about the morphology of the materials discussed here.

I thank my committee for their insight throughout my graduate studies and in particular Professor Gui Bazan for reminding me to always keep sight of the critical scientific questions I seek to answer.

Finally, I thank the tax payers of the United States of America for contributing to the government institutions that in turn funded my graduate work and indeed all of my formal education starting from elementary school. I thank the National Science Foundation, the International Center for Materials Research and the Frenkel Foundation for fellowships that funded most of my graduate studies and international collaborations. The work described here was also funded by the Office of Naval Research.

VITA OF CHRISTOPHER M. PROCTOR  
June 2015

EDUCATION

Bachelor of Science with Distinction in Interdisciplinary Physics, University of Michigan, Ann Arbor, April 2008

Doctor of Philosophy in Materials, University of California, Santa Barbara, June 2015 (expected)

PROFESSIONAL EMPLOYMENT

2008-10: General Scientist, U.S. Nuclear Regulatory Commission

AWARDS AND FELLOWSHIPS

2015 Whitaker International Post Doctoral Scholar Grant

2014 MRS Graduate Student Silver Award

2014 MRS Best Presentation Award

2014 UCSB Institute for Energy Efficiency Frenkel Foundation Fellowship

2014 School for Scientific Thought Teaching Fellowship

2013 Toastmasters International Competent Communicator Certification

2013 Materials Research Lab - DOW Travel Fellowship

2012 National Science Foundation Graduate Research Fellowship

2012 International Center for Materials Research Fellowship

PUBLICATIONS

- **C. M. Proctor**; Nguyen, TQ, " Effect Leakage Current and Shunt Resistance on the Light Intensity Dependence of Organic Solar Cells ", *App. Phys. Let.*, 106, 083301, 2015
- **C. M. Proctor\***, S. Mukherjee\*, J. Tumbleston, T.-Q. Nguyen, H. Ade, "Effect of domain purity and molecular packing on the performance of high-efficiency solution-processed small-molecule solar cells", *Adv. Mater.* doi: 10.1002/adma.201404388, Dec. 2014 \*equal contribution
- N. A. Ran, M. Kuik, J. A. Love, **C. M. Proctor**, I. Nagao, G. C. Bazan, and T.-Q. Nguyen, "Understanding the Charge-Transfer State and Singlet Exciton Emission from Solution-Processed Small-Molecule Organic Solar Cells," *Adv. Mater.*, vol. 26, no. 43, pp. 7405–7412, Nov. 2014.
- Z. Li, J. D. A. Lin, H. Phan, A. Sharenko, **C. M. Proctor**, P. Zalar, Z. Chen, A. Facchetti, and T.-Q. Nguyen, "Competitive Absorption and Inefficient Exciton Harvesting: Lessons Learned from Bulk Heterojunction Organic Photovoltaics Utilizing the Polymer Acceptor P(NDI2OD-T2)," *Adv. Funct. Mater.*, p. DOI: 10.1002/adfm.201401367, Sep. 2014.
- **C. M. Proctor**, J. A. Love, and T.-Q. Nguyen, "Mobility Guidelines for High Fill Factor Solution-Processed Solar Cells," *Adv. Mater.*, vol. 26, no. 34, pp. 5957–5961, Sep. 2014.

- **C. M. Proctor**, S. Albrecht, M. Kuik, D. Neher, and T.-Q. Nguyen, “Overcoming Geminate Recombination and Enhancing Extraction in Solution-Processed Small Molecule Solar Cells,” *Adv. Energy Mater.*, vol. 4, no. 10, p. DOI 10.1002/aenm.201400230, Jul. 2014.
- M. Guide, J. D. A. Lin, **C. M. Proctor**, J. Chen, C. García-Cervera, and T.-Q. Nguyen, “Effect of copper metalation of tetrabenzoporphyrin donor material on organic solar cell performance,” *J. Mater. Chem. A*, vol. 2, no. 21, pp. 7890–7896, May 2014.
- J. D. A. Lin, J. Liu, C. Kim, A. B. Tamayo, **C. M. Proctor**, and T.-Q. Nguyen, “Effect of structural variation on photovoltaic characteristics of phenyl substituted diketopyrrolopyrroles,” *RSC Adv.*, vol. 4, no. 27, pp. 14101–14108, Mar. 2014.
- Y. Zhang, M. Wang, S. D. Collins, H. Zhou, H. Phan, **C. M. Proctor**, A. Mikhailovsky, F. Wudl, and T.-Q. Nguyen, “Enhancement of the Photoresponse in Organic Field-Effect Transistors by Incorporating Thin DNA Layers,” *Angew. Chem. Int. Ed.*, vol. 53, no. 1, pp. 244–249, Jan. 2014.
- **C. M. Proctor**, M. Kuik, and T.-Q. Nguyen, “Charge carrier recombination in organic solar cells,” *Prog. Polym. Sci.*, vol. 38, no. 12, pp. 1941–1960, Dec. 2013.
- J. Liu, Y. Sun, P. Moonsin, M. Kuik, **C. M. Proctor**, J. Lin, B. B. Hsu, V. Promarak, A. J. Heeger, and T.-Q. Nguyen, “Tri-Diketopyrrolopyrrole Molecular Donor Materials for High-Performance Solution-Processed Bulk Heterojunction Solar Cells,” *Adv. Mater.*, vol. 25, no. 41, pp. 5898–5903, Nov. 2013.
- J. A. Love, **C. M. Proctor**, J. Liu, C. J. Takacs, A. Sharenko, T. S. van der Poll, A. J. Heeger, G. C. Bazan, and T.-Q. Nguyen, “Film Morphology of High Efficiency Solution-Processed Small-Molecule Solar Cells,” *Adv. Funct. Mater.*, vol. 23, no. 40, pp. 5019–5026, Oct. 2013.
- Sharenko, **C. M. Proctor**, T. S. van der Poll, Z. B. Henson, T.-Q. Nguyen, and G. C. Bazan, “A High-Performing Solution-Processed Small Molecule:Perylene Diimide Bulk Heterojunction Solar Cell,” *Adv. Mater.*, vol. 25, no. 32, pp. 4403–4406, 2013.
- **C. M. Proctor**, C. Kim, D. Neher, and T.-Q. Nguyen, “Nongeminate Recombination and Charge Transport Limitations in Diketopyrrolopyrrole-Based Solution-Processed Small Molecule Solar Cells,” *Adv. Funct. Mater.*, vol. 23, no. 28, pp. 3584–3594, 2013.
- Walker, J. Liu, C. Kim, G. C. Welch, J. K. Park, J. Lin, P. Zalar, **C. M. Proctor**, J. H. Seo, G. C. Bazan, and T.-Q. Nguyen, “Optimization of energy levels by molecular design: evaluation of bis-diketopyrrolopyrrole molecular donor materials for bulk heterojunction solar cells,” *Energy Environ. Sci.*, vol. 6, no. 3, pp. 952–962, Feb. 2013.

#### WORKS IN PROGRESS

- **C. M. Proctor**; S. Albrecht; D. Neher; Nguyen, TQ, " Bias Dependent Spectral Losses in Small Molecule Solar Cells"
- **C. M. Proctor**; Kher, A; Sharenko, A; Love, J; Huang, J; Bazan, G; Kramer, E; Nguyen, TQ, "Understanding Charge Transport in Solution Processed Small Molecule Based Solar Cells"
- S.D. Collins, **C. M. Proctor**, N. Ran, Nguyen, TQ, "Understanding voltage loss through the density of states in organic solar cells"
- S. Mukherjee, **C. M. Proctor**, T.-Q. Nguyen, H. Ade, “Significance of average domain purity and mixed domains on the photovoltaic performance of high-efficiency solution-processed small-molecule BHJ solar cells”, *Adv. Ener. Mater.* (in press)

## ABSTRACT

### Loss Mechanisms in Solution-Processed Small Molecule Bulk Heterojunction Solar Cells

by

Christopher M. Proctor

Amidst looming concerns over increasing carbon emissions and global climate change, solar cells made from solution processed small molecules have garnered considerable attention because of their potential to serve as an economically viable, low-carbon source of electricity. However, as with the other classes of organic materials, organic solar cells made from solution processed small molecules are not yet efficient enough to be commercially viable. The aim of this dissertation is to understand the loss mechanisms that limit the power conversion efficiency of these organic solar cells and to suggest strategies for improvement.

Using a combination of electrical characterization techniques, it was found that two of the primary loss mechanisms in solar cells made from solution processed small molecules include field dependent generation and the recombination of free charge carriers. While field dependent generation is a significant loss mechanism in some cases, it was shown that it can also be completely overcome by careful control of the film morphology. The reduction of field dependent generation was found to be correlated with progressively purer and more ordered domains within the small molecule film.

In contrast to field dependent generation, it was found that in all small molecule solar cells, there is some degree of free carrier recombination particularly at low fields close to open circuit. The nature of this recombination was found to be primarily bimolecular – meaning a free hole recombining with a free electron (as opposed to a trap mediated process). While there is some variation in the rate coefficient of bimolecular recombination between systems, it was shown empirically that the charge carrier mobility is typically the most important determinant of the degree of voltage dependent recombination losses. For a 100 nm solar cell, both holes and electron mobilities should be at least  $10^{-4}$  cm<sup>2</sup>/Vs in order to efficiently extract charge carriers before they recombine. In most material systems, it was found that the hole transporting molecule was the limiting factor in the charge transport of blend films and the hole mobility measured in neat films sets the upper limit for blend films. Further investigation revealed that increased order along the  $\pi$ - $\pi$  stacking direction in donor molecules is correlated with lower activation energy for hole transport however even if donor crystallization is achieved the transport in blend films may still be limited by the number of conductive pathways

## TABLE OF CONTENTS

I.	Introduction.....	1
II.	Charge Carrier Recombination in Organic Solar Cells.....	5
	1. Introduction.....	5
	2. Geminate Recombination.....	10
	2.1 Geminate Recombination Theory and Terminology.....	11
	2.2 Exciton transport to donor/acceptor interface.....	12
	2.3 Charge separation vs. geminate recombination at the donor-acceptor interface.....	13
	2.4 Electric field dependent geminate recombination.....	18
	3. Nongeminate Recombination.....	21
	3.1 Mechanisms of nongeminate recombination .....	22
	3.2 Space charge effects.....	37
	3.3 Surface recombination.....	38
	3.4 Experimental probes of nongeminate recombination.....	38
	3.5 Summary of how nongeminate recombination affects solar cell metrics.....	45
	4. Summary and Perspective.....	46
	5. References.....	48
III.	Nongeminate Recombination and Charge Transport Limitation in Diketopyrrolopyrrole based Solution Processed Small Molecule Solar Cells.....	57
	1. Introduction.....	57

2. Results and discussion.....	59
3. Conclusions.....	80
4. Experimental.....	81
5. Supporting Information.....	88
3. References.....	85
IV. Overcoming Geminate Recombination and Enhancing Extraction in Solution Processed Small Molecule Solar Cells.....	89
1. The Story.....	89
2. Experimental.....	104
3. Supporting Information.....	106
4. References.....	111
V. Importance of Domain Purity and Molecular Packing in Efficient Solution Processed Small Molecule Solar Cells.....	113
1. The Story.....	113
2. Experimental.....	128
3. Supporting Information.....	129
4. References.....	134
VI. Mobility Guidelines for High Fill Factor Solution-Processed Small Molecule Solar Cells.....	137
1. The Story.....	137

2. Experimental.....	147
3. Supporting Information.....	148
4. References.....	152
VII. Understanding Charge Transport in terms of Order and Percolation in Molecular Blend Films.....	155
1. The Story.....	155
2. Summary and Conclusions.....	170
3. Experimental.....	171
4. Supporting Information.....	173
5. References.....	176
VIII. Effect of Leakage current and Shunt Resistance on the Light Intensity Dependence of Organic Solar Cells.....	178
1. The Story.....	178
2. References.....	189
IX. Summary and Outlook.....	190
1. Summary.....	190
2. Outlook.....	191

## **Chapter I**

### **Introduction**

Amidst looming concerns over increasing carbon emissions and global climate change, organic solar cells have garnered considerable attention because of their potential to serve as an economically viable, low-carbon source of electricity. In the context of organic solar cells, there are three primary classes of materials that have shown promising results to date: vacuum deposited small molecules, solution processed polymers and solution processed small molecules. Of these, solution processed small molecules are perhaps the most promising as they offer the advantages of being discrete molecular components (where as polymers suffer from variations in molecular weight and polydispersity) and the ability to be processed on a large scale via techniques such as roll to roll coating and ink-jet printing. However, as with the other classes of organic materials, organic solar cells made from solution processed small molecules are not yet efficient enough to be commercially viable. The aim of this dissertation is to understand the loss mechanisms that limit the power conversion efficiency of these organic solar cells and to suggest strategies for improvement.

Solar cells are typically evaluated by measuring the current density ( $J$ ) as a function of applied voltage ( $V$ ) while the device is illuminated by a solar simulator that matches the AM1.5 solar spectrum. The PCE is then calculated as the ratio of the maximum power output over the incident power of the light source ( $100\text{mW}/\text{cm}^2$  for 1 sun). The maximum

power output ( $P_{out}$ ) of the device is where the product of the current and applied bias is maximum – this is commonly referred to as the maximum power point (mpp). For convenience,  $P_{out}$  is typically calculated from the product of the short circuit current ( $J_{sc}$ ), the open circuit voltage ( $V_{oc}$ ) and the fill factor (FF). The FF is tabulated from the power at the mpp over the product of the  $J_{sc}$  and  $V_{oc}$ . The FF is thus a measure of the voltage dependence of the current between short and open circuit. A FF of 100% would mean the JV curve is a perfect square shape. The current of a diode will always exhibit an exponential dependence on voltage thus a FF of 100% is not theoretically possible however, FF's of 80% in an organic solar cell have recently been predicted and demonstrated<sup>1-3</sup>.

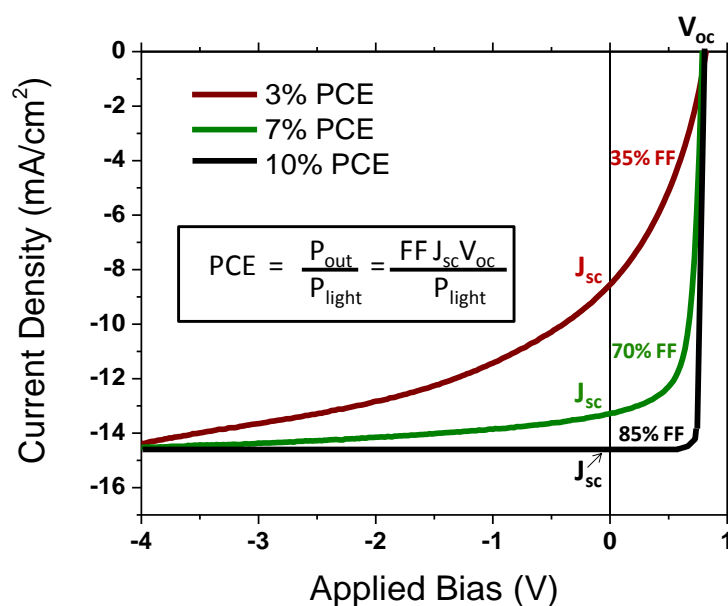


Figure 1.1: Current density versus applied bias for three organic solar cells under 1 sun illumination with PCEs ranging from 3% to 10%.

At the onset of this dissertation, voltage dependent losses were the primary limitation to the efficiency of solution processes small molecule solar cells<sup>4</sup>. Thus, much of the work describe here is focused on understanding the origin of these voltage dependent losses. The

effect of voltage dependent losses on the PCE is illustrated in **Figure 1.1** which shows the JV curves of three different solar cells with PCEs ranging from 3% to 10%. At an applied bias of -4V the three devices have approximately the same current density. However, as the applied bias is reduced shifting to a forward (positive) applied bias the current of the less efficient devices steadily decreases while the current of the 10% PCE device is virtually independent of voltage up until voltages near  $V_{oc}$ . The strong voltage dependence of the 3% and 7% devices reduces their  $J_{sc}$  and FF which in turn leads to a lower PCE compared to the 10% device. To date, the majority of solution processable small molecules that have been used to make solar cells have yielded JV curves that closely resemble the shape of the 3% device shown here where as the ideal case would be JV curves the shape of the 10% device. The origins of these losses are investigated in detail in the subsequent chapters.

With the exception of this chapter and Chapter IX, the work described here has been published or is pending publishing in peer-reviewed journals (see references) and thus the Chapters are composed as standalone works. A brief synopsis of each chapter is below.

- **Chapter II** - A review of research and concepts regarding charge carrier recombination in organic solar cells<sup>5</sup>.
- **Chapter III**- A study investigating the role of nongeminate recombination and charge transport properties on the performance of high and low fill factor solution processed small molecule solar cells<sup>6</sup>.
- **Chapter IV** – A study investigating the influence of field dependent generation and nongeminate recombination in a model small molecule system as a function of device processing conditions<sup>7</sup>.

- **Chapter V** – A study investigating the morphological origins of geminate and nongeminate recombination in a model small molecule system<sup>8</sup>.
- **Chapter VI** – A study on the influence of charge carrier mobility on the solar cell performance of a wide range of small molecule systems<sup>9</sup>.
- **Chapter VII** – A study investigating the nature of and limitations to charge carrier mobility in small molecule based solar cells solar cells<sup>10</sup>.
- **Chapter VIII** – A study investigating the influence of leakage current and shunt resistance on a commonly used technique for understanding the nature of loss mechanisms in organic solar cells<sup>11</sup>.
- **Chapter IX** – A summary of the work described in this dissertation and comments on the outlook for small molecule based organic solar cells.

## References

- [1] D. Bartesaghi, I. del C. Pérez, J. Kniepert, S. Roland, M. Turbiez, D. Neher, L. J. A. Koster, *Nat. Commun.* **2015**, *6*.
- [2] S. M. Sze, *Physics of Semiconductor Devices*, John Wiley & Sons, **1981**.
- [3] X. Guo, N. Zhou, S. J. Lou, J. Smith, D. B. Tice, J. W. Hennek, R. P. Ortiz, J. T. L. Navarrete, S. Li, J. Strzalka, L. X. Chen, R. P. H. Chang, A. Facchetti, T. J. Marks, *Nat. Photonics* **2013**, *7*, 825–833.
- [4] B. Walker, C. Kim, T.-Q. Nguyen, *Chem Mater* **2010**, *23*, 470–482.
- [5] C. M. Proctor, M. Kuik, T.-Q. Nguyen, *Prog. Polym. Sci.* **2013**, *38*, 1941–1960.
- [6] C. M. Proctor, C. Kim, D. Neher, T.-Q. Nguyen, *Adv. Funct. Mater.* **2013**, *23*, 3584–3594.
- [7] C. M. Proctor, S. Albrecht, M. Kuik, D. Neher, T.-Q. Nguyen, *Adv. Energy Mater.* **2014**, *4*.
- [8] S. Mukherjee, C. M. Proctor, J. R. Tumbleston, G. C. Bazan, T.-Q. Nguyen, H. Ade, *Adv. Mater.* **2015**, *27*, 1105–1111.
- [9] C. M. Proctor, J. A. Love, T.-Q. Nguyen, *Adv. Mater.* **2014**, *26*, 5957–5961.
- [10] C.M. Proctor, Y. Huang, A. Kher, A. Sharenko, J.A. Love, E. Kramer, G. Bazan, T.Q. Nguyen, (in preparation).
- [11] C. M. Proctor, T.-Q. Nguyen, *Appl. Phys. Lett.* **2015**, *106*, 083301.

## Chapter II

### Charge Carrier Recombination in Organic Solar Cells

#### 1. Introduction

After humble beginnings [1], organic solar cells have advanced exponentially with recent reports of power conversion efficiencies (PCE) up to 12% [2,3] with a high of 9% in peer-reviewed literature [4]. This remarkable progress means the PCE of organic photovoltaics (OPVs) are now comparable to inorganic PV technologies such as amorphous silicon [5]. In order to maintain momentum and enable further increases in efficiency[6–11], it is vital that the factors governing the performance of OPV devices are identified and understood. Although inorganic and organic PV devices both convert photons to electrical power, the underlying physics and device architectures in organic photovoltaics differ significantly from inorganic photovoltaics. Due to the low dielectric constant of organic materials (approximately 2 - 4) absorbed photons create coulombically bound electron-hole pairs known as excitons that require an additional driving force to separate into free charges. Additionally, while in inorganic semiconductors charges move via band transport, because of the disorder and weak intermolecular forces associated with organic semiconductors their charge transport mechanism is based on localized charge carriers that hop from state to state [12]. Initial organic solar cell development consisted of bilayer device architectures of an electron donating (donor) and an electron accepting (acceptor) material similar to inorganic

p-n junctions [13]. The use of donor and acceptor materials facilitates the splitting of excitons by providing an energetic offset between the materials' lowest unoccupied molecular orbitals (LUMO). Due to the limited exciton diffusion length in organic materials (~10 nm) [14], the transition was made to bulk heterojunction (BHJ) solar cells. In a BHJ architecture the photoactive layer consists of a complex network of interpenetrating donor and acceptor phases with average domain sizes on the order of tens of nanometers. A BHJ morphology thereby greatly increases the interfacial area between donor and acceptor, thus increasing the probability an exciton encounters a donor-acceptor interface and separates into free charge carriers before relaxing to the ground state. The most widely studied BHJ systems are blends of conjugated electron donating polymers with electron accepting fullerene derivatives [4,15,16]. However, BHJs consisting of two small molecules deposited either by solution [17–19] or vacuum sublimation [2,20] have also achieved impressive PCEs.

A simplified overview of the photovoltaic process in OPVs is presented in **Figure 2.1** (for the case of absorption in the donor phase). First, a photon is absorbed creating an exciton. The exciton then transports to an interface with an acceptor. Once at the donor/acceptor (D/A) interface, the electron and hole form a charge transfer (CT) state with the electron on the acceptor and the hole on the donor [21–23]. If the binding energy of the CT state can be overcome the electron will be transferred to the LUMO of the acceptor while the hole is transferred back to the highest occupied molecular orbital (HOMO) of the donor. Due to the internal electric field created by the asymmetry of the electrode work functions, the hole will then drift through the donor domains towards the anode and the electron

through the acceptor domains towards the cathode. Ultimately, these photogenerated charges are collected at their respective electrodes thereby creating a measurable photocurrent.

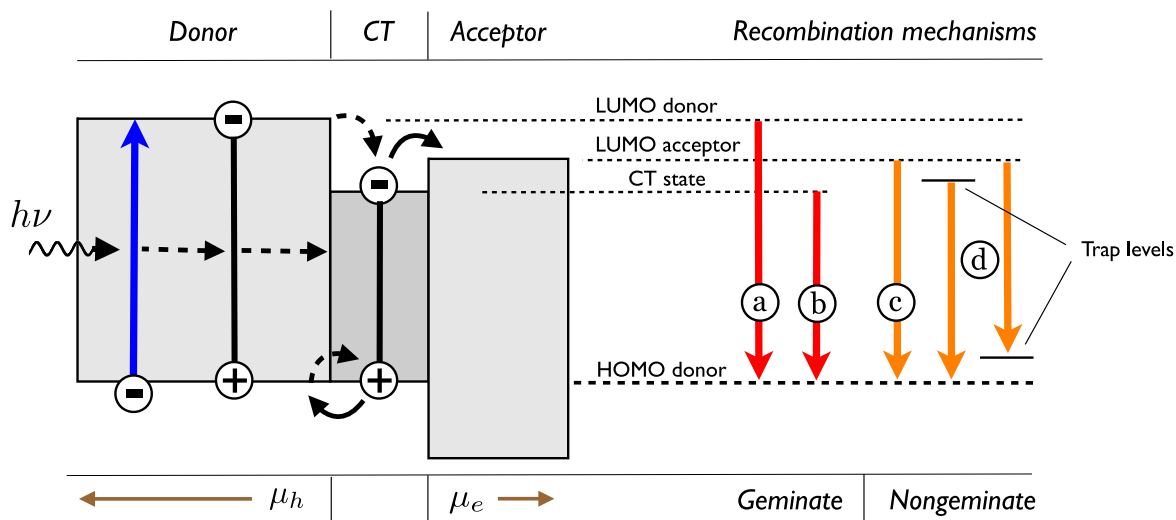


**Fig. 2.1.** *Left:* From left to right. Incoming light is absorbed in the donor material (blue arrow); a bound exciton is formed. The exciton diffuses toward the donor acceptor interface. The exciton transfers onto the interface state i.e. CT state (dashed arrows), after which the exciton dissociates (solid arrows) and the free hole and electron drift through the donor and acceptor phase respectively, to the extracting contacts (brown arrows). *Right:* An overview of the four most encountered recombination mechanisms. The geminate mechanisms: a) exciton decay after excitation, b) recombination through the CT state, and the nongeminate mechanisms: c) recombination of free holes and electrons, d) recombination of free carrier with carrier trapped on sites within the band gap.

Ideally, every incident photon would be successfully converted into an electron and hole that are collected at the electrodes. However, in reality each step of the above photovoltaic process from absorption to collection is wrought with potential loss mechanisms that limit the overall PCE of OPV devices. Once a photon is absorbed, the exciton only has a few nanoseconds to reach a donor-acceptor interface before it relaxes to the ground state (see a. in Figure 2.1). If the domain sizes are larger than the exciton diffusion length the electron-hole pair is more likely to recombine than separate. Those

excitons that do make it to a D/A interface to form a CT state still have some probability of recombining rather than dissociating into free charge carriers (see b. in Figure 2.1). These recombination processes involving an electron-hole pair that originated from a single photon event are referred to as *geminate recombination*. The term geminate comes from the Latin word *gemini* meaning twins – in this context the electron-hole pair are twins born from the absorption of a single photon. Exactly what influences whether a geminate pair will recombine or dissociate into free carriers remains an area of active research. Much initial research focused on the importance of domain size and energetic offsets between the donor and acceptor [16,24,25]. However recent work suggests that other factors such as the delocalization of CT states, molecular reorganization energies, excess energy from above-gap photons, energy of triplet states, phase purity and the internal electric field may also play a significant role in the competition between geminate recombination and the generation of free charge carriers.

After geminate pairs are successfully dissociated into free carriers, the electrons and holes have to make it to their respective electrodes without recombining with another oppositely charged free carrier. This recombination of free electron and holes is referred to as *nongeminate recombination*. The key distinction from geminate recombination is that the hole and electron in nongeminate recombination do not originate from the same photon. As shown in Figure 2.1, nongeminate recombination includes the recombination of a free electron and a free hole known as bimolecular recombination (Figure 2.1b) and trap-assisted recombination (Figure 2.1c) which occurs when a trapped electron (hole) recombines with a free hole (electron). It has been shown that a variety of factors can influence nongeminate recombination in OPV devices including charge carrier mobilities, phase separation,

energetic disorder, chemical impurities and active layer thickness. Several noteworthy trends have emerged from the investigation of nongeminate recombination. First and foremost, it is evident that bimolecular recombination is the primary loss mechanism in most efficient OPV systems. Furthermore this recombination can be significantly reduced compared to the Langevin description of bimolecular recombination in disordered materials due to the spatial dependence of carrier density distributions, phase separation, energetic disorder and the re-release of free carriers that form a CT state before recombining. Just as noteworthy is the suggestion that energetic traps may play a significant role in shaping the kinetics of nongeminate recombination not only in systems with known chemical impurities but also in the more efficient OPV systems where bimolecular recombination dominates.

In this review article on recombination mechanisms in organic solar cells we will present the theory and experimental evidence for the various recombination processes described above. The article naturally divides into two parts: 1) geminate recombination and 2) nongeminate recombination. As these topics have been reviewed in the past [26–32], a particular emphasis will be placed on more recent advances and emerging trends. Special attention will also be given to highlighting experimental techniques and relating recombination mechanisms to the basic solar cell metrics (short circuit current ( $J_{sc}$ ), fill factor ( $FF$ ) and open circuit voltage ( $V_{oc}$ )). Finally, we will conclude with a summary of the current understanding of recombination in organic solar cells while highlighting areas that are still not well understood and that therefore should serve as the focus of future investigations.

## 2. Geminate Recombination

As discussed in the introduction, there exist two distinct processes that must occur in order for a photovoltaic device to work: 1) photogeneration of free charge carriers and 2) collection of photogenerated charge carriers. In OPVs, this first step, the process of going from absorbed photon to free charge carriers, is complicated by the relatively strong Coulomb force between the photo-excited geminate electron-hole pair. In order for a geminate pair to separate into free charges, the Coulomb binding energy must be overcome; otherwise the pair will recombine in a process commonly referred to as geminate recombination. For simplicity, in this article we use the term free charge carriers to describe electron and holes that are not Coulombically bound however, it should be noted that the often used term polaron, which is a charge plus the accompanying lattice distortion, is technically more correct in the context of organic semiconductors.

It is known that some OPV systems convert absorbed photons to free electrons with near 100% efficiency, however, many more systems evidently do not [19,26,27,29]. In such systems, geminate recombination losses can significantly limit the photocurrent ( $J_{sc}$ ). It has also been shown that the magnitude of geminate recombination can increase with an applied bias thereby also limiting the  $FF$  [33–35]. Thus, overcoming geminate recombination losses is essential in order to maximize PCE. In the subsequent sections we will present the theory and terminology associated with geminate recombination and then discuss the implications of recent studies into the basic mechanisms of charge generation.

## 2.1 Geminate Recombination Theory and Terminology

Geminate recombination occurs when a hole and electron that originate from the same photon recombine before separating into free charges. By definition, this includes the loss of excitons that relax to the ground state before they can diffuse to an interface as well as geminate pairs that recombine at a D/A interface. It is worth noting, however that many reports in the literature limit the use of geminate recombination to describe only the recombination of geminate pairs at a D/A interface. Typically, this interfacial geminate recombination occurs after formation of a CT state where the electron resides in the acceptor and the hole in the donor. In this review, we use the term CT state to describe geminate pairs at the D/A interface however there are multiple synonyms in the literature including exciplex, bound polaron pair, CT complex and CT exciton [36]. Regardless of what processes are involved in separating CT states, geminate recombination is driven by the Coulomb attraction between the geminate electron-hole pair.

Geminate recombination is considered a single body, monomolecular process. The number of geminate pairs that are able to recombine geminately scales linearly with the number of absorbed photons. However, it is important to note that at light intensities comparable to one sun the probability of any given geminate pair recombining is independent of the total density of geminate pairs. The consequence of this is that the *fraction* of geminate pairs lost to geminate recombination is the same at low light intensities as it is at higher light intensities. Thus, the photocurrent of a system limited only by geminate recombination would scale linearly with light intensity. At light intensities exceeding several suns, other recombination processes such as exciton-exciton or exciton-charge annihilation may become significant [37].

## *2.2 Exciton transport to donor/acceptor interface*

Once a singlet exciton is created it must migrate to a D/A interface in order to dissociate into free charge carriers. Until recently it was generally thought that this transport occurs entirely by diffusion. Thus donor and acceptor domain sizes have long been targeted to be similar to the exciton diffusion length – typically 3 – 30 nm for OPV materials [14,38,39]. However, ultrafast transient absorption studies suggest that a majority of free carriers in efficient OPV systems are photogenerated within 100 fs, far too fast a process to involve exciton diffusion [26,40–45]. Kaake et al. observed photogeneration on sub 100 fs times scales followed by additional generation on picoseconds timescales thought to be from excitons diffusing to charge-separating heterojunctions [46]. The authors posited that the ultrafast transport mechanism is made possible by delocalized excited states consistent with the previous observation of crystalline domains in the same system [47]. Though the precise mechanism of ultrafast migration to the D/A interface remains unclear, it is worth noting that it has been shown that this ultrafast process is also influenced by domain size in a manner similar to that expected for an exciton diffusion process [40]. This may help explain the strong correlation between domain size and generation efficiency seen in many systems [40,48–50].

Experimentally, the efficiency of exciton transport to the D/A interface is typically gauged by comparing the photoluminescence (PL) of the blend film to the PL of the neat material. Excitons that are not quenched by reaching the D/A interface have some probability of recombining radiatively just as they would in the neat film. Therefore, PL spectrally similar to that of the neat material detected in the blend film is suggestive of excitons that originate in domains larger than the exciton diffusion length. Optimized BHJ

OPV systems have been shown to exhibit PL quenching exceeding 99% indicating that nearly every exciton reaches an interface [44]. It is worth noting that this comparison assumes 100% quenching efficiency of the acceptor, which at least has been shown to be the case for fullerene derivative acceptors such as phenyl-C<sub>61</sub>-butyric acid methyl ester (PCBM) [44].

### *2.3 Charge separation vs. geminate recombination at the donor-acceptor interface*

When an electron-hole pair reaches the D/A interface, charge transfer is initiated by the energetic offset between donor and acceptor. However, the electron-hole pair remains coulombically bound across the D/A interface due to the poorly screened Coulomb potential, forming what is known as a charge transfer state [31,32,36,51–53]. The binding energy of this CT state has been estimated to be a few hundred millielectronvolts [32,54,55] – an order of magnitude higher than the thermal energy at room temperature. As shown in **Figure 2**, once electron-hole pairs form a CT state, dissociation into separated charges (CS) is in competition with geminate recombination to the ground state and transfer to a triplet state. If the triplet state is sufficiently lower in energy than the CT state ( $< 0.1$  eV) it can serve as a loss mechanism by providing an efficient pathway to deactivation of CT states [32,56,57]. In the case that transfer to the triplet state is not energetically favorable, geminate recombination directly to the ground state will be the primary loss mechanism for CT states. This recombination can be radiative as evidenced by PL emission that is characteristically red-shifted compared to the pure material film emission [51,58]. Measuring non-radiative geminate recombination from CT states is experimentally challenging as geminate recombination typically occurs on sub-nanosecond timescales. However, geminate losses in a variety of OPV systems have been observed optically and electrically using transient

absorption techniques [31,57,59–66] and time delayed collection field experiments (TDCF) [33,67–69]. Multiple reports have also inferred geminate losses based on analysis of device photocurrents and quantum efficiencies [70–73].

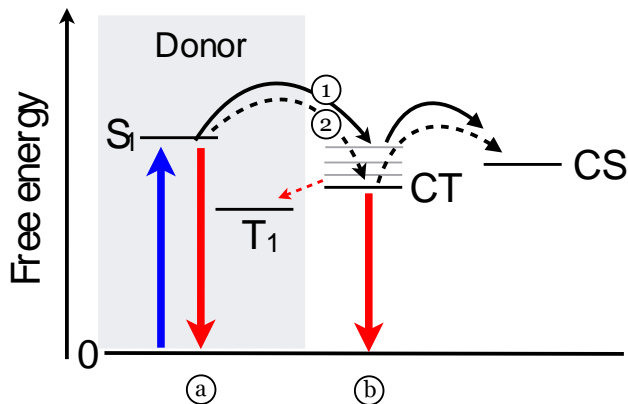


**Fig. 2.2.** This Jablonski diagram shows the excitation of the donor singlet state and the recombination into the triplet state from the CT state (dashed red arrow). The solid black arrows labeled (1) represents geminate pairs that transfer into higher energy, hot CT states (grey lines) before almost instantaneous separation into the charge-separated state (CS). The black dashed arrows labeled (2) indicate the transfer of electron and hole from the donor singlet state to the CT state with the possibility to relax down to the CT ground state (solid line) where they *may* need additional energy to dissociate into the charge-separated state (CS). The red arrow labeled (a) indicates decay of an exciton to the ground state before it can make it to the D/A interface while the red arrow labeled (b) represents geminate recombination at the D/A through the CT state.

There has been much discussion in the literature about what determines whether electron-hole pairs at D/A interfaces will dissociate into free charges or recombine. In principle, electron-hole pairs will only split into free charges if the energy gain in doing so is larger than the Coulombic binding energy. Electron transfer from donor to acceptor and/or hole transfer from acceptor to donor produces an electron or hole, respectively, at a lower potential, thus providing the driving force for exciton dissociation. A distinct trend of increasing D/A energetic offsets (both  $LUMO_D-LUMO_A$  and  $HOMO_D-HOMO_A$ ) corresponding with greater charge separation efficiency has been observed in a variety of OPV material systems[57,74,75]. Several other studies in the literature often cite a 0.3 eV

offset between donor and acceptor LUMO levels as a universal prerequisite for efficient exciton separation. However the theoretical basis for this standard is limited [31] and numerous exceptions have been observed [58,76,77]. It is also worth noting that LUMO energy levels measured of single materials by solution cyclic voltametry or optical transitions can only be taken as a rough estimate of the energetics that influence the charge dissociation process in material blends [27,32]. In addition to energy level offsets, other studies have proposed that doping[78], charged defects[79], mixed phases[80] and entropy gains from increased electron and hole separation[31,81] may contribute to the free energy gradient and thereby help charge separation.

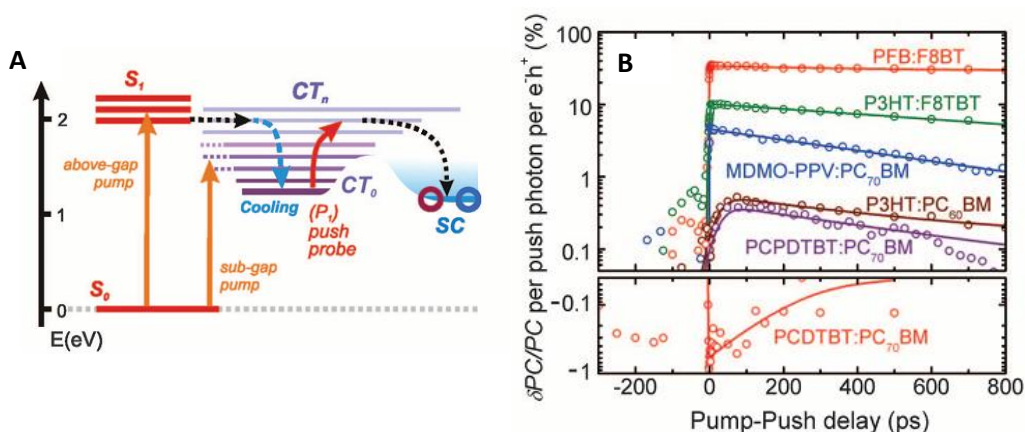


**Fig. 2.3:** (A) Free energy state diagram for an OPV system showing the Singlet states ( $S_1$ ), relaxed CT state ( $CT_0$ ), higher energy CT band states ( $CT_n$ ) and separated-charge states (SC). The increasing width of  $CT_n$  states is indicative of increasing delocalization. Solid arrows show optical transitions and dashed arrows indicate energy and charge transfer pathways involved in photoconversion. The red arrow represents the IR push pulse in the experiments conducted by Bakulin et al. (B) The results of pump-IR push photocurrent experiments on a set of OPV systems under above-gap excitation [60].

The role of electronic delocalization in the charge separation process has also been explored. There is compelling evidence that short lived, ( $<1$ ps) hot, and delocalized CT band states can enable geminate pairs to overcome their Coulombic attraction by increasing the

effective electron-hole pair separation [31,32,57,60,64,65,82–84]. For instance, using an electro-optical pump-push experiment, Bakulin et al. found that after exciting a variety of OPV systems either in the visible range or directly into sub-bandgap CT states, a subsequent infrared (IR) push pulse yielded an increase in photogenerated charges [60]. These results are shown in **Figure 2.3** where  $\delta PC/PC$  is the percent change in photocurrent after the IR push. The effect of the IR push on photogeneration roughly scaled with the amount of bound charges in localized CT states for each system. The authors concluded the IR push pulse gives geminate pairs that have relaxed to bound CT states a second chance to dissociate by pushing them back to higher energy states similar to the early time hot states formed directly after the separation of singlet excitons. Further evidence of hot CT states came from Jailaubekov et al [83]. In this work, transient two-photon photoemission spectroscopy was used to directly measure the photoemission of electrons from hot charge transfer states in films with copper phthalocyanine (CuPc) and C<sub>60</sub>. They found electrons from hot CT states to be about 0.3 eV higher in energy than electrons from relaxed CT states and conducted simulations to show the interfacial charge distribution for hot CT states is more favorable for charge separation. Other recent studies have observed that in some low bandgap polymer/fullerene systems, the excess energy from absorbing above bandgap photons leads to faster and more efficient generation of free charge carriers consistent with a hot CT state framework [82,84]. In a separate study Bakulin et al. [74] noted that the probability of populating hot CT states favorable for charge separation increases with the energetic offsets between LUMO<sub>D</sub>-LUMO<sub>A</sub> and HOMO<sub>D</sub>-HOMO<sub>A</sub>. This may explain why the generation efficiency in systems with large energetic offsets are insensitive to temperature [85,86] and

excitation wavelength [87,88] while some systems with small offsets ( $< 0.1\text{eV}$ ) are sensitive [82,84].

The evidence supporting the importance of hot CT states is not, however, ubiquitous. A similar generation efficiency for direct excitation of CT states and above band gap excitations has been reported in several polymer/fullerene systems, implying that at least for the systems considered hot CT states are not essential to the generation process [58,89,90]. Jailaubekov et al. speculated that in these particular systems it may be that the presence of favorable gradients in the interfacial energy landscape that reduces the energy barrier for charge separation to less than the thermal energy. In support of this it was noted that at lower temperatures it's expected that the excess energy of hot CT states may be more important as was observed [89]. Simulations have indicated the difference in ionization potentials and polarizations at the D/A interface compared to the bulk is likely to mitigate the importance of hot CT states in the generation process [91]. The notion that the influence of excess energy would be system dependent is clearly demonstrated in **Figure 2.3**. Depending on the system pushing relaxed CT states back into higher energy hot CT states can have almost no effect or it can almost double the observed photocurrent. In the case of the highly efficient poly[N - 9'-hepta-decanyl-2,7-carbazole- alt-5,5-(4',7'-di-2-thienyl-2',1',3'-benzothiadiazole)] (PCDTBT):PCBM system [87] it was observed to have a slightly negative influence on the photocurrent which was attributed to increased fast nongeminate recombination. Thus, it stands to reason that in the highly efficient systems like PCDTBT:PCBM the relaxed CT state is sufficiently delocalized negating the need for excess energy to facilitate efficient charge separation. Nonetheless, further investigation is needed to understand why some

systems exhibit efficient charge generation from relaxed CT states [58,89,90] while in others it appears that charges in relaxed CT states are most likely to recombine [60].

Arguments about hot vs. relaxed CT states aside, further evidence for the role of delocalization in the generation process comes from studies that have looked at the influence of aggregated and crystalline domains on the charge separation efficiency. The prevailing theme in these studies is that aggregated and crystalline domains reduce geminate recombination in favor of increased charge separation at the D/A interface [45,48,66,92–96]. Given the established relation between aggregated or crystalline domains and electronic delocalization [60], this trend strongly supports the notion that delocalized states enhance the charge separation efficiency.

Altogether the breadth of work from the literature suggests that the accessibility of delocalized CT states is a function of not only molecular properties (ie. conjugation length [97], reorganization energy [60,82,83], LUMO degeneracy[92,93], etc.) but also film properties (alignment of donor molecular orbital relative to the acceptor [32,98], degree of crystallinity, etc.). Nonetheless, further study of basic structure-functional relationships is needed in order to better define the general guidelines for the development of new materials and processing techniques that can take advantage of delocalized CT states to allow for near unity charge separation efficiency.

#### *2.4 Electric field dependent geminate recombination*

It has been observed that the charge separation efficiency is electric field dependent in some, but not all, OPV systems [34,35,69,99–101]. Though no universal standards have emerged, it does seem that the most efficient OPV systems with  $FF$ 's exceeding 0.65 generally do not exhibit field dependent geminate recombination losses [26,67,69,102,103].

Interestingly, it has also been observed that the field dependence of generation can be phase dependent— particularly in systems with large PCBM domains [101,104].

In systems known to have field dependent geminate losses, the internal electric field in the device helps dissociate geminate charge pairs into free charges. Thus, the rate of dissociation and with this the magnitude of geminate recombination changes with applied bias – a reverse bias increases the magnitude of the internal field, thereby increasing the charge separation efficiency, while a forward bias weakens the internal field, thereby increasing the probability of geminate recombination. Due in part to the complexity of differentiating the voltage dependence of dissociation from the voltage dependence of extraction and nongeminate recombination, the issue of field dependent geminate recombination has been the subject of much debate in the literature. Further complicating the matter is the fact that the strength of the field dependence of geminate recombination varies between different materials systems and even processing conditions for the same system [33,99,101]. This phenomenon was well illustrated by the TDCF experiments conducted on a low band gap polymer:fullerene system [33]. In TDCF, a bias is applied to a solar cell device which is then pulsed with a laser. After a delay time as short as 10 ns, a strong collection bias is applied to sweep out all photogenerated charge carriers. Using this technique, the voltage dependence of geminate recombination can be measured directly by observing the total photogenerated charges collected ( $Q_{tot}$ ) as a function of the initial applied bias. As shown in **Figure 2.4**, Albrecht et al. found that the  $Q_{tot}$  from solar cell devices pulsed with a laser depended strongly on the voltage applied within the first ten nanoseconds after absorption. Processing devices with diiodooctane (DIO) solvent additive slightly mitigated this field dependence. However, it is evident that the field dependent geminate

recombination still heavily influenced the steady-state current voltage characteristics even in the device with DIO as shown in Figure 2.4.

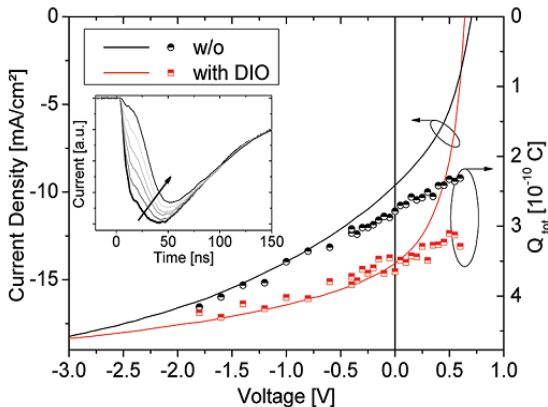


**Fig. 2.4:** Current-voltage response of a polymer:fullerene device processed with (red line) and without DIO (black line) plotted along the  $Q_{tot}$  measured as a function of voltage in the same devices (red and black symbols, right y-axis) using TDCF. The inset presents the TDCF measured photocurrent transients for an exemplary device with the arrow pointing in the direction of increasing forward bias [33].

The development of a theory that accurately describes the precise relation between charge separation efficiency and electric field remains an area of active research. Many studies have used the Onsager-Braun formalism [105,106] to model the field dependence in OPVs [27,72,96,107], however, it has since been shown that many systems do not exhibit the electric field or temperature dependencies predicted by the Onsager-Braun model [26,67,102]. According to Monte Carlo simulations by Deibel et al., varying degrees of delocalization along conjugated segments could account for differences in field dependent geminate recombination [97]. Other models and experimental evidence further indicate that there is a connection between crystalline phases that form extended, loosely bound CT states and the electric field dependence of charge separation [33,80,99]. Additionally, there is evidence that the molecular geometry at the D/A interface can significantly affect the

binding energy of the CT state and thus may also influence the electric field dependence and hence the  $FF$  and/or magnitude of the device  $J_{sc}$  [91,98,108,109]. Probing the molecular orientation at the D/A interface is experimentally challenging. Nonetheless recent work on model bilayer systems [98,108] and the development of new characterization techniques [110,111] provide a viable path for future experimental investigation and understanding of the role donor-acceptor molecular interfacial geometry plays in the charge generation process.

### 3. Nongeminate Recombination

Once a photogenerated charge carrier successfully separates from its geminate counter charge, the internal electric field in the device drives it toward the electrodes. Holes drift to the anode while electrons drift to the cathode. The maximum photocurrent is achieved when all of these charges are collected at the electrodes. However, even in the best OPV devices, as a forward bias is applied the driving force for charge extraction decreases and so too does the charge collection efficiency [26,27]. How sensitive the charge collection efficiency in a given system is to a change in bias is reflected in the fill factor. A high  $FF$  ( $>0.65$ ) indicates that a forward bias has only a small effect on the collection efficiency up until the maximum power point. Regardless of how high the  $FF$  is, when the forward bias is equal to the open circuit voltage, all photogenerated free charge carriers recombine and the net current flowing out of the device is zero. Thus, unlike geminate recombination losses which can be completely overcome, *all* OPV devices are subject to the recombination of free charges - at least at low internal fields (ie. close to  $V_{oc}$ ) [26,27]. This recombination is known as *nongeminate recombination*. As we will discuss in the subsequent sections,

depending on the system and incident light intensity, nongeminate recombination may limit the  $J_{sc}$ ,  $FF$  and  $V_{oc}$ .

### 3.1 Mechanisms of nongeminate recombination

The term nongeminate recombination encompasses the recombination of any free charge carriers that do not originate from absorption of a single photon. In addition to photogenerated charge carriers, nongeminate recombination may also involve injected charge carriers. The recombination originating from these nongeminate charge carriers can be observed as three fundamentally different mechanisms: trap-assisted (monomolecular, **Figure 2.5a**), bimolecular (**Figure 2.5b**), and auger (trimolecular, **Figure 2.5c**). As we will discuss below these three processes exhibit first, second and third order dependence on charge carrier density respectively.

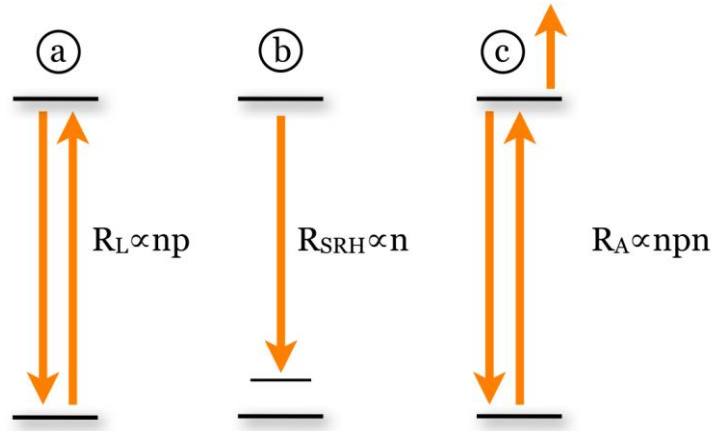


**Fig. 2.5:** This figure depicts the nongeminate recombination mechanisms. a) Represents bimolecular Langevin recombination where the rate is dependent on both hole and electron mobilities and densities. b) Represents trap-assisted Shockley-Read-Hall recombination where the rate depends on the electron (hole) mobility and density combined with the amount of hole (electron) traps. c) Depicts Auger recombination wherein the recombination of an electron-hole pair excites an electron from the HOMO back into the LUMO and the rate therefore has a third order dependence on carrier density.

#### 3.1.1 Bimolecular Recombination

The most commonly observed [26] nongeminate recombination in OPV devices is that of the bimolecular mechanism: the recombination of a free electron with a free hole as depicted in **Figure 2.5a**. In a disordered semiconductor with localized charge carriers, bimolecular recombination is limited by the rate at which oppositely charged carriers find one another. The faster charge carriers move, the faster they will find each other; consequently, the rate of bimolecular recombination in OPV is proportional to the charge carrier mobilities. This is described by the Langevin expression [112] following the relation,

$$R_L = \frac{q}{\varepsilon} (\mu_n + \mu_p)(np - n_i^2), \quad (2.1)$$

where  $q$  is the elementary charge,  $\varepsilon$  the dielectric constant,  $\mu_n$  the mobility of the electrons through the LUMO of the acceptor,  $\mu_p$  the mobility of the holes through the HOMO of the donor,  $n$  and  $p$  represent the electron and hole charge density respectively and  $n_i$  is the intrinsic carrier concentration. This relation describes recombination of two mobile opposing charge carriers attracted to each other in their mutual Coulomb field. Such a behavior is characteristic for materials in which the mean free path of the charge carriers is smaller than the Coulomb capture radius

$$r_c = \frac{q^2}{4\pi\varepsilon_0\varepsilon_r k_B T} \quad (2.2)$$

,where  $T$  is temperature, at which the Coulomb binding energy between an electron and hole equals the thermal energy  $k_B T$ . The charge transport in organic semiconductors is of a hopping nature, with a typical hopping distance of 1–2 nm, whereas  $r_c$  amounts to about 18.5 nm at  $T = 300$  K ( $\epsilon_r = 3$ ). Therefore, the manifestation of Langevin recombination in organic semiconductors is expected [113] and observed [114]. Though the rate is often reduced relative to Equation 1 (See Section 3.1.1.2), Langevin-type recombination has been observed in a large variety of OPV systems [115–119].

Obviously the observation of nongeminate recombination is not restricted to organic solar cells alone; the principle mechanism of organic light emitting diodes is of the nongeminate Langevin-type [120–122]. Being originally derived in 1903 from recombination processes of ions in a gas, the applicability of the Langevin expression in organic semiconductors in general has been an evolving process. Where the recombination in gases is isotropic, the transport, and thus recombination, in organic materials is shown to be of a percolative nature [123] leading to a filamentary transport structure with differences in local current densities that can vary over many orders of magnitude [124–128]. Inconsistencies in the active layer that arise from common film preparation methods such as spin-coating [129] may also contribute to predicted perturbations of Langevin type recombination [130,131].

In particular, an accurate description of the mobility in the Langevin expression for organic solar cells has taken time to develop. In the early years of organic solar cells, mobilities were considered as constant with the argumentation that a solar cell will operate at very low voltages, below  $V_{oc}$ , so the possible field dependence of the mobility will not play an important role [72][132]. Later, it was shown that multiple processes (photocurrent,

geminate recombination, etc.) exhibit a field dependence thus motivating the inclusion of field dependent mobilities in the Langevin equation [33]. The fact that the active layer in OPV devices is a blend of hole and electron transporting materials further complicates the issue. Since carrier transport has a percolative behavior the individual carrier transport mechanisms are heavily influenced by the ratio and morphology in the blend [49,133]. For example, pristine poly[2-methoxy-5-(3',7'-dimethyloctyloxy)-1,4-phenylenevinylene] (MDMO-PPV) comprises a hole mobility of  $5 \times 10^{-11} \text{ m}^2/\text{Vs}$ . In an optimized blend with 80wt% PCBM the hole mobility increases 2 orders of magnitude up to  $1.4 \times 10^{-8} \text{ m}^2/\text{Vs}$  [134]. Pristine poly(3-hexylthiophene) (P3HT) has a hole mobility of  $1.4 \times 10^{-8} \text{ m}^2/\text{Vs}$  [134] and is hardly affected by thermal annealing. In an as cast blend with PCBM the P3HT hole mobility drops almost 4 orders of magnitude and the PCBM electron mobility drops by 1 order of magnitude with respect to its pristine value of  $2 \times 10^{-7} \text{ m}^2/\text{Vs}$ . After annealing at 120 °C, favorable phase separation leads back to pristine values for P3HT hole and PCBM electron mobilities [135]. Thus in terms of the Langevin description, it is evident that blend film mobilities are the relevant measure as the pristine film mobility is not necessarily representative of transport in the solar cell device.

### *3.1.1.1 Implications for mobility*

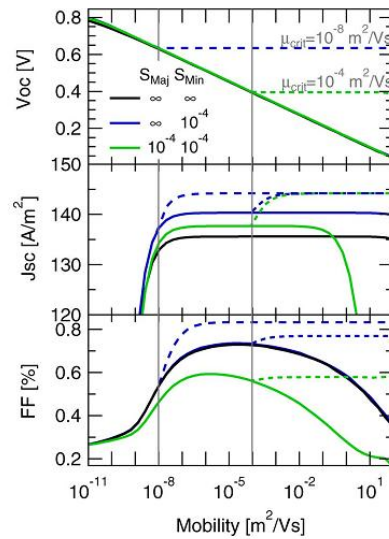


**Fig. 2.6:** Calculated dependence of  $V_{oc}$ ,  $J_{sc}$ , and  $FF$  on charge carrier mobility assuming reduced Langevin recombination ( $\zeta = 0.1$ ). Solid black, blue, and green lines represent different surface recombination velocity combinations for majority ( $S_{maj}$ ) and minority ( $S_{min}$ ) carriers; dashed lines are for the case in which the mobilities that determine the recombination rate are capped at  $\mu_{crit} = 10^{-8}$  (blue) and  $10^{-4}$  (green)  $m^2V^{-1}s^{-1}$  [136].

Surveying the Langevin expression one may expect that higher mobility materials would yield solar cell devices with higher recombination rates. However, simulations have shown that the net bimolecular recombination yield in OPV devices generally decreases with increasing mobility[136,137]. This is because increased mobility also reduces the charge carrier density as a result of improved charge extraction. Thus, in the context of organic solar cells, increased mobility is not expected to lead to a net increase in nongeminate recombination. In contrast, if the charge carrier mobility is too low than the inability to efficiently sweep out photogenerated charges will lead to more nongeminate recombination because the charge carrier density within the device will be higher. As shown in **Figure 2.6**, simulations by Wagenpfahl et al. suggest that for an active layer thickness of 100 nm, the  $FF$  and  $J_{sc}$  will drop off sharply for charge carrier mobilities less than  $10^{-8} m^2/Vs$  [136,137].

Empirical evidence across a wide range of systems presents a similar trend between mobility and FF [137–141] indicating that  $10^{-8} \text{ m}^2/\text{Vs}$  may serve as a rule of thumb for the minimum mobility required for efficient OPV performance. Note that this applies to both hole and electron mobilities. As we will discuss in Section 3.2, imbalanced mobilities can lead to a buildup of space charge that inhibits charge collection.

### 3.1.1.2 Reduced Langevin Recombination

While the presence of Langevin recombination has been satisfyingly confirmed in many organic semiconductors, the strength of this mechanism in OPV devices is often found to be less than that predicted by the Langevin expression [27,28,33,99,102,116,139,142–146] and not higher. This has led to the addition of another term,  $\zeta$ , commonly referred to as the Langevin-reduction factor in expressions for the net bimolecular recombination rate,  $R_{BI}$ . Neglecting the relatively small  $n_i$  and assuming the density of holes and electrons is the same ( $n = p$ ),

$$R_{BI} = \gamma_{BMR} n^2 \quad (2.3)$$

where  $\gamma_{BMR}$  is bimolecular recombination coefficient defined as  $\gamma_{BMR} = \zeta \frac{q}{\epsilon} (\mu_n + \mu_p)$ .

Most polymer:fullerene BHJ systems studied to date seem to have a  $\zeta$  between 0.01 to 1 [28,99,116,139,142,143,147] with some reports for the P3HT:PCBM system finding  $\zeta$  as low as  $10^{-3}$  [145,146].

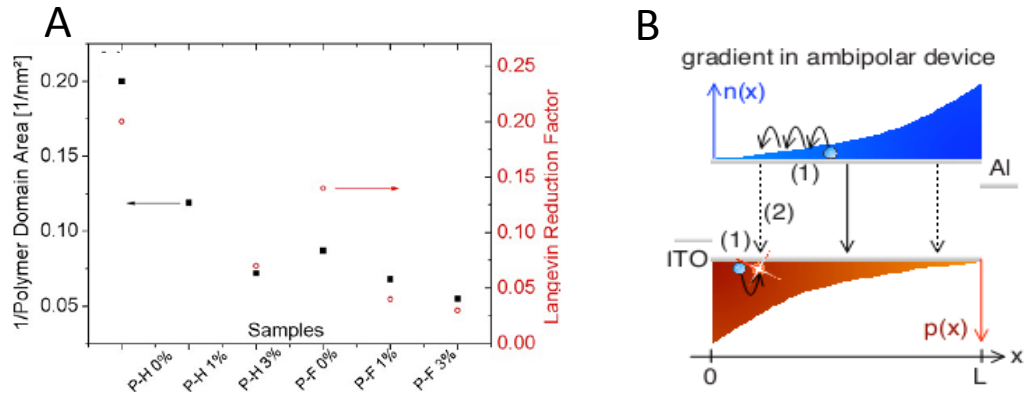


**Fig. 2.7 (a)** Comparison of the inverse mean polymer domain area estimated from energy filtered TEM (left scale, black) with the Langevin reduction factor (right scale red) for two different polymer:fullerene systems (P-H and P-F) processed with different concentrations of DIO solvent additive (0%, 1% and 3%) [99]. **(b)** Illustration of expected hole and electron spatial gradients as a function of position ( $x$ ) in a device of thickness  $L$  [148].

The origin of reduced Langevin recombination (also commonly referred to as non-Langevin recombination) has been explored by several groups. Generally speaking it is expected that the inherent phase separation in BHJ blends would reduce the probability of opposing charge carriers finding one another thereby suppressing the recombination rate compared to a system in which holes and electrons were homogeneously distributed. Multiple studies have observed a correlation between increased phase separation (larger domain sizes) and reduced Langevin recombination [44,45,99,115]. **Figure 2.7a** presents the results of one such study that considered two different polymer:fullerene systems (noted as P-H and P-F in **Figure 2.7a**) as a function of processing with different DIO concentrations (0%, 1% and 3%) [99]. The polymer domain area, estimated from plasmon based energy-filtered transmission electron microscopy (TEM), clearly shows a correlation with the measured Langevin reduction factors across all conditions.

After the first observations of reduced recombination, the presence of phase separation lead to the suggestion that recombination is actually limited by the rate at which the slowest charge carrier can reach a D/A interface instead of the fastest carrier as would follow from Equation 1 (which is in most cases is the electron transport through the fullerene [149,150]). This was strengthened by the notion that the mobility should be taken as a spatial average [72][151], as was originally proposed by Langevin [112]. Subsequent investigation however, found that such a model is inconsistent with the observed temperature dependence of  $\zeta$  and it was proposed that  $\zeta$  is at least in part due to the spatial variation of electron and hole carrier densities [148] (see **Figure 2.7b**). Combined with the earlier finding that the carrier density in organic LEDs is heavily influenced by carrier diffusion from the contacts [152] this notion is particularly important because most optimized organic solar cells are rather thin, in the 100 nm range, making them very susceptible to this effect [153]. Spatial variation in the carrier density profile may well explain why some systems (such as P-H 0% in **Figure 2.7a**) with an apparently homogenous mixture of donor and acceptor still exhibit reduced recombination.

Modeling by Groves and Greenham led to the conclusion that the combination of the effect of domain size, electron-hole mobility mismatch, and energetic disorder can only account for reduction factors up to about one order of magnitude. It was then suggested that further reductions in P3HT:PCBM are likely the result of deep carrier trapping [130]. The idea of deep trapping contributing to  $\zeta \ll 0.1$  seems to be consistent with other observations of trap-assisted recombination in the highly reduced P3HT:PCBM system but not in other systems with more modest reduction factors ( $>0.1$ ) [149,154]. This subject remains

controversial however as other studies have looked for but not found evidence of deep traps in P3HT:PCBM [155].

Another important consideration in the context of reduced Langevin recombination is that since bimolecular recombination primarily happens at the D/A interface, much like geminate recombination it too likely occurs via CT states. Measurements of electroluminescence from injected charges recombining radiatively through CT states seemingly confirm that this is the case [36,52]. It follows then that once the CT state is formed by two free carriers there may still be some probability that these carriers will separate again [27,105,106]. Therefore the same factors that suppress geminate recombination via CT states (energetic cascades, increased delocalization, etc.) may also contribute to suppressed bimolecular recombination. Recent experimental and theoretical work seems to support this conclusion [92,156–158] which only adds to the imperative to further define exactly how to enhance the charge separation efficiency out of CT states.

### *3.1.2 Trap-assisted recombination*

Trap-assisted recombination is a first order process in which one electron and one hole recombine through a localized energetic trap (**Figure 2.5b**). Though it involves two carriers, it is still considered monomolecular recombination because it involves one carrier at a time; first one carrier is trapped and then the second, oppositely charged, carrier must find the trapped carrier. The recombination rate is ultimately determined by the amount of sites that act as traps and by how quickly the free carrier can find the trapped carrier. A model for trap-assisted recombination in inorganic semiconductors, known as Shockley-Read-Hall (SRH) recombination[159][160], was established in 1952 and has recently been applied to organic systems including PLEDs [120–122,161,162] and OPVs [26,141,147,149,154,163–168].

According to SRH, the rate of this trap-assisted recombination process is described by the relation,

$$R_{SRH} = \frac{C_n C_p N_{tr} (np - n_i^2)}{[C_n (n + n_1) + C_p (p + p_1)]} \quad (2.4)$$

where  $C_n$  denotes the probability per unit time that an electron in the conduction band will be captured for the case that the trap is empty and able to capture an electron. Correspondingly,  $C_p$  indicates the probability per unit time that a hole will be captured when a trap is filled with an electron and able to capture the hole.  $N_{tr}$  is the density of electron traps. And  $n_1 p_1 = n_i^2$  their product under equilibrium conditions in the case that the Fermi level coincides with the position of the recombination centers where  $n_i$  denotes the intrinsic carrier concentration in the sample.

Application of the Shockley-Read-Hall formalism has led to the introduction of an additional observable: the capture coefficient. Fortunately it has been recently suggested [132], and demonstrated [161], that in organic devices where  $n = p$  and  $np \gg n_1 p_1$  for the case of electron traps the SRH equation reduces to  $R_{SRH} = C_p N_{tr} p$ , where the capture coefficient is observed to be thermally activated leading to  $C_p = \frac{q}{\epsilon} \mu_p$ . This essentially implies that trap-assisted recombination in organic semiconductors is governed by the diffusion of the free carrier (hole/electron) towards the trapped carrier (electron/hole), similar to the Langevin recombination for free carriers where both carriers are mobile. As a

result, similar to Langevin recombination, trap-assisted recombination is also shown to be thermally activated and dictated by the free carrier transport [161].

In most BHJ solar cells, the electron mobility originates from transport through the LUMO of the acceptor phase (often PCBM) to the cathode, whereas the hole mobility is governed by transport through the HOMO of the donor material towards the anode. The transport through pristine PCBM is found to be trap free,  $\mu_n = 2 \times 10^{-7} \text{ V/m}^2\text{s}$ , and limited by space charge [150]. Since in most cases fullerene derivatives are known to be trap free, traps in the donor material or general impurities are the origin of most trap-assisted recombination processes observed in organic photovoltaics [163,164,166], [169]. It is worth mentioning, the observation of space charge does not rule out the presence of traps and trap-assisted recombination will be present to some degree in presumably any organic bipolar diode simply because organic systems do not comprise ultra clean pristine materials [154,170]. The key issue is that it is the number of traps and their energetics that governs the general trap-free or trap-limited nature of the transport [154,170], [171].

Trap-assisted recombination was originally introduced in 2007 by Mandoc et al. in order to explain the behavior of polymer:polymer solar cells where the acceptor polymer was shown to have trap-limited electron transport [141]. It has been observed that many of these systems might suffer from this monomolecular recombination mechanism [172,173]. Notably other recent work seems to indicate that for the vast majority of semiconducting polymers, in a diode configuration, the electron transport is trap-limited [174]. The implication of this finding is that any organic material with a LUMO level above approximately 3.6 eV is predicted to include electron trapping, which will induce trap-

assisted recombination in any device where both carriers are present. The consequence for OPVs is that any organic material intended to be used as an acceptor should have a LUMO below this energy level since higher LUMOs may provoke an additional recombination channel which will ultimately limit the OPV device performance [175].

Despite the known presence of traps in common materials used for OPV devices, the majority of efficient OPV systems do not appear to be limited by trap-assisted recombination [26]. For the most part, studies on the trapping in OPV have focused on systems where chemical impurities were intentionally introduced [163,164,169]. It is worth considering whether the intrinsic phase separation in high performing OPV devices may help explain the apparently limited role of trap-assisted recombination [176]. Because holes and electrons transport through isolated domains trapped carriers must at least be within hopping/tunneling distance of a D/A interface in order to recombine with a free carrier of the opposite charge. Consequently it may be that trapped carriers far from a D/A interface are more likely to be thermally reemitted after some time than they are to recombine. It should be noted though that this also raises the difficult to probe fundamental question as to how pure the D/A domains really are.

### *3.1.3 Auger Recombination*

The third possible nongeminate recombination process is that of Auger recombination also known as trimolecular recombination because it is a three-particle process [177] (**Figure 2.5c**). In Auger recombination, an electron in the LUMO recombines with a hole in the HOMO after which the energy is transferred to a third electron which is then excited to a higher energetic state. The Auger recombination rate,  $R_{Auger}$ , has been described by the expression

$$R_{Auger} = \Gamma_n n(np - n_i^2) + \Gamma_p p(np - n_i^2) \quad (2.5)$$

where  $\Gamma_n$  and  $\Gamma_p$  are the Auger coefficients. A requirement for Auger recombination is a high charge density, generally not believed to be present in organic solar cells and as such Auger recombination has not been directly observed in OPV devices[27,178]. Nonetheless, there have been a few reports of a recombination mechanism with a third order dependence on carrier density in P3HT:PCBM solar cell devices [142,179,180] as discussed in the subsequent section.

#### *3.1.4 Carrier density dependence greater than quadratic*

The carrier density dependence of the nongeminate recombination rate, often referred to as the order of recombination, has been observed to be higher than that expected for Langevin recombination and temperature dependent for several polymer:fullerene systems[142,153,176,179–185]. Both Deibel et al. and Shuttle et al. suggested that this phenomenon is more likely related to a carrier density dependent recombination rate coefficient rather than a truly trimolecular process. This would not be an entirely unreasonable assumption; Tanase et al., and others, have shown that in pristine organic materials carrier transport at room temperature is mostly governed by carrier density [186–188]. Combined with the previously mentioned finding that carrier density is heavily influenced by carrier diffusion from the contacts [152] this is particularly important because, again, most optimized organic solar cells are rather thin, in the 100nm range, making them very susceptible to this effect. Kirchartz and Nelson recently modeled the effect of spatial

distributions in carrier density originating from the contacts in OPV devices and found that indeed the order of recombination can range from over 8 to 2 when going from an active layer thickness of 50 nm to 300 nm [153]. Likewise it has been shown that for pristine PLEDs the Langevin recombination depends not only on electric field and carrier densities, but also on temperature due to the energetic disorder governing the mobilities in the materials [114,121,131]. Recombination in organic solar cells has been found to possess similar dependencies [189]. Thus it is clear that higher reaction orders at least in part originate from spatial gradients of the carrier density and the carrier density dependence of the mobility.

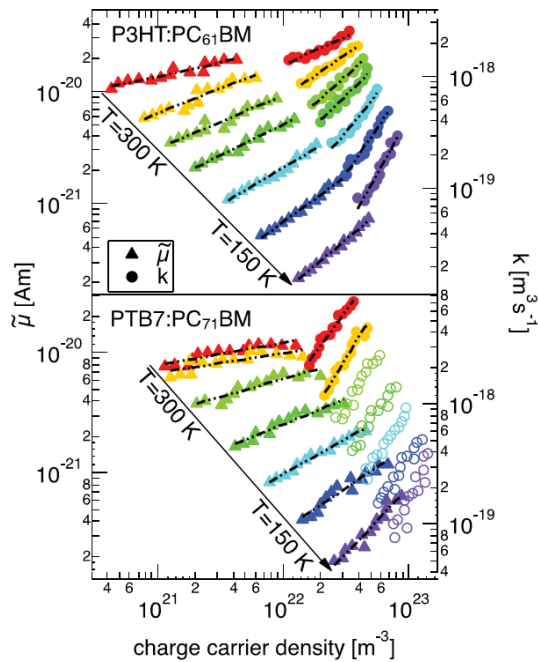


**Fig. 2.8:** Charge carrier density dependence of effective mobility (triangles, left axis) and the recombination rate coefficient,  $k$ , (circles, right axis) for P3HT:PCBM (top) and PTB7:PCBM (bottom). Solid circles were used for temperatures where the contacts are ohmic and open circles for where the device was limited by injection barriers [176].

What remains an intriguing open question is why the dependence of the bimolecular recombination coefficient in some systems appears to have a stronger temperature

dependence than the temperature dependence of the mobilities in the Langevin expression [176,184]. As shown in **Figure 2.8**, Rauh et al., recently found that for two different polymer:fullerene systems, the mobility dependence could only partially explain the temperature dependence of the recombination rate coefficient (shown as  $k$  in **Figure 2.8**). They interpret this as evidence in support of previous suggestions that the reemission of trapped carriers can increase the order of recombination [182,190]. This reasoning follows by positing that in an OPV device there are both free and trapped carriers both of which are captured in experimental measures of the total charge carrier density. However, due to the intrinsic phase separation of free electrons and holes, the only trapped carriers that are likely to recombine with an opposing charge carrier are those that are trapped near a D/A interface. Trapped carriers that are far from an interface are more likely to eventually be thermally reemitted back to the transport level. Thus despite the presence of trapped carriers the dominant recombination process is still bimolecular. The rate of which depends only on the density of *free* carriers. Due to the finite number of trap sites, as the *total* carrier density increases the ratio of free carriers to trapped carriers will increase in favor of more free carriers. Thus the number of free carriers in the device will rise superlinearly with experimentally measured total charge carrier density. Since the recombination order is taken to be the dependence of the recombination rate on the *total* carrier density, this leads to recombination orders in excess of two. Following this reasoning, the carrier density dependence of  $k(n)$  in **Figure 2.8** increases at low temperatures because the ratio of trapped to free carriers increases even more at low temperatures where the probability of thermally activated reemission of trapped carriers is lowered.

With that said, it is worth noting that the stronger dependence observed in the poly[[4,8-bis[(2-ethylhexyl)oxy]benzo[1,2-b:4,5-b']dithiophene-2,6-diyl][3-fluoro-2-[(2-ethylhexyl)carbonyl]thieno[3,4-b]thiophenediyl]] (PTB7):PCBM system compared to the P3HT:PCBM system may in part be due to the smaller active layer thickness (105 nm vs 200 nm) as described above. Furthermore, it has been shown that the temperature dependence of mobility is highly sensitive to the carrier density regime with notable differences in the space charge regime versus the transistor regime [186]. Nonetheless, this intriguing theory certainly warrants further investigation.

### 3.2 Space charge effects

As mentioned in earlier sections, in most cases the mobility of the electron through the fullerene exceeds that of the hole through the donor. The physical consequence of this is that after dissociation of an exciton the electron will be swept out of the active layer faster than the hole. Goodman and Rose have treated the extraction of photogenerated electrons and holes from a semiconductor in 1971 [191]. They showed that with noninjecting contacts the photocurrent becomes saturated when all photogenerated free electrons and holes are extracted from the semiconductor. This implies that the mean electron and hole drift lengths  $w_{e(h)} = \mu_{e(h)} \tau_{e(h)} E$  are equal to or longer than the specimen thickness  $L$ : with  $\mu_{e(h)}$  the charge carrier mobility of electrons (holes),  $\tau_{e(h)}$  the charge carrier lifetime, and  $E$  the electric field, respectively. For the case that  $w_e < L$  or  $w_h < L$  or both are smaller than  $L$ , space charge accumulates and the recombination of free charge carriers becomes significant. The most significant implication of this is that a thicker device essentially amplifies a space charge buildup if an imbalance of carrier mobilities is present, increasing bimolecular recombination and lowering the  $FF$  [192,193]. It is worth pointing out that, as addressed

before, even relatively high pristine hole mobilities in a donor material cannot be held as a guarantee for balanced transport in the blend [135,138,194–196] due to the percolative nature of the transport. Additionally, while the presence of space charge effects has been satisfyingly confirmed for polymer systems with mobility imbalances exceeding a factor of 1000 [138], the lower threshold for how imbalanced mobilities can be without invoking space charge effects is still unclear.

### *3.3 Surface recombination*

Though the topic has not received as much attention in the OPV literature as bulk recombination, recombination losses due to surface recombination may also significantly impact overall device performance [136,151,189,197]. In general surface recombination is governed by the charge injection/extraction behavior of the contacts. The presence of a minority carrier at a contact will govern the recombination. Electrons that diffuse to the anode recombine with injected holes and holes that diffuse to the cathode recombine with injected electrons. Typically the surface recombination velocity of this process is assumed infinite, all minority carriers recombine. Naturally the presence of minority carriers at a contact will reduce the device performance because those charges will not be collected. Since surface recombination is a bimolecular process the fastest carrier governs its rate [197]. Consequently, through modeling high carrier mobility is shown to increase the influence of surface recombination [151] reducing the device performance.

### *3.4 Experimental probes of nongeminate recombination*

A variety of optical and electrical techniques have been used to probe nongeminate recombination losses in OPV devices. These include, but are not limited to, transient absorption [102,198], charge extraction (CE) [199], transient photovoltage (TPV)

[179,181], transient photoconductivity [200], light and temperature dependent  $JV$  measurements [102,138], impedance spectroscopy [116,201], time-resolved microwave photoconductivity [156], TDCF [67], and charge extraction from a linear increasing voltage (CELIV) [29,139,143]. In this section, we will highlight how some of these techniques have been used to distinguish nongeminate mechanisms and to measure the charge carrier density and effective charge carrier lifetime in operating OPV devices.

### *3.4.1 Distinguishing nongeminate mechanism by light intensity dependence of $JV$ curves*

The simplest and most common method to distinguish between bimolecular recombination and trap-assisted recombination is probing the  $V_{oc}$  dependence on incident light intensity. For free carrier transport it was proposed by Koster et al. that the dependence of the  $V_{oc}$  on light intensity is shaped by the relation:

$$V_{oc} = \frac{E_{gap}}{q} - \frac{k_B T}{q} \ln \left( \frac{N_{cv}^2}{n_e n_h} \right), \quad (2.6)$$

here  $E_{gap}$  represents the effective energy gap between the offset of the LUMO of the acceptor and the HOMO of the donor,  $N_{cv}$  is the effective density of states in the donor and acceptor, and  $n_e$  and  $n_h$  denote the dissociated carrier densities varying with the applied light intensity [202]. Consequently, trap-free carrier recombination is predicted to have a  $k_B T/q$  dependence on light intensity. As can also be observed in **Figure 2.9a**, this relation has proven to be universal for trap free transport in organic solar cells [116,147,154,203]. However, when trap assisted recombination is present this relation becomes perturbed and a higher than  $k_B T/q$  slope is observed [141,161,163,164] as shown in **Figure 2.9b** for the case of P3HT:PCBM.

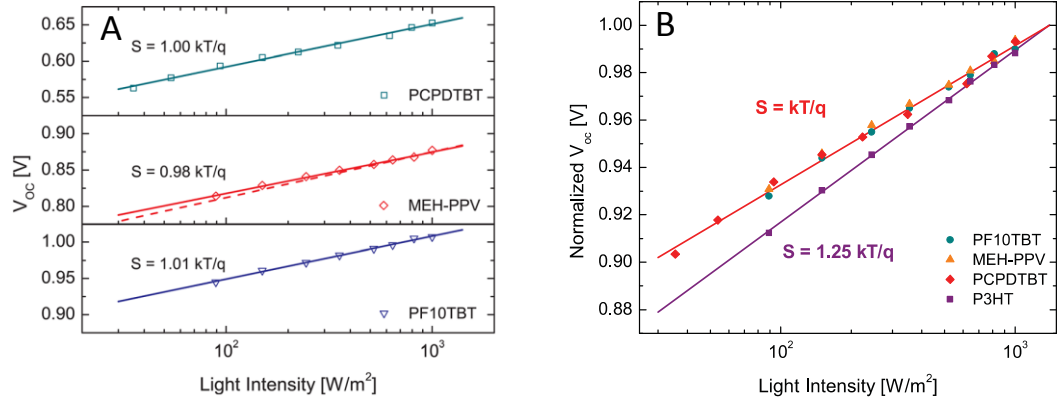


**Fig. 2.9:** **A**  $V_{oc}$  vs light intensity for three polymer:fullerene systems that are dominated by bimolecular recombination at the open circuit condition. The solid lines represent best fits to the data for a natural logarithmic dependence of  $V_{oc}$  on light with a slope of  $S$  [149]. **B** Normalized  $V_{oc}$  vs light intensity for the same three polymer systems in **A** along with data from a P3HT:PCBM device that exhibits a slope of  $S = 1.25$  indicating the presence of both bimolecular and trap-assisted recombination [154].

It is worth mentioning that this technique requires reasonable quality solar cells where the parasitic leakage current (ie. injected dark carriers) is low enough such that it does not interfere with the  $V_{oc}$  dependence at low light intensities. A simple way to gauge this is by looking at the  $FF$  dependence on light. Generally speaking if the  $FF$  starts to drop at lower light intensities, then the leakage current is significantly interfering with the photocurrent at those intensities and the slope of the  $V_{oc}$  vs. light intensity will be misleadingly inflated.

Determining the nature of nongeminate losses away from the open circuit condition is more challenging. However, measuring the photocurrent as a function of light intensity has proven to be an insightful probe of bimolecular recombination and space charge effects [138, 203]. In this case, the photocurrent is taken to be the light current minus the dark current – which is a fair approximation so long as the series resistance is small [204]. Generally a sub-linear dependence of the photocurrent on light intensity is indicative of

bimolecular recombination. It should be said though that a linear dependence on light intensity is less insightful. A linear dependence may result from either no recombination or monomolecular recombination and can be especially misleading if at the bias condition considered the photogenerated carrier density is not much larger than the density of injected carriers [205].

#### *3.4.2 Measures of charge carrier density*

As nongeminate recombination depends strongly on charge carrier density, reliable measures of the charge carrier density are essential. Techniques such as TDCF, TPC, and CELIV typically use a short laser pulse to create photogenerated charges the density of which can then be determined by integrating the resulting photocurrent transients. While these techniques have proven to be quite insightful they come with the inherent disadvantage that they do not measure steady state conditions – the consequences of which are not well understood. Alternatively, CE and impedance spectroscopy are two techniques that allow for a direct measure of the charge carrier density at steady state conditions and illumination intensities similar to typical solar cell operating conditions. In the charge extraction technique, a solar cell is held at fixed bias and illumination condition then the light is quickly turned off while the device is simultaneously short circuited. The resulting photocurrent transient can then be integrated to determine the average charge carrier density present in the device at the initial bias and illumination condition [199]. Shuttle et al. used this technique to experimentally show, for the first time, how the carrier density in a P3HT:PCBM device depends on the applied bias [206]. As shown in **Figure 2.10a**, the carrier density increases sharply with forward bias. This is due both to the decreasing driving force for extraction of photogenerated charges and the increasing injection of dark charge

carriers. Near open circuit ( $V_{cell} \sim 0.55$  V) the dark carrier density dominates the total carrier density. For comparison, Shuttle et al. also included the carrier density dependence on voltage expected for conventional doped inorganic semiconductors in which  $n$  remains independent of voltage up to within a few  $k_B T$  of the  $V_{oc}$  and then increases with a Boltzmann-like form (referred to as the Shockley limit) [206]. This stark contrast in carrier density dependence is due largely to charge injection from the contacts well below the built in voltage of the device.

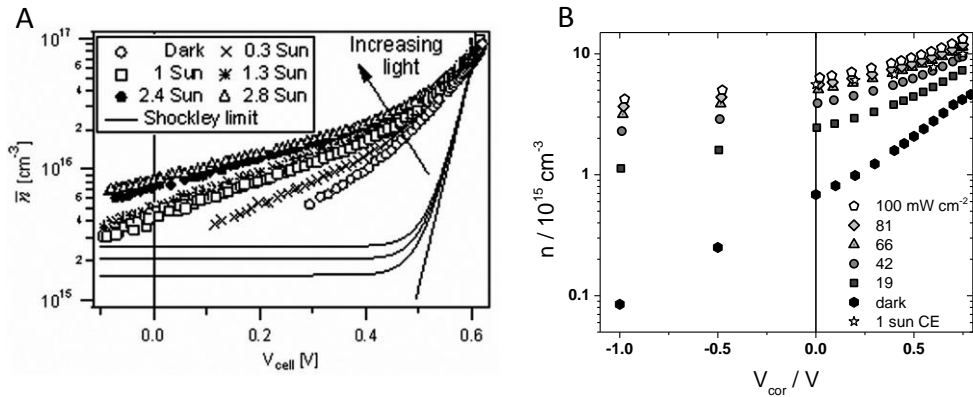


**Fig. 2.10:** (A) Bias dependence of the charge carrier density in a P3HT:PCBM solar cell device measured using the CE technique (symbols) and carrier density response expected from Shockley limit (lines) [207]. (B) Bias dependence of the charge carrier density in a small molecule BHJ solar cell device measured using impedance spectroscopy at a range of illumination intensities and a CE technique at one sun equivalent illumination (stay symbols) [116].  $V_{cell}$  and  $V_{cor}$  both represent the applied bias corrected for the voltage drop due to the device series resistance.

In a recent study published by our group, we demonstrated that impedance spectroscopy can also be used to measure the steady state carrier density in operating OPV devices as a function of bias and light intensity [116]. In this measurement, a solar cell device is illuminated and held at a fixed DC bias condition while the impedance responses from a small (20 mV) AC bias is measured as a function of frequency. In the case of impedance spectra that can be modeled with a simple parallel resistor-capacitor circuit, the

active layer capacitance can be directly extracted. The carrier density as a function of bias can then be obtained by measuring and integrating the active layer capacitance starting from the voltage where the photocurrent saturates up to the  $V_{oc}$ . The carrier density as a function of bias measured using this technique in a small molecule:PCBM BHJ device is presented in Figure 2.10b. Once again, it was found that the carrier density rises steadily with forward bias and the dark carrier injection becomes an increasingly significant portion of the total carrier density. We note that the dark carriers do not appear to be as significant in this system as was observed for the P3HT:PCBM system which is consistent with other reports that the strong dark carrier injection in P3HT:PCBM is atypical [156]. For comparison the carrier density for this particular small molecule system was also measured using a CE technique (star symbols). The carrier density from CE agrees well with the impedance measured  $n$  within a reasonable variation attributable to device to device variations, deviations from the assumed uniform carrier density profile and limitations in the extraction technique arising from the imbalanced charge carrier mobilities. Though impedance response of organic semiconductors is notoriously difficult to interpret, we posit that this method may prove a useful tool for the characterization of a variety of OPV systems in the future.

### 3.4.3 Measures of effective charge carrier lifetime

It is sometimes useful to consider a general expression for the nongeminate recombination using an effective charge carrier lifetime,  $\tau$ , that encapsulates all nongeminate recombination processes.  $\tau$  is a measure of the average time a free charge carrier lives before recombining nongeminately. The nongeminate recombination rate can then be expressed as

$$R_{NG} = \frac{n}{\tau(n)} \quad (2.7)$$

where  $\tau$  may itself be a function of carrier density. The effective carrier lifetime in an OPV device has been measured experimentally using a variety of optoelectronic techniques including CELIV [142], TPV [179,181] and impedance spectroscopy [116,201]. Systems measured under 1 sun illumination intensity at open circuit typically exhibit effective carrier lifetimes on the order of microseconds [116,139,181].

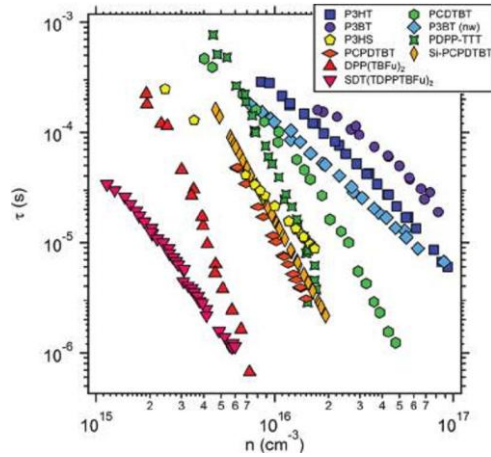


**Fig. 2.11:** Effective carrier lifetime ( $\tau$ ) versus average charge carrier density ( $n$ ) for a variety of polymer and small molecule OPV systems with PCBM as the acceptor measured by a combination TPV and CE techniques [185].

Using a combination of CE and TPV, Credington et al. recently measured the effective carrier lifetime at open circuit as a function of carrier density for a large range of OPV systems (Figure 11) [185]. In TPV, a solar cell is illuminated and held at the open circuit condition and then pumped with a low-intensity nanosecond laser pulse to introduce a small quantity of additional non-equilibrium carriers which subsequently recombine. The transient photovoltage produced by the laser pulse is measured and fit to a mono-exponential decay which allows for direct calculation of  $\tau$  [207]. All systems that were examined by Credington et al. were observed to have a power-law-like behavior of effective carrier

lifetime on carrier density such that  $\tau(n) \propto n^{-\lambda}$  with  $\lambda < -1$ . This is consistent with a bimolecular recombination mechanism in which the recombination rate coefficient also depends on carrier density as discussed in Section 3.1.4. Equally noteworthy is that the effective carrier lifetimes measured at the same carrier density vary over several orders of magnitude which illustrates that different OPV systems can exhibit substantially different recombination rate coefficients.

### *3.5 Summary of how nongeminate recombination affects solar cell metrics*

Any nongeminate recombination event is effectively eliminating charge carriers that could otherwise contribute to the photocurrent. Thus generally speaking, the biggest effect of nongeminate recombination is to reduce the photocurrent. Exactly how much nongeminate recombination reduces the photocurrent depends on a number factors including the carrier mobility, film thickness and degree of phase separation as discussed in the previous sections. Due in large part to the carrier density dependence of the nongeminate recombination, the percentage of photogenerated carriers lost to nongeminate recombination is highly voltage dependent. Near short circuit, the internal field sweeps out most carriers before they can recombine however as a forward bias is applied this driving force decreases leaving more and more carriers in the device. This leads to acceleration in bimolecular recombination particularly as the bias approaches  $V_{oc}$  and injection of dark carriers becomes significant. The key to limiting the effects of nongeminate recombination on  $J_{sc}$  and  $FF$  seems to be first and foremost to establish efficient (see **Figure 2.6**) and balanced charge carrier mobilities. Combined with a strong internal field created by the device's built in voltage, this will enable the efficient collection of photogenerated carriers. Optimizing the device thickness is

also essential for the same reason. Generally speaking, it takes longer to extract a charge carrier from a thicker active layer. If the active thickness is too large such that the charge carrier extraction time approaches the effective carrier lifetime then nongeminate recombination losses will become significant.

Nongeminate recombination is known to affect the  $V_{oc}$  as well [53,181,185,190]. This can be understood by considering that at the open circuit condition the current flowing out of the device is zero precisely because the photogenerated current is entirely cancelled out by the nongeminate recombination current. It naturally follows then that reducing the rate of nongeminate recombination would allow devices to reach higher voltages before the photocurrent is cancelled completely by recombination. Such gains could be significant. As shown by Credington et al., the  $V_{oc}$  of highly intermixed systems with fast recombination may lose up to 300 mV compared to systems with highly phase-segregated domains and thus slower recombination [185].

#### **4. Summary and Perspective**

In summary, a complex picture of the photogeneration is emerging in which energetic offsets and domain size are not the only factors that determine whether excitons will recombine or separate into free carriers. Once an electron-hole pair reaches a D/A interface, whether the charges can escape their coulomb attraction and avoid geminate recombination depends on how tightly bound they are. There is compelling evidence that delocalized band states at the D/A interface can reduce this binding energy. The accessibility of delocalized states is a function of not only molecular properties (ie. conjugation length, energetic offsets, reorganization energy, LUMO degeneracy, etc.) but also film properties (alignment of donor molecular orbital relative to the acceptor, degree of crystallinity, etc.).

The fact these properties are both dependent on materials and device processing conditions helps explain long running disagreements in the literature about the roles of the internal electric field and excess excitation energy in suppressing geminate recombination. In the context of overcoming geminate recombination, key issues for further research are to develop a comprehensive quantum mechanical model that encompasses the many processes that contribute to charge separation at the donor-acceptor interface and to better define the general guidelines for material design.

Where it has been shown that with careful choice of materials and processing conditions geminate recombination losses can be almost entirely overcome, nongeminate losses will always be present. This means that the nongeminate recombination processes govern the characteristic solar cell parameters:  $J_{sc}$ ,  $V_{oc}$  and  $FF$ . Luckily, it seems that some external variables can potentially reduce nongeminate recombination. The blend morphology is of major influence on both the carrier mobility as well as the recombination process. A favorable phase separation can both reduce bimolecular recombination and enhance charge transport. Moreover, the same factors that help charge separation out of CT states may also reduce nongeminate recombination. Minimizing chemical impurities and choosing the right acceptor material will eliminate the possibility of an additional trap-assisted recombination channel. Optimizing the device thickness is also important. For a thick device charges need more time to reach the contacts rendering them more susceptible to bimolecular recombination, where the most extreme case will result in the buildup of space charge. On the other hand, a thin device will suffer more from contact effects as an increased carrier density or minority carriers enhance bimolecular recombination. Altogether, it is clear that

future material design and device fabrication techniques must aim to maintain efficient charge transport properties while encouraging sufficient phase separation in the blend.

Finally we emphasize that while the recent efficiency gains in the OPV field have been remarkable they have generally come along with more complex and expensive materials [209]. Thus, further developing the fundamental understandings of organic photovoltaics may be essential to not only increased efficiencies but also to the design of more cost effective conjugated polymers and small molecules for high performing photovoltaic devices.

## 5. References

- [1] G. A. Chamberlain, *Solar Cells* **1983**, 8, 47–83.
- [2] Heliatek consolidates its technology leadership by establishing a new world record for organic solar technology with a cell efficiency of 12%. *Heliatek*.
- [3] M. A. Green, K. Emery, Y. Hishikawa, W. Warta, E. D. Dunlop, *Progress in Photovoltaics: Research and Applications* **2012**, 20, 606–614.
- [4] Z. He, C. Zhong, S. Su, M. Xu, H. Wu, Y. Cao, *Nature Photonics* **2012**, 6, 593–597.
- [5] NREL efficiency chart.
- [6] W. Shockley, H. J. Queisser, *Journal of Applied Physics* **1961**, 32, 510.
- [7] M. C. Scharber, D. Mühlbacher, M. Koppe, P. Denk, C. Waldauf, A. J. Heeger, C. J. Brabec, *Advanced Materials* **2006**, 18, 789–794.
- [8] R. A. J. Janssen, J. Nelson, **2012**, 1–33.
- [9] L. J. A. Koster, S. E. Shaheen, J. C. Hummelen, *Advanced Energy Materials* **2012**, 2, 1246–1253.
- [10] R. R. Lunt, T. P. Osedach, P. R. Brown, J. A. Rowehl, V. Bulović, *Advanced Materials* **2011**, 23, 5712–5727.
- [11] B. Minnaert, M. Burgelman, *Progress in Photovoltaics: Research and Applications* **2007**, 15, 741–748.
- [12] H. Bässler, *physica status solidi (b)* **1993**, 175, 15–56.
- [13] C. W. Tang, *Applied Physics Letters* **1986**, 48, 183–185.
- [14] P. Peumans, A. Yakimov, S. R. Forrest, *Journal of Applied Physics* **2003**, 93, 3693.
- [15] S. E. Shaheen, C. J. Brabec, N. S. Sariciftci, F. Padinger, T. Fromherz, J. C. Hummelen, *Appl. Phys. Lett.* **2001**, 78, 841.
- [16] W. Ma, C. Yang, X. Gong, K. Lee, A. J. Heeger, *Advanced Functional Materials* **2005**, 15, 1617–1622.

- [17] T. S. van der Poll, J. A. Love, T.-Q. Nguyen, G. C. Bazan, *Advanced Materials* **2012**, *24*, 3646–3649.
- [18] J. Zhou, X. Wan, Y. Liu, Y. Zuo, Z. Li, G. He, G. Long, W. Ni, C. Li, X. Su, Y. Chen, *Journal Of The American Chemical Society* **2012**, *134*, 16345–16351.
- [19] B. Walker, C. Kim, T.-Q. Nguyen, *Chem. Mater.* **2010**, *23*, 470–482.
- [20] K. Walzer, B. Maennig, M. Pfeiffer, K. Leo, *Chemical Reviews* **2007**, *107*, 1233–1271.
- [21] K. Hasharoni, M. Keshavarz-K, A. Sastre, R. Gonzalez, C. Bellavia-Lund, Y. Greenwald, T. Swager, F. Wudl, A. J. Heeger, *The Journal of chemical physics* **1997**, *107*, 2308.
- [22] M. A. Loi, S. Toffanin, M. Muccini, M. Forster, U. Scherf, M. Scharber, *Adv. Funct. Mater.* **2007**, *17*, 2111–2116.
- [23] K. Vandewal, A. Gadisa, W. D. Oosterbaan, S. Bertho, F. Banishoeib, I. van Severen, L. Lutsen, T. J. Cleij, D. Vanderzande, J. V. Manca, *Adv. Funct. Mater.* **2008**, *18*, 2064–2070.
- [24] J. J. M. Halls, J. Cornil, D. A. dos Santos, R. Silbey, D.-H. Hwang, A. B. Holmes, J. L. Brédas, R. H. Friend, *Phys. Rev. B* **1999**, *60*, 5721–5727.
- [25] B. Rand, D. Burk, S. Forrest, *Physical Review B* **2007**, *75*, 115327.
- [26] S. R. Cowan, N. Banerji, W. L. Leong, A. J. Heeger, *Advanced Functional Materials* **2012**, *22*, 1116–1128.
- [27] C. Deibel, V. Dyakonov, *Reports on Progress in Physics* **2010**, *73*, 096401.
- [28] A. Pivrikas, N. S. Sariciftci, G. Juška, R. Österbacka, *Progress in Photovoltaics: Research and Applications* **2007**, *15*, 677–696.
- [29] A. Pivrikas, H. Neugebauer, N. S. Sariciftci, *IEEE Journal of Selected Topics in Quantum Electronics* **2010**, *16*, 1746–1758.
- [30] P. W. M. Blom, V. D. Mihailetschi, L. J. A. Koster, D. E. Markov, *Advanced Materials* **2007**, *19*, 1551–1566.
- [31] T. M. Clarke, J. R. Durrant, *Chem. Rev.* **2010**, *110*, 6736–6767.
- [32] J.-L. Brédas, J. E. Norton, J. Cornil, V. Coropceanu, *Acc. Chem. Res.* **2009**, *42*, 1691–1699.
- [33] S. Albrecht, W. Schindler, J. Kurpiers, J. Kniepert, J. C. Blakesley, I. Dumsch, S. Allard, K. Fostiropoulos, U. Scherf, D. Neher, *J. Phys. Chem. Lett.* **2012**, *3*, 640–645.
- [34] D. Credgington, F. C. Jamieson, B. Walker, T. Nguyen, J. R. Durrant, *Advanced Materials*.
- [35] G. F. A. Dibb, F. C. Jamieson, A. Maurano, J. Nelson, J. R. Durrant, *J. Phys. Chem. Lett.* **2013**, 803–808.
- [36] C. Deibel, T. Strobel, V. Dyakonov, *Advanced Materials* **2010**, *22*, 4097–4111.
- [37] J. M. Hodgkiss, S. Albert-Seifried, A. Rao, A. J. Barker, A. R. Campbell, R. A. Marsh, R. H. Friend, *Advanced Functional Materials* **2012**, *22*, 1567–1577.
- [38] T. Stübinger, W. Brütting, *Journal of Applied Physics* **2001**, *90*, 3632–3641.
- [39] O. V. Mikhnenko, J. Lin, Y. Shu, J. E. Anthony, P. W. M. Blom, T.-Q. Nguyen, M. A. Loi, *Physical Chemistry Chemical Physics* **2012**, *14*, 14196.
- [40] A. A. Bakulin, J. C. Hummelen, M. S. Pshenichnikov, P. H. M. van Loosdrecht, *Advanced Functional Materials* **2010**, *20*, 1653–1660.

- [41] C. J. Brabec, G. Zerza, G. Cerullo, S. De Silvestri, S. Luzzati, J. C. Hummelen, S. Sariciftci, *Chemical Physics Letters* **2001**, *340*, 232–236.
- [42] F. Zhang, K. G. Jespersen, C. Björström, M. Svensson, M. R. Andersson, V. Sundström, K. Magnusson, E. Moons, A. Yartsev, O. Inganäs, *Advanced Functional Materials* **2006**, *16*, 667–674.
- [43] K. G. Jespersen, F. Zhang, A. Gadisa, V. Sundström, A. Yartsev, O. Inganäs, *Organic Electronics* **2006**, *7*, 235–242.
- [44] J. Guo, H. Ohkita, H. Benten, S. Ito, *J. Am. Chem. Soc.* **2010**, *132*, 6154–6164.
- [45] I. A. Howard, R. Mauer, M. Meister, F. Laquai, *J. Am. Chem. Soc.* **2010**, *132*, 14866–14876.
- [46] L. G. Kaake, J. J. Jasieniak, R. C. Bakus, G. C. Welch, D. Moses, G. C. Bazan, A. J. Heeger, *J. Am. Chem. Soc.* **2012**, *134*, 19828–19838.
- [47] Y. Sun, G. C. Welch, W. L. Leong, C. J. Takacs, G. C. Bazan, A. J. Heeger, *Nat Mater* **2011**, *advance online publication*.
- [48] P. E. Keivanidis, T. M. Clarke, S. Lilliu, T. Agostinelli, J. E. Macdonald, J. R. Durrant, D. D. C. Bradley, J. Nelson, *J. Phys. Chem. Lett.* **2010**, *1*, 734–738.
- [49] B. Walker, A. B. Tamayo, X. Dang, P. Zalar, J. H. Seo, A. Garcia, M. Tantiwiwat, T. Nguyen, *Advanced Functional Materials* **2009**, *19*, 3063–3069.
- [50] B. A. Collins, Z. Li, J. R. Tumbleston, E. Gann, C. R. McNeill, H. Ade, *Advanced Energy Materials* **2012**, n/a–n/a.
- [51] K. Tvingstedt, K. Vandewal, F. Zhang, O. Inganäs, *J. Phys. Chem. C* **2010**, *114*, 21824–21832.
- [52] K. Tvingstedt, K. Vandewal, A. Gadisa, F. Zhang, J. Manca, O. Inganäs, *J. Am. Chem. Soc.* **2009**, *131*, 11819–11824.
- [53] K. Vandewal, K. Tvingstedt, A. Gadisa, O. Inganäs, J. V. Manca, *Nat Mater* **2009**, *8*, 904–909.
- [54] S. Gélinas, O. Paré-Labrosse, C.-N. Brosseau, S. Albert-Seifried, C. R. McNeill, K. R. Kirov, I. A. Howard, R. Leonelli, R. H. Friend, C. Silva, *J. Phys. Chem. C* **2011**, *115*, 7114–7119.
- [55] X.-Y. Zhu, Q. Yang, M. Muntwiler, *Acc. Chem. Res.* **2009**, *42*, 1779–1787.
- [56] D. Veldman, S. C. J. Meskers, R. A. J. Janssen, *Advanced Functional Materials* **2009**, *19*, 1939–1948.
- [57] H. Ohkita, S. Cook, Y. Astuti, W. Duffy, S. Tierney, W. Zhang, M. Heeney, I. McCulloch, J. Nelson, D. D. C. Bradley, J. R. Durrant, *J. Am. Chem. Soc.* **2008**, *130*, 3030–3042.
- [58] Y. Zhou, K. Tvingstedt, F. Zhang, C. Du, W.-X. Ni, M. R. Andersson, O. Inganäs, *Advanced Functional Materials* **2009**, *19*, 3293–3299.
- [59] I. A. Howard, F. Laquai, *Macromolecular Chemistry and Physics* **2010**, *211*, 2063–2070.
- [60] A. A. Bakulin, A. Rao, V. G. Pavelyev, P. H. M. Van Loosdrecht, M. S. Pshenichnikov, D. Niedzialek, J. Cornil, D. Beljonne, R. H. Friend, *Science* **2012**, *335*, 1340–1344.
- [61] S. De, T. Pascher, M. Maiti, K. G. Jespersen, T. Kesti, F. Zhang, O. Inganäs, A. Yartsev, V. Sundström, *J. Am. Chem. Soc.* **2007**, *129*, 8466–8472.

- [62] N. Banerji, S. Cowan, M. Leclerc, E. Vauthey, A. J. Heeger, *J. Am. Chem. Soc.* **2010**, *132*, 17459–17470.
- [63] R. A. Marsh, J. M. Hodgkiss, R. H. Friend, *Advanced Materials* **2010**, *22*, 3672–3676.
- [64] T. M. Clarke, A. M. Ballantyne, J. Nelson, D. D. C. Bradley, J. R. Durrant, *Advanced Functional Materials* **2008**, *18*, 4029–4035.
- [65] J. G. Müller, J. M. Lupton, J. Feldmann, U. Lemmer, M. C. Scharber, N. S. Sariciftci, C. J. Brabec, U. Scherf, *Phys. Rev. B* **2005**, *72*, 195208.
- [66] S. Massip, P. M. Oberhumer, G. Tu, S. Albert-Seifried, W. T. S. Huck, R. H. Friend, N. C. Greenham, *J. Phys. Chem. C* **2011**, *115*, 25046–25055.
- [67] J. Kniepert, M. Schubert, J. C. Blakesley, D. Neher, *J. Phys. Chem. Lett.* **2011**, *2*, 700–705.
- [68] T. Offermans, S. C. J. Meskers, R. A. J. Janssen, *Journal of Applied Physics* **2006**, *100*, 074509–074509–7.
- [69] M. Mingeback, S. Walter, V. Dyakonov, C. Deibel, *Applied Physics Letters* **2012**, *100*, 193302–193302–4.
- [70] M. Lenes, M. Morana, C. J. Brabec, P. W. M. Blom, *Advanced Functional Materials* **2009**, *19*, 1106–1111.
- [71] W. Li, W. S. C. Roelofs, M. M. Wienk, R. A. J. Janssen, *J. Am. Chem. Soc.* **2012**, *134*, 13787–13795.
- [72] L. J. A. Koster, E. C. P. Smits, V. D. Mihailetschi, P. W. M. Blom, *Phys. Rev. B* **2005**, *72*, 085205.
- [73] R. A. Marsh, C. R. McNeill, A. Abrusci, A. R. Campbell, R. H. Friend, *Nano Lett.* **2008**, *8*, 1393–1398.
- [74] A. A. Bakulin, S. D. Dimitrov, A. Rao, P. C. Y. Chow, C. B. Nielsen, B. C. Schroeder, I. McCulloch, H. J. Bakker, J. R. Durrant, R. H. Friend, *J. Phys. Chem. Lett.* **2013**, *4*, 209–215.
- [75] E. T. Hoke, K. Vandewal, J. A. Bartelt, W. R. Mateker, J. D. Douglas, R. Noriega, K. R. Graham, J. M. J. Fréchet, A. Salleo, M. D. McGehee, *Advanced Energy Materials* **2012**, n/a–n/a.
- [76] K. Vandewal, Z. Ma, J. Bergqvist, Z. Tang, E. Wang, P. Henriksson, K. Tvingstedt, M. R. Andersson, F. Zhang, O. Inganäs, *Advanced Functional Materials* **2012**, *22*, 3480–3490.
- [77] X. Gong, M. Tong, F. G. Brunetti, J. Seo, Y. Sun, D. Moses, F. Wudl, A. J. Heeger, *Advanced Materials* **2011**, *23*, 2272–2277.
- [78] A. Liu, S. Zhao, S.-B. Rim, J. Wu, M. Könemann, P. Erk, P. Peumans, *Advanced Materials* **2008**, *20*, 1065–1070.
- [79] B. A. Gregg, *Soft Matter* **2009**, *5*, 2985–2989.
- [80] C. Groves, *Energy Environ. Sci.* **2013**.
- [81] B. A. Gregg, *J. Phys. Chem. Lett.* **2011**, *2*, 3013–3015.
- [82] G. Grancini, M. Maiuri, D. Fazzi, A. Petrozza, H.-J. Egelhaaf, D. Brida, G. Cerullo, G. Lanzani, *Nature Materials* **2013**, *12*, 29–33.
- [83] A. E. Jailaubekov, A. P. Willard, J. R. Tritsch, W.-L. Chan, N. Sai, R. Gearba, L. G. Kaake, K. J. Williams, K. Leung, P. J. Rossky, X.-Y. Zhu, *Nature Materials* **2013**, *12*, 66–73.

- [84] S. D. Dimitrov, A. A. Bakulin, C. B. Nielsen, B. C. Schroeder, J. Du, H. Bronstein, I. McCulloch, R. H. Friend, J. R. Durrant, *J. Am. Chem. Soc.* **2012**, *134*, 18189–18192.
- [85] W. J. Grzegorzczak, T. J. Savenije, T. E. Dykstra, J. Piris, J. M. Schins, L. D. A. Siebbeles, *J. Phys. Chem. C* **2010**, *114*, 5182–5186.
- [86] R. D. Pensack, J. B. Asbury, *J. Am. Chem. Soc.* **2009**, *131*, 15986–15987.
- [87] S. H. Park, A. Roy, S. Beaupré, S. Cho, N. Coates, J. S. Moon, D. Moses, M. Leclerc, K. Lee, A. J. Heeger, *Nature Photonics* **2009**, *3*, 297–302.
- [88] G. F. Burkhard, E. T. Hoke, M. D. McGehee, *Advanced Materials* **2010**, *22*, 3293–3297.
- [89] J. Lee, K. Vandewal, S. R. Yost, M. E. Bahlke, L. Goris, M. A. Baldo, J. V. Manca, T. V. Voorhis, *J. Am. Chem. Soc.* **2010**, *132*, 11878–11880.
- [90] T. G. J. van der Hofstad, D. Di Nuzzo, M. van den Berg, R. A. J. Janssen, S. C. J. Meskers, *Advanced Energy Materials* **2012**, *2*, 1095–1099.
- [91] S. R. Yost, L.-P. Wang, T. Van Voorhis, *J. Phys. Chem. C* **2011**, *115*, 14431–14436.
- [92] D. P. McMahon, D. L. Cheung, A. Troisi, *J. Phys. Chem. Lett.* **2011**, *2*, 2737–2741.
- [93] T. Liu, A. Troisi, *Advanced Materials* **2013**, *25*, 1038–1041.
- [94] W. Chen, T. Xu, F. He, W. Wang, C. Wang, J. Strzalka, Y. Liu, J. Wen, D. J. Miller, J. Chen, K. Hong, L. Yu, S. B. Darling, *Nano Lett.* **2011**, *11*, 3707–3713.
- [95] G. Grancini, D. Polli, D. Fazzi, J. Cabanillas-Gonzalez, G. Cerullo, G. Lanzani, *J. Phys. Chem. Lett.* **2011**, *2*, 1099–1105.
- [96] D. Veldman, O. İpek, S. C. J. Meskers, J. Sweelssen, M. M. Koetse, S. C. Veenstra, J. M. Kroon, S. S. van Bavel, J. Loos, R. A. J. Janssen, *J. Am. Chem. Soc.* **2008**, *130*, 7721–7735.
- [97] C. Deibel, T. Strobel, V. Dyakonov, *Phys. Rev. Lett.* **2009**, *103*, 036402.
- [98] A. Ojala, A. Petersen, A. Fuchs, R. Lovrincic, C. Pölking, J. Trollmann, J. Hwang, C. Lennartz, H. Reichelt, H. W. Höffken, A. Pucci, P. Erk, T. Kirchartz, F. Würthner, *Advanced Functional Materials* **2012**, *22*, 86–96.
- [99] S. Albrecht, S. Janietz, W. Schindler, J. Frisch, J. Kurpiers, J. Kniepert, S. Inal, P. Pingel, K. Fostiropoulos, N. Koch, D. Neher, *J. Am. Chem. Soc.* **2012**.
- [100] Y. Zhang, J. Liu, T.-Q. Nguyen, *ACS Appl. Mater. Interfaces* **2013**.
- [101] T. J. K. Brenner, Z. Li, C. R. McNeill, *J. Phys. Chem. C* **2011**, *115*, 22075–22083.
- [102] R. Mauer, I. A. Howard, F. Laquai, *J. Phys. Chem. Lett.* **2010**, *1*, 3500–3505.
- [103] R. A. Street, S. Cowan, A. J. Heeger, *Phys. Rev. B* **2010**, *82*, 121301.
- [104] G. F. Burkhard, E. T. Hoke, Z. M. Beiley, M. D. McGehee, *J. Phys. Chem. C* **2012**.
- [105] L. Onsager, *Phys. Rev.* **1938**, *54*, 554–557.
- [106] C. L. Braun, *The Journal of Chemical Physics* **1984**, *80*, 4157.
- [107] V. D. Mihailetschi, L. J. A. Koster, J. C. Hummelen, P. W. M. Blom, *Phys. Rev. Lett.* **2004**, *93*, 216601.
- [108] B. P. Rand, D. Cheyns, K. Vasseur, N. C. Giebink, S. Mothy, Y. Yi, V. Coropceanu, D. Beljonne, J. Cornil, J. Brédas, J. Genoe, *Advanced Functional Materials*.
- [109] T. W. Holcombe, J. E. Norton, J. Rivnay, C. H. Woo, L. Goris, C. Piliego, G. Griffini, A. Sellinger, J.-L. Brédas, A. Salleo, J. M. J. Fréchet, *J. Am. Chem. Soc.* **2011**, *133*, 12106–12114.

- [110] B. A. Collins, J. E. Cochran, H. Yan, E. Gann, C. Hub, R. Fink, C. Wang, T. Schuettfort, C. R. McNeill, M. L. Chabynec, H. Ade, *Nature Materials* **2012**, *11*, 536–543.
- [111] W. Ma, J. R. Tumbleston, M. Wang, E. Gann, F. Huang, H. Ade, *Advanced Energy Materials* **2013**, n/a–n/a.
- [112] P. Langevin, *Ann Chim Phys* **1903**, *28*, 433–530.
- [113] U. Albrecht, H. Bässler, *physica status solidi (b)* **1995**, *191*, 455–459.
- [114] P. Blom, M. De Jong, *Philips journal of research* **1998**, *51*, 479–494.
- [115] L. J. A. Koster, O. Stenzel, S. D. Oosterhout, M. M. Wienk, V. Schmidt, R. A. J. Janssen, *Advanced Energy Materials* **2013**, n/a–n/a.
- [116] C. M. Proctor, C. Kim, D. Neher, T.-Q. Nguyen, *Advanced Functional Materials* **2013**, n/a–n/a.
- [117] H. H. P. Gommans, M. Kemerink, J. M. Kramer, R. A. J. Janssen, *Applied Physics Letters* **2005**, *87*, 122104–122104–3.
- [118] T. Kirchartz, B. E. Pieters, K. Taretto, U. Rau, *Journal of Applied Physics* **2008**, *104*, 094513–094513–9.
- [119] J. Szmytkowski, *Chemical Physics Letters* **2009**, *470*, 123–125.
- [120] M. Kuik, G.-J. A. H. Wetzelaer, J. G. Laddé, H. T. Nicolai, J. Wildeman, J. Sweelssen, P. W. M. Blom, *Advanced Functional Materials* **2011**, *21*, 4502–4509.
- [121] M. Kuik, H. T. Nicolai, M. Lenes, G.-J. A. H. Wetzelaer, M. Lu, P. W. M. Blom, *Applied Physics Letters* **2011**, *98*, 093301.
- [122] G. A. H. Wetzelaer, M. Kuik, H. T. Nicolai, P. W. M. Blom, *Physical Review B* **2011**, *83*, 165204.
- [123] **1998**, 1–4.
- [124] Z. G. Yu, D. L. Smith, A. Saxena, R. L. Martin, A. R. Bishop, *Phys. Rev. B* **2001**, *63*, 085202.
- [125] E. Tutiş, D. Berner, L. Zuppiroli, *Journal of Applied Physics* **2003**, *93*, 4594.
- [126] K. d. Meisel, W. f. Pasveer, J. Cottaar, C. Tanase, R. Coehoorn, P. a. Bobbert, P. w. m. Blom, D. m. de Leeuw, M. a. j. Michels, *physica status solidi (c)* **2006**, *3*, 267–270.
- [127] J. J. Kwiatkowski, J. Nelson, H. Li, J. L. Bredas, W. Wenzel, C. Lennartz, *Phys. Chem. Chem. Phys.* **2008**, *10*, 1852–1858.
- [128] J. van der Holst, M. Uijtewaal, B. Ramachandran, R. Coehoorn, P. Bobbert, G. de Wijs, R. de Groot, *Physical Review B* **2009**, *79*, 085203.
- [129] O. V. Mikhnenko, F. Cordella, A. B. Sieval, J. C. Hummelen, P. W. M. Blom, M. A. Loi, *The Journal of Physical Chemistry B* **2009**, *113*, 9104–9109.
- [130] C. Groves, N. Greenham, *Physical Review B* **2008**, *78*, 155205.
- [131] J. J. M. van der Holst, F. W. A. van Oost, R. Coehoorn, P. A. Bobbert, *Physical Review B* **2009**, *80*, 235202.
- [132] T. Kirchartz, B. E. Pieters, J. Kirkpatrick, U. Rau, J. Nelson, *Physical Review B* **2011**, *83*, 115209.
- [133] X. Guo, M. Zhang, J. Tan, S. Zhang, L. Huo, W. Hu, Y. Li, J. Hou, *Advanced Materials* **2012**, n/a–n/a.
- [134] V. D. Mihailetchi, L. J. A. Koster, P. W. M. Blom, C. Melzer, B. de Boer, J. K. J. van Duren, R. A. J. Janssen, *Advanced Functional Materials* **2005**, *15*, 795–801.

- [135] V. D. Mihailetschi, H. X. Xie, B. de Boer, L. J. A. Koster, P. W. M. Blom, *Advanced Functional Materials* **2006**, *16*, 699–708.
- [136] A. Wagenpfahl, C. Deibel, V. Dyakonov, *Selected Topics in Quantum Electronics, IEEE Journal of* **2010**, *16*, 1759–1763.
- [137] C. Deibel, A. Wagenpfahl, V. Dyakonov, *physica status solidi (RRL) – Rapid Research Letters* **2008**, *2*, 175–177.
- [138] V. Mihailetschi, J. Wildeman, P. Blom, *Physical Review Letters* **2005**, *94*, 126602.
- [139] A. Baumann, J. Lormann, D. Rauh, C. Deibel, V. Dyakonov, *Advanced Materials* **2012**, n/a–n/a.
- [140] N. Tessler, N. Rappaport, *Applied Physics Letters* **2006**, *89*, 013504–013504–3.
- [141] M. M. Mandoc, W. Veurman, L. J. A. Koster, B. de Boer, P. W. M. Blom, *Advanced Functional Materials* **2007**, *17*, 2167–2173.
- [142] C. Deibel, A. Baumann, V. Dyakonov, *Applied Physics Letters* **2008**, *93*, 163303–163303–3.
- [143] A. Armin, M. Velusamy, P. L. Burn, P. Meredith, A. Pivrikas, *Applied Physics Letters* **2012**, *101*, 083306–083306–5.
- [144] R. Hamilton, C. G. Shuttle, B. O’Regan, T. C. Hammant, J. Nelson, J. R. Durrant, *J. Phys. Chem. Lett.* **2010**, *1*, 1432–1436.
- [145] L. J. A. Koster, V. D. Mihailetschi, P. W. M. Blom, *Applied Physics Letters* **2006**, *88*, 052104–052104–3.
- [146] G. Juška, K. Arlauskas, J. Stuchlik, R. Österbacka, *Journal of Non-Crystalline Solids* **2006**, *352*, 1167–1171.
- [147] S. R. Cowan, A. Roy, A. J. Heeger, *Phys. Rev. B* **2010**, *82*, 245207.
- [148] C. Deibel, A. Wagenpfahl, V. Dyakonov, *Phys. Rev. B* **2009**, *80*, 075203.
- [149] G. A. H. Wetzelaer, M. Kuik, M. Lenes, P. W. M. Blom, *Applied Physics Letters* **2011**, *99*, 153506.
- [150] V. D. Mihailetschi, J. K. . van Duren, P. W. . Blom, J. C. Hummelen, R. A. . Janssen, J. M. Kroon, M. T. Rispens, W. J. . Verhees, M. M. Wienk, *Advanced Functional Materials* **2003**, *13*, 43–46.
- [151] T. Kirchartz, B. Pieters, K. Taretto, U. Rau, *Physical Review B* **2009**, *80*, 035334.
- [152] N. Craciun, J. Brondijk, P. Blom, *Physical Review B* **2008**, *77*, 035206.
- [153] T. Kirchartz, J. Nelson, *Phys. Rev. B* **2012**, *86*, 165201.
- [154] G.-J. A. H. Wetzelaer, M. Kuik, P. W. M. Blom, *Advanced Energy Materials* **2012**, *2*, 1232–1237.
- [155] C. G. Shuttle, N. D. Treat, J. D. Douglas, J. M. J. Fréchet, M. L. Chabiny, *Advanced Energy Materials* **2012**, *2*, 111–119.
- [156] A. J. Ferguson, N. Kopidakis, S. E. Shaheen, G. Rumbles, *J. Phys. Chem. C* **2011**, *115*, 23134–23148.
- [157] D. H. K. Murthy, A. Melianas, Z. Tang, G. Juška, K. Arlauskas, F. Zhang, L. D. A. Siebbeles, O. Inganäs, T. J. Savenije, *Advanced Functional Materials* **2013**, n/a–n/a.
- [158] M. Hilczler, M. Tachiya, *J. Phys. Chem. C* **2010**, *114*, 6808–6813.
- [159] W. Shockley, W. T. Read, *Phys. Rev.* **1952**, *87*, 835–842.
- [160] R. N. Hall, *Phys. Rev.* **1952**, *87*, 387–387.
- [161] M. Kuik, L. J. A. Koster, G. A. H. Wetzelaer, P. W. M. Blom, *Physical Review Letters* **2011**, *107*, 256805.

- [162] H. T. Nicolai, A. Hof, P. W. M. Blom, *Advanced Functional Materials* **2012**, *22*, 2040–2047.
- [163] M. M. Mandoc, F. B. Kooistra, J. C. Hummelen, B. de Boer, P. W. M. Blom, *Applied Physics Letters* **2007**, *91*, 263505.
- [164] S. R. Cowan, W. L. Leong, N. Banerji, G. Dennler, A. J. Heeger, *Advanced Functional Materials* **2011**, *21*, 3083–3092.
- [165] R. A. Street, A. Krakaris, S. R. Cowan, *Advanced Functional Materials* **2012**, *22*, 4608–4619.
- [166] L. Kaake, X.-D. Dang, W. L. Leong, Y. Zhang, A. Heeger, T.-Q. Nguyen, *Advanced Materials* **2012**, n/a–n/a.
- [167] L. Burtone, J. Fischer, K. Leo, M. Riede, *Phys. Rev. B* **2013**, *87*, 045432.
- [168] L. Tzabari, N. Tessler, *Journal of Applied Physics* **2011**, *109*, 064501.
- [169] W. L. Leong, G. C. Welch, L. G. Kaake, C. J. Takacs, Y. Sun, G. C. Bazan, A. J. Heeger, *Chem. Sci.* **2012**, *3*, 2103–2109.
- [170] G. A. H. Wetzelaer, L. J. A. Koster, P. W. M. Blom, *Physical Review Letters* **2011**, *107*, 066605.
- [171] H. T. Nicolai, M. M. Mandoc, P. W. M. Blom, *Physical Review B* **2011**, *83*, 195204.
- [172] C. R. McNeill, S. Westenhoff, C. Groves, R. H. Friend, N. C. Greenham, *J. Phys. Chem. C* **2007**, *111*, 19153–19160.
- [173] C. Yin, T. Kietzke, D. Neher, H.-H. Hörhold, *Applied Physics Letters* **2007**, *90*, 092117–092117–3.
- [174] H. T. Nicolai, M. Kuik, G. A. H. Wetzelaer, B. de Boer, C. Campbell, C. Risko, J. L. Brédas, P. W. M. Blom, *Nature Materials* **2012**, *11*, 1–6.
- [175] M. Lenes, S. W. Shelton, A. B. Sieval, D. F. Kronholm, J. C. K. Hummelen, P. W. M. Blom, *Advanced Functional Materials* **2009**, *19*, 3002–3007.
- [176] D. Rauh, C. Deibel, V. Dyakonov, *Advanced Functional Materials* **2012**, n/a–n/a.
- [177] V. I. Klimov, A. A. Mikhailovsky, S. Xu, A. Malko, J. A. Hollingsworth, C. A. Leatherdale, H.-J. Eisler, M. G. Bawendi, *Science* **2000**, *290*, 314–317.
- [178] R. A. Street, M. Schoendorf, A. Roy, J. H. Lee, *Phys. Rev. B* **2010**, *81*, 205307.
- [179] C. G. Shuttle, B. O'Regan, A. M. Ballantyne, J. Nelson, D. D. C. Bradley, J. de Mello, J. R. Durrant, *Applied Physics Letters* **2008**, *92*, 093311.
- [180] G. Juška, K. Genevičius, N. Nekrašas, G. Sliaužys, G. Dennler, *Applied Physics Letters* **2008**, *93*, 143303–143303–3.
- [181] A. Maurano, R. Hamilton, C. G. Shuttle, A. M. Ballantyne, J. Nelson, B. O'Regan, W. Zhang, I. McCulloch, H. Azimi, M. Morana, C. J. Brabec, J. R. Durrant, *Advanced Materials* **2010**, *22*, 4987–4992.
- [182] A. Foertig, A. Baumann, D. Rauh, V. Dyakonov, C. Deibel, *Applied Physics Letters* **2009**, *95*, 052104–052104–3.
- [183] T. Clarke, A. Ballantyne, F. Jamieson, C. Brabec, J. Nelson, J. Durrant, *Chemical Communications* **2009**, 89.
- [184] A. Baumann, T. J. Savenije, D. H. K. Murthy, M. Heeney, V. Dyakonov, C. Deibel, *Advanced Functional Materials* **2011**, *21*, 1687–1692.
- [185] D. Credgington, J. R. Durrant, *J. Phys. Chem. Lett.* **2012**, *3*, 1465–1478.
- [186] C. Tanase, P. Blom, D. de Leeuw, *Physical Review B* **2004**, *70*, 193202.

- [187] W. Pasveer, J. Cottaar, C. Tanase, R. Coehoorn, P. Bobbert, P. Blom, D. de Leeuw, M. Michels, *Physical Review Letters* **2005**, *94*, 206601.
- [188] C. Tanase, P. W. M. Blom, D. M. de Leeuw, E. J. Meijer, *physica status solidi (a)* **2004**, *201*, 1236–1245.
- [189] J. Nelson, *Physical Review B* **2003**, *67*, 155209.
- [190] J. C. Blakesley, D. Neher, *Phys. Rev. B* **2011**, *84*, 075210.
- [191] C. Tanase, P. W. M. Blom, D. M. de Leeuw, *Phys. Rev. B* **2004**, *70*, 193202.
- [192] A. M. Goodman, A. Rose, *Journal of Applied Physics* **1971**, *42*, 2823–2830.
- [193] M. Lenes, L. J. A. Koster, V. D. Mihailetschi, P. W. M. Blom, *Applied Physics Letters* **2006**, *88*, 243502.
- [194] T. Kirchartz, T. Agostinelli, M. Campoy-Quiles, W. Gong, J. Nelson, *J. Phys. Chem. Lett.* **2012**, *3*, 3470–3475.
- [195] L. M. Andersson, Y.-T. Hsu, K. Vandewal, A. B. Sieval, M. R. Andersson, O. Inganäs, *ORGANIC ELECTRONICS* **2012**, *13*, 2856–2864.
- [196] L. M. Andersson, O. Inganäs, *Applied Physics Letters* **2006**, *88*, 082103–082103–3.
- [197] L. M. Andersson, *Organic Electronics* **2011**, *12*, 300–305.
- [198] J. C. Scott, G. G. Malliaras, *Chemical Physics Letters* **1999**, *299*, 115–119.
- [199] T. M. Clarke, F. C. Jamieson, J. R. Durrant, *J. Phys. Chem. C* **2009**, *113*, 20934–20941.
- [200] C. G. Shuttle, A. Maurano, R. Hamilton, B. O’Regan, J. C. de Mello, J. R. Durrant, *Applied Physics Letters* **2008**, *93*, 183501.
- [201] S. R. Cowan, R. A. Street, S. Cho, A. J. Heeger, *Phys. Rev. B* **2011**, *83*, 035205.
- [202] G. Garcia-Belmonte, A. Munar, E. M. Barea, J. Bisquert, I. Ugarte, R. Pacios, *Organic Electronics* **2008**, *9*, 847–851.
- [203] L. J. A. Koster, V. D. Mihailetschi, R. Ramaker, P. W. M. Blom, *Applied Physics Letters* **2005**, *86*, 123509.
- [204] L. J. A. Koster, M. Kemerink, M. M. Wienk, K. Maturova, R. A. J. Janssen, *Advanced Materials* **2011**, *23*, 1670–1674.
- [205] R. A. Street, K. W. Song, S. Cowan, *Organic Electronics* **2011**, *12*, 244–248.
- [206] G. F. A. Dibb, T. Kirchartz, D. Credgington, J. R. Durrant, J. Nelson, *J. Phys. Chem. Lett.* **2011**, *2*, 2407–2411.
- [207] C. G. Shuttle, R. Hamilton, B. C. O’Regan, J. Nelson, J. R. Durrant, *Proceedings of the National Academy of Sciences* **2010**, *107*, 16448–16452.
- [208] B. C. O’Regan, J. R. Durrant, P. M. Sommeling, N. J. Bakker, *J. Phys. Chem. C* **2007**, *111*, 14001–14010.
- [209] T. P. Osedach, T. L. Andrew, V. Bulović, *Energy Environ. Sci.* **2013**, *6*, 711–718.

## Chapter III

### Nongeminate Recombination and Charge Transport Limitations in Diketopyrrolopyrrole Based Solution Processed Small Molecule Solar Cells

#### 1. Introduction

Solution processed small molecule bulk heterojunction solar cells (SSMBHSCs) with power conversion efficiencies (PCE) of 7% have recently been reported.<sup>[1]</sup> This achievement demonstrates that SSMBHSCs fabricated from blends of small molecule donors and fullerene acceptors are a viable alternative to polymer:fullerene based systems. However, despite the recent gains in efficiency several of the most efficient SSMBHSCs exhibit strong voltage dependent losses which limits both the fill factor ( $FF$ ) and short circuit current ( $J_{sc}$ ).<sup>[2-6]</sup> To date there have been few fundamental investigations into the recombination mechanisms that lead to these losses.<sup>[7,8]</sup> Significant improvements in PCE may result from a deeper understanding of the voltage dependent loss mechanisms within small molecule based photovoltaic systems.

The nature of the voltage dependent losses in polymer:fullerene based solar cells has been the subject of much research. There is evidence that poor charge transport properties,<sup>[9,10]</sup> geminate recombination<sup>[11-13]</sup> and both bimolecular (Langevin)<sup>[14-18]</sup> and trap-assisted (Shockley-Read-Hall)<sup>[19,20]</sup> recombination (nongeminate recombination) mechanisms may all play a role depending on materials and device processing conditions. Geminate recombination occurs when a coulombically bound electron-hole pair generated from absorption of a single photon recombines *before* the electron and hole can separate into free charge carriers. Nongeminate recombination is the recombination of free charge carriers

and encompasses both trap-assisted and bimolecular mechanisms. Experimentally, geminate and nongeminate mechanisms can be distinguished by observing the timescale at which they occur and their dependence on carrier density. The probability of geminate recombination is independent of carrier density and geminate losses happen within nanoseconds of absorption<sup>[8,11,13,17]</sup>. In contrast, nongeminate losses are carrier density dependent and typically occur after micro-to milli-seconds when illumination conditions are comparable to 1 sun.<sup>[14–16,18,21]</sup> Initial studies of SSMBHSCs based on diketopyrrolopyrrole (DPP) materials have concluded both geminate and nongeminate recombination can influence small molecule systems.<sup>[8]</sup> However, it is not known if this is true for all SSMBHSCs nor is it understood how these loss mechanisms can be overcome.

In this work, we study charge transport and voltage dependent recombination in two SSMBHSC systems consisting of DPP based donor molecules blended with [6,6] phenyl-C71-butyric acid methyl ester (PCBM). The first system 2,5-di-(2-ethylhexyl)-3,6-bis-(5''-n-hexyl – [2,2',5',2'']terthiophen-5-yl) – pyrrolo[3,4-c]pyrrole-1,4-dione (mono-DPP), has previously achieved a PCE of 3% when blended with PCBM despite a low *FF* of only 0.44.<sup>[4]</sup> The second system 4,7-bis{2-[2,5-bis(2-ethylhexyl)-3-(5-hexyl-2,2':5',2'']-terthiophene-5''-yl)-pyrrolo[3,4-c]pyrrolo-1,4-dione-6-yl]-thiophene-5-yl}-2,1,3-benzothiadiazole (bis-DPP) was reported as a material with high ambipolar mobility in field effect transistors.<sup>[22]</sup> We first use single carrier diodes to gauge the hole and electron mobilities of each system. Impedance spectroscopy is then used to directly measure the voltage dependence of the series resistance and average charge carrier density. Additionally, we conduct effective carrier lifetime and light intensity measurements of operating solar cells to gauge the influence of nongeminate recombination. Compiling these data we are able

to determine the physical origin of the difference in voltage dependence and accordingly a strategy for the future molecular design of high performing solution processed donor molecules for bulk heterojunction solar cells.

## 2. Results and Discussion

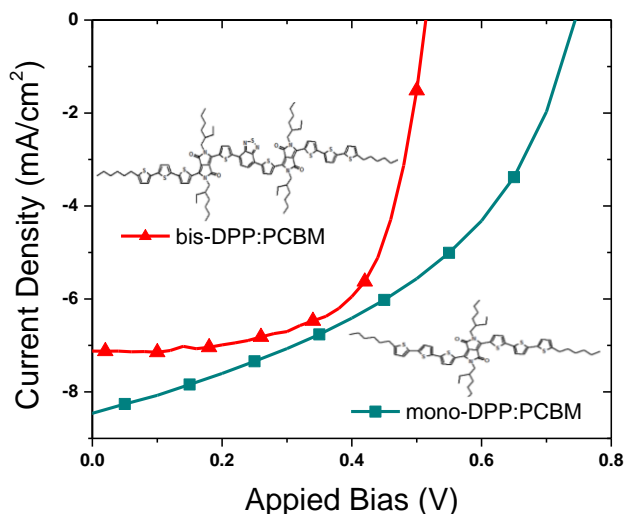


**Figure 3.1.**  $J$ - $V$  characteristics of optimized bis-DPP:PCBM and mono-DPP:PCBM solar cell devices irradiated with  $100\text{mW cm}^{-2}$  light intensity. Inset: chemical structure of bis-DPP and mono-DPP.

The mono-DPP:PCBM solar cell devices studied here averaged a  $0.46 FF$ ,  $8.0\text{ mA cm}^{-2} J_{sc}$ ,  $0.75\text{ V}$  open circuit voltage ( $V_{oc}$ ), and  $2.8\%$  PCE while the bis-DPP:PCBM devices averaged a  $0.62 FF$ ,  $6.6\text{ mA cm}^{-2} J_{sc}$ ,  $0.51\text{ V}_{oc}$ , and  $2.1\%$  PCE (measured under AM1.5 irradiation  $100\text{ mW cm}^{-2}$ ). **Figure 3.1** shows the current density-voltage ( $J$ - $V$ ) response of typical devices measured along with the chemical structures of the mono- and bis-DPP materials (inset). The bis-DPP:PCBM system exhibits only minimal voltage dependent losses up until the  $V_{oc}$  while the mono-DPP:PCBM system features significant voltage dependent losses throughout the operating regime (from  $0\text{V}$  to  $V_{oc}$ ). As discussed in the

introduction, multiple processes could lead to this difference in voltage dependence. We will begin our analysis by exploring the charge transport properties of each system.

## 2.1 Charge transport in mono-DPP:PCBM and bis-DPP:PCBM devices

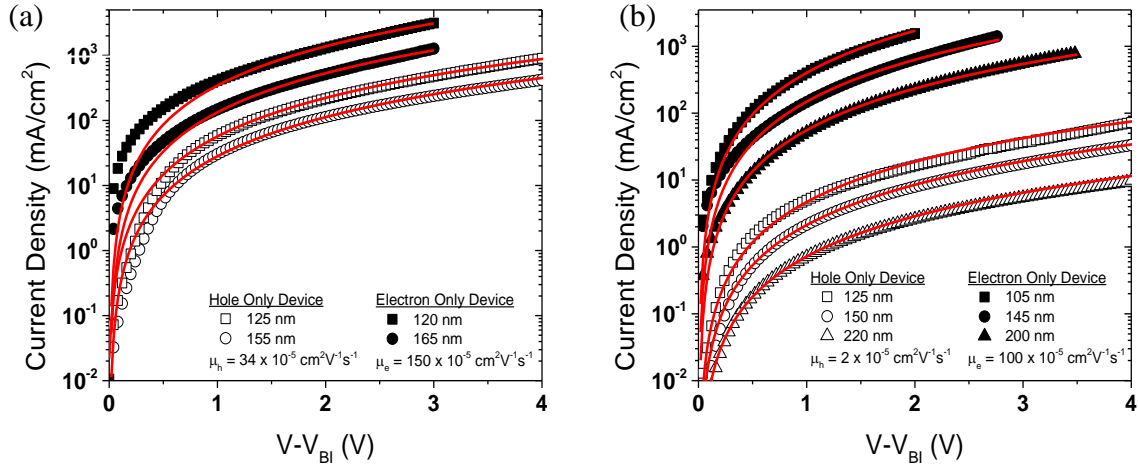


**Figure 3.2.**  $J$ - $V$  characteristics of electron and hole only devices with bis-DPP:PCBM (a) and mono-DPP:PCBM (b) active layers. Red lines are fits to Equation 1.

The relation between charge transport and device performance in polymer:fullerene systems is well established.<sup>[9,10,23–25]</sup> If the hole and electron carrier mobilities are too low or heavily unbalanced, charges cannot be swept out efficiently before recombination resulting in low  $FF$ s and quantum efficiencies. In principal, it is expected that the same relations would hold for small molecule based solar cells thus we start our analysis by measuring the hole and electron mobilities in the optimized blend films. As mentioned above, bis-DPP was previously reported to have high field effect mobilities.<sup>[22]</sup> This demonstrates the material's efficient transport properties laterally but cannot be taken as a measure of the carrier mobility in a solar cell device, which occurs in the direction normal to the substrate. An

initial estimate of the carrier mobilities of mono-DPP:PCBM devices was also reported,<sup>[4]</sup> however, these measurements were not confirmed across a range of film thicknesses. Here, the charge carrier mobilities in bis-DPP:PCBM and mono-DPP:PCBM blends are measured in a device geometry similar to solar cell devices for a range of thicknesses as shown in **Figure 3.2 a** and **b**, respectively. The  $J$ - $V$  characteristics of both electron-only (Indium-Tin-Oxide (ITO)/Al/blend/Ca/Al) and hole-only (ITO/ Poly(3,4-ethylenedioxythiophene) poly(styrenesulfonate (PEDOT:PSS)/blend/Au) diodes show an excellent fit to the Mott-Gurney relation for space charge limited current.<sup>[26]</sup>

$$J = \frac{9\epsilon_r\epsilon_0\mu V^2}{8L^3} \quad (3.1)$$

where  $\epsilon_r$  is the relative dielectric constant,  $\epsilon_0$  the permittivity of free space,  $\mu$  the zero-field mobility and  $L$  the active layer thickness. The single-carrier devices for both systems demonstrate the  $L^{-3}$  dependence confirming that these devices truly exhibit space charge limited behavior. Using a relative dielectric constant of 4 as measured by impedance spectroscopy, the electron mobility,  $\mu_e$ , of bis-DPP:PCBM is  $150 \times 10^{-5} \text{ cm}^2\text{V}^{-1}\text{s}^{-1}$  and the hole mobility,  $\mu_h$ , is  $34 \times 10^{-5} \text{ cm}^2\text{V}^{-1}\text{s}^{-1}$ , a factor of 4.4 lower than the electron mobility. An equivalent measurement of single-carrier diodes with mono-DPP:PCBM reveals a significantly lower  $\mu_h$  of only  $2 \times 10^{-5} \text{ cm}^2\text{V}^{-1}\text{s}^{-1}$ . Inclusion of a small field dependent term ( $e^{\gamma\sqrt{V/L}}$  with  $\gamma = 5.5 \times 10^{-5}$ ) was necessary for an accurate analysis of the current in the mono-DPP:PCBM electron-only devices yielding a  $\mu_e$  of  $100 \times 10^{-5} \text{ cm}^2\text{V}^{-1}\text{s}^{-1}$ , a full 50 times higher than the hole mobility. That the mono-DPP:PCBM mobilities reported here are slightly different than previously reported may be attributable to a difference in processing conditions (80°C annealed in this study vs. as-cast in the previous report<sup>[4]</sup>) and to the

influence of electrodes when the active layer is not sufficiently thick<sup>[28]</sup> (the previous report<sup>[4]</sup> used an 80 nm active layer). The similar  $\mu_e$  observed in each system is consistent with the expectation that the  $\mu_e$  in blend films should be comparable to the electron mobility of pristine PCBM films.<sup>[29,30]</sup>

The one order of magnitude lower hole mobility measured in the mono-DPP:PCBM diodes suggests that mono-DPP:PCBM solar cells may be transport limited. Nonetheless, the observation of lower charge carrier mobility alone is not sufficient evidence to conclude that the difference in voltage dependence observed in the mono-DPP:PCBM and bis-DPP:PCBM devices is solely an issue of charge transport. Geminate recombination or a short charge carrier lifetime (due to trapping or bimolecular recombination) could also contribute to the low  $FF$  observed in the mono-DPP:PCBM solar cells. Thus, further study of the recombination mechanisms is warranted.

## **2.2 Light intensity dependence of mono-DPP:PCBM and bis-DPP:PCBM solar cells**

Measuring the light intensity dependence of solar cell  $J$ - $V$  characteristics has been demonstrated to be a powerful tool for probing the dominant recombination mechanisms.<sup>[9,25,31–33]</sup> Here we study the light intensity dependence of optimized mono-DPP:PCBM and bis-DPP:PCBM solar cell devices. The light intensity dependence of the  $FF$  and  $V_{oc}$  for each system are presented in **Figure 3.3 a** and **b** respectively. The fact that the  $FF$  does not decrease at lower light intensities and that the  $V_{oc}$  shows a linear behavior over the entire intensity range in a semi-logarithmic plot can be held as an indication that the quality of the devices used in this analysis is good and the parasitical leakage current is sufficiently low. The  $FF$  of the mono-DPP:PCBM decreases with increasing light intensity

as does the  $FF$  of the bis-DPP:PCBM system though not quite as significantly. To understand this trend, we first consider that the photogenerated charge carrier density scales with incident light intensity. Geminate recombination is independent of charge carrier density and consequently the probability of a geminate pair recombining should be independent of light intensity within the range studied here (0.1-1 sun). Nongeminate recombination in contrast *does* depend on charge carrier density; for instance, an increase in charge carrier density would mean there is a greater probability of a free electron and hole “finding” one another and then recombining. Following this reasoning, the decrease in  $FF$  at higher light intensities is evidence that the  $FF$  of both systems is heavily influenced by nongeminate recombination at intensities close to 1 sun.<sup>[15,33]</sup>

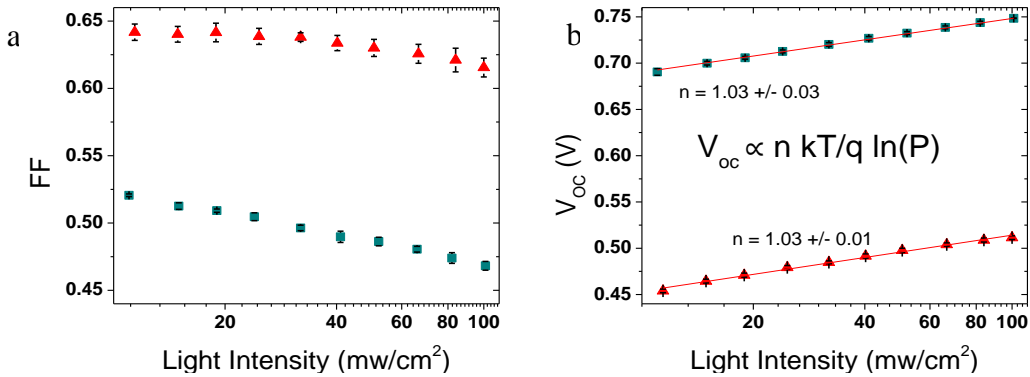


**Figure 3.3.** Light intensity dependence of  $FF$  (a) and  $V_{oc}$  (b) in bis-DPP:PCBM (triangles) and mono-DPP:PCBM (squares) solar cell devices.

Multiple studies have demonstrated that the light intensity dependence of the  $V_{oc}$  can provide insight into the role of trap-assisted recombination versus bimolecular recombination at the open circuit condition.<sup>[21,34]</sup> Both mono-DPP:PCBM and bis-DPP:PCBM exhibit a logarithmic dependence on light intensity ( $V_{oc} \propto n kT/q \ln(P)$ ) where  $n$

is a constant,  $k$  is Boltzmann's constant,  $T$  is temperature,  $q$  is the elementary charge and  $P$  is the incident light intensity) with a slope of  $\sim 1.0 kT/q$ . This indicates that trap states do not play a significant role at the open circuit condition in either of these systems. Thus as has been found for the majority of the polymer:fullerene systems,<sup>[19,32]</sup> bimolecular recombination dominates at open circuit in these SSMBHSCs.

In order to probe the recombination mechanisms away from open circuit the photocurrent ( $J_{ph}$ ) for each system is analyzed as a function of bias and light intensity. For a system with negligible series resistance,  $J_{ph} = J_L - J_D$ , where  $J_L$  and  $J_D$  are the measured light and dark currents, respectively. **Figure 3.4** shows the  $J_{ph}$  of the bis-DPP:PCBM (**a**) and mono-DPP:PCBM (**b**) devices plotted versus the effective voltage ( $V_{eff} = V_o - V_{ap}$ ) measured at several light intensities, where  $V_o$  is the voltage at which  $J_{ph} = 0$  and  $V_{ap}$  is the applied bias. In the case of bis-DPP:PCBM, the photocurrent shows two primary regimes: a linear dependence on  $V_o - V_{ap}$  and a regime in which the photocurrent quickly saturates ( $V_{eff} \approx 1V$ ). The presence of only these two regimes suggests that this system has zero net trapped charge and the electric field is uniform throughout the active layer.<sup>[35]</sup> The photocurrent of the mono-DPP:PCBM system in contrast shows a stronger field-dependence across a large bias range not fully saturating until  $V_{eff} \approx -5V$ . This can be explained in terms of the difference in charge carrier mobilities; the lower  $\mu$  of mono-DPP:PCBM requires a stronger electric field to sweep out all of the photogenerated charges before they recombine. A complimentary possibility is that in mono-DPP:PCBM the separation of geminate electron-hole pairs can be assisted by a strong electric field. By this theory, the  $J_{ph}$  increases at higher effective voltage (reverse bias) because of a decrease in geminate recombination; however, analysis of the

photocurrent alone cannot determine the influence of geminate recombination therefore an alternative approach is needed to evaluate this possibility.

Interestingly, despite the  $\mu_h$  being 50 times less than the  $\mu_e$ , the photocurrent in mono-DPP:PCBM does not appear to be space charge limited. Following the work of Goodman and Rose<sup>[35]</sup>, Mihailetchi et al.<sup>[9]</sup> showed that an imbalance in mobilities can lead to a buildup of space charge resulting in a photocurrent with a square root dependence on the effective voltage ( $J_{ph} \propto V_{eff}^{1/2}$ ). We observe no significant bias range with such a dependence in mono-DPP:PCBM devices. Mihailetchi et al. also demonstrated that a space charge limited photocurrent scales with a three-quarters power dependence on light intensity. **Figure 3.4c** presents the light intensity dependence of  $J_{ph}$  in mono-DPP:PCBM and bis-DPP:PCBM devices measured at different effective voltage conditions and fit to a simple power law relation  $J_{ph} \propto P^S$ . The  $J_{ph}$  in the mono-DPP:PCBM device does not approach the space charge limit of  $S = 0.75$  even at lower effective voltages confirming that this system is not space charge limited. With that said, the slight sub-linear dependence of  $J_{ph}$  on light intensity indicates that space charge effects may still play a minor role. This sub-linear dependence could also be a sign of significant bimolecular recombination.<sup>[31]</sup>

It is worth noting that the linear light dependence seen for the  $J_{ph}$  in the bis-DPP:PCBM device should not be taken as evidence that there is no bimolecular recombination as has been done in other studies.<sup>[32,36]</sup> It has been shown that even systems dominated by bimolecular recombination can exhibit a  $J_{ph}$  with a linear dependence on light intensity up to 1 sun.<sup>[37, 38]</sup>

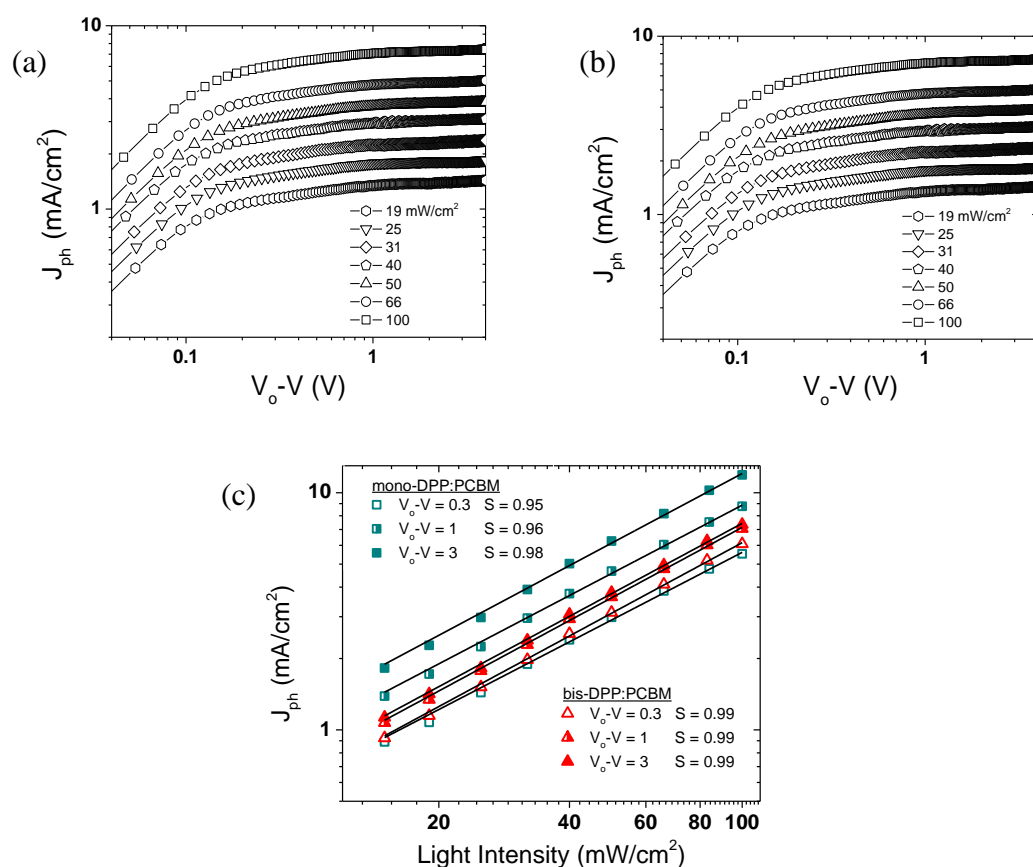


**Figure 3.4:** Photocurrent versus effective voltage in bis-DPP:PCBM (a) and mono-DPP:PCBM solar cell devices (b). Light intensity dependence of the photocurrent in bis-DPP:PCBM and mono-DPP:PCBM solar cell devices with fit lines to  $J_{ph} \propto P^S$ .

To summarize the light intensity dependence results, it is evident that for both the mono-DPP:PCBM and bis-DPP:PCBM systems (i) bimolecular recombination dominates at open circuit and (ii) the  $FF$  is heavily influenced by a nongeminate recombination mechanism. Based on the photocurrent analysis, the bis-DPP:PCBM system is nearly ideal with no evidence of trapping, space charge effects, or mobility limitations. In contrast, the  $J_{ph}$  in the mono-DPP:PCBM system shows a strong field dependence even at reverse bias conditions which is a direct result of the low hole mobility and may also be a sign of voltage dependent geminate recombination.

### 2.3 Impedance analysis of mono-DPP:PCBM and bis-DPP:PCBM devices

To further understand the nature of the voltage dependent losses in mono-DPP:PCBM and bis-DPP:PCBM solar cell devices, differential resistance and capacitance analyses were conducted using an impedance analyzer. Impedance spectroscopy (IS) has been demonstrated to be a powerful tool for analyzing a variety of electronic devices including dye-sensitized solar cells,<sup>[39]</sup> light emitting diodes<sup>[40,41]</sup> and more recently organic photovoltaics.<sup>[7,42–45]</sup> The advantage of impedance spectroscopy compared to other optoelectronic techniques is that impedance measurements are nondestructive and can be conducted at steady state for a range of bias conditions using standard device geometries and normal solar cell operating light intensities. Differential resistance analysis of impedance spectra also allows for a direct measurement of the series resistance which is crucial for an accurate characterization of the loss mechanisms in devices.<sup>[15,43,46]</sup>

In this study, the impedance response of mono-DPP:PCBM and bis-DPP:PCBM solar cell devices were measured at a range of DC bias conditions ( $-5\text{V}$  to  $V_{oc}$ ) and illumination intensities ( $0$  to  $100\text{ mW/cm}^2$ ). For each bias and light condition, a constant DC bias was held across the illuminated device while the frequency of a  $20\text{ mV}$  AC bias was swept from  $50\text{Hz}$ – $1.6\text{MHz}$ . A Cole-Cole plot of the impedance spectra from a representative mono-DPP:PCBM solar cell measured at an incident light intensity of  $42\text{ mW/cm}^2$  is presented in the **Figure 3.5a**. The symbols represent measured data points while the lines are fits to a simple RC circuit model (inset of **Figure 3.5b**). The circuit model used to fit the impedance spectra contains three elements: the series resistance ( $R_s$ ), the device capacitance ( $C_u$ ) and the differential diode resistance ( $R_{diff}$ ).  $R_s$  represents the series resistance from both the

experimental setup (cables and leads) and the device contacts.  $C_u$  originates from charges stored on the electrodes as well as the separation of positively charged donor (mono-DPP) domains and negatively charged acceptor (PCBM) domains within the photoactive layer.  $R_{diff}$  is a measure of the inverse slope of the  $JV$  curve at a given DC bias condition. As we will show, measuring  $R_s$ ,  $C_u$  and  $R_{diff}$  as a function of DC bias allows for reconstruction of the  $J-V$  characteristics and determination of the series resistance corrected voltage scale and the average charge carrier density as a function of bias.

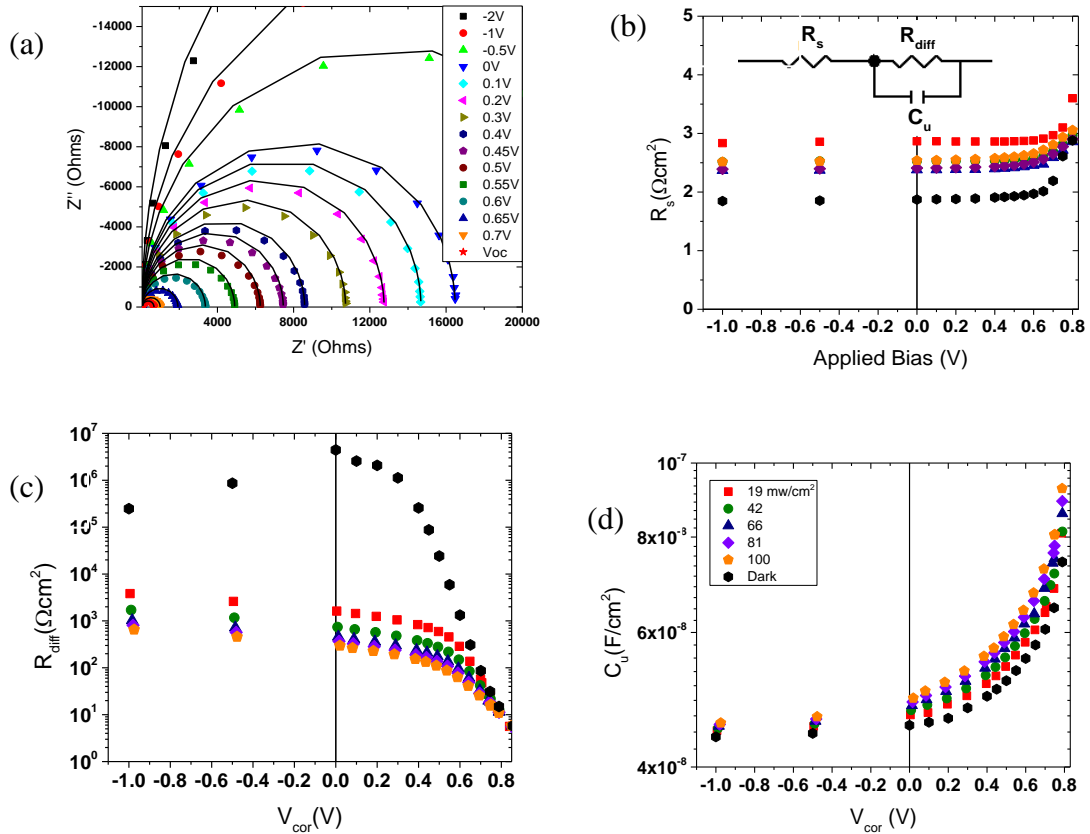


**Figure 3.5:** Measured impedance response of mono-DPP:PCBM device as a function of DC bias illuminated at 42  $\text{mW}/\text{cm}^2$  (symbols) and corresponding fits (lines) using circuit model (inset in b) (a). Series resistance (b),  $R_{diff}$  (c) and  $C_u$  (d) as a function of bias and light intensity extracted from circuit model fits.

### 2.3.1 Series resistance and corrected voltage scale

As shown in **Figure 3.5b**, mono-DPP:PCBM exhibits a relatively small series resistance of  $\sim 3\Omega\text{cm}^2$  indicating that losses at the contacts are not the primary limitation to  $FF$ . The increase in  $R_s$  at higher  $V_{ap}$  suggests that the series resistance is influenced by charge injection from the contacts and may also capture some charge transport properties.<sup>[39,43,47]</sup> Measuring  $R_s$  as a function of bias allows for a precise correction of the voltage scale to account for the voltage drop due to the series resistance. The voltage drop due to the series resistance is  $V_{Rs} = J_L A R_s$  where  $A$  is the electrode area. Thus, the actual voltage applied across the active layer is

$$V_{cor} = V_{ap} - V_{Rs}. \quad (3.2)$$

As this study is primarily concerned with losses occurring within the active layer, the subsequent analysis will make use of the corrected voltage scale ( $V_{cor}$ ).

### 2.3.2 Differential resistance and J-V matching

With the corrected the voltage scale in hand, we can now consider the relation between  $R_{diff}$  and the  $J$ - $V$  curve. Solar cells are not ohmic devices (ie. the current is not directly proportional voltage across the device) therefore the resistor  $R_{diff}$  is not ohmic in nature either. Rather,  $R_{diff}$  is a differential resistance which can be expressed as

$$R_{diff} = \left( \frac{dJ_L}{dV_{cor}} \right)^{-1}. \quad (3.3)$$

In words,  $R_{diff}$  is a measure of the inverse slope of the  $JV$  curve at a fixed bias condition. **Figure 3.5c** displays the  $R_{diff}$  measured for a mono-DPP:PCBM device. As expected from Equation (3.3),  $R_{diff}$  decreases with forward bias consistent with the changing slope of the  $JV$  curves. As the light intensity increases so too does  $R_{diff}$ . Similar to the  $FF$  light dependence, this can be explained by a carrier density dependent recombination mechanism (nongeminate

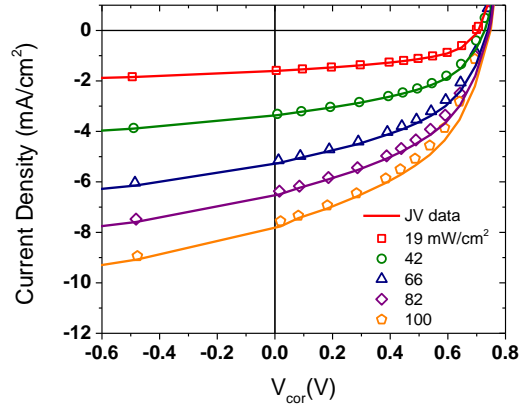
recombination) that limits charge extraction more and more as carrier density increases. The  $R_{diff}$  dependence on light intensity decreases as  $V_{cor}$  approaches  $V_{oc}$  as injected carriers play an increasingly significant role in the recombination dynamics.

Using a similar circuit model analysis to characterize poly(3-hexylthiophene):PCBM devices, Boix et al. recently demonstrated that fitting  $R_{diff}$  to an exponential relation around  $V_{cor} = V_{oc}$  allows for recreation of the  $J$ - $V$  characteristics.<sup>[43]</sup> However, in contrast to their findings, in the case of mono-DPP:PCBM even with the decreasing light dependence of  $R_{diff}$  near  $V_{oc}$ , it is not observed that  $R_{diff}$  collapses to a single curve independent of light intensity. Furthermore, one observes there is some ambiguity in fitting an exponential relation to  $R_{diff}$  around  $V_{oc}$  depending on the bias range considered. Therefore, an alternative approach is needed to evaluate the influence of  $R_{diff}$  on the  $J$ - $V$  characteristics.

A simple rearrangement of Equation (3.3) allows for a direct calculation of  $J_L$  from the measured  $R_{diff}$  values:

$$J_L(V_{cor}) = J_L(V_x) + \int_{V_x}^{V_{cor}} \frac{dV_{cor}}{R_{diff}} \quad (3.4)$$

where  $V_x$  determines the lower limit of the bias range and could in principal be set at any voltage less than  $V_{oc}$ . Figure 3.6 shows the  $J$ - $V$  characteristics for mono-DPP:PCBM as determined from  $R_{diff}$  using Equation (3.4) (symbols) align well with the  $J$ - $V$  curve from the standard current voltage measurement (lines). The same procedure is also found to recreate the  $J$ - $V$  characteristics with great precision for bis-DPP:PCBM and mono-DPP:PCBM devices with  $V_x = -5V$  (See Supporting Information, Figure S3.1). Thus, the shape of the  $J$ - $V$  curve from  $V_x$  to  $V_{oc}$  is clearly captured by  $R_{diff}$  as expected by the relation in Equation (3.3). This confirms the high quality of the impedance measurements.



x

**Figure 3.6:**  $J$ - $V$  curve from impedance data using Equation 3.4 (symbols) and measured  $J$ - $V$  curves (lines) for mono-DPP:PCBM.

### 2.3.3 Capacitance and average charge carrier density

Having evaluated the resistive elements of the simple circuit model, we now turn to the capacitive element to determine the charge carrier density as a function of applied bias. The device capacitance measured in a mono-DPP:PCBM device is plotted versus  $V_{cor}$  in **Figure 3.5d**. That  $C_u$  steadily increases with light intensity is strong evidence that it originates from photogenerated charges within the active layer. Notably,  $C_u$  also increases with forward bias in both illuminated *and* dark conditions. This implies that in addition to photogenerated charges,  $C_u$  is influenced by charge injection from the electrodes. Under reverse bias, where injection is minimal and most photogenerated charges are collected at the electrodes,  $C_u$  converges toward the geometrical capacitance ( $C_g$ ). The device capacitance measured in the dark under appropriate reverse bias conditions (-1V in this case) is precisely the geometric capacitance; for the mono-DPP:PCBM system this corresponds to a relative dielectric constant of  $\sim 4.0$ .

To determine the average carrier density within in the active layer ( $n$ ) from  $C_u$ , one must first account for the capacitive contribution from the electrodes. The internal capacitance originating from only photogenerated and injected charges ( $C_{in}$ ) is then

$$C_{in} = C_u - C_g. \quad (3.5)$$

Capacitance is the derivative of charge with respect to voltage thus it follows that

$$C_{in} = qAL \frac{dn}{dV_{cor}} \quad (3.6)$$

where  $q$  is the elementary charge and  $A$  is the electrode area. Rearranging Equation 4 and defining the carrier density at the saturation voltage to be  $n_{sat}$  leads to an expression for the carrier density as function of applied bias such that

$$n(V_{cor}) = n_{sat} + \frac{1}{qAL} \int_{V_{sat}}^{V_{cor}} C_{in} dV_{cor} \quad (3.7)$$

where  $V_{sat}$  is the voltage at which the photocurrent saturates. In principle, the lower limit for the integral in Equation (7) could start from any voltage ( $V_x$ ) so long as  $n(V_x)$  is known. The advantage of starting from  $V_{sat}$  is that  $n_{sat}$  can be determined directly from the impedance measured capacitance. Assuming that at  $V_{sat}$ , the generation rate is constant and recombination losses are negligible, it can be shown that

$$n_{sat} = \frac{1}{qAL} C_{sat} (V_0 - V_{sat}) \quad (3.8)$$

where  $C_{sat}$  is the internal capacitance measured at  $V_{sat}$  (see Supporting Information).

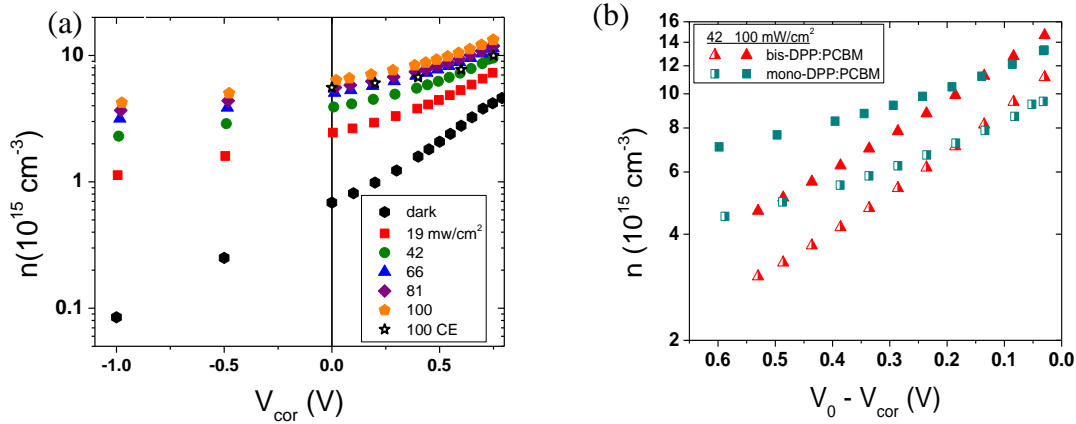


**Figure 3.7:** (a) Charge carrier density versus the corrected voltage for the mono-DPP:PCBM system measured at different incident light intensities. The star symbols represent measurements made using a charge extraction technique. (b) Charge carrier density versus effective voltage for mono-DPP:PCBM and bis-DPP:PCBM devices measured at 42  $\text{mW/cm}^2$  and 100  $\text{mW/cm}^2$ .

Having measured  $C_u$  from  $V_{sat}$  to  $V_{oc}$  we can now use Equations 3.5-8 to determine the average carrier density in mono-DPP:PCBM devices as a function of bias and light intensity (**Figure 3.7a**). As expected, the carrier density increases with both light intensity and applied bias. At open circuit, injected carriers account for approximately one third of the carrier density measured at 100  $\text{mW/cm}^2$ . This observation is consistent with the findings of Shuttle et al. that the average charge carrier density in polymer:fullerene devices originates from both photogenerated charges and charges injected at the electrodes.<sup>[15]</sup>

Capacitances measured by impedance spectroscopy<sup>[7]</sup> and transient photovoltage in combination with transient photocurrent<sup>[48]</sup> have previously been used to determine the carrier density in an organic solar cell at open circuit. However, to the best of our knowledge, this is the first time IS measured capacitances have been used to determine the carrier density as a function of applied bias in an organic solar cell. To validate the technique

the charge carrier density was also measured by a charge extraction technique (CE)<sup>[49]</sup> with a reverse extraction bias<sup>[50]</sup>. The carrier density measured by CE for a mono-DPP:PCBM device illuminated with LEDs at approximately one sun equivalent intensity is presented in **Figure 3.7a** (star symbols). The carrier density from CE agrees well with the impedance measured  $n$  within a reasonable variation attributable to device to device variations, deviations from the assumed uniform carrier density profile and limitations in the extraction technique arising from the imbalanced charge carrier mobilities.

**Figure 3.7b** presents the carrier density measured in bis-DPP:PCBM solar cells using the same impedance analysis alongside the  $n$  measured in mono-DPP:PCBM devices plotted versus effective voltage. The trend in  $n$  measured at effective voltages close to short circuit (0.78 V and .052 V for mono-DPP:PCBM and bis-DPP:PCBM respectively) corresponds well with the respective short circuit currents. However, the  $n$  in the bis-DPP:PCBM system exhibits a steeper rise with forward bias leading to a carrier density at open circuit ( $n_{oc}$ ) that is slightly greater than the  $n_{oc}$  measured in the mono-DPP:PCBM devices. This trend is indicative of comparatively weaker recombination in the bis-DPP:PCBM system consistent with the higher FF.

#### 2.4 Recombination current and effective carrier lifetime

The impedance analysis in Section 2.3 measured the voltage dependence of the series resistance and the charge carrier density. Coupling this information with a simple analysis of the light current allows for estimation of the average time that a free charge carrier lives before recombining. This effective charge carrier lifetime,  $\tau_{eff}$ , can be considered a measure of how fast recombination occurs – a longer  $\tau_{eff}$  means photogenerated charges have more time to be swept out and collected at the electrodes before they are lost to recombination.

To determine  $\tau_{eff}$  we first consider the recombination current,  $J_{rec}$ , which by definition is the current lost to recombination at any given bias condition. When the light current saturates, recombination losses are negligible meaning  $J_{rec}(V_{sat}) = 0$ , thus it follows that:

$$J_{rec}(V_{cor}) = J_{sat} + J_L(V_{cor}) \quad . \quad (3.9)$$

In principle,  $J_{rec}$  encompasses *all* recombination loss mechanisms that can cause a small change in current - both geminate and nongeminate. With that said, it is clear from the light intensity measurements in Section 2.2 that both systems considered here are heavily influenced by nongeminate recombination losses at 1 sun incident light intensity. This suggests that  $J_{rec}$  at 1 sun is primarily a measure of the nongeminate recombination current. Therefore our subsequent analysis will assume that voltage dependent geminate losses are negligible. A discussion of the case in which geminate losses are more significant is included in the Supporting Information.

If  $J_{rec}$  is purely nongeminate recombination it can be expressed as

$$J_{rec}(V_{cor}) = qL \frac{n(V_{cor})}{\tau_{eff}(V_{cor})} \quad (3.10)$$

where  $\tau_{eff}$  may be influenced by charge trapping and/or bimolecular recombination. As we have already measured  $n(V_{cor})$  and  $J_{rec}(V_{cor})$ ,  $\tau_{eff}(V_{cor})$  can be extracted from the relation in Equation (3.10). The effective charge carrier lifetime in mono-DPP:PCBM and bis-DPP:PCBM devices measured at 1 sun incident light intensity is presented as a function of effective voltage in **Figure 3.8**. For  $V_0 - V_{cor} > 0.2V$ , the  $\tau_{eff}$  in bis-DPP:PCBM is more than three times that measured in mono-DPP:PCBM which means that on average charge carriers recombine at least three times faster in the mono-DPP:PCBM system. This is consistent with the intensity dependence of the photocurrent noted earlier that indicated

mono-DPP:PCBM has a stronger bimolecular recombination rate. The  $\tau_{eff}$  in bis-DPP:PCBM decreases sharply at low effective voltages (close to  $V_{oc}$ ) falling to within a factor of two of the  $\tau_{eff}$  in mono-DPP:PCBM. This may be related to a field dependent mobility<sup>[13]</sup> or increased recombination near the electrodes due to charge injection. The surprisingly weak voltage dependence for  $\tau_{eff}$  in the mono-DPP:PCBM system may be indicative of a charge trapping mechanism and/or voltage dependent geminate losses. Future investigations will explore these possibilities in more detail.

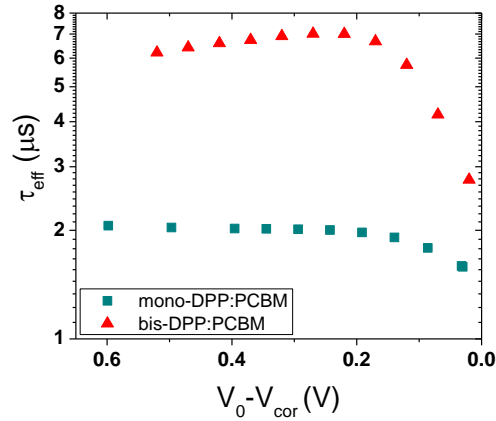


**Figure 3.8:** Effective charge carrier lifetime versus effective voltage in mono-DPP:PCBM and bis-DPP:PCBM devices measured at 100 mW/cm<sup>2</sup> incident light intensity.

We can further our analysis by considering that at open circuit all photogenerated charges recombine and therefore the generation rate,  $G$ , is equal to the recombination rate  $R$ . Maintaining the assumption that voltage dependent geminate recombination is negligible,  $G$  can be determined from the saturated photocurrent by the relation  $J_{ph, sat} = qLG$ .<sup>[9]</sup> As discussed in Section 2.2 the light intensity dependence of the  $V_{oc}$  indicates that bimolecular recombination dominates at open circuit in both mono-DPP:PCBM and bis-DPP:PCBM. Therefore the recombination rate at  $V_{oc}$  can be expressed as  $R = \gamma n_{oc}^2$  where  $\gamma$  is the bimolecular recombination rate constant<sup>[32]</sup>. Coupling these relations, we estimate that at 1

sun for mono-DPP:PCBM  $\gamma \approx 5.3 \times 10^{-17} \text{ m}^3 \text{ s}^{-1}$  and for bis-DPP:PCBM,  $\gamma \approx 2.6 \times 10^{-17} \text{ m}^3 \text{ s}^{-1}$ . This corresponds to Langevin reduction factors of 0.11 and 0.03 for mono-DPP:PCBM and bis-DPP:PCBM respectively compared to the predicted  $\gamma$  from the Langevin model ( $\gamma = q/\epsilon(\mu_e + \mu_h)$ ). It is worth noting that the Langevin reduction factors found here are on the lower end of what has been reported for most polymer:fullerene systems. It has been suggested that the origin of reduced Langevin rates may be the inherent assumption that the density of holes and electrons is equal everywhere when in reality the active layer may have significant inhomogeneity in the hole and electron densities due to the separated domains of donor and acceptor materials.<sup>[51, 52]</sup> Following this reasoning, it may be that the small molecule blends studied here are more homogeneous than most polymer:fullerene blends. This topic will be the subject of future study.

## 2.5 Effect of carrier lifetime and mobility on solar cell performance

Up to this point, we have shown the mono-DPP:PCBM system exhibits a lower hole mobility and a shorter effective carrier lifetime than the bis-DPP:PCBM system. We now attempt to differentiate the influence of  $\mu$  and  $\tau_{eff}$  on solar cell performance. The Hecht formula<sup>[10,36,53]</sup> can be used to directly assess the effect of the  $\mu\tau_{eff}$  product on  $Q/Q_0$ , the fraction of photogenerated charges which are collected before recombination. As first described by Hecht,

$$\frac{Q}{Q_0} = \frac{\mu\tau_{eff}F}{L/2} \left( 1 - \exp\left(\frac{-L/2}{\mu\tau_{eff}F}\right) \right) \quad (3.11)$$

where  $F = (V_o - V_{cor})/L$  is the electric field across the device thickness  $L$ , and  $L/2$  is the average depth of photogenerated carriers assuming uniform photogeneration throughout the device. **Figure 3.9** shows  $Q/Q_0$  calculated for mono-DPP:PCBM and bis-DPP:PCBM as a

function of  $F$  using the lifetime data presented in **Figure 3.8** with  $L = 90$  nm. For the mobilities, we assume transport to be limited by the slowest carrier and input only the measured hole mobilities. The Hecht formula seems to slightly underestimate the collection efficiency for mono-DPP:PCBM, which is not surprising given the inherent assumptions of uniform photogeneration, constant electric field and fixed mobility. This may also be an indication that there are indeed field dependent geminate recombination losses. Nonetheless, the trends in **Figure 3.9** are consistent with the experimentally measured photocurrent. Compared to bis-DPP:PCBM (triangle symbols),  $Q/Q_0$  for the mono-DPP:PCBM system (square symbols) is highly field-dependent – only reaching towards ~60% collection at fields equivalent to short circuit while dropping steadily at lower effective voltages. The stark contrast between the two systems illustrates the effect of the lower mobility and shorter lifetime in the mono-DPP:PCBM system. In order to separate the influences of  $\mu$  and  $\tau_{eff}$ , **Figure 3.9** also includes the results of Equation (3.11) with a  $\mu\tau_{eff}$  using the  $\mu$  in bis-DPP:PCBM and the  $\tau_{eff}$  in mono-DPP:PCBM (dashed-dot line) and the  $\mu$  in mono-DPP:PCBM and the  $\tau_{eff}$  in bis-DPP:PCBM (dashed line). In the low  $\mu$  comparison (dashed line vs squares), it is clear that increasing the  $\tau_{eff}$  in mono-DPP:PCBM to that measured in the high  $FF$  bis-DPP:PCBM system would result in a modest reduction of the carrier collection field dependence. However, the field dependence of  $Q/Q_0$  and thus the  $FF$ , would still be much worse than observed in the bis-DPP:PCBM system (triangle symbols). Alternatively, increasing the mobility of mono-DPP:PCBM to that of bis-DPP:PCBM while maintaining the same  $\tau_{eff}$  (dashed dot line vs triangle symbols) would have a much greater impact on the field dependence of charge collection. In this case, it appears that even with a

shorter  $\tau_{eff}$  mono-DPP:PCBM would show a similar field-dependence as bis-DPP:PCBM. In practice, this would lead to both an increase in  $FF$  and short circuit current as the photocurrent would saturate at much lower fields. Therefore, we conclude that the mono-DPP:PCBM system is primarily limited by (hole) mobility.

The conclusion that mobility is the primary limitation to  $FF$  and also limits  $J_{sc}$  in mono-DPP:PCBM devices may have broad implications for future molecular design. Indeed, the bis-DPP:PCBM mobility values reported here are similar to those reported for efficient polymer:fullerene systems with high  $FFs$ <sup>[20,54]</sup> while the mono-DPP:PCBM mobility is similar to other small molecule<sup>[3,5,6,55]</sup> and polymer<sup>[10,25]</sup> systems with relatively low  $FFs$ . This trend of mobility and  $FF$  has also been predicted in device simulations.<sup>[23]</sup>

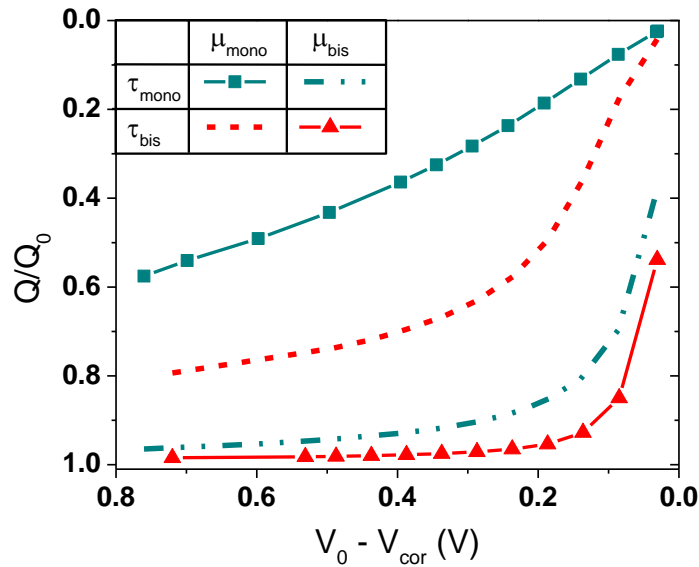


**Figure 3.9:** Ratio of generated charges versus collected charge ( $Q/Q_0$ ) as a function of effective voltage for bis-DPP:PCBM and mono-DPP:PCBM calculated using the measured  $\tau_{eff}$  and hole mobilities. The “mono” and “bis” subscripts in the legend correspond to mono-DPP:PCBM and bis-DPP:PCBM respectively.

Comparing the chemical structures of mono-DPP and bis-DPP suggests that extending conjugation length is one approach to enhancing charge transport properties. This may help improve  $\pi$ - $\pi$  stacking between donor molecules yielding a more continuous network within blended films. The positive correlation between conjugation length and mobility was observed in another recent study on solution processable small molecules<sup>[56]</sup> and seems to be a successful platform for highly efficient SSMBHSCs.<sup>[1,57]</sup> Other molecular design strategies such as incorporating planar  $\pi$ -stacking moieties have also been shown to enhance mobility and increase  $FF$  in SSMBHSCs.<sup>[58]</sup> Based on these findings, we recommend that design rules for efficient charge transport be considered in the design of future donor molecules for SSMBHSCs.

### **3. Conclusions**

In this study, we have investigated the charge transport properties and recombination mechanisms of the low  $FF$  mono-DPP:PCBM system and the high  $FF$  bis-DPP:PCBM system. Single carrier diodes indicate that while both systems have similar electron mobilities, the hole mobility in the mono-DPP:PCBM system is over one order lower than that in the bis-DPP:PCBM system. Light intensity measurements of the  $J$ - $V$  characteristics of optimized solar cells reveal that for both systems bimolecular recombination dominates at open circuit and the  $FF$  is limited by a nongeminate recombination mechanism. Analysis of the differential resistances and capacitances extracted from impedance measurements further illustrates the influence of carrier density dependent nongeminate recombination. The mono-DPP:PCBM system was found to have a shorter effective carrier lifetime compared to the bis-DPP:PCBM system. However, modeling the effect of the mobility-lifetime product on charge collection reveals that the low charge carrier mobility is the primary source of the

highly field-dependent photocurrent in mono-DPP:PCBM devices. Increasing the hole mobility of mono-DPP:PCBM by an order of magnitude would allow for efficient charge collection at lower fields leading to significant increases in both the short circuit current and  $FF$ . Based on these findings, we conclude that in addition to tuning the optical absorption and energy levels of donor materials, future molecular design should aim to increase charge carrier mobility, thereby enabling faster sweep out of charge carriers before they are lost to nongeminate recombination.

#### **4. Experimental**

The mono-DPP and bis-DPP materials were synthesized according to previously described procedures [4,22]. The PCBM was purchased from Solenne BV and used as received. Solar cell devices and hole-only devices were fabricated by spin-casting a 40 nm PEDOT:PSS (H.C. Stark Baytron P 4083) atop Corning 1737 glass patterned with 150 nm of ITO (ShenZen NanBo Display Technology Co.) and then baking the substrates at 140 °C for 20 minutes. The active layers were spun cast onto the ITO/PEDOT:PSS substrates from solutions with a 1:1 donor:PCBM ratio dissolved in chloroform. The bis-DPP:PCBM solutions also contained 0.5% 1,8-diiodooctane by volume. The solar cell device active layer thicknesses were approximately 90 nm as measured by an Ambios XP-100 Stylus Profilometer. The hole only-device active layer thicknesses were controlled by varying solution concentration (17 mg mL<sup>-1</sup> to 35 mg mL<sup>-1</sup>) and ranged from 100 nm to 240 nm. For solar cell (hole-only) devices, 100 nm of aluminum (gold) was deposited onto the active layer at a pressure of 10<sup>-6</sup> Torr through shadow mask to form a 4.5 mm<sup>2</sup> electrode area. Prior to characterization, mono-DPP:PCBM devices were thermally annealed in a nitrogen atmosphere at 80 °C for 10 minutes. Electron only devices were made by depositing 100 nm

of aluminum onto ITO substrates at a rate of  $15 \text{ \AA s}^{-1}$ . Active layer blends from the same solutions used for hole only devices were then spun cast on top of the ITO/Al substrates to yield a range of thicknesses (100 nm to 200 nm). The same  $4.5 \text{ mm}^2$  shadow masks were used while thermally evaporating 10 nm of calcium followed by 100 nm of aluminum to form the top contacts.

Solar cell device characterizations were carried out in nitrogen environment under simulated  $100 \text{ mW cm}^{-2}$  AM1.5G irradiation from a 300 W Xe arc lamp with an AM 1.5 global filter. For other illumination intensities, a Newport 5215 optical density filter wheel was placed in between the samples and the light source. The light intensity was calibrated using an NREL certified silicon diode with an integrated KG1 optical filter. Impedance measurements were conducted using a Solartron 1260 impedance analyzer under nitrogen. Charge extraction measurements used white light LEDs with an intensity that yielded the same open circuit voltage as measured using the solar simulator at one sun. Devices were held at a fixed bias condition under illumination before the LED was switched off and a -3V extraction bias was applied. The carrier density was determined by integrating the resulting photocurrent transient. Further details of this technique will be provided in a future publication [50].

## 5. Supporting Information

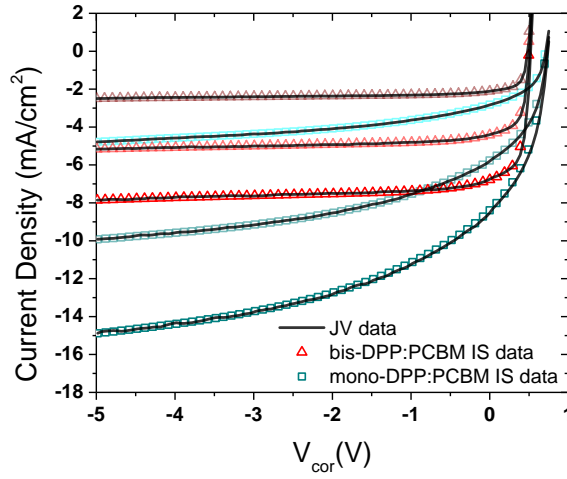


**Figure S3.1:**  $J$ - $V$  curve from impedance data using Equation 5 (symbols) and measured  $J$ - $V$  curves (lines) for mono-DPP:PCBM and bis-DPP:PCBM measured at 32 mW/cm<sup>2</sup>, 66 mW/cm<sup>2</sup> and 100 mW/cm<sup>2</sup>.

### 5.1 Derivation of the expression for $n_{sat}$

In a solar cell under reverse bias, the current,  $J$ , is determined by drift current such that

$$J = qn\mu F \quad (\text{S3.1})$$

where  $q$  is the elementary charge,  $n$  the electron (or hole) density,  $\mu$  is the electron (or hole), and  $F$  is the internal electric field in the device. For applied voltage at or more in reverse than the saturation voltage,  $V_{sat}$ , the photocurrent does not increase. At this condition, all voltage dependent recombination losses are negligible. The current is then directly proportional to the generation rate,  $G$ , such that

$$J(V_{sat}) = qLG. \quad (\text{S3.2})$$

Combining (S1) and (S2) leads to an expression for  $n_{sat}$ , the charge carrier density at the saturation voltage:

$$n_{sat} = \frac{LG}{\mu F} \quad (S3.3)$$

Assuming a uniform field,  $F$  can be expressed as

$$F = \frac{V_0 - V}{L} \quad (S3.4)$$

where  $V_0$  is the built in voltage (experimentally estimated to be the voltage at which the photocurrent is zero),  $V$  is the applied bias and  $L$  is the active layer thickness. The internal capacitance of the photoactive layer,  $C$ , is proportional to the derivative of the carrier density with respect to voltage ( $C = qLA \frac{dn}{dV}$ ) which is simply

$$\frac{dn_{sat}}{dV} = \frac{L^2 G}{\mu(V_0 - V)^2} = \frac{n_{sat}}{(V_0 - V)}. \quad (S3.5)$$

This allows for an expression relating  $C_{sat}$  and  $n_{sat}$  such that

$$C_{sat} = \frac{qLA n_{sat}}{(V_0 - V)} \quad (S3.6)$$

where  $C_{sat}$  is the internal capacitance measured at  $V_{sat}$ . Finally, rearranging (S3.6) yields an expression for  $n_{sat}$ :

$$n_{sat} = \frac{1}{qAL} C_{sat} (V_0 - V_{sat}). \quad (S7)$$

## 5.2 Accounting for voltage dependent geminate recombination

In the case that there are indeed voltage dependent geminate recombination losses the effective carrier lifetime analysis presented in **Section 2.4** would be skewed towards shorter  $\tau_{eff}$ . This can be understood by considering that the  $J_{rec}$  used in Equation (3.10) ( $J_{rec} = qnL/\tau_{eff}$ ) would be greater than it should be (as it then would include both nongeminate *and* geminate recombination). To understand the potential implications for the analysis in **Section 2.4**, we consider the case in which the bis-DPP:PCBM system has no voltage dependent geminate losses and the mono-DPP:PCBM system does (given the difference in FFs this is the most likely scenario). Assuming behavior similar to the most extreme field dependence of geminate recombination reported in the literature [1] for mono-DPP:PCBM would mean that only half of  $J_{rec}$  is attributable to nongeminate losses. This would mean the  $\tau_{eff}$  for mono-DPP:PCBM reported in **Section 2.4** should be twice as long. However, even in this case, the bis-DPP:PCBM system would still exhibit an effective carrier lifetime 50% longer than in the mono-DPP:PCBM system. This smaller difference in the effective carrier lifetime would actually add even more credence to the conclusion that it is primarily the better hole-transport properties of the bis-DPP:PCBM that enables the higher collection efficiency and thus higher FF.

## 6. References

- [1] T. S. Van der Poll, J. A. Love, T.-Q. Nguyen, G. C. Bazan, *Adv. Mater.* **2012**, *24*, 3646–3649.
- [2] B. Walker, C. Kim, T.-Q. Nguyen, *Chem. Mater.* **2010**, *23*, 470–482.

- [3] B. Walker, A. B. Tamayo, X. Dang, P. Zalar, J. H. Seo, A. Garcia, M. Tantiwiwat, T. Nguyen, *Adv. Funct. Mater.* **2009**, *19*, 3063–3069.
- [4] A. B. Tamayo, X.-D. Dang, B. Walker, J. Seo, T. Kent, T.-Q. Nguyen, *Appl. Phys. Lett.* **2009**, *94*, 103301.
- [5] Z. Li, G. He, X. Wan, Y. Liu, J. Zhou, G. Long, Y. Zuo, M. Zhang, Y. Chen, *Adv. Energy Mater.* **2012**, *2*, 74–77.
- [6] G. C. Welch, L. A. Perez, C. V. Hoven, Y. Zhang, X.-D. Dang, A. Sharenko, M. F. Toney, E. J. Kramer, T.-Q. Nguyen, G. C. Bazan, *J. Mater. Chem.* **2011**, *21*, 12700–12709.
- [7] Y. Zhang, X. Dang, C. Kim, T.-Q. Nguyen, *Adv. Energy Mater.* **2011**, *1*, 610–617.
- [8] D. Credgington, F. C. Jamieson, B. Walker, T.-Q. Nguyen, J. R. Durrant, *Adv. Mater.* **2012**, *24*, 2135–2141.
- [9] V. D. Mihailetschi, J. Wildeman, P. W. M. Blom, *Phys. Rev. Lett.* **2005**, *94*, 126602.
- [10] A. Baumann, J. Lorrmann, D. Rauh, C. Deibel, V. Dyakonov, *Adv. Mater.* **2012**, *24*, 4381–4386.
- [11] R. A. Marsh, J. M. Hodgkiss, R. H. Friend, *Adv. Mater.* **2010**, *22*, 3672–3676.
- [12] T. J. K. Brenner, Z. Li, C. R. McNeill, *J. Phys. Chem. C* **2011**, *115*, 22075–22083.
- [13] S. Albrecht, W. Schindler, J. Kurpiers, J. Kniepert, J. C. Blakesley, I. Dumsch, S. Allard, K. Fostiropoulos, U. Scherf, D. Neher, *J. Phys. Chem. Lett.* **2012**, *3*, 640–645.
- [14] C. G. Shuttle, B. O'Regan, A. M. Ballantyne, J. Nelson, D. D. C. Bradley, J. R. Durrant, *Phys. Rev. B* **2008**, *78*, 113201.
- [15] C. G. Shuttle, R. Hamilton, B. C. O'Regan, J. Nelson, J. R. Durrant, *Proceedings of the National Academy of Sciences* **2010**, *107*, 16448–16452.
- [16] S. R. Cowan, N. Banerji, W. L. Leong, A. J. Heeger, *Adv. Funct. Mater.* **2012**, *22*, 1116–1128.
- [17] J. Kniepert, M. Schubert, J. C. Blakesley, D. Neher, *J. Phys. Chem. Lett.* **2011**, *2*, 700–705.
- [18] R. Mauer, I. A. Howard, F. Laquai, *J. Phys. Chem. Lett.* **2011**, *2*, 1736–1741.
- [19] G.-J. A. H. Wetzelaer, M. Kuik, P. W. M. Blom, *Adv. Energy Mater.* **2012**, DOI: 10.1002/aenm.201200009
- [20] A. Pivrikas, H. Neugebauer, N. S. Sariciftci, *IEEE Journal of Selected Topics in Quantum Electronics* **2010**, *16*, 1746–1758.
- [21] S. R. Cowan, W. L. Leong, N. Banerji, G. Dennler, A. J. Heeger, *Adv. Funct. Mater.* **2011**, *21*, 3083–3092.
- [22] Y. Zhang, C. Kim, J. Lin, T.-Q. Nguyen, *Adv. Funct. Mater.* **2012**, *22*, 97–105.
- [23] C. Deibel, A. Wagenpfahl, V. Dyakonov, *Physica Status Solidi (RRL) – Rapid Research Letters* **2008**, *2*, 175–177.
- [24] N. Tessler, N. Rappaport, *Appl. Phys. Lett.* **2006**, *89*, 013504.
- [25] M. M. Mandoc, W. Veurman, L. J. A. Koster, B. de Boer, P. W. M. Blom, *Adv. Funct. Mater.* **2007**, *17*, 2167–2173.
- [26] P. W. M. Blom, M. J. M. de Jong, J. J. M. Vlegaar, *Appl. Phys. Lett.* **1996**, *68*, 3308–3310.
- [27] P. N. Murgatroyd, *J. Phys. D: Appl. Phys.* **1970**, *3*, 151–156.
- [28] N. I. Craciun, J. J. Brondijk, P. W. M. Blom, *Phys. Rev. B* **2008**, *77*, 035206.

- [29] S. M. Tuladhar, D. Poplavskyy, S. A. Choulis, J. R. Durrant, D. D. C. Bradley, J. Nelson, *Adv. Funct. Mater.* **2005**, *15*, 1171–1182.
- [30] V. D. Mihailetschi, J. K. van Duren, P. W. M. Blom, J. C. Hummelen, R. A. Janssen, J. M. Kroon, M. T. Rispens, W. J. Verhees, M. M. Wienk, *Adv. Funct. Mater.* **2003**, *13*, 43–46.
- [31] L. J. A. Koster, M. Kemerink, M. M. Wienk, K. Maturová, R. A. J. Janssen, *Adv. Mater.* **2011**, *23*, 1670–1674.
- [32] S. R. Cowan, A. Roy, A. J. Heeger, *Phys. Rev. B* **2010**, *82*, 245207.
- [33] R. Mauer, I. A. Howard, F. Laquai, *J. Phys. Chem. Lett.* **2010**, *1*, 3500–3505.
- [34] L. J. A. Koster, V. D. Mihailetschi, R. Ramaker, P. W. M. Blom, *Appl. Phys. Lett.* **2005**, *86*, 123509.
- [35] A. M. Goodman, A. Rose, *J. Appl. Phys.* **1971**, *42*, 2823–2830.
- [36] R. A. Street, M. Schoendorf, A. Roy, J. H. Lee, *Phys. Rev. B* **2010**, *81*, 205307.
- [37] C. Deibel, A. Wagenpfahl, *Phys. Rev. B* **2010**, *82*, 207301.
- [38] G.F.A. Dibb, T. Kirchartz, D. Credington, J. Durrant, J. Nelson, *J. Phys. Chem. Lett.* **2011**, *2*, 2407–2411.
- [39] F. Fabregat-Santiago, G. Garcia-Belmonte, I. Mora-Seró, J. Bisquert, *Phys. Chem. Chem. Phys.* **2011**, *13*, 9083–9118.
- [40] I. H. Campbell, D. L. Smith, J. P. Ferraris, *Appl. Phys. Lett.* **1995**, *66*, 3030–3032.
- [41] M. Meier, S. Karg, W. Riess, *J. Appl. Phys.* **1997**, *82*, 1961–1966.
- [42] L. Burtone, D. Ray, K. Leo, M. Riede, *J. Appl. Phys.* **2012**, *111*, 064503.
- [43] P. P. Boix, A. Guerrero, L. F. Marchesi, G. Garcia-Belmonte, J. Bisquert, *Adv. Energy Mater.* **2012**, *1*, 1073–1078.
- [44] G. Garcia-Belmonte, A. Munar, E. M. Barea, J. Bisquert, I. Ugarte, R. Pacios, *Organic Electronics* **2008**, *9*, 847–851.
- [45] W. L. Leong, G. C. Welch, L. G. Kaake, C. J. Takacs, Y. Sun, G. C. Bazan, A. J. Heeger, *Chem. Sci.* **2012**, *3*, 2103–2109.
- [46] R. A. Street, K. W. Song, S. Cowan, *Organic Electronics* **2011**, *12*, 244–248.
- [47] A. Guerrero, T. Ripolles-Sanchis, P. P. Boix, G. Garcia-Belmonte, *Organic Electronics* **2012**, *13*, 2326–2332.
- [48] C. G. Shuttle, B. O'Regan, A. M. Ballantyne, J. Nelson, D.D.C. Bradley, J. C. de Mello, J. R. Durrant, *App. Phys. Lett.* **2008**, *92*, 093311
- [49] C. G. Shuttle, A. Maurano, Hamilton, R., B. O'Regan, J. C. de Mello, J. R. Durrant, *App. Phys. Lett.* **2008**, *93*, 183501
- [50] J. Kniepert, I. Lange, D. Neher (*unpublished*)
- [51] C. Deibel, A. Wagenpfahl, V. Dyakonov, *Phys. Rev. B* **2009**, *80*, 075203.
- [52] C. Groves, N.C. Greenham, *Phys. Rev. B* **2008**, *78*, 155205.
- [53] K. Hecht, *Zeitschrift für Physik A Hadrons and Nuclei* **1932**, *77*, 235–245.
- [54] Y. Liang, Z. Xu, J. Xia, S. Tsai, Y. Wu, G. Li, C. Ray, L. Yu, *Adv. Mater.* **2010**, *22*, E135–E138.
- [55] A. B. Tamayo, B. Walker, T.-Q. Nguyen, *J. Phys. Chem. C* **2008**, *112*, 11545–11551.
- [56] C. Kim, J. Liu, J. Lin, A. B. Tamayo, B. Walker, G. Wu, T.-Q. Nguyen, *Chem. Mater.* **2012**, *24*, 1699–1709.
- [57] Y. Sun, G. C. Welch, W. L. Leong, C. J. Takacs, G. C. Bazan, A. J. Heeger, *Nat. Mater.* **2012**, *11*, 44–48.

- [58] O. P. Lee, A. T. Yiu, P. M. Beaujuge, C. H. Woo, T. W. Holcombe, J. E. Millstone, J. D. Douglas, M. S. Chen, J. M. J. Fréchet, *Adv. Mater.* **2011**, *23*, 5359–5363.
- [59] S. Albrecht, S. Janietz, W. Schindler, J. Frisch, J. Kurpiers, J. Kniepert, S. Inal, P. Pingel, K. Fostiropoulos, N. Koch, D. Neher, *J. Am. Chem. Soc.* **2012**, *134* (36), pp 14932–14944

## Chapter IV

### Overcoming Geminate Recombination and Enhancing Extraction in Solution

#### Processed Small Molecule Solar Cells

##### 1. The story

Solution processed small molecule based (SSM) bulk heterojunction solar cells have proven to be a viable alternative to polymer:fullerene system with reported power conversion efficiencies (PCE) exceeding 8%.<sup>[1]</sup> However, despite the rapid rise in PCE, there have been few fundamental investigations into the fundamental processes that govern the device performance of SSM solar cells.<sup>[2-4]</sup> A deeper understanding of these processes may enable the design of materials that are more efficient and easier to synthesize – both of which will aid future commercialization efforts.<sup>[5]</sup>

The origin of the voltage dependence of the photocurrent in SSM solar cell devices is of particular interest as many SSM systems suffer from low fill factors ( $FF$ ) and short circuit currents ( $J_{sc}$ ).<sup>[6]</sup> Previous studies on polymer:fullerene and SSM solar cells have shown that the current-voltage ( $JV$ ) characteristics of organic photovoltaics depend strongly on the specifics of the charge generation and charge collection processes within the device.<sup>[7,8]</sup> The efficiency of charge generation is determined by the competition between the photo-generation of free charge carriers and geminate recombination. Geminate recombination is the recombination of an electron-hole pair that originated from a single absorption event. Though the origin is not well understood, it has been shown that in some systems the

magnitude of geminate recombination can depend on the internal electric field.<sup>[4,9–14]</sup> Consequently, in such systems the photocurrent exhibits a strong voltage dependence that generally decreases as a forward bias is applied reducing the internal electrical field and thereby reducing the  $FF$  and  $J_{sc}$ . After free charge carriers are generated, there is a subsequent competition between the collection of charge carriers at the electrodes and nongeminate recombination. Nongeminate recombination is the recombination of free charge carriers that did not originate from the same absorption event and includes trap-assisted as well as bimolecular processes. If the rate of nongeminate recombination is too fast<sup>[15,16]</sup> or the charge carrier mobility (of at least one type of charge carrier) too low,<sup>[2,17,18]</sup> losses due to nongeminate recombination can also significantly limit both the  $FF$  and  $J_{sc}$ .

In this study, we report on the nature and origin of the recombination mechanisms that govern the  $JV$  characteristics of the highly efficient SSM system using 7,7'-(4,4-bis(2-ethylhexyl)-4H-silolo[3,2-b:4,5-b']dithiophene-2,6-diyl)bis(6-fluoro-4-(5'-hexyl-[2,2'-bithiophen]-5-yl)benzo[*c*][1,2,5]thiadiazole), ( $p$ -DTS(FBTTh<sub>2</sub>)<sub>2</sub>) as the donor material with phenyl-C71-butyric acid methyl ester (PC<sub>71</sub>BM) as the acceptor.<sup>[19]</sup> Time delayed collection field (TDCF), bias assisted charge extraction (BACE) and photocharge extraction by linearly increasing voltage (photo-CELIV) measurements were performed on  $p$ -DTS(FBTTh<sub>2</sub>)<sub>2</sub>:PC<sub>71</sub>BM solar cell devices prepared both with and without diiodooctane (DIO) as well as on thermally annealed devices. These measurements reveal the voltage dependence of geminate recombination, the rate of nongeminate (bimolecular) recombination and the charge carrier mobilities as a function of device processing conditions. Combined with our previous morphological characterization of  $p$ -DTS(FBTTh<sub>2</sub>)<sub>2</sub>:PC<sub>71</sub>BM blend films,<sup>[20]</sup> these results shed light on the morphological and

electrical properties that can suppress both geminate and nongeminate recombination losses in SSM solar cells.

As shown in **Figure 4.1**, the current-voltage response of  $p$ -DTS(FBTTh<sub>2</sub>)<sub>2</sub>:PC<sub>71</sub>BM solar cell devices is strongly dependent on the device processing conditions leading to PCEs of 2.8, 5.2, and 7.1% for as cast, 125 °C thermally annealed and DIO processed devices, respectively. The DIO processed devices were spin cast from a chlorobenzene solution containing 0.4% DIO by volume while the as cast and annealed samples were prepared from chlorobenzene solutions without DIO (see Experimental for further details). These three conditions, all with a 3:2  $p$ -DTS(FBTTh<sub>2</sub>)<sub>2</sub>:PC<sub>71</sub>BM blend ratio, have been shown to exhibit remarkably different film morphologies as well.<sup>[20]</sup> The most notable difference in device performance between the three conditions is the voltage dependence of the current density. The as cast system exhibits the strongest voltage dependence leading to the lowest  $FF$  of only 0.41 and a  $J_{sc}$  of 8.3 mA/cm<sup>2</sup> despite a similar current density to the DIO processed device at -4 V (see **Table 4.1**). Thermally annealed devices show improved  $FF$  of 0.58 and  $J_{sc}$  of 10.9 mA/cm<sup>2</sup> however, the DIO processed devices are better still with a  $FF$  approaching 0.70 and  $J_{sc}$  of 13 mA/cm<sup>2</sup>.

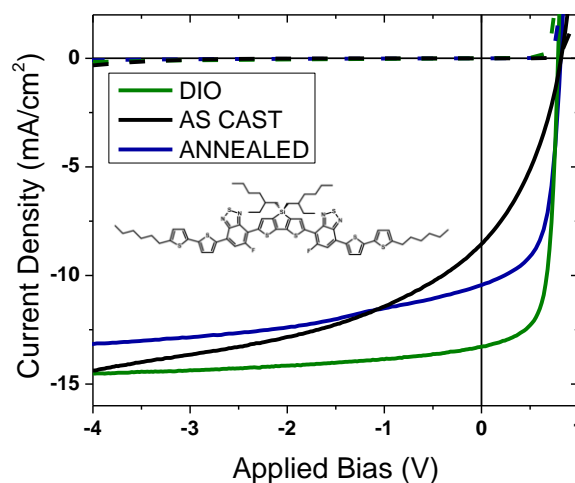


**Figure 4.1:** *JV* curves of *p*-DTS(FBTTh<sub>2</sub>)<sub>2</sub>:PC<sub>71</sub>BM solar cell devices measured under AM 1.5 G illumination with 100 mW/cm<sup>2</sup> (solid lines) and in the dark (dashed lines). The chemical structure of *p*-DTS(FBTTh<sub>2</sub>)<sub>2</sub> is shown in the inset.

TDCF experiments were conducted in order to distinguish the processes leading to the dramatic difference in voltage dependence between the three processing conditions. In TDCF, a pre-bias ( $V_{pre}$ ) is applied to a solar cell device that is then pulsed with a laser. After a fixed delay time ( $t_d$ ), a strong collection bias ( $V_{coll}$ ) is applied to the device in order to sweep out all remaining photogenerated charge carriers. The resulting photocurrent transient can be integrated to determine the total collected charge ( $Q_{tot}$ ). Measuring  $Q_{tot}$  as a function of  $V_{pre}$  using a short  $t_d$  (~10 ns) and low pulse fluence such that nongeminate recombination losses are negligible during delay can be taken as a direct measure of voltage dependence of geminate recombination for most organic systems.<sup>[9,21]</sup>

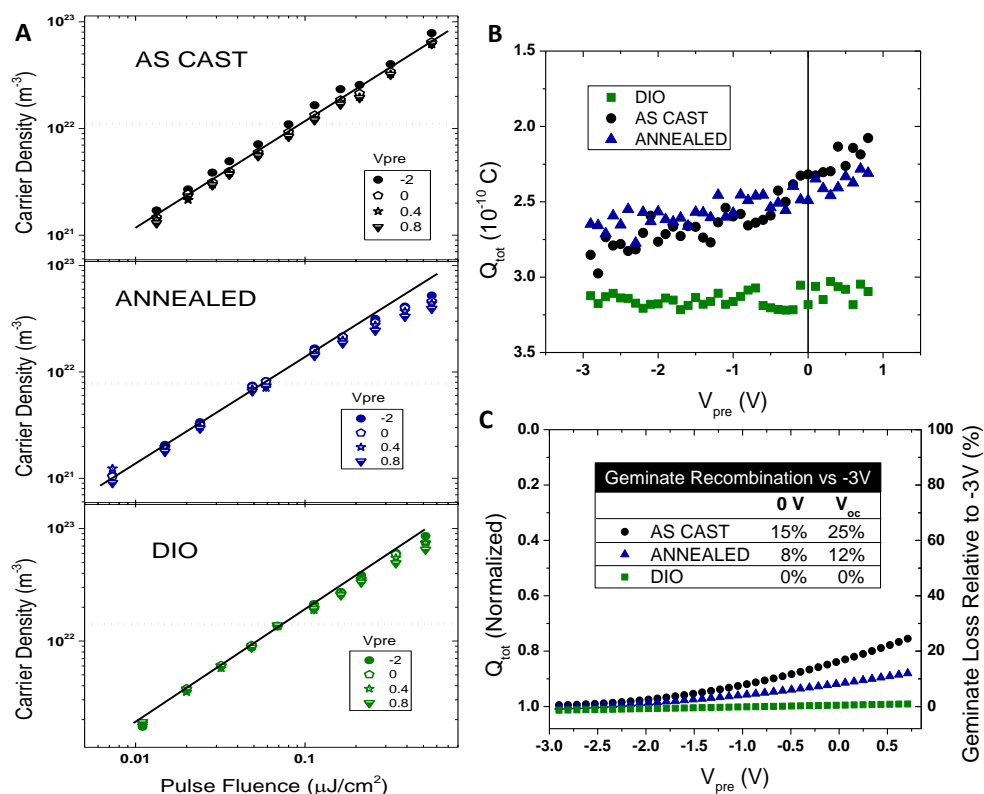


**Figure 4.2:** (A) Dependence of the photogenerated charge carrier density on the excitation pulse fluence. The symbols correspond to the applied pre bias. The solid lines are included as a guide for the eyes and represent a perfectly linear dependence of total charge on pulse fluence. The dotted lines show the carrier density at open circuit measured in the same devices from steady state conditions under 1 sun illumination using a charge extraction technique. (B) Total extracted charge as a function of pre bias for  $p$ -DTS(FBTTh<sub>2</sub>)<sub>2</sub>:PC<sub>71</sub>BM solar cell devices measured with TDCF using an 10 ns delay time, -4 V collection bias and pulse fluence of 0.08  $\mu J/cm^2$ . (C) Polynomial fit to the same data normalized to  $Q_{tot}$  at -3V. The inset table shows the percentage of photogenerated carriers at short circuit and open circuit lost to geminate recombination relative to -3V.

In order to test for the influence of voltage dependent geminate recombination in  $p$ -DTS(FBTTh<sub>2</sub>)<sub>2</sub>:PC<sub>71</sub>BM devices, TDCF measurements were performed with a delay time of 10 ns and a  $V_{coll}$  of -4 V. The pulse fluence was varied from 0.01 and 0.10  $\mu J/cm^2$  – a range which yielded a strictly linear dependence of the photogenerated charge carrier density on light intensity (**Figure 4.2a**). The excitation wavelength was chosen to be 650 nm, well within the absorption range of the blend films.<sup>[19]</sup> BACE measurements (see

Experimental)<sup>[22]</sup> performed on the same devices indicated that a pulse fluence of  $\sim 0.07 \mu\text{J}/\text{cm}^2$  yielded initial photo-generated carrier densities comparable to steady-state densities at open circuit under AM 1.5G illumination (dotted lines, Figure 2a).

Processing	$J$ (-4V) [mA/cm <sup>2</sup> ]	$J_{sc}$ [mA/cm <sup>2</sup> ]	$FF$ [%]	$V_{oc}$ [V]	PCE [%]
as cast	14.3	8.3	41	0.83	2.8
annealed	13.1	10.9	58	0.82	5.2
with DIO	14.5	13.0	69	0.79	7.1

**Table 4.1:** Parameters from  $JV$  characteristics of  $p$ -DTS(FBTTh<sub>2</sub>)<sub>2</sub>:PC<sub>71</sub>BM devices measured under AM1.5G illumination with 100 mW/cm<sup>2</sup>.

The external quantum efficiency of each device was measured as a function of excitation wavelength and applied bias in order to check the validity of comparing the TDCF data measured at 650 nm to the  $JV$  response measured under white light. For the as cast and DIO processed devices the bias dependence of the photocurrent was found to be independent of excitation wavelength within +/- 5% (**Figure S4.1**). For the annealed devices, a slightly stronger voltage dependence, not exceeding 10% in the operating regime, was observed at shorter wavelengths where PCBM absorption dominates (**Figure S4.2**). A similar phenomenon has also been reported for polymer:fullerene blends<sup>[24]</sup> and recently assigned to free carrier generation in large PCBM domains.<sup>[25]</sup> However, TDCF measurements performed at 500 nm on annealed devices showed only negligible changes in field dependence compared to 650 nm excitation. Furthermore,  $JV$  measurements of annealed devices illuminated with blue, green, and near-IR LEDs yielded only 2-3% change in  $FF$  compared to white light illumination (**Figure S4.2**). Collectively, these findings suggest that the TDCF results for all three device processing conditions can reasonably be correlated with the  $JV$  characteristics measured under white light.

The results of the TDCF experiments are shown in **Figure 4.2b** where it is clear that for the as cast devices  $Q_{tot}$  depends strongly on the bias applied during the generation process as has been observed in other OPV systems.<sup>[9–11,23]</sup> The  $Q_{tot}$  for annealed devices exhibits a somewhat weaker voltage dependence. Remarkably, the  $Q_{tot}$  measured in devices processed with DIO is independent of  $V_{pre}$  indicating that the voltage dependent geminate recombination losses are completely overcome. The trend in the absolute values of  $Q_{tot}$  for the three conditions is also consistent with the trend in the light current under reverse bias (Figure 1). At -4V, the current in the as cast device approaches that of the DIO device while the current of annealed devices saturates at slightly lower values. That the  $Q_{tot}$  values also mirror this trend suggests that the lower photo current in the annealed device is due to a lower photogeneration rate which is not surprising given annealed *p*-DTS(FBTTh<sub>2</sub>)<sub>2</sub>:PC<sub>71</sub>BM films are known to have large crystalline domains that extend several times longer than the exciton diffusion length.<sup>[20]</sup> **Figure 4.2c** shows a polynomial fit for the data in Figure 2b normalized to the  $Q_{tot}$  measured at -3V. As shown in the inset table, based on this analysis it is evident that geminate recombination losses relative to -3V are approximately 15% and 25% for the as cast system at short circuit and open circuit conditions respectively while the annealed devices exhibit relative geminate recombination losses of 8% and 12%. The devices processed with DIO show only negligible losses at all bias conditions. This trend in voltage dependent geminate losses explains in part the trend in *FF* and  $J_{sc}$  across the three processing conditions considered here. Evidently, the absence of voltage dependent geminate recombination losses in the DIO processed devices enables the system to achieve the highest *FF* and  $J_{sc}$ . The voltage dependence of geminate

recombination in the as cast devices also helps explain why a strong reverse bias is needed to yield a similar photocurrent to that of DIO processed devices.

Considering these results in light of our recent report on the morphology of *p*-DTS(FBTTh<sub>2</sub>)<sub>2</sub>:PC<sub>71</sub>BM blend films provides insight on the origin of field dependent free carrier generation. As described by Love et al.,<sup>[20]</sup> UV-visible absorption and TEM measurements indicate that while the as cast films are a homogeneous blend with no apparent crystalline domains, the DIO and annealed films have highly ordered wire-like *p*-DTS(FBTTh<sub>2</sub>)<sub>2</sub> domains on the order of 30 and 50 nm respectively. Thus as in other studies of polymer:fullerene systems,<sup>[10,14]</sup> it is observed here that a weaker field dependence of free carrier generation is well correlated with the formation of ordered domains. This supports the notion that ordered (crystalline) domains may foster delocalized charge transfer states at the donor-acceptor interface which in turn decreases the energetic barrier for separating geminate electron-hole pairs.<sup>[10,26,27]</sup> It is worth noting however that the presence of a weak field dependence in the annealed device does suggest that variables beyond domain order may influence the field dependence of charge generation. Other factors which are difficult to gauge with standard TEM and absorption techniques such as domain purity<sup>[28]</sup> and molecular orientation at the donor-acceptor interface<sup>[29]</sup> or a mix of ordered and disordered domains may also contribute to the trends in voltage dependent generation observed here.

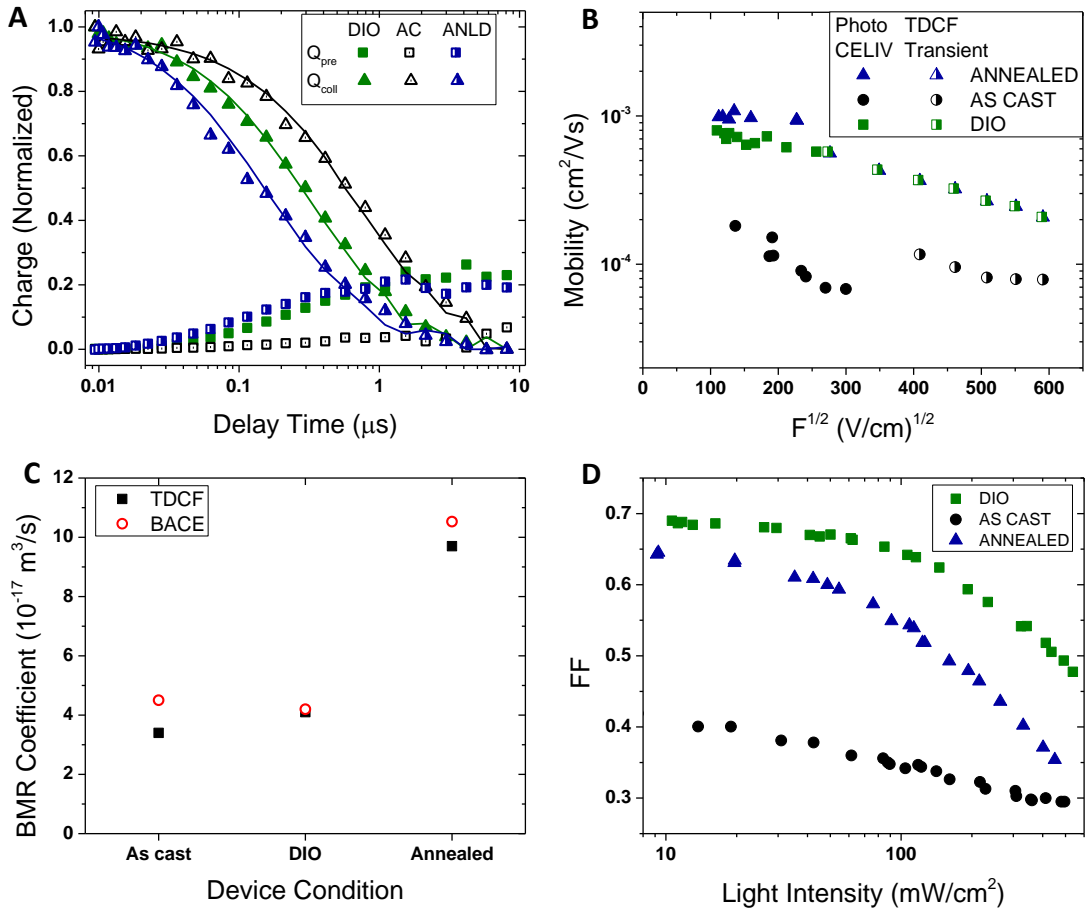


**Figure 4.3:** (A) Precharge  $Q_{pre}$  and collected charge  $Q_{coll}$  from TDCF transients with different delay times for a pre-bias setting close to  $V_{oc}$  ( $V_{pre} = 0.8 \text{ V}$ ) in as cast (AC), annealed (ANLD) and DIO processed devices. The solid lines are fits to a BMR model. Data are normalized to the initially photogenerated charge. (B) Charge carrier mobility extracted from photo-CELIV (closed symbols) and TDCF photo-transients (half symbols) as a function of internal electric field ( $F$ ). (C) BMR coefficients determined by fitting TDCF delay time measurements at  $V_{pre} = 0.8 \text{ V}$  (closed symbols) and from the carrier density measured at open circuit with BACE (open symbols). (D)  $FF$  as a function of light intensity.

As discussed in the introduction, the competition between the extraction of photogenerated charge carriers and nongeminate recombination also shapes the  $JV$  characteristics of organic solar cells. The kinetics of nongeminate recombination were probed by conducting TDCF experiments with increasing time delay  $t_d$  between the

generation and collection of charge carriers. Integration of the transients during and after  $t_d$  yielded the quantities  $Q_{pre}(t_d)$  and  $Q_{coll}(t_d)$  respectively where  $Q_{tot}(t_d) = Q_{pre}(t_d) + Q_{coll}(t_d)$ . **Figure 4.3a** shows  $Q_{pre}$  and  $Q_{coll}$  as a function of  $t_d$  with a  $V_{pre}$  close to  $V_{oc}$  (0.8 V) for as cast, annealed and DIO processed devices. The rise of  $Q_{pre}$  with  $t_d$  is due to extraction of photogenerated carriers at the pre bias condition.  $Q_{coll}$  decreases with  $t_d$  due to a combination of more carriers being extracted before  $t_d$  (represented by  $Q_{pre}$ ) and the loss of charge carriers to (bimolecular) recombination. It was observed that  $Q_{pre}$  rises faster with  $t_d$  in the annealed and DIO devices as compared to the as cast devices for all  $V_{pre}$  conditions ranging from 0 to 0.8 V which is indicative of more efficient charge extraction (see **Figure S4.3**). This is in line with the charge carrier mobility of the blend films shown in **Figure 4.3b** determined by photo-CELIV<sup>[30]</sup> and from TDCF photocurrent transients.<sup>[9]</sup> The DIO and annealed devices were observed to have upwards of one order higher charge carrier mobility compared to as cast devices. Altogether, these findings indicate that the morphology of the thermally annealed and DIO processed blends allows for faster extraction of photogenerated charge carriers.

The solid lines in Figure 3a are fits to the experimental data using an iterative routine<sup>[9]</sup> that accounts for losses due to bimolecular recombination (BMR) with a recombination rate coefficient  $\gamma_{BMR}$ . Given that  $\gamma_{BMR}$  is the only adjustable fit parameter the good agreement between model and experimental data strongly suggests that the nongeminate recombination losses are bimolecular in nature for all three processing conditions as has been reported for other small molecule<sup>[2,3]</sup> and polymer based systems.<sup>[10,15,21,31]</sup> Indeed for all  $V_{pre}$  conditions from 0 V to 0.8 V, the charge decay was found to fit well to a BMR model suggesting that bimolecular recombination is the primary

nongeminate loss mechanism across the entire operating regime (Figure S4.3). From the BMR fits in Figure 4.3a, it was found that  $\gamma_{\text{BMR}}$  at approximately open circuit conditions ( $V_{\text{pre}} = 0.8$  V) is largest for the annealed sample, up to  $10^{-16}$  m<sup>3</sup>/s, while the values for the as cast and DIO system remain at ca.  $4 \times 10^{-17}$  m<sup>3</sup>/s (**Figure 4.3c**). The faster non-geminate recombination observed in the annealed sample at  $V_{\text{oc}}$  is consistent with Figure 2a wherein at higher pulse fluences the deviation of  $Q_{\text{tot}}$  from a linear dependence on pulse fluence is strongest in the annealed devices, somewhat weaker in the DIO devices, and nonexistent in the as cast devices over the considered fluence range. The dependence of  $FF$  on light intensity, which is known to result from nongeminate (bimolecular) recombination,<sup>[2,32]</sup> shows a similar trend (Figure 4.3d).

Interestingly, using TDCF to determine  $\gamma_{\text{BMR}}$  at different  $V_{\text{pre}}$  conditions, a notable increase in  $\gamma_{\text{BMR}}$  was observed as  $V_{\text{pre}}$  went from 0.4 V to 0.8 V for the annealed and DIO samples while the  $\gamma_{\text{BMR}}$  in as cast devices was found to be independent of  $V_{\text{pre}}$  (**Figure S4.4**). Our previous work on polymer:fullerene devices observed a correlation between the field dependence of  $\gamma_{\text{BMR}}$  and a negative field dependence of mobility.<sup>[9,10]</sup> However, mobilities extracted from photo-CELIV and TDCF transients as a function of internal electric field for the three processing conditions do not appear to exhibit a similar correlation (Figure 4.3b). Rather it seems more likely that the stronger voltage dependence of  $\gamma_{\text{BMR}}$  in the annealed and DIO system is related to a stronger carrier density dependence of the recombination rate as has been observed in many other OPV systems<sup>[7,31]</sup> and which has sometimes been attributed to the influence of trapped charges.<sup>[33,34]</sup> Such density dependence would also contribute to the observed drop of the  $FF$  with increasing light intensity as is particularly obvious for the annealed device.

In order to verify our  $\gamma_{\text{BMR}}$  measurements from TDCF, we determined the recombination rate coefficient at the open circuit condition from using the carrier density measured under 1 sun steady state conditions by charge extraction<sup>[35]</sup> and accounting for the losses due to voltage dependent generation (see Supporting Information). Again, we found that at open circuit for the annealed devices  $\gamma_{\text{BMR}} \approx 10^{-16} \text{ m}^3/\text{s}$ , while for the as cast and DIO system  $\gamma_{\text{BMR}} \approx 4 \times 10^{-17} \text{ m}^3/\text{s}$  (Figure 4.3c, open symbols). This remarkable agreement with the TDCF  $\gamma_{\text{BMR}}$  values fortifies the assertion that despite the transient nature, the results of TDCF experiments are directly correlated to steady state properties. Furthermore, it suggests that in the case of *p*-DTS(FBTTh<sub>2</sub>)<sub>2</sub>:PC<sub>71</sub>BM the kinetics of bimolecular recombination on a 10-100 ns timescale are not strongly influenced by thermally excited carriers that have a higher mobility immediately after charge separation.<sup>[9]</sup>

Knowing the charge carrier mobility and the  $\gamma_{\text{BMR}}$  we can now determine the Langevin reduction factor for each sample. From the Langevin expression for recombination in a homogenous medium, the Langevin rate coefficient is  $\gamma_{\text{L}} = \frac{q}{\epsilon} (\mu_{\text{e}} + \mu_{\text{h}})$  where  $\epsilon$  is the dielectric constant,  $\mu_{\text{e}}$  the mobility of electrons and  $\mu_{\text{h}}$  the mobility of holes. Most organic solar cell blends have been found to exhibit a reduced recombination rate as compared to  $\gamma_{\text{L}}$  which is often quantified by a reduction factor  $\zeta = \gamma_{\text{BMR}} / \gamma_{\text{L}}$  less than one.<sup>[7,36]</sup> Using the low field photo-CELIV mobilities for the fastest carrier with the slower carrier imbalanced by the same factor measured in single carrier diodes (40, 17, and 2.5 times – Figure S4.5), the Langevin reduction factors at open circuit are found to be 0.19, 0.12 and 0.07 for the as cast, annealed and DIO processed devices, respectively. These  $\zeta$  values are comparable to what has been observed in a similarly structured fluorinated polymer:fullerene system<sup>[10]</sup> and other

efficient polymer:fullerene systems.<sup>[18,38–41]</sup> The reduction factor in the DIO processed system is among the lowest reported for a SSM system to date. Multiple studies have observed a correlation between increased phase separation (larger domain sizes) and reduced Langevin recombination.<sup>[10,42,43]</sup> As noted previously, for the *p*-DTS(FBTTh<sub>2</sub>)<sub>2</sub>:PC<sub>71</sub>BM system the as cast blend is known to be a homogeneous mixture lacking discernible phase separation while the DIO processed and annealed blends exhibit crystalline *p*-DTS(FBTTh<sub>2</sub>)<sub>2</sub> phases on the order of tens of nanometers.<sup>[20]</sup> Comparing the  $\zeta$  for the as cast to annealed and DIO systems, it seems that the trend between phase separation and reduced recombination follows here as well. However, this correlation is seemingly inverted for the annealed versus the DIO processed devices as based on TEM imaging the annealed blends exhibit *p*-DTS(FBTTh<sub>2</sub>)<sub>2</sub> domains over twice the size of those in the DIO blends. This apparent contradiction likely has the same origins as the weak field dependence of generation observed in the annealed system as compared to the field-independent generation in the DIO processed sample. Together these phenomenon hint that despite the large crystalline domains in the annealed blend observed in TEM, there may still be relatively impure phases or donor-acceptor interfaces at which both geminate and nongeminate recombination are more favorable. While further study is needed to confirm this hypothesis it is worth noting that recent experimental and theoretical work support the conclusion that the factors suppressing geminate recombination also help suppress bimolecular recombination.<sup>[44–47]</sup>

Having thoroughly investigated the voltage dependent recombination mechanisms and the charge transport properties for each system, the complete picture of the mechanisms determining the *JV* characteristics now emerges. In **Figure 4.4**, we illustrate the varying

influences of geminate and bimolecular recombination on the  $JV$  characteristics of  $p$ -DTS(FBTTh<sub>2</sub>)<sub>2</sub>:PC<sub>71</sub>BM devices for the three processing conditions. The symbols are from TDCF measurements of the field dependence of generation and are scaled appropriately to show losses attributable to voltage dependent geminate recombination (GR, red region). The yellow region between the symbols and  $JV$  curve (line) indicates losses due to bimolecular recombination. As discussed earlier, losses due to voltage dependent geminate recombination (field dependent generation) are observed to limit both the  $FF$  and  $J_{sc}$  in the as cast and annealed devices (Figure 4.4a and b respectively) while no such limitation is present in the DIO processed devices (Figure 4.4c). Equally significant is the trend in bimolecular recombination losses. Despite a similar bimolecular recombination rate coefficient to the DIO processed device, the lower charge carrier mobility in the as cast devices increases the number of remaining charges in the device which enhances the loss due to bimolecular recombination. In contrast, the crystalline phases in the annealed and DIO processed devices improve the charge transport properties and further reduce  $\zeta$  which then enables most photogenerated carriers to be collected before they recombine bimolecularly. The combination of only negligible geminate losses and significantly reduced bimolecular recombination allows the DIO devices to exhibit the highest  $FF$  and  $J_{sc}$  with only minimal losses at the short circuit condition consistent with the previously measured internal quantum efficiency exceeding 90%.<sup>[20]</sup>

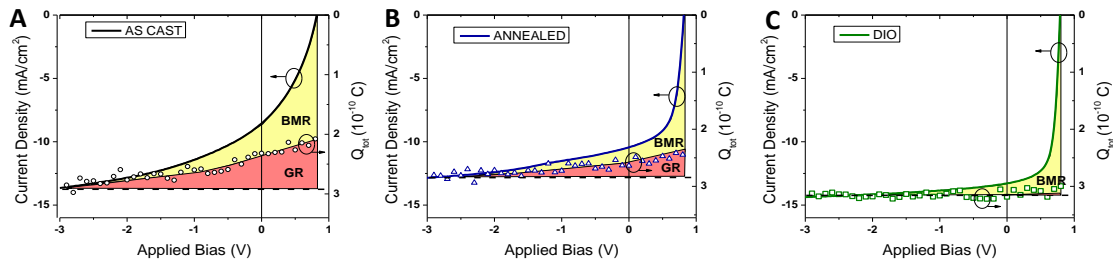


**Figure 4.4:** *JV* curves for as cast (A), annealed (B) and DIO processed (C) devices measured under AM 1.5 G illumination with  $100 \text{ mW/cm}^2$  plotted with results from TDCF measurements from Figure 4.2. Voltage dependent geminate recombination (GR) losses are highlighted in red while losses attributable to bimolecular recombination are painted yellow.

In conclusion, TDCF and photo-CELIV measurements were conducted to determine the nature of voltage dependent recombination losses and to measure the charge carrier transport properties in *p*-DTS(FBTTh<sub>2</sub>)<sub>2</sub>:PC<sub>71</sub>BM solar cell devices as a function of processing conditions. This analysis provides a complete picture of the mechanisms that determine the drastically different *JV* characteristics in as cast, annealed and DIO processed devices. The low *FF* and *J<sub>sc</sub>* in the as cast devices are a consequence of both voltage dependent geminate recombination and strong bimolecular recombination. Thermally annealing devices partially suppresses both mechanisms thereby increasing the *FF* and *J<sub>sc</sub>*. Processing devices with DIO allows free carriers to be generated independent of the internal field at the same time as reducing bimolecular recombination. Coupling these results with knowledge of the blend film morphologies, suggests a correlation between highly ordered crystalline domains and a reduced field dependence of generation as well as increased charge carrier mobility. These results highlight that a field dependent generation mechanism is not necessarily an inherent molecular property. With careful control of the blend film morphology, geminate recombination can be completely overcome while simultaneously

reducing bimolecular recombination to allow for efficient generation and collection of photogenerated charge carriers.

## 2. Experimental Section

*Device preparation:* The solar cell-, TDCF- as well as photo-CELIV devices were fabricated on structured ITO coated glass slides (Optrex) pre-cleaned in acetone, detergent, DI-water, isopropanol and dried under a nitrogen stream. The pre-cleaned ITO substrate was plasma-cleaned and a 50-60 nm layer of PEDOT:PSS (Clevios AI 4083) was spin cast on top. The sample was subsequently transferred into a nitrogen filled glove-box followed by annealing at 180 °C for 10 min. The active layer was spin cast from solutions containing 3:2 (by weight) blend ratios of p-TS(FBTTh<sub>2</sub>)<sub>2</sub> (1material) and PC<sub>71</sub>BM (99%, Solenne) to make a ~110 nm film. Chlorobenzene was used as the solvent. Samples were prepared with and without 0.4 vol% diiodooctane (DIO) as processing agent. DIO and Annealed samples were thermally annealed at 70 °C for 10 min. The annealed devices were subsequently thermally annealed at 125 °C for 10 min. Finally 10 nm Ca and 100 nm Al were thermally evaporated with a base pressure below 10<sup>-6</sup> mbar through shadow masks to define the active area to be 1.1 mm<sup>2</sup>. Such small area was used to realize a small RC-constant of the device. Samples for Photo-CELIV or TDCF were encapsulated with two component epoxy resin and a glass lid prior to air exposure.

*TDCF experiments:* The measurement-scheme was described in detail elsewhere.<sup>[9,21]</sup> The pulsed excitation (5.5 ns pulse width, 500 Hz repetition rate, 10 ns jitter) was done with a diode-pumped, Q-switched Nd:YAG laser (NT242,EKSPLA). The current through the device

was measured via a  $50\Omega$  resistor in series with the sample and was recorded with a Yokogawa DL9140 oscilloscope. The pulse fluence was measured with a Ophir Vega power meter equipped with a photodiode sensor.

*Photo-CELIV:* Measurements employing the current extraction under linearly increasing voltages (CELIV) technique were realized with the same laser and excitation wavelength as used for TDCF. The linear increasing voltage ramp was applied with an Agilent 33220A wave form generator and a fast custom-built amplifier. The resulting current transients were measured with a fast current amplifier (Femto DHPCA-100) and a digital oscilloscope (Yokogawa DL9040). Mobility values were determined using previously described analysis.<sup>30</sup>

*Charge extraction:* Charge extraction measurements used white light LEDs with an intensity that yielded the same open circuit voltage as measured using the solar simulator at one sun. Devices were held at a fixed bias condition under illumination before the LED was switched off and a  $-3$  V extraction bias was applied. The carrier density was determined by integrating the resulting photocurrent transient.

### 3. Supporting Information

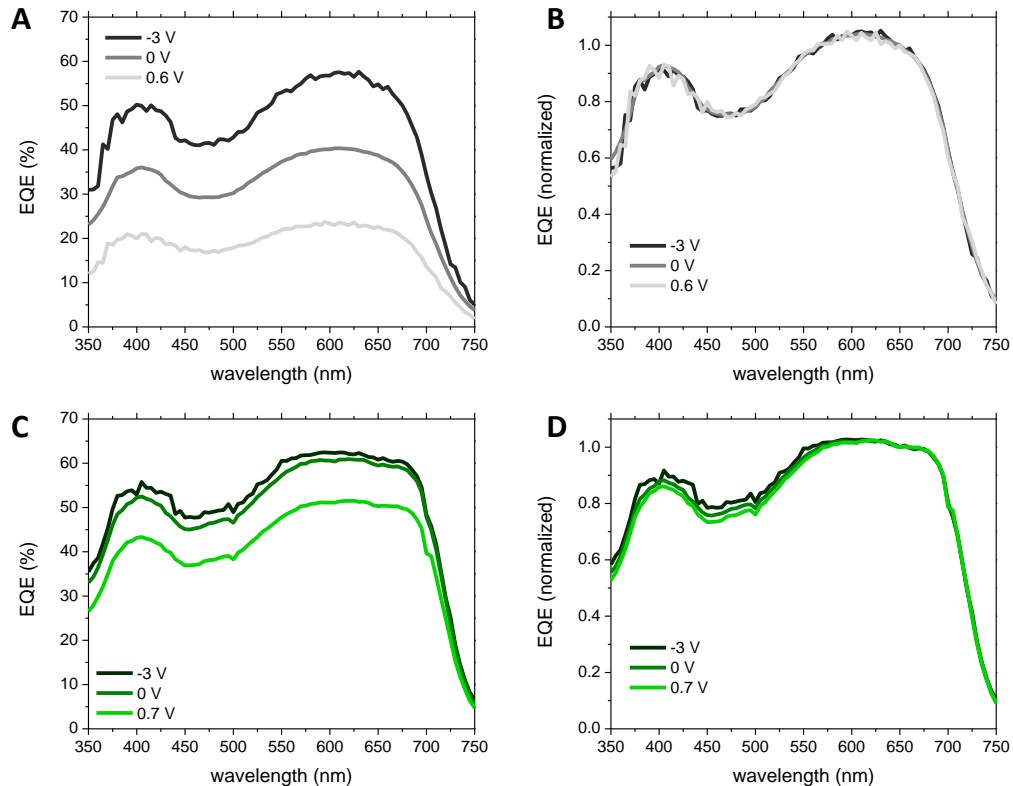


**Figure S4.1:** External quantum efficiency of DTS(FBTTh<sub>2</sub>)<sub>2</sub>:PC<sub>71</sub>BM solar cell devices measured as a function of excitation wavelength and applied bias. (A) raw as cast device data, (B) normalized as cast device data, (C) raw with DIO device data, (D) normalized with DIO device data.

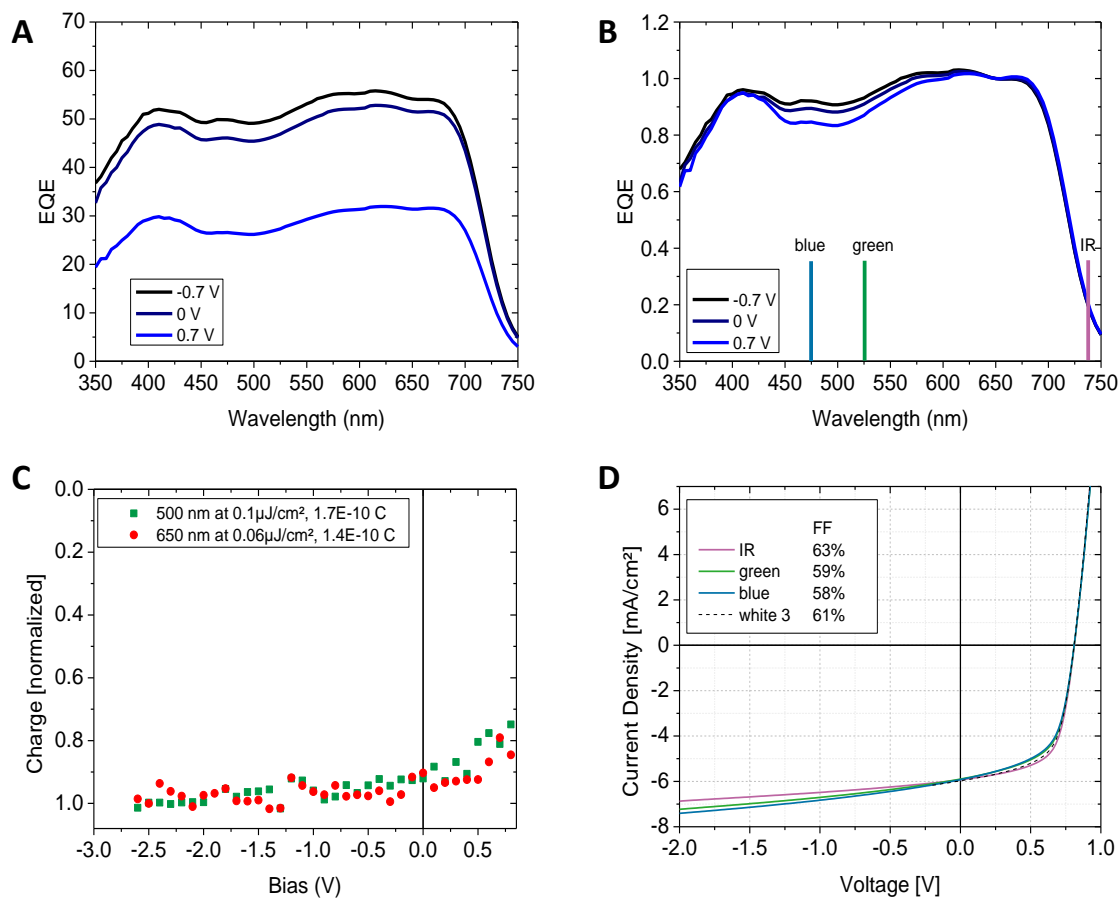


**Figure S4.2:** (A) Raw and (B) normalized external quantum efficiency of annealed DTS(FBTTh<sub>2</sub>)<sub>2</sub>:PC<sub>71</sub>BM solar cell devices measured as a function of excitation wavelength and applied bias. The colored lines in (A) indicate the wavelength of the LEDs used in (D). (C) Normalized TDCF data of annealed DTS(FBTTh<sub>2</sub>)<sub>2</sub>:PC<sub>71</sub>BM solar cell devices measured with 500 nm and 650 nm laser pulse excitations. (D) Current voltage response and fill factor of DTS(FBTTh<sub>2</sub>)<sub>2</sub>:PC<sub>71</sub>BM solar cell devices measured with green, blue, IR and white LEDs at an illumination intensity of approximately 0.5 suns.

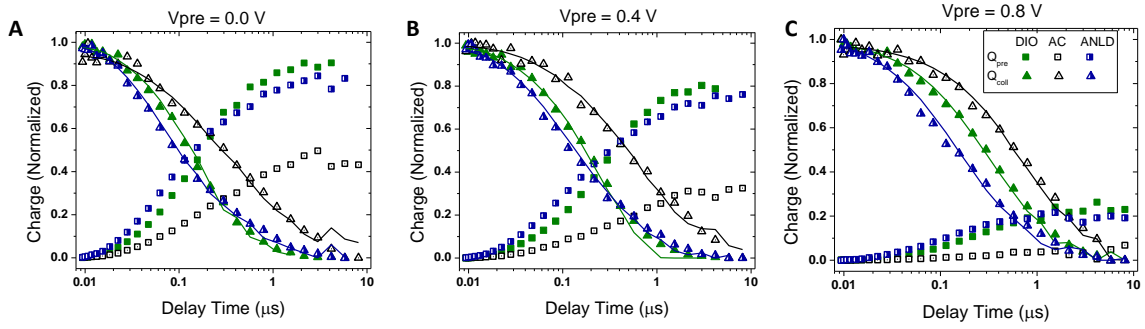


**Figure S4.3:** Precharge  $Q_{pre}$  and collected charge  $Q_{coll}$  from TDCF transients with different delay times in as cast (AC), annealed (ANLD) and DIO processed devices. for a pre-bias settings of 0 V (A), 0.4V (B) and 0.8V (C) The solid lines are fits to a BMR model. Data are normalized to the initially photogenerated charge.

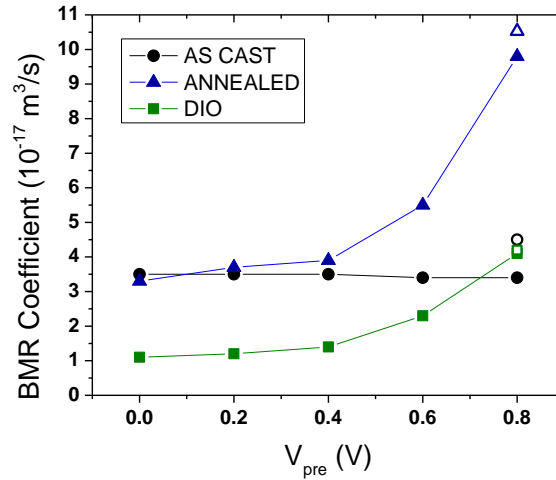


**Figure S4.4:** BMR coefficients determined by fitting TDCF delay time measurements at various prebiases ( $V_{pre}$ ) (closed symbols) and from the carrier density measured at open circuit with BACE (open symbols).

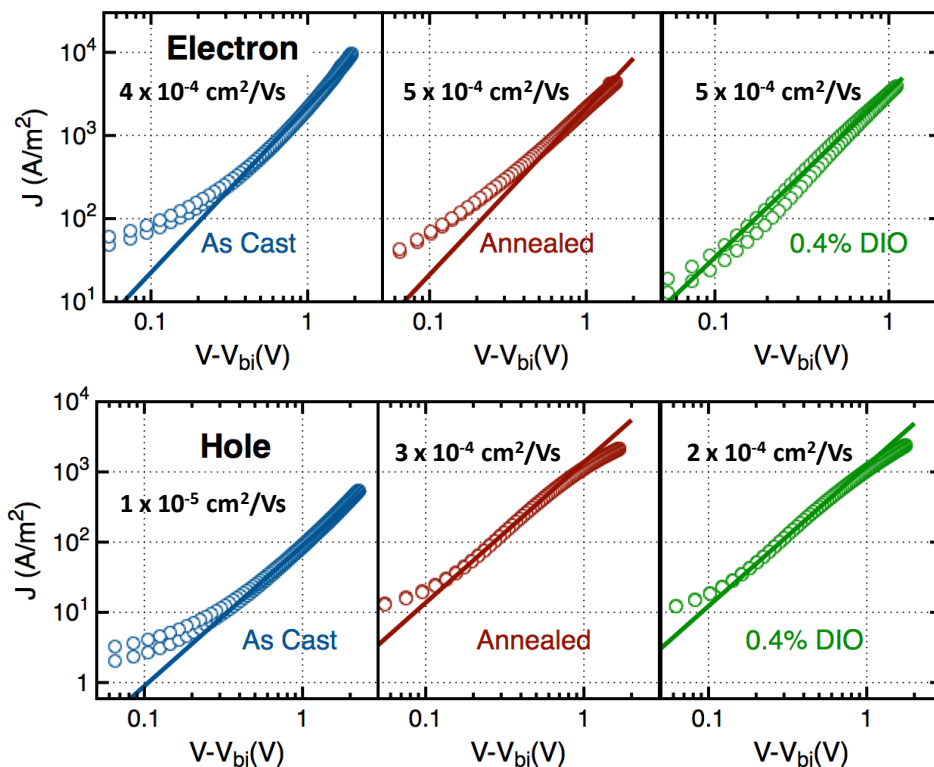


**Figure S4.5:** Current voltage curves of electron only (Al/ p-DTS(FBTTh<sub>2</sub>)<sub>2</sub>:PC<sub>71</sub>BM /Ca/Al) and hole only (ITO/PEDOT:PSS/p-DTS(FBTTh<sub>2</sub>)<sub>2</sub>:PC<sub>71</sub>BM/Au) diodes (symbols). The extracted mobility values from fits (lines) to the Mott-Gurney Law for space charge limited current are included in each plot.

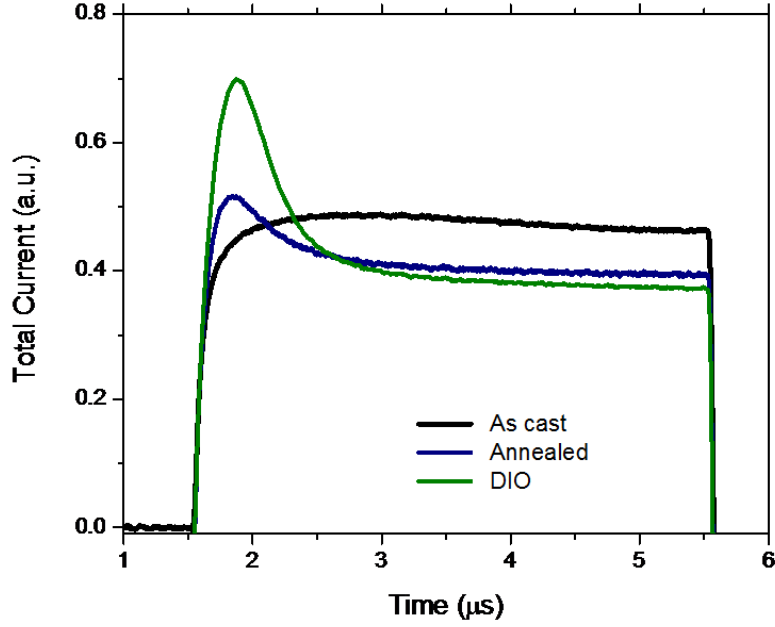


**Figure S4.6:** Photo-CELIV current transients for as cast, annealed, and DIO processed solar cell devices using a 4  $\mu\text{s}$  time delay and laser pulse fluence of  $0.30 \mu\text{J}/\text{cm}^2$ , .

Bimolecular recombination coefficient determined from CE measured carrier density.

At open circuit, all carriers recombine and thus the generation rate,  $G(V_{oc})$ , is equal to the recombination rate,  $R(V_{oc})$ . Assuming bimolecular recombination dominates,

$$R(V_{oc}) = \gamma_{BMR} n_{oc}^2 \quad (\text{S4.1})$$

where  $n_{oc}$  is the experimentally measured charge carrier density at open circuit. We account for the voltage dependence of  $G$  using the relation

$$G(V_{oc}) = \frac{J_{ph}(-3V)}{qL} \frac{Q_{tot}(V_{oc})}{Q_{tot}(-3V)} \quad (\text{S4.2})$$

where  $J_{ph}$  is the photocurrent,  $q$  the elementary charge,  $L$  the active layer thickness and  $Q_{tot}$  comes from the TDCF data presented in **Figure 4.2**. This analysis assumes nongeminate losses are negligible at -3V which is consistent with our observation that for all three conditions  $J_{ph}(-3V)$  depends linearly on light intensity and that the field dependence of

generations fits the photocurrent quite well around this bias. Equating Equations S4.1 and S4.2 thus enables one to solve for  $\gamma_{\text{BMR}}$ .

#### 4. References

- [1] J. Zhou, Y. Zuo, X. Wan, G. Long, Q. Zhang, W. Ni, Y. Liu, Z. Li, G. He, C. Li, B. Kan, M. Li, Y. Chen, *J. Am. Chem. Soc.* **2013**, *135*, 8484–8487.
- [2] C. M. Proctor, C. Kim, D. Neher, T.-Q. Nguyen, *Adv. Funct. Mater.* **2013**, *23*, 3584–3594.
- [3] L. G. Kaake, Y. Sun, G. C. Bazan, A. J. Heeger, *Appl. Phys. Lett.* **2013**, *102*, 133302–133302–3.
- [4] D. Credgington, F. C. Jamieson, B. Walker, T.-Q. Nguyen, J. R. Durrant, *Adv. Mater.* **2012**, *24*, 2135–2141.
- [5] T. P. Osedach, T. L. Andrew, V. Bulović, *Energy Environ. Sci.* **2013**, *6*, 711–718.
- [6] B. Walker, C. Kim, T.-Q. Nguyen, *Chem Mater* **2010**, *23*, 470–482.
- [7] C. M. Proctor, M. Kuik, T.-Q. Nguyen, *Prog. Polym. Sci.* **2013**, 10.1016/j.progpolymsci.2013.08.008.
- [8] A. Pivrikas, H. Neugebauer, N. S. Sariciftci, *IEEE J. Sel. Top. Quantum Electron.* **2010**, *16*, 1746–1758.
- [9] S. Albrecht, W. Schindler, J. Kurpiers, J. Kniepert, J. C. Blakesley, I. Dumsch, S. Allard, K. Fostiropoulos, U. Scherf, D. Neher, *J. Phys. Chem. Lett.* **2012**, *3*, 640–645.
- [10] S. Albrecht, S. Janietz, W. Schindler, J. Frisch, J. Kurpiers, J. Kniepert, S. Inal, P. Pingel, K. Fostiropoulos, N. Koch, D. Neher, *J. Am. Chem. Soc.* **2012**, *134*, 14932–14944.
- [11] G. F. A. Dibb, F. C. Jamieson, A. Maurano, J. Nelson, J. R. Durrant, *J. Phys. Chem. Lett.* **2013**, 803–808.
- [12] Y. Zhang, J. Liu, T.-Q. Nguyen, *ACS Appl. Mater. Interfaces* **2013**, *5*, 2347–2353.
- [13] M. Mingebach, S. Walter, V. Dyakonov, C. Deibel, *Appl. Phys. Lett.* **2012**, *100*, 193302–193302–4.
- [14] A. Foertig, J. Kniepert, M. Gluecker, T. Brenner, V. Dyakonov, D. Neher, C. Deibel, *Adv. Funct. Mater.* **2013**, 10.1002/adfm.201302134.
- [15] S. R. Cowan, N. Banerji, W. L. Leong, A. J. Heeger, *Adv. Funct. Mater.* **2012**, *22*, 1116–1128.
- [16] C. Deibel, V. Dyakonov, *Rep. Prog. Phys.* **2010**, *73*, 096401.
- [17] V. D. Mihailetschi, J. Wildeman, P. W. M. Blom, *Phys. Rev. Lett.* **2005**, *94*, 126602.
- [18] A. Baumann, J. Lorrman, D. Rauh, C. Deibel, V. Dyakonov, *Adv. Mater.* **2012**, *24*, 4381–4386.
- [19] T. S. Van der Poll, J. A. Love, T.-Q. Nguyen, G. C. Bazan, *Adv. Mater.* **2012**, *24*, 3646–3649.
- [20] J. A. Love, C. M. Proctor, J. Liu, C. J. Takacs, A. Sharenko, T. S. van der Poll, A. J. Heeger, G. C. Bazan, T.-Q. Nguyen, *Adv. Funct. Mater.* **2013**, 10.1002/adfm.201300099.

- [21] J. Kniepert, M. Schubert, J. C. Blakesley, D. Neher, *J Phys Chem Lett* **2011**, *2*, 700–705.
- [22] I. Lange, J. Kniepert, P. Pingel, I. Dumsch, S. Allard, S. Janietz, U. Scherf, D. Neher, *J. Phys. Chem. Lett.* **2013**, *4*, 3865–3871.
- [23] D. Credgington, F. C. Jamieson, B. Walker, T. Nguyen, J. R. Durrant, *Adv. Mater.*
- [24] T. J. K. Brenner, Z. Li, C. R. McNeill, *J Phys Chem C* **2011**, *115*, 22075–22083.
- [25] G. F. Burkhard, E. T. Hoke, Z. M. Beiley, M. D. McGehee, *J. Phys. Chem. C* **2012**, *116*, 26674–26678.
- [26] A. A. Bakulin, A. Rao, V. G. Pavelyev, P. H. M. Van Loosdrecht, M. S. Pshenichnikov, D. Niedzialek, J. Cornil, D. Beljonne, R. H. Friend, *Science* **2012**, *335*, 1340–1344.
- [27] A. E. Jailaubekov, A. P. Willard, J. R. Tritsch, W.-L. Chan, N. Sai, R. Gearba, L. G. Kaake, K. J. Williams, K. Leung, P. J. Rossky, X.-Y. Zhu, *Nat. Mater.* **2013**, *12*, 66–73.
- [28] C. Groves, *Energy Environ. Sci.* **2013**, *6*, 1546–1551.
- [29] A. Ojala, A. Petersen, A. Fuchs, R. Lovrincic, C. Pölking, J. Trollmann, J. Hwang, C. Lennartz, H. Reichelt, H. W. Höffken, A. Pucci, P. Erk, T. Kirchartz, F. Würthner, *Adv. Funct. Mater.* **2012**, *22*, 86–96.
- [30] S. Bange, M. Schubert, D. Neher, *Phys. Rev. B* **2010**, *81*, 035209.
- [31] D. Credgington, J. R. Durrant, *J. Phys. Chem. Lett.* **2012**, *3*, 1465–1478.
- [32] R. Mauer, I. A. Howard, F. Laquai, *J Phys Chem Lett* **2010**, *1*, 3500–3505.
- [33] D. Rauh, C. Deibel, V. Dyakonov, *Adv. Funct. Mater.* **2012**, *22*, 3371–3377.
- [34] T. Kirchartz, B. E. Pieters, J. Kirkpatrick, U. Rau, J. Nelson, *Phys. Rev. B* **2011**, *83*, 115209.
- [35] C. G. Shuttle, A. Maurano, R. Hamilton, B. O’Regan, J. C. de Mello, J. R. Durrant, *Appl. Phys. Lett.* **2008**, *93*, 183501.
- [36] C. Deibel, A. Wagenpfahl, V. Dyakonov, *Phys. Rev. B* **2009**, *80*, 075203.
- [37] M. Kuik, J. A. Love, Ran, Niva, T.-Q. Nguyen, unpublished.
- [38] A. Pivrikas, N. S. Sariciftci, G. Juška, R. Österbacka, *Prog. Photovolt. Res. Appl.* **2007**, *15*, 677–696.
- [39] A. Armin, M. Velusamy, P. L. Burn, P. Meredith, A. Pivrikas, *Appl. Phys. Lett.* **2012**, *101*, 083306–083306–5.
- [40] C. Deibel, A. Baumann, V. Dyakonov, *Appl. Phys. Lett.* **2008**, *93*, 163303–163303–3.
- [41] S. R. Cowan, A. Roy, A. J. Heeger, *Phys. Rev. B* **2010**, *82*, 245207.
- [42] J. Guo, H. Ohkita, H. Benten, S. Ito, *J Am Chem Soc* **2010**, *132*, 6154–6164.
- [43] I. A. Howard, R. Mauer, M. Meister, F. Laquai, *J Am Chem Soc* **2010**, *132*, 14866–14876.
- [44] D. P. McMahon, D. L. Cheung, A. Troisi, *J. Phys. Chem. Lett.* **2011**, *2*, 2737–2741.
- [45] A. J. Ferguson, N. Kopidakis, S. E. Shaheen, G. Rumbles, *J. Phys. Chem. C* **2011**, *115*, 23134–23148.
- [46] D. H. K. Murthy, A. Melianas, Z. Tang, G. Juška, K. Arlauskas, F. Zhang, L. D. A. Siebbeles, O. Inganäs, T. J. Savenije, *Adv. Funct. Mater.* **2013**, *23*, 4262–4268.
- [47] M. Hilczner, M. Tachiya, *J. Phys. Chem. C* **2010**, *114*, 6808–6813.

## Chapter V

### Importance of Domain Purity and Molecular Packing in Efficient Solution Processed Small Molecule Solar Cells

#### 1. The Story

Organic solar cells made from a solution-processed blend of electron-donating and electron-accepting small molecules have been demonstrated to be viable alternatives to their conjugated polymer-based or evaporated small molecule counterparts.<sup>[1, 2, 3]</sup> As in polymer based devices, controlling and understanding the surprisingly complex nanoscale morphology of the active layer in molecular bulk heterojunction (BHJ) devices remains a principal challenge. Several methods to modify the nanoscale morphology have been devised, including thermal<sup>[4]</sup> and solvent annealing.<sup>[5]</sup> The most versatile and widely employed technique, however, is the use of solvent additives,<sup>[2, 3, 6, 7]</sup> which act during the timescale of film formation.<sup>[7, 8]</sup> Solvent additives have been shown to be able to increase the carrier mobility,<sup>[9]</sup> and thereby improve the competition between extraction and recombination,<sup>[10]</sup> and to mitigate the voltage dependence of splitting electron-hole pairs (i.e. geminate recombination) during the photogeneration process.<sup>[11, 12]</sup> However, the detailed structural mechanisms and their effect on charge generation and extraction remain elusive.

For most BHJ systems, improved solar cell performance has been achieved by varying the film processing conditions often leading to a distinctly different morphology from those seen in lower performing devices. This has led to the paradigm and expectations that pure domains with lateral in-plane dimensions of ~10 nm need to be matched with the

exciton diffusion length. More recently, it was reported that the miscibility of the fullerene in the donor can be considerable and that the mixed component domains can provide excellent exciton quenching and charge generation.<sup>[12, 13, 14]</sup> The actual morphologies might thus comprise three phases, with relatively pure, aggregated donor and acceptor domains in addition to mixed amorphous regions. It has been suggested that indeed this three phase morphology may be favorable as the electronic structure of both the donor and acceptor depends on the level of aggregation, thus providing an electronic landscape that can help to sweep charges out of the mixed domains.<sup>[15]</sup> On the other hand, even the most conductive pathways can have relatively low domain purity, which can lead to significant geminate or bimolecular recombination.<sup>[16]</sup> As a result, the performance of many systems is likely a compromise in the tradeoff between domain size and domain purity.<sup>[14, 16-18, 19]</sup> To date however, due to a paucity of readily available quantitative characterization methods, only a few studies have been able to establish relations between such details of the morphology and short-circuit current ( $J_{sc}$ ), fill factor ( $FF$ ), and mobility in polymer based photovoltaics.<sup>[14, 17, 20]</sup> The effects of average domain purity in solar cell devices based on solution processed molecules remain unexplored.

In this communication, we delineate connections between solar cell performance, charge carrier mobilities, relative composition fluctuations (average domain purity) and coherence lengths of both the fullerene and donor components in a high performance molecular solar cell. The subject of the study is the molecular donor 7,7'-(4,4-bis(2-ethylhexyl)-4H-silolo[3,2-b:4,5-b']dithiophene-2,6-diyl)bis(6-fluoro-4-(5'-hexyl-[2,2'-bithiophen]-5-yl)benzo[c][1,2,5]thiadiazole) (p-DTS(FBTTh<sub>2</sub>)<sub>2</sub>), blended with phenyl-C71-butyric acid methyl ester (PC<sub>71</sub>BM) as it is known to yield one of the most efficient

solution-processed molecular BHJ solar cells to date. The performance of p-DTS(FBTTh<sub>2</sub>)<sub>2</sub>:PC<sub>71</sub>BM is extremely sensitive to the solvent additive 1,8-diiodooctane (DIO) and the presence of a “sweet spot” in the DIO concentration ([DIO]) with best performance makes it ideal for manipulating the morphology in complex ways.<sup>[3]</sup> Prior efforts directed towards understanding the morphology of p-DTS(FBTTh<sub>2</sub>)<sub>2</sub>:PC<sub>71</sub>BM films have shown the differences in crystallinity of films prepared using optimized additive and annealing conditions.<sup>[21, 22]</sup> Here, we delineate the causative relations between morphology, carrier mobilities, and device parameters of p-DTS(FBTTh<sub>2</sub>)<sub>2</sub>:PC<sub>71</sub>BM blends by using small changes in [DIO] to make such relations discernable. The  $J_{sc}$  and  $FF$  exhibit a non-monotonic behavior with additive amount thus indicating the effects of competing processes during the morphology formation. Utilizing resonant soft X-ray scattering (R-SoXS), which probes both crystalline as well as mixed domains, it is found that devices prepared with the optimum additive content have the maximum relative composition variation (phase purity) and an intermediate domain size. Furthermore, the crystallization behavior of the blends revealed by grazing incidence wide-angle X-ray scattering (GIWAXS) can be linked to the purity of the domains as well as the hole and electron mobilities. These findings offer unique and comprehensive insights into the evolution of the morphology with additive concentration and its relation to device performance and the observed tradeoffs in  $J_{sc}$  and  $FF$ .

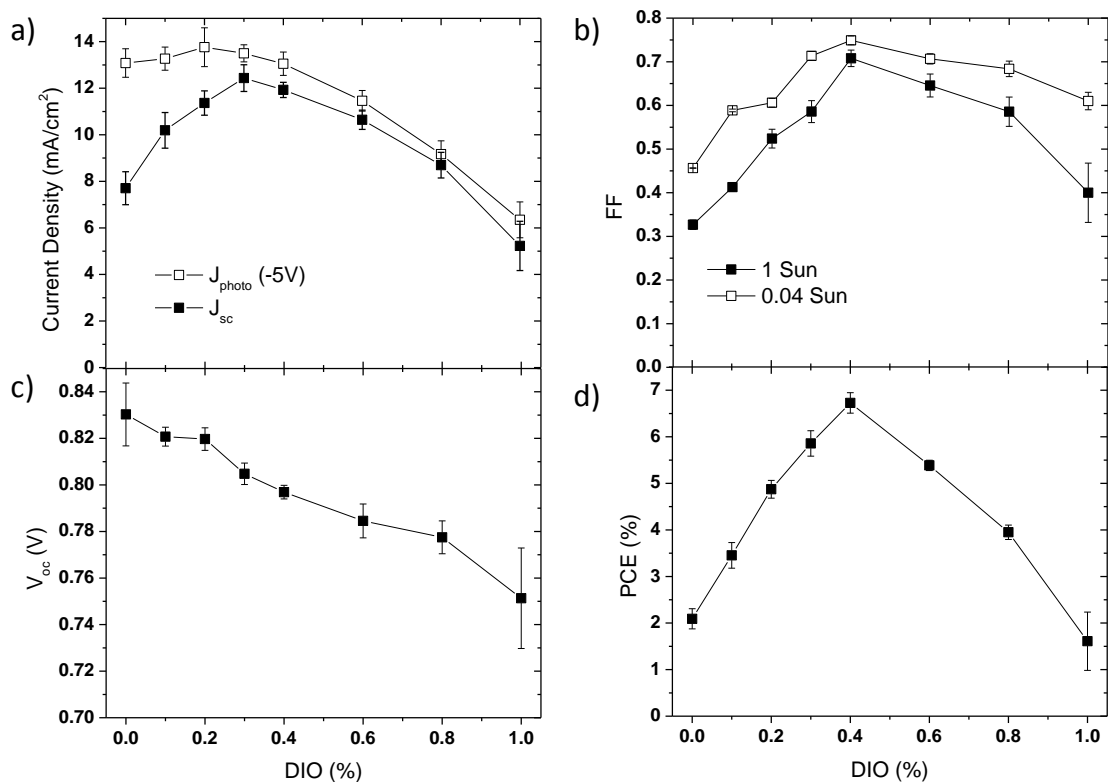


**Figure 5.1:** Average solar cell device parameters: (a) photogenerated current at -5V (open symbols) and  $J_{sc}$ , (solid symbols), (b)  $FF$  at two different light intensities (0.04 sun, open symbols; 1 sun, solid symbols), (c)  $V_{oc}$  and (d) PCE at 1 sun for different [DIO]. Error bars represent +/- one standard deviation.

In order to prepare the photoactive films p-DTS(FBTTh<sub>2</sub>)<sub>2</sub>:PC<sub>71</sub>BM devices were prepared using a range of [DIO]. The resulting average  $FF$ ,  $J_{sc}$ , open circuit voltage ( $V_{oc}$ ) and power conversion efficiency (PCE) for solar cell devices measured under AM1.5 solar irradiance are shown in **Figure 5.1**. [DIO] is reported in terms of volume percentage relative to the principal chlorobenzene solvent. Notwithstanding the continuous decrease of  $V_{oc}$  with increasing [DIO], the other device parameters exhibit a non-monotonic dependence and a much larger relative variation on [DIO] with an optimal concentration at 0.3% for  $J_{sc}$  and

0.4% for  $FF$ . Consequently, the PCE also shows a non-monotonic dependence with a clear peak at 0.4% DIO (**Figure 5.1d**). In addition to the  $J_{sc}$ , **Figure 5.1a** shows the trend in device photocurrent measured at -5V ( $J_{photo}(-5V)$ ) where photocurrent is defined as the difference between light and dark current. In contrast to the  $J_{sc}$ ,  $J_{photo}(-5V)$  is relatively constant at ca. 13 mA/cm<sup>2</sup> from 0.0% DIO up until 0.4% DIO, after which it decreases in line with the  $J_{sc}$ . The modest difference between  $J_{sc}$  and  $J_{photo}(-5V)$  from 0.4% to 1.0% DIO suggests that within this concentration range the change in photocurrent is primarily due to a mechanism that does not depend on the applied voltage. Conversely, from 0.0% to 0.3% DIO it is evident that the change in  $J_{sc}$  is primarily due to a change in the voltage dependence of the photocurrent. This is consistent with our recent finding that a combination of voltage dependent geminate recombination and bimolecular recombination limit the photocurrent of p-DTS(FBTTh<sub>2</sub>)<sub>2</sub>:PC<sub>71</sub>BM devices without DIO, while devices made with 0.4% DIO exhibit only negligible voltage dependent geminate recombination losses.<sup>[11]</sup>

Current voltage characteristics of each device were measured at an illumination intensity of only 0.04 Sun in order to sort out the influence of different recombination mechanisms on the voltage dependence of the photocurrent. The resulting  $FF$ s are shown in **Figure 5.1b** (open symbols). For all [DIO], the  $FF$  measured at 0.04 Sun is higher than the 1 Sun  $FF$ . This response is typical of organic BHJ solar cells as the rate of bimolecular recombination depends quadratically on the charge carrier density and therefore as the photogenerated carrier density decreases with decreasing light intensity so does the influence of bimolecular recombination.<sup>[23, 24]</sup> The relative change in  $FF$  from 0.04 to 1 Sun appears smallest at 0.4% DIO and generally increases at lower and higher [DIO] values suggesting that the relative loss due to bimolecular recombination follows a similar trend. The trend in

the absolute value of the 0.04 Sun  $FF$  is rather intriguing in the context of our previous finding that 0.0% DIO devices show significant voltage dependent geminate recombination while 0.4% DIO devices do not suffer from such losses.<sup>[11]</sup> The 0.04 Sun  $FF$  rises steadily from  $\sim 0.45$  to  $\sim 0.75$  as [DIO] increases from 0.0% to 0.4% and then gradually decreased to 0.60 as [DIO] increases to 1.0%. Further reducing the incident light intensity below 0.04 Sun does not lead to significant changes in  $FF$ , thus it is reasonable to consider that at 0.04 Sun bimolecular recombination losses are nearly minimized. In contrast to bimolecular recombination, the influence of voltage dependent geminate recombination on  $FF$  is expected to be independent of the incident light intensity.<sup>[24]</sup> Following this reasoning, it may be that the 0.04 Sun  $FF$  is largely limited by geminate recombination and thus the trend in the absolute value of the 0.04 Sun  $FF$  mirrors the change in losses from voltage dependent geminate recombination.

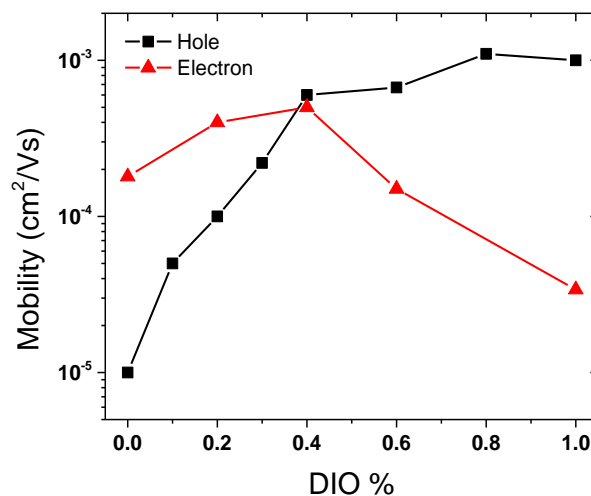


**Figure 5.2.** Hole and electron mobility as a function of [DIO] measured in single carrier diodes.

Hole and electron charge carrier mobilities were measured as a function of [DIO] by fitting the current voltage response of single carrier diodes to the Mott-Gurney Law for space charge limited current.<sup>[25]</sup> As shown in **Figure 5.2**, the hole mobility rises sharply from 0.0% to 0.4% DIO and then rises only modestly from 0.4% to 1.0% DIO. The electron mobility also increases slightly from 0.0% to 0.4% DIO then drops significantly as the [DIO] increases to 1.0%. Note that the trend of the slowest carrier mobility (hole from 0.0-0.4%, electron from 0.4-1.0%) correlates well with the trend in 1 Sun *FF* and is consistent with a recent report<sup>[26]</sup> that found both carrier mobilities must be at least  $10^{-4}$  cm<sup>2</sup>/Vs in order to achieve a *FF* > 0.65. This can be understood by considering that the charge carrier sweep out time is proportional to the mobility so if the mobility is too low, the average charge carrier density in the device will be higher and oppositely charged carriers are more likely to recombine with one another before they are collected at the electrodes. We now turn our attention to understanding how the thin film morphology evolves with [DIO]. R-SoXS was utilized to probe the characteristic length scales and spatial frequency distribution of the morphology, and average composition fluctuations over length scales spanning ~10-1000 nm.<sup>[17, 28, 29]</sup> This technique utilizes the unique optical contrast (**Figure S5.1**) between the donor molecule and fullerene near the carbon 1s absorption edge to achieve high sensitivity. **Figure 5.3a** shows the scattering profiles acquired at 284.2 eV for p-DTS(FBTTh<sub>2</sub>)<sub>2</sub>:PC<sub>71</sub>BM films processed with different amounts of DIO at the photon energy of 284.2 eV normalized for absorption and thickness.

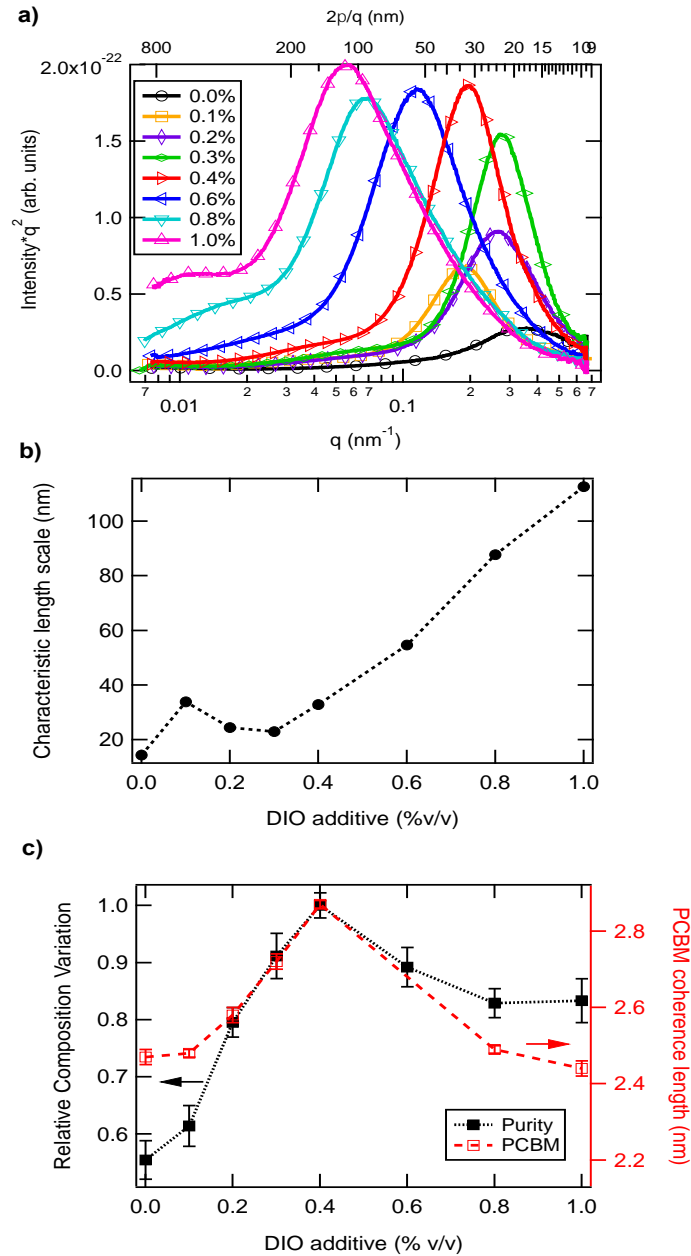


**Figure 5.3.** (a) Lorentz corrected<sup>[27]</sup> and normalized RSoXS scattering profiles (284.2 eV) of blend films processed with different amounts of additive (% v/v) as indicated. Top axis is provided to aid conversion of long period to real-space values. (b) Characteristic size scale of morphology and, (c) average composition variation (solid squares) obtained from integrations of the scattering profiles in (a) compared to PC<sub>71</sub>BM coherence length (open squares) from GIWAXS. The initial rise in size scale at 0.1% DIO occurs due the formation of a metastable polymorph (for details see text). The relative composition variation (i.e., purity) values were normalizing with respect to those of the optimized device (0.4% DIO).

The scattering profiles represent the distribution function of spatial frequency,  $s$  ( $s = \frac{2\pi}{q}$ ), of the samples with the dominant peak (long period) representing the domain spacing or the characteristic size scale of the blend. The variation of the characteristic size scale with [DIO] is shown in **Figure 5.3b**. By integrating the scattering profiles and ensuring that scattering originates from materials and not mass-thickness contrast, the total scattering intensity (TSI) reveals the relative composition variations between the blends over the length scales probed.<sup>[19]</sup> Thus along with the distribution of domain spacings, the average relative composition variations (domain purity) is also extracted from R-SoXS measurements (**Figure 5.3c**).

Analyzing the trends in domain size as well as the composition variation offers a clearer picture of the film morphology and helps explain the trends observed in **Figures 5.1** and **5.2**. The 0.0% DIO sample shows the smallest average domain size in addition to the smallest composition variation indicating it to be a relatively homogeneous mixture lacking discernible phase separation as has been observed qualitatively by transmission electron microscopy (TEM).<sup>[21]</sup> As [DIO] increases up to the optimum value of 0.4%, the average domain spacing increases only slightly (see below for discussion of the intensity spike for 0.1% DIO). From 0.4% to 1.0% DIO, the average domain spacing increases nearly threefold. The trends in domain spacing (**Figure 5.3b**) seem to explain the trend in  $J_{photo}(-5V)$ . From 0.0%-0.4% little change is seen for either parameter indicating that for this [DIO] range the domain spacing is not limiting the diffusion of excitons to a donor-acceptor interface. However as the domain spacing increases at higher [DIO],  $J_{photo}(-5V)$  decreases. This decrease is presumably because at [DIO] > 0.4% the domains become larger than the exciton

diffusion length thereby leading to a significant decrease in exciton separation efficiency as more excitons relax to the ground state before reaching a donor-acceptor interface. The  $J_{sc}$  does not follow the overall trend in domain spacing as the change in  $J_{sc}$  is dominated by the change in voltage dependence of the photocurrent, which is best captured by the trend in  $FF$ .

Importantly, the dependence of the relative phase purity on [DIO] (**Figure 5.3c**) mirrors the dependence of  $FF$  on [DIO] (**Figure 5.1b**). From 0.0% DIO to 0.4% DIO the relative composition variation steadily increases. This shows that addition of DIO helps in phase separation resulting in larger and purer domains. These purer domains in turn enable more efficient charge transport and reduce bimolecular charge recombination (**Figure 5.2**) leading to a higher  $FF$ . The rise in the 0.04 Sun  $FF$  over the same range suggests that increasing the phase purity may also help diminish voltage dependent geminate recombination. As the additive concentration is increased beyond 0.4%, the purity is seen to decrease and the  $FF$  follows suit. On the other hand the domain size measuring composition continues to increase monotonically. Given the low miscibility of the donor material (**Figure S5.2**) this is a counterintuitive result, which indicates that increasing [DIO] > 0.4% results in larger but progressively impure phase separations. Nevertheless, these facts can be reconciled if one considers the presence of multiple processes during the film formation. A high boiling point additive like DIO would decrease the evaporation rate of the film thus allowing for continued molecular rearrangement over a much longer timescale compared with pure chlorobenzene.<sup>[30]</sup> On the other hand DIO has the additional property of being a preferential solvent for PC<sub>71</sub>BM. Therefore, one possible explanation is that beyond a certain concentration (determined by the turning point of the composition variation) it may be that instead of helping phase separation and purifying domains, DIO dissolves PC<sub>71</sub>BM domains.

In essence, the quench depth into the 2-phase region of the phase diagram is impacted. This reduces the composition variation and at the same time elongates the evaporation process leading to larger donor domains and crystallites. Indeed the size scales observed for the 1.0% DIO blend films matches with the domain sizes observed in TEM as well as from scanning transmission X-ray microscopy (STXM) measurements (**Figure S5.3**).<sup>[21]</sup> These findings are consistent with the trends of hole and electron mobilities shown in **Figure 5.2**, wherein at [DIO] >0.4% the hole mobility continues to increase slightly and the electron mobility decreases sharply.

In addition to size and composition variation (purity), molecular ordering relative to the dominant, discrete donor-acceptor interface can also be a critical structure parameter that impacts performance. This ordering may influence exciton dissociation and charge transport near an interface, with “face-on” orientation being correlated to improved  $J_{sc}$  and  $FF$ .<sup>[14, 29, 31]</sup> The extent of such molecular orientation in the p-DTS(FBTTh<sub>2</sub>)<sub>2</sub>:PC<sub>71</sub>BM devices was quantified by following previously established procedures (results shown in **Figure S5.4**).<sup>[29]</sup> Positive values of the anisotropy order parameter between 0.09 and 0.14 are observed for all samples, except for 1.0% DIO, which yielded an anisotropy of ~0.04. In general this ordering was found to decrease with increasing DIO but does not vary much for 0.2 – 0.8% DIO. The positive values indicate that the beneficial “face-on” orientation with respect to fullerene-rich domains has been achieved. The lack of variation of this parameter and the correlation with device parameters indicates that in the p-DTS(FBTTh<sub>2</sub>)<sub>2</sub>:PC<sub>71</sub>BM system performance is controlled by other structural and morphological parameters.

In order to further substantiate the morphological understanding gained from R-SoXS, GIWAXS was employed as a complimentary probe to track the PC<sub>71</sub>BM

agglomeration and crystallographic changes of the donor molecules in the blend films. The broad peak occurring around  $1.35\text{\AA}^{-1}$  in the scattering profiles (see **Figure S5.5**) obtained of the 2-dimensional scattering data is known to correspond to relatively disordered PC<sub>71</sub>BM aggregates with very few coherent diffraction planes.<sup>[32, 33]</sup> A simple analysis using the Scherrer equation<sup>[34]</sup> of the peak reveals the coherence length within the PC<sub>71</sub>BM aggregates, which, on account to volume fraction conservation, should have similar size than the domain size derived from R-SoXS. In order to minimize contributions from the peaks corresponding to the donor crystallites, a cake slice at  $75^\circ$  relative to the in-plane direction was chosen for the analysis based on experiments with neat p-DTS(FBTTh<sub>2</sub>)<sub>2</sub> film (details in SI, **Figure S5.6**). The PCBM coherence length observed for the blends with different DIO is shown in **Figure 5.3c** and exhibits a similar behavior as the composition variations, electron mobility and *FF*, all peaking at 0.4% DIO. It should be noted here that due to the highly paracrystalline nature of the PC<sub>71</sub>BM agglomerates, the coherence lengths represent a local ordering within the PC<sub>71</sub>BM domains.<sup>[35]</sup> Consequently, in the absence of discrete peaks due to small PC<sub>71</sub>BM crystals,<sup>[32, 36]</sup> the coherence lengths obtained show a degradation of the local ordering of PC<sub>71</sub>BM domains when  $[\text{DIO}] > 0.4\%$ . This degradation coincides with the progressively impure phase separations observed by RSoXS. It stands to reason that the decrease in PC<sub>71</sub>BM ordering in combination with the formation of large p-DTS(FBTTh<sub>2</sub>)<sub>2</sub> domains ultimately leads to the decrease in electron mobility observed at high  $[\text{DIO}]$  (**Figure 5.2**).

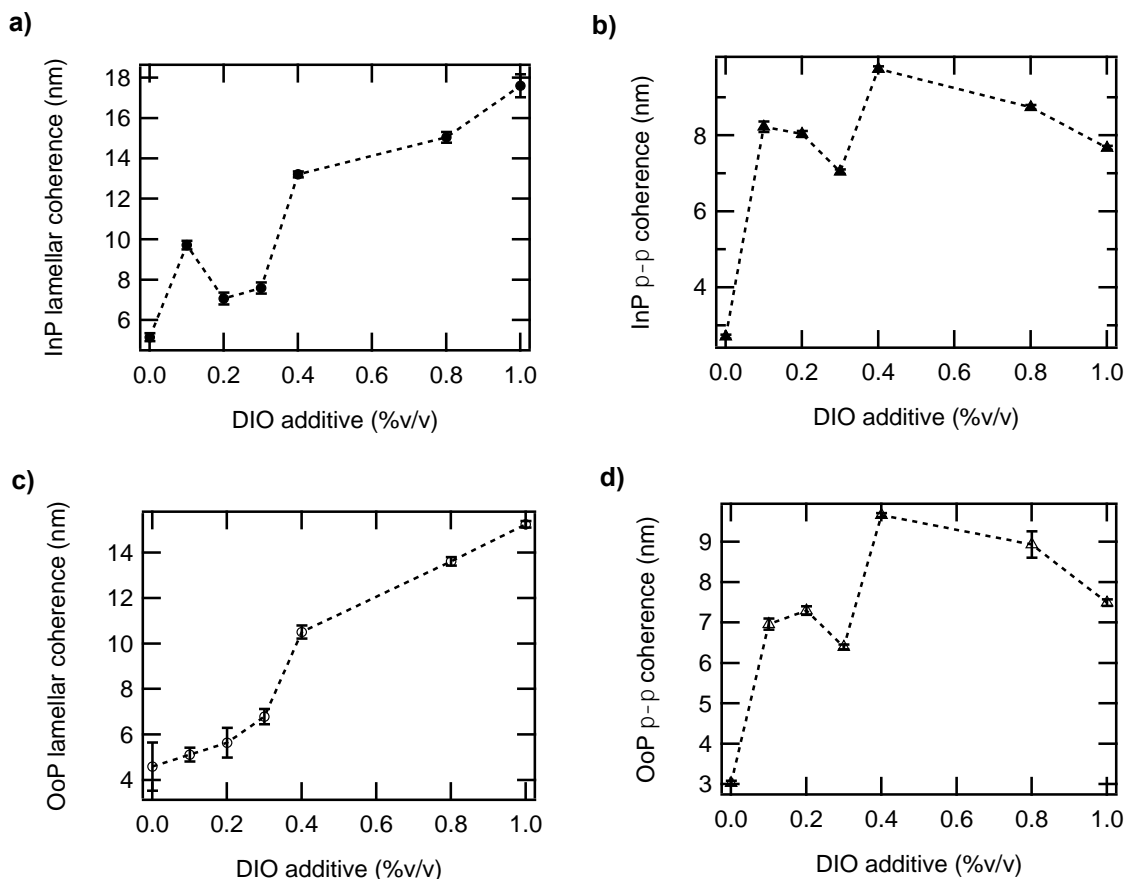


**Figure 5.4.** Coherence lengths from GIWAXS. (a) In-plane (InP) alkyl lamellar correlation; (b) In-plane  $\pi$ - $\pi$  correlation; (c) Out-of-plane (OoP) alkyl lamellar correlation; (d) Out-of-plane  $\pi$ - $\pi$  correlation. Error bars are obtained from fitting Voigt functions to scattering peaks.

GIWAXS data also offer insight into the change of p-DTS(FBTTh<sub>2</sub>)<sub>2</sub> crystallinity within the films. In-plane and out-of-plane alkyl lamellar and  $\pi$ - $\pi$  coherence lengths for p-DTS(FBTTh<sub>2</sub>)<sub>2</sub> obtained from Scherrer analysis using in-plane and out-of-plane cake slices of the 2-dimensional data are shown in **Figure 5.4**. It is interesting to note here that at [DIO] around 0.1% an additional peak was observed in the in-plane lamellar coherence lengths from GIWAXS just as was observed in the domain spacings from R-SoXS, which also probe the in-plane morphology. Recent dynamic GIWAXS studies<sup>[30]</sup> have shown that during the

early stages of film formation in the presence of 0.4% DIO a metastable polymorph with a higher lattice spacing is formed. It is possible that a similar metastable polymorph (in accordance with Ostwald's rule) is formed at low DIO content, which is quenched during casting on account of the more rapid solidification at low [DIO]. A gradual transition to the stable polymorph is observed and enabled as DIO is increased to 0.3%. The 0.1% DIO films aside, the in-plane as well as the out-of-plane lamellar coherence lengths exhibit a generally monotonic trend indicating the increase of donor crystallite sizes consistent with the RSoXS data and interpretation that the growth in domain size is primarily attributable to p-DTS(FBTTh<sub>2</sub>)<sub>2</sub> rich, crystalline domains.

The variation of the in-plane and out-of-plane  $\pi$ - $\pi$  coherence length with [DIO] is shown in **Figures 5.4c** and **d**. It is interesting to note that unlike the lamellar coherence lengths the non-monotonic trends for the in-plane as well as the out-of-plane  $\pi$ - $\pi$  coherence lengths are similar to those observed for the *FF* as well as RSoXS composition variations and achieve a maximum at 0.4% DIO. Better  $\pi$ - $\pi$  stacking is known to promote better intermolecular orbital overlap which is an important factor for charge separation and charge transport analogous to the effect of face-on crystallite orientation with respect to the substrate.<sup>[14, 29]</sup> Although recently the importance of  $\pi$ -stacking coherence for achieving high electron mobilities has been discussed for n-type organic field effect transistors<sup>[37]</sup> such relations have not been made explicitly for organic BHJs. Our findings suggest that indeed there is an overall correlation between better  $\pi$ - $\pi$  coherence and higher charge carrier mobility (**Figures 5.2** and **5.4**), with some divergence at high [DIO]. However, as discussed previously, addition of DIO can simultaneously lead to increased phase separation, so in this case it is not possible to entirely decouple the influence of molecular packing versus

compositional morphology on the charge carrier mobility. Likewise, the trends in the  $\pi$ - $\pi$  stacking of p-DTS(FBTTh<sub>2</sub>)<sub>2</sub> at low [DIO] indicate that, as with relative domain purity, increased  $\pi$ - $\pi$  stacking is correlated with higher  $FF$  even at very low light intensities. This suggests that establishing molecular ordering and relatively pure domains may both assist in overcoming the geminate and nongeminate recombination losses that are known to plague solution processed small molecule solar cell systems.<sup>[11, 24, 38]</sup>

In summary, we report herein the first delineation of the interrelationships between relative domain purity, donor and PC<sub>71</sub>BM coherence lengths, charge transport and solar cell performance in a high performance small molecule BHJ system. The combination of data from solar cell devices, single carrier diodes, R-SoXS and GIWAXS revealed that variations in  $J_{sc}$  and  $FF$  can be understood in terms of the film morphology. There are two distinct [DIO] regimes in the case of p-DTS(FBTTh<sub>2</sub>)<sub>2</sub>:PC<sub>71</sub>BM that give rise to markedly different changes in thin film morphology. When increasing [DIO] from 0.0% to 0.4% DIO, the average coherence lengths of both PC<sub>71</sub>BM and p-DTS(FBTTh<sub>2</sub>)<sub>2</sub> increase, as does the relative composition variation (phase purity). The increased structural order and phase separation leads to a significant increase in the hole mobility and a modest increase in the electron mobility, which in turn leads to a sharp rise in  $FF$  and  $J_{sc}$ . Light intensity dependence measurements suggest that voltage dependent geminate recombination losses also steadily decrease in line with the increasing phase purity and structural order. The relative composition variation, PC<sub>71</sub>BM coherence length, p-DTS(FBTTh<sub>2</sub>)<sub>2</sub>  $\pi$ - $\pi$  stacking coherence length, solar cell  $FF$  and PCE were all found to peak at 0.4% DIO. As [DIO] increased from 0.4% to 1.0%, it was found that while the average domain size increased, the relative phase purity and PC<sub>71</sub>BM coherence length decreased leading to a degradation of the

local ordering and integrity of PC<sub>71</sub>BM domains resulting in slower electron transport. Consequently, the photogeneration efficiency was found to decrease with increasing domain sizes, while the *FF* dropped along with the electron mobility primarily due to reduced extraction and thus increased bimolecular recombination. In their composite, these results delineate why this p-DTS(FBTTh<sub>2</sub>)<sub>2</sub>:PC<sub>71</sub>BM system is not optimized yet (e.g. *J<sub>sc</sub>* and *FF* peaks occur for different [DIO]) and illustrate the complexity of solvent additive effects. Our work suggests that maximizing relative phase purity and structural order while simultaneously limiting domain size may be essential for achieving optimal solar cell performance in solution processed small molecule solar cells.

## **2. Experimental Section**

*Device preparation:* The solar cell and single carrier devices were fabricated on ITO coated glass slides pre-cleaned in acetone, detergent, DI-water, isopropanol and dried under a nitrogen stream. For solar cell and hole only devices the pre-cleaned ITO substrate was plasma-cleaned and a 40-50 nm layer of PEDOT:PSS (Clevios AI 4083) was spin cast on top. The samples were subsequently annealed at 140°C for 25 min in ambient conditions before being moved to a nitrogen filled glovebox. For electron only devices, 100 nm of aluminum was thermally evaporated onto the ITO substrate prior to the active layer. The active layer was spin cast from solutions containing 3:2 (by weight) blend ratios of p-DTS(FBTTh<sub>2</sub>)<sub>2</sub> (1material) and PC<sub>71</sub>BM (99%, Solenne) to make a ~100 nm film. Chlorobenzene was used as the solvent along with the specified concentration of DIO. DIO samples were thermally annealed at 70 °C for 10 min. For solar cell and electron only devices 12 nm Ca and 100 nm Al were thermally evaporated with a base pressure below 10<sup>-6</sup>

mbar through shadow masks. Hole only devices had 50 nm of Au evaporated through shadow masks.

*Measurements:* RSoXS, GIWAXS, and reference spectroscopy/miscibility measurements were performed at beamline 11.0.1.2,<sup>[39]</sup> beamline 7.3.3,<sup>[40]</sup> and beamline 5.3.2.2,<sup>[41]</sup> respectively, at the Advanced Light Source, Berkeley, CA.

### 3. Supporting Information

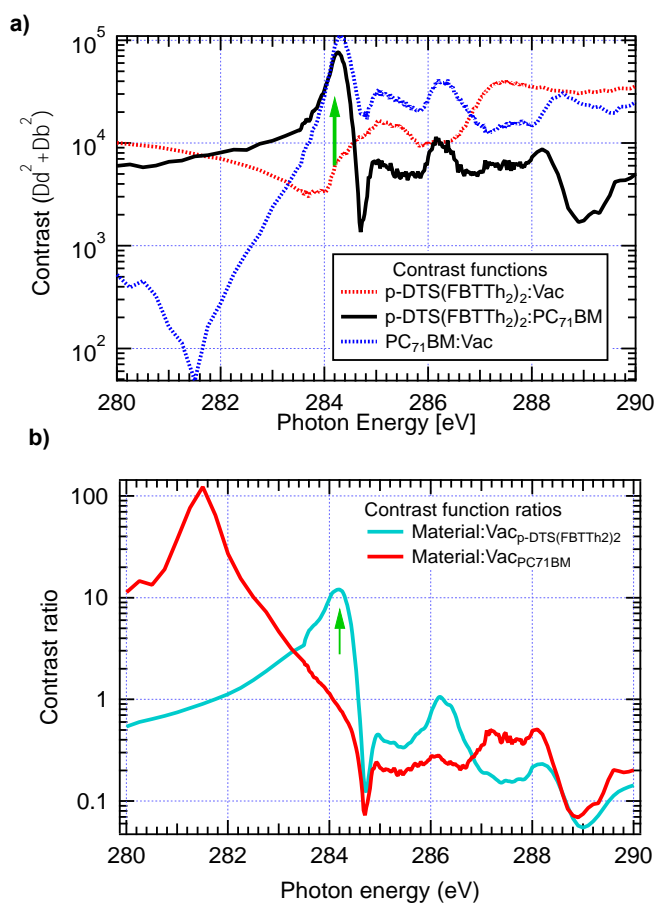


**Figure S5.1:** a) p-DTS(FBTTh<sub>2</sub>)<sub>2</sub>:PC<sub>71</sub>BM material contrast (solid line) and vacuum contrast (broken line) functions; b) Material:vacuum contrast ratios. The real dispersive part of the refractive index,  $1 - \delta$ , and the imaginary absorptive part,  $\beta$ , for p-DTS(FBTTh<sub>2</sub>)<sub>2</sub> and PC<sub>71</sub>BM are unique fingerprints of each material and provide scattering contrast that is

proportional to  $\Delta n^2 = \Delta \delta^2 + \Delta \beta^2$ . Data were acquired below the absorption edge at 284.2 eV (as indicated in above figure) to optimize the material contrast over the mass-thickness contrast and to avoid damage and fluorescence background.<sup>[42]</sup>

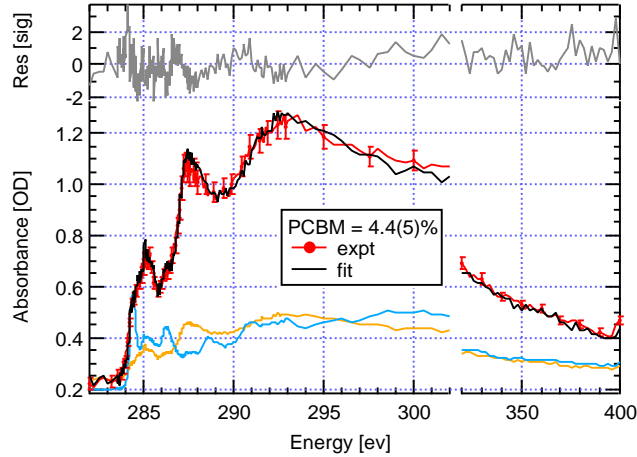


**Figure S5.2:** STXM measurement of the residual PCBM concentration that resides in the amorphous parts of the matrix of an aggressively annealed blend of *p*-DTS(FBTTh<sub>2</sub>)<sub>2</sub>:PC<sub>71</sub>BM blend prepared with 3% v/v DIO. The value of 4.4% represents the average of the mixed amorphous regions and the crystalline *p*-DTS(FBTTh<sub>2</sub>)<sub>2</sub> regions, i.e. the denominator includes all the donor material. The residual PCBM likely resides in the disordered donor regions.

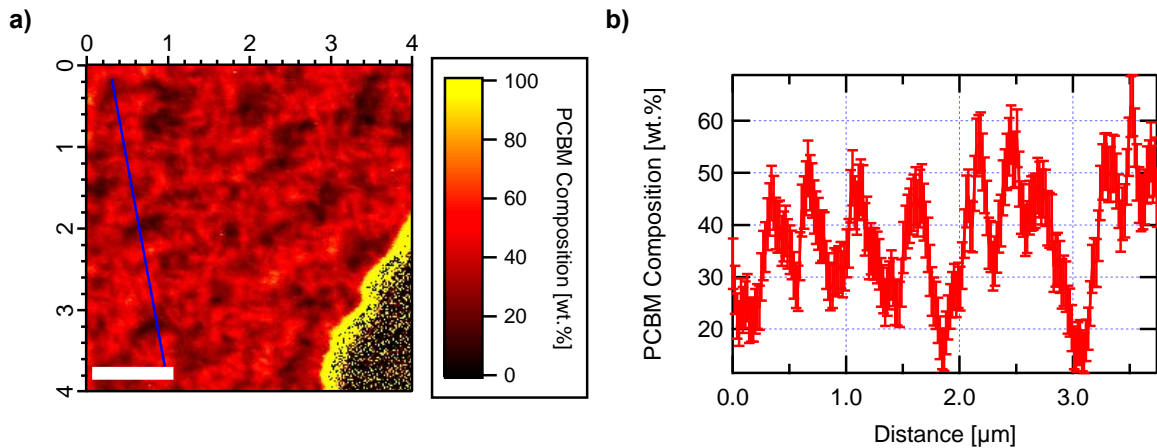


**Figure S5.3:** (a) STXM composition map for *p*-DTS(FBTTh<sub>2</sub>)<sub>2</sub>:PC<sub>71</sub>BM blend sample prepared with 1.0% DIO. The map was obtained using two STXM images acquired at different energy (284.4 and 320 eV) following previous methodology,<sup>[19]</sup> (b) Composition line profile taken from the blue line in (a), indicating that neither donor nor acceptor domains are very pure.

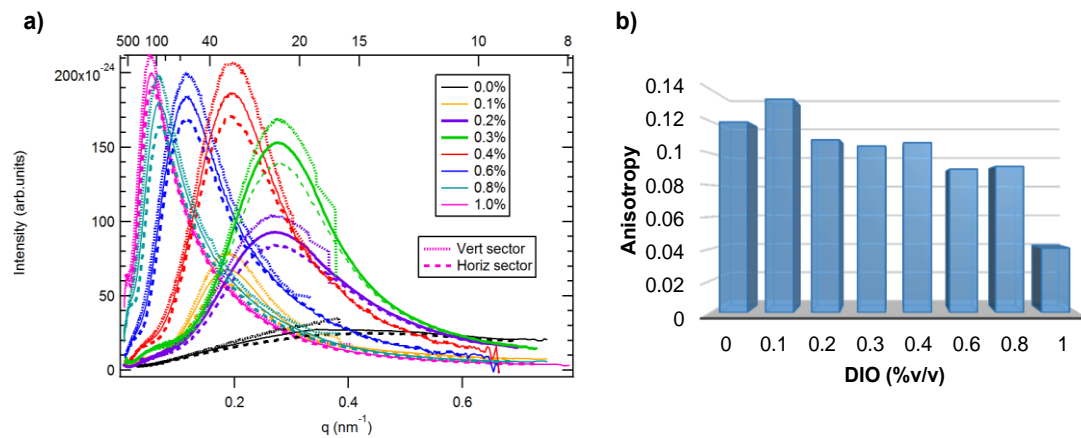


**Figure S5.4:** (a) Circular average, horizontal and vertical sector scattering profiles from 2-d RSoXS data acquired at 284.2 eV; (b) Relative degree of average face-on orientation as obtained from the difference over the sum ratio of the vertical and horizontal sector intensities.<sup>[29]</sup>

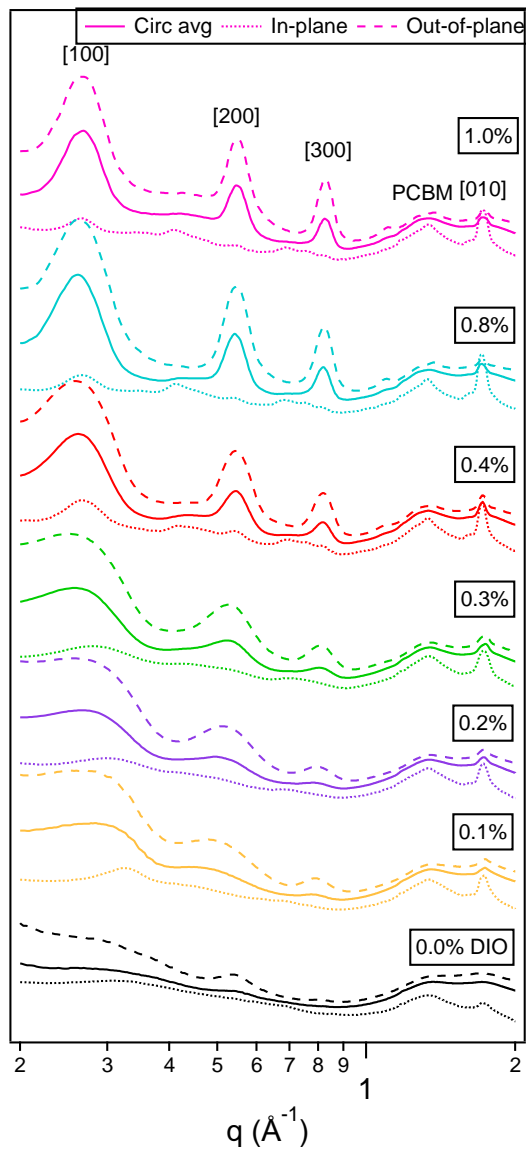


**Figure S5.5:** 1-dimensional out-of-plane, in-plane and circular averaged GIWAXS profiles obtained from 2-dimensional scattering data.

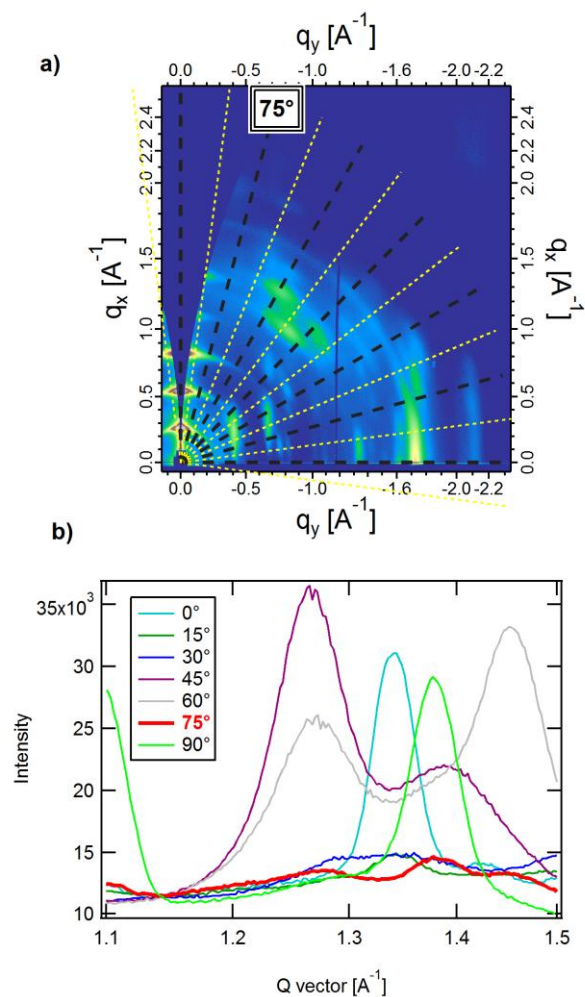


**Figure S5.6:** (a) 2-dimensional GIWAXS data of neat  $p$ -DTS(FBTTh<sub>2</sub>)<sub>2</sub> film showing the different cake slices. (b) 1-dimensional scattering profiles from each cake slice indicated in (a). As the intensity of the pure donor peaks are minimum in the region around 1.35  $\text{\AA}^{-1}$  for the 75 deg cake slice (red curve in (b)) the latter was chosen for comparing the PC<sub>71</sub>BM coherence length obtained from the circular average.

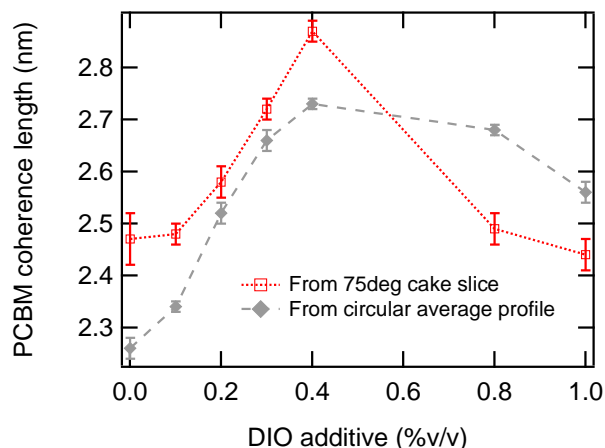


**Figure S5.7:** PC<sub>71</sub>BM coherence length obtained from circular averaged profile compared with that obtained from a sector where the pure donor peaks are minimum (**Figure S6**).

#### 4. References:

- [1] A. Mishra, P. Bäuerle, *Angewandte Chemie International Edition* 2012, 51, 2020; Y. Liu, C.-C. Chen, Z. Hong, J. Gao, Y. Yang, H. Zhou, L. Dou, G. Li, Y. Yang, *Sci. Rep.* 2013, 3; J. Roncali, P. Leriche, P. Blanchard, *Advanced Materials* 2014, 26, 3821; J. D. Douglas, M. S. Chen, J. R. Niskala, O. P. Lee, A. T. Yiu, E. P. Young, J. M. J. Fréchet, *Advanced Materials* 2014, 26, 4313; Y. Lin, Y. Li, X. Zhan, *Chemical Society Reviews* 2012, 41, 4245; G. Chen, H. Sasabe, Z. Wang, X.-F. Wang, Z. Hong, Y. Yang, J. Kido, *Advanced Materials* 2012, 24, 2768.
- [2] Y. Sun, G. C. Welch, W. L. Leong, C. J. Takacs, G. C. Bazan, A. J. Heeger, *Nat Mater* 2012, 11, 44.
- [3] T. S. van der Poll, J. A. Love, T. Q. Nguyen, G. C. Bazan, *Adv Mater* 2012, 24, 3646.
- [4] W. Ma, C. Yang, X. Gong, K. Lee, A. J. Heeger, *Advanced Functional Materials* 2005, 15, 1617.
- [5] G. Li, V. Shrotriya, J. Huang, Y. Yao, T. Moriarty, K. Emery, Y. Yang, *Nature Materials* 2005, 4, 864; G. Wei, S. Wang, K. Sun, M. E. Thompson, S. R. Forrest, *Advanced Energy Materials* 2011, 1, 184; H. Chen, S. Hu, H. Zang, B. Hu, M. Dadmun, *Advanced Functional Materials* 2013, 23, 1701.
- [6] J. Peet, J. Y. Kim, N. E. Coates, W. L. Ma, D. Moses, A. J. Heeger, G. C. Bazan, *Nature Materials* 2007, 6, 497; L. G. Kaake, G. C. Welch, D. Moses, G. C. Bazan, A. J. Heeger, *J Phys Chem Lett* 2012, 3, 1253.
- [7] J. T. Rogers, K. Schmidt, M. F. Toney, E. J. Kramer, G. C. Bazan, *Adv. Mater.* 2011, 23, 2284.

- [8] T. Salim, L. H. Wong, B. Brauer, R. Kukreja, Y. L. Foo, Z. N. Bao, Y. M. Lam, *Journal of Materials Chemistry* 2011, 21, 242.
- [9] J. S. Moon, C. J. Takacs, S. Cho, R. C. Coffin, H. Kim, G. C. Bazan, A. J. Heeger, *Nano Letters* 2010, 10, 4005; H.-Y. Chen, H. Yang, G. Yang, S. Sista, R. Zadayan, G. Li, Y. Yang, *The Journal of Physical Chemistry C* 2009, 113, 7946.
- [10] S. R. Cowan, A. Roy, A. J. Heeger, *Physical Review B* 2010, 82, 245207.
- [11] C. M. Proctor, S. Albrecht, M. Kuik, D. Neher, T. Q. Nguyen, *Advanced Energy Materials* 2014, 4, n/a.
- [12] S. Albrecht, W. Schindler, J. Kurpiers, J. Kniepert, J. C. Blakesley, I. Dumsch, S. Allard, K. Fostiropoulos, U. Scherf, D. Neher, *J Phys Chem Lett* 2012, 3, 640.
- [13] B. A. Collins, E. Gann, L. Guignard, X. He, C. R. McNeill, H. Ade, *The Journal of Physical Chemistry Letters* 2010, 1, 3160; B. A. Collins, J. R. Tumbleston, H. Ade, *J Phys Chem Lett* 2011, 2, 3135; N. D. Treat, M. A. Brady, G. Smith, M. F. Toney, E. J. Kramer, C. J. Hawker, M. L. Chabynec, *Adv. Energy Mater.* 2011, 1, 82; N. D. Treat, A. Varotto, C. J. Takacs, N. Batara, M. Al-Hashimi, M. J. Heeney, A. J. Heeger, F. Wudl, C. J. Hawker, M. L. Chabynec, *J. Am. Chem. Soc.* 2012, 134, 15869; A. C. Mayer, M. F. Toney, S. R. Scully, J. Rivnay, C. J. Brabec, M. Scharber, M. Koppe, M. Heeney, I. McCulloch, M. D. McGehee, *Advanced Functional Materials* 2009, 19, 1173; D. Chen, A. Nakahara, D. Wei, D. Nordlund, T. P. Russell, *Nano Letters* 2010, 11, 561; D. Chen, F. Liu, C. Wang, A. Nakahara, T. P. Russell, *Nano Letters* 2011, 11, 2071; H. Chen, J. Peet, S. Hu, J. Azoulay, G. Bazan, M. Dadmun, *Advanced Functional Materials* 2014, 24, 140.
- [14] W. Ma, J. R. Tumbleston, M. Wang, E. Gann, F. Huang, H. Ade, *Advanced Energy Materials* 2013, 3, 864.
- [15] T. M. Burke, M. D. McGehee, *Advanced Materials* 2014, 26, 1923; E. Buchaca-Domingo, A. J. Ferguson, F. C. Jamieson, T. McCarthy-Ward, S. Shoaee, J. R. Tumbleston, O. G. Reid, L. Yu, M. B. Madec, M. Pfannmöller, F. Hermerschmidt, R. R. Schröder, S. E. Watkins, N. Kopidakis, G. Portale, A. Amassian, M. Heeney, H. Ade, G. Rumbles, J. R. Durrant, N. Stingelin, *Materials Horizons* 2014, 1, 270; F. C. Jamieson, E. B. Domingo, T. McCarthy-Ward, M. Heeney, N. Stingelin, J. R. Durrant, *Chemical Science* 2012, 3, 485.
- [16] B. P. Lyons, N. Clarke, C. Groves, *Energy Environ. Sci.* 2012, 5, 7657.
- [17] W. Ma, J. R. Tumbleston, L. Ye, C. Wang, J. Hou, H. Ade, *Adv Mater* 2014, 26, 4234.
- [18] J. A. Bartelt, Z. M. Beiley, E. T. Hoke, W. R. Mateker, J. D. Douglas, B. A. Collins, J. R. Tumbleston, K. R. Graham, A. Amassian, H. Ade, J. M. J. Fréchet, M. F. Toney, M. D. McGehee, *Advanced Energy Materials* 2013, 3, 364; S. Albrecht, W. Schindler, J. Kurpiers, J. Kniepert, J. C. Blakesley, I. Dumsch, S. Allard, K. Fostiropoulos, U. Scherf, D. Neher, *J. Phys. Chem. Lett.* 2012, 3, 640.
- [19] B. A. Collins, Z. Li, J. R. Tumbleston, E. Gann, C. R. McNeill, H. Ade, *Adv. Energy Mater.* 2013, 3, 65.
- [20] S. Albrecht, K. Vandewal, J. R. Tumbleston, F. S. Fischer, J. D. Douglas, J. M. Fréchet, S. Ludwigs, H. Ade, A. Salleo, D. Neher, *Adv Mater* 2014, 26, 2533; W. Ma, L. Ye, S. Q. Zhang, J. H. Hou, H. Ade, *Journal of Materials Chemistry C* 2013, 1, 5023.
- [21] J. A. Love, C. M. Proctor, J. Liu, C. J. Takacs, A. Sharenko, T. S. van der Poll, A. J. Heeger, G. C. Bazan, T.-Q. Nguyen, *Advanced Functional Materials* 2013, 23, 5019.

- [22] A. K. K. Kyaw, D. H. Wang, C. Luo, Y. Cao, T. Q. Nguyen, G. C. Bazan, A. J. Heeger, *Advanced Energy Materials* 2014, 4, n/a.
- [23] C. M. Proctor, M. Kuik, T. Q. Nguyen, *Progress in Polymer Science* 2013, 38, 1941; R. Mauer, I. A. Howard, F. Laquai, *J Phys Chem Lett* 2010, 1, 3500.
- [24] C. M. Proctor, C. Kim, D. Neher, T. Q. Nguyen, *Advanced Functional Materials* 2013, 23, 3584.
- [25] M. A. Lampert, P. Mark, *Current Injection in Solids*, Academic Press, New York, 1970.
- [26] C. M. Proctor, J. A. Love, T. Q. Nguyen, *Adv Mater* 2014, 10.1002/adma.201401725, n/a.
- [27] N. Stribeck, *X-Ray Scattering of Soft Matter* Springer, Berlin, Berlin 2007.
- [28] B. A. Collins, J. E. Cochran, H. Yan, E. Gann, C. Hub, R. Fink, C. Wang, T. Schuettfort, C. R. McNeill, M. L. Chabiny, H. Ade, *Nat. Mater.* 2012, 11, 536.
- [29] J. R. Tumbleston, B. A. Collins, L. Q. Yang, A. C. Stuart, E. Gann, W. Ma, W. You, H. Ade, *Nat Photonics* 2014, 8, 385.
- [30] L. A. Perez, K. W. Chou, J. A. Love, T. S. van der Poll, D.-M. Smilgies, T.-Q. Nguyen, E. J. Kramer, A. Amassian, G. C. Bazan, *Advanced Materials* 2013, 25, 6380.
- [31] B. P. Rand, D. Cheyng, K. Vasseur, N. C. Giebink, S. Mothy, Y. Yi, V. Coropceanu, D. Beljonne, J. Cornil, J.-L. Brédas, J. Genoe, *Adv. Funct. Mater.* 2012, 22, 2987.
- [32] M. A. Brady, G. M. Su, M. L. Chabiny, *Soft Matter* 2011, 7, 11065.
- [33] S. V. Kesava, Z. Fei, A. D. Rimshaw, C. Wang, A. Hexemer, J. B. Asbury, M. Heeney, E. D. Gomez, *Advanced Energy Materials* 2014, 4, n/a.
- [34] D.-M. Smilgies, *Journal of Applied Crystallography* 2009, 42, 1030.
- [35] J. Rivnay, S. C. B. Mannsfeld, C. E. Miller, A. Salleo, M. F. Toney, *Chem. Rev.* 2012, 112, 5488.
- [36] R. M. Beal, A. Stavrinadis, J. H. Warner, J. M. Smith, H. E. Assender, A. A. R. Watt, *Macromolecules* 2010, 43, 2343; K. Vandewal, K. Tvingstedt, A. Gadisa, O. Inganas, J. V. Manca, *Nat. Mater.* 2009, 8, 904; D. R. Kozub, K. Vakhshouri, L. M. Orme, C. Wang, A. Hexemer, E. D. Gomez, *Macromolecules* 2011, 44, 5722; M. A. Ruderer, S. Guo, R. Meier, H. Y. Chiang, V. Korstgens, J. Wiedersich, J. Perlich, S. V. Roth, P. Muller-Buschbaum, *Adv. Funct. Mater.* 2011, 21, 3382.
- [37] R. Steyrlleuthner, R. Di Pietro, B. A. Collins, F. Polzer, S. Himmelberger, M. Schubert, Z. Chen, S. Zhang, A. Salleo, H. Ade, A. Facchetti, D. Neher, *J Am Chem Soc* 2014, 136, 4245.
- [38] D. Credgington, F. C. Jamieson, B. Walker, T.-Q. Nguyen, J. R. Durrant, *Advanced Materials* 2012, 24, 2135.
- [39] E. Gann, A. Young, B. A. Collins, H. Yan, J. Nasiatka, H. A. Padmore, H. Ade, A. Hexemer, C. Wang, *Rev. Sci. Instrum.* 2012, 83, 045110.
- [40] A. Hexemer, W. Bras, J. Glossinger, E. Schaible, E. Gann, R. Kirian, A. MacDowell, M. Church, B. Rude, H. Padmore, *J Phys Conf Ser* 2010, 247, 012007.
- [41] A. L. D. Kilcoyne, T. Tyliczszak, W. F. Steele, S. Fakra, P. Hitchcock, K. Franck, E. Anderson, B. Harteneck, E. G. Rightor, G. E. Mitchell, A. P. Hitchcock, L. Yang, T. Warwick, H. Ade, *Journal of Synchrotron Radiation* 2003, 10, 125.
- [42] T. Coffey, S. G. Urquhart, H. Ade, *J. Electron Spectrosc. Relat. Phenom* 2002, 122, 65.

## Chapter VI

### Mobility Guidelines for High Fill Factor Solution-Processed Small Molecule Solar Cells

#### 1. The Story

Solution processed small molecule-based bulk heterojunction (SSM BHJ) solar cells have shown remarkable progress in recent years with power conversion efficiencies (PCEs) exceeding 8% reported for a variety of molecular architectures.<sup>1,2</sup> The rise in efficiency from the previous PCE record of ~4% first reported in 2009,<sup>3</sup> can largely be attributed to a significant increase in device fill factor ( $FF$ ). Initial reports of SSM BHJ solar cells typically showed  $FFs < 45\%$ .<sup>4</sup> Since then SSM BHJ solar cells with  $FFs > 65\%$  have become commonplace.<sup>1,5-8</sup> This rise in  $FF$  has likely also contributed to the rise in reported short circuit currents ( $J_{sc}$ ) as the same loss mechanisms that limit  $FF$  are also known to limit  $J_{sc}$ .<sup>9,10</sup> Despite this progress, the underlying factors that have enabled recently reported SSM BHJ solar cells to achieve high  $FFs$  are not well understood.

It has been shown that similar to polymer based BHJ photovoltaics,<sup>11,12</sup> the  $FF$  in SSM solar cells can be influenced by a variety of factors including choice of electrodes,<sup>13</sup> field dependent generation (geminate recombination),<sup>10,14</sup> and the competition between nongeminate recombination and charge collection.<sup>9</sup> While contact issues and field dependent generation can in some cases be overcome, all organic photovoltaic devices are subject to losses due to nongeminate recombination. However, it has been suggested that the influence of nongeminate recombination on  $FF$  in particular can be mitigated if the charge carrier mobilities (hole and electron) are sufficiently high and balanced.<sup>9,15-17</sup> This follows from

work that has shown that if charge carrier mobilities are extremely unbalanced the photocurrent may become limited by a build-up of space charge<sup>15</sup>. While other work has shown that if charge carrier mobilities are too low, bimolecular recombination may compete favorably with the collection of photogenerated charge carrier at the electrodes<sup>9,16</sup>. Nonetheless, an empirical determination of how high and balanced hole and electron mobilities should be for efficient solar cell performance has not clearly emerged to date. Furthermore, despite the demonstrated importance of charge carrier mobilities, few studies have considered what determines the upper limit of charge carrier mobilities in blend films of solution processed small molecules.

In this study, we report on the relationship between SSM BHJ solar cell *FF* and experimentally measured hole and electron mobilities across a range of molecular donor material systems (**Figure 6.1**) using phenyl-C71-butyric acid methyl ester (PC<sub>71</sub>BM) as the electron acceptor. The relationship between mobilities measured in neat films (films with only the donor molecule) and blend films (films with donor molecule and PC<sub>71</sub>BM) is also explored thereby illustrating the utility of neat film mobility measurements. Molecules **1-4** were first presented by Kim et. al<sup>18</sup> with subsequent solar cell performance reported more recently.<sup>19</sup> The other diketopyrrolopyrrole (DPP) based molecules **5**, **6**, **7**, and **11** were reported in references <sup>3,5,20,21</sup> respectively. The oligothiophene based molecule **8** was reported by Zhou et. al<sup>22</sup> while the 5-fluorobenzo[c][1,2,5]thiadiazole (FBT) containing molecules, **9** and **10**, were first described in references <sup>6,8</sup>. Together these DPP, oligothiophene and FBT based materials represent three of the most successful and well-studied classes of solution processable molecular donors used in SSM BHJ solar cells. This diverse set of materials has yielded a large range in solar cell device performance with PCEs

from 1% to 8%, *FF*s from 30% up to 70%, and hole and electron mobilities that vary over three orders of magnitude. The performance of the individual molecular systems varies widely with processing conditions and donor-acceptor blend ratio as well. Thus, this set of materials is ideal for exploring systematic trends and relationships that govern solar cell device performance.

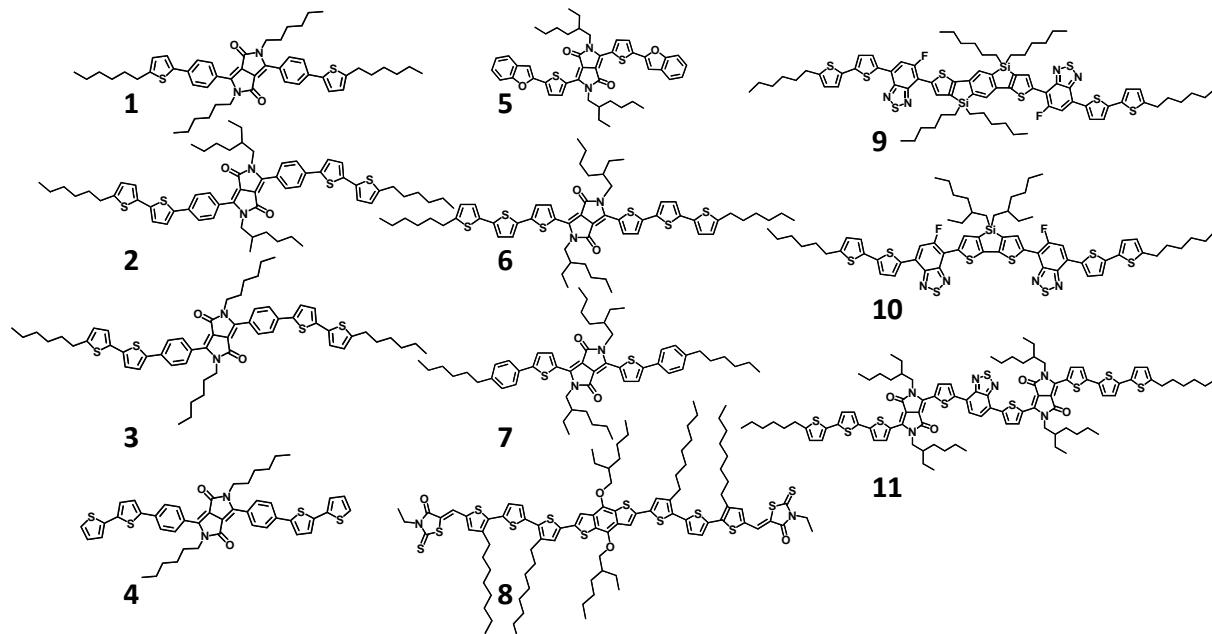


**Figure 6.1:** Donor molecules included in this study.

In order to understand the relationship between charge carrier mobilities and *FF* in SSM solar cell devices, the hole and electron mobilities for blend films using molecules **1-11** as the donor materials and PC<sub>71</sub>BM as the acceptor were compiled from a combination of previously reported results and new experimental data (see Supplementary Information Table S1). In all cases, the mobility values were extracted from the current-voltage curves of single carrier diodes following the Mott-Gurney Law for space charge limited current (SCLC).<sup>23</sup> Careful attention was taken to ensure that all mobility fits were conducted appropriately as mobility values extracted from single carrier diodes can be severely

distorted by leakage currents and improper fits.<sup>24</sup> **Figure 6.2a** shows a 3-dimensional plot of hole and electron mobilities measured in blend films versus the  $FF$  measured in solar cell devices using the same processing conditions as those of single-carrier diodes (spheres). The open symbols represent the 2-dimensional projection of the data for hole mobility vs  $FF$  (red circles) and electron mobility vs  $FF$  (green circles). The data set includes devices processed with a large range of donor-acceptor blend ratios and processing conditions including thermal annealing and solvent additives (see Table S1). All solar cell devices were measured under AM1.5 illumination and solar cell active layer thicknesses were approximately  $100 \text{ nm} \pm 10 \text{ nm}$ .

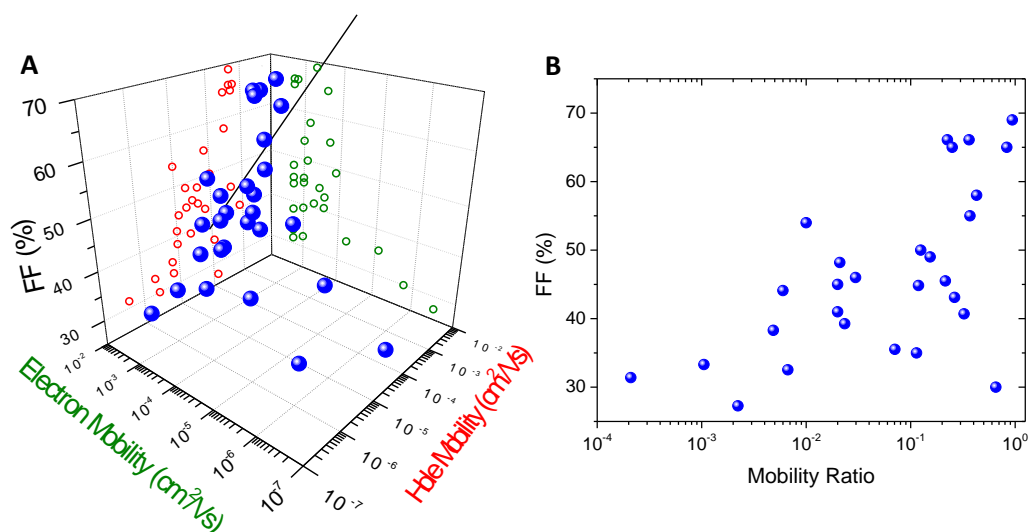


**Figure 6.2:** A) 3-dimensional plot of hole and electron mobilities measured in blend films versus the  $FF$  measured in solar cell devices using the same processing conditions for the blend film. The open symbols represent the 2-dimensional projection of the data for hole mobility vs  $FF$  (red) and electron mobility vs  $FF$  (green). The lines connecting the open symbols to the black spheres are meant as guide for the eyes to help illustrate the 3-dimensional positioning of each data point. B) Mobility ratio, defined as the ratio of the slowest carrier mobility to the fastest carrier mobility, calculated from the data in (A) versus the corresponding  $FF$ .

There are several interesting trends observable in Figure 6.2a. Perhaps most noteworthy is that there are no data points with  $FF > 65\%$  where either the hole or electron

mobility is less than  $\sim 2 \times 10^{-4} \text{ cm}^2/\text{Vs}$ . That this holds true across such a wide range of material systems and processing conditions, suggests that  $10^{-4} \text{ cm}^2/\text{Vs}$  could be considered as a general requirement for the minimum mobility needed for high  $FF$  in a SSM BHJ device with an active layer thickness ca. 100 nm. This threshold mobility and indeed the general trend of mobility vs.  $FF$  agree well with the results of drift-diffusion simulations<sup>17,25,26</sup> and is consistent with reports on polymer based photovoltaics<sup>11,15,16</sup> which typically have high  $FF$ s and charge carrier mobilities  $> 10^{-4} \text{ cm}^2/\text{Vs}$ .

This minimum mobility is most likely a consequence of the fact that the charge carrier sweep-out time is inversely proportional to mobility and internal electric field<sup>27</sup>. As explained by Mandoc et al., for lower mobilities the longer sweep out time leads to a higher equilibrium carrier density in the polymer device.<sup>26</sup> This effect is compounded by the fact that the (nongeminate) recombination coefficient is directly proportional to mobility and therefore reduces as mobility decreases. The effect of the reduced recombination coefficient on the net recombination loss is, however, overshadowed by the fact that the recombination rate scales quadratically with carrier density. The net loss due to the recombination of free carriers is therefore strongly enhanced in lower mobility systems. This in turn is reflected in the  $FF$  because as a forward bias is applied, the carrier density increases further due to the reduced internal field and increasingly more charge carriers recombine.

At the same time, high mobility alone, evidently, does not automatically yield high  $FF$  as there are a few data points in Figure 6.2a with relatively high mobilities that still have low  $FF$ . It may be that the  $FF$  of such systems is primarily limited by a loss mechanism other than bimolecular recombination such as voltage dependent geminate recombination which has been shown to limit the  $FF$  of some SSM BHJ solar cells.<sup>10,14</sup> Variations in the kinetics

of bimolecular recombination between different SSM systems may also be a contributing factor<sup>9,10,28</sup>.

In addition to suggesting minimum mobility requirements, the data from Figure 6.2a clarifies the importance of having balanced charge carrier mobilities. To clearly illustrate this, the mobility ratio for each data point, defined as the ratio of the slower carrier mobility to the faster carrier mobility, was calculated and plotted versus the corresponding  $FF$  (**Figure 6.2b**). All observed systems with  $FF > 65\%$  have a mobility ratio  $> 0.1$  meaning that the hole and electron mobilities are balanced within one order of magnitude. This trend agrees well with simulations and is expected to become even more pronounced as film thickness increases.<sup>29,30</sup> Establishing balanced mobilities by itself however is not sufficient for achieving high  $FF$  as is clearly illustrated by the many data points with balanced mobilities but low  $FF$ . Most of these points can be attributed to cases where the mobilities were balanced but less than  $10^{-4} \text{ cm}^2/\text{Vs}$ . Thus, it stands to reason that in the case of new materials for SSM BHJ solar cells the focus should be on establishing relatively high mobilities  $> 10^{-4} \text{ cm}^2/\text{Vs}$  rather than simply balancing mobilities.

Further analysis of this data set offers some insight into how such high mobilities can be achieved. Close inspection of Figure 6.2a reveals that for the systems considered here, the electron mobility was primarily the faster carrier mobility. Measured blend film electron mobilities were typically  $\sim 10^{-3} \text{ cm}^2/\text{Vs}$  which is consistent with the high electron mobility of pristine fullerene films.<sup>31,32</sup> Exceptions are mostly attributable to blend films with low PCBM content and/or films lacking adequate phase separation.<sup>19,33</sup> In contrast, blend film hole mobilities were more or less evenly distributed across over three orders of magnitude ranging as low as  $\sim 4 \times 10^{-7} \text{ cm}^2/\text{Vs}$ . The measured blend film hole mobilities versus the

corresponding solar cell *FF*s are re-plotted in **Figure 6.3a** for clarity along with a few additional data points (See Table S1). From this data, it is evident that in many SSM BHJ systems the *FF* is limited by relatively poor hole transport properties. This may in part explain why SSM BHJ solar cells were long plagued by low *FF*s<sup>4</sup> before recent advances in molecular design and device fabrication techniques started to yield SSM BHJ devices with high blend film hole mobility and thus high *FF*.<sup>1,5-8</sup>

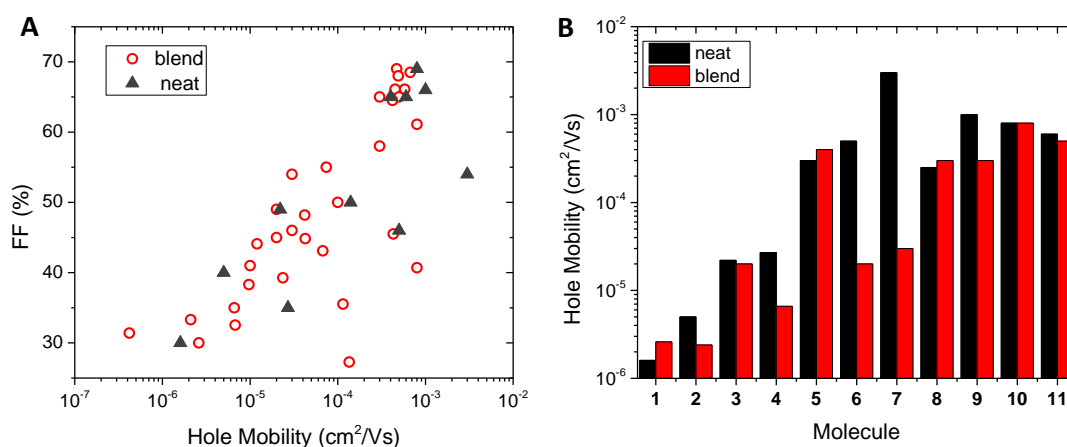


**Figure 6.3:** A) Blend film hole mobility (red open circles) vs. *FF* measured in corresponding blend film solar cell and neat film hole mobility (dark triangles) vs. maximum *FF* obtained in a solar cell using that material as the electron donor and PC<sub>71</sub>BM as the acceptor. B) Neat film hole mobility and blend film hole mobility measured in the device with the best *FF* for each molecule from Figure 1.

To better understand the origins of low blend film hole mobilities, the neat film hole mobilities for molecules **1-11** are plotted versus the highest reported *FF* achieved for a SSM BHJ solar cell using the same material as the electron-donor (triangles, Figure 6.3a). Interestingly, the neat film hole mobilities show a similar relation with *FF* as the blend film mobilities. All donor materials that yield high *FF* solar cell devices appear to have a neat film hole mobility  $> 2 \times 10^{-4} \text{ cm}^2/\text{Vs}$ . The relation between neat film hole mobility and blend

film hole mobility for molecules **1-11** is presented in Figure 6.3b. The blend film hole mobilities correspond to the film conditions that achieved the highest  $FF$  in a SSM BHJ solar cell. For all compounds the neat film mobility is approximately equal to or greater than the blend film mobility. This finding for solution processable small molecules is in stark contrast to amorphous and low band gap conjugated polymers that exhibit significantly higher hole mobility when blended with PCBM compared to neat films.<sup>34-36</sup> That the SSM neat film mobility is roughly the upper limit for SSM blend film mobility explains the trend of neat mobility versus peak  $FF$  (Figure 6.3a) as only materials with high neat film mobility are able to achieve high hole mobility in the blend film. The implication of this is that neat film mobility measurements could be used as a screening tool for testing the viability of newly synthesized materials for use in SSM BHJ solar cells. Such screening may also have the added benefit of detecting materials with chemical impurities that act as traps<sup>37,38</sup> and identifying optimal electrodes for a given material.<sup>39</sup>

Having established the importance of neat and blend film mobilities, we now consider lessons learned from molecules **1-11** about molecular design guidelines for high mobility donor materials. As can be seen in Figure 6.3a, molecules **1-4** have the poorest hole transport properties of the materials considered here. This can be understood by looking at the single crystal structures for each of these materials which shows that they have a nonplanar conformation due to the steric hindrance of the phenyl groups adjacent to the DPP core.<sup>18</sup> In the case of **1-4**, evidently neither alterations to the solubilizing groups nor changes in the number of thiophene units are able to overcome the hindrance to charge transport created by the nonplanar conformation. In contrast, molecules **5**, **6** and **9** are known to be planar<sup>19,40,41</sup> while the same is expected of **7**, **8**, **10** and **11**; all of these molecules manage

hole mobilities  $> 10^{-4}$  cm<sup>2</sup>/Vs in the neat film. A strong correlation between neat film mobility and planarity was also observed in a study that considered the effect of heteroatom substitution on molecule **5**<sup>40</sup>. It's worth noting that in each case x-ray scattering techniques have found that the thin film crystal structure is the same as the single crystal structure<sup>18,19,40,41</sup>. Furthermore, other high *FF* SSM systems have also been achieved by specifically targeting planar compounds.<sup>42,43</sup>

While planarity is strongly correlated with high neat film hole mobility, it is clearly not the only requisite for achieving high blend film mobility. It has been shown that blend film mobilities depend strongly on different acceptors,<sup>4,44</sup> the ratio of donor to acceptor<sup>3,41</sup> and the blend film morphology.<sup>6,10,28,33</sup> As seen in Figure 6.3b, molecules **5** and **6** exhibit a tremendous drop in hole mobility when going from neat film to a blend film with PC<sub>71</sub>BM. This may be attributable to the disruption of order in the donor phase and/or a loss of continuous hole transport pathways in the blend films. Indeed, the effect of processing conditions, including both thermal treatment and the use of solvent additives, on blend film mobility of **5**:PC<sub>71</sub>BM and **10**:PC<sub>71</sub>BM suggests that maintaining crystallinity of the donor material in the blend film is essential to achieving mobilities near that of the neat film.<sup>10,28,33,41</sup> The effect of thermal processing on neat film hole mobility measurements hints at the importance of crystallinity to efficient hole transport as well (see Figure S6.1). In the case of blend films, in addition ordering the hole transport phase, crystallization of donor material may also drive phase separation which is beneficial for charge transport of both holes and electrons.<sup>33</sup>

It is interesting to note, that with the exception of **5**, the compounds that manage the highest mobilities in both the blend and neat film, **8-11**, are relatively large with molecular

weights exceeding 1200 Da while molecules **1-7** are all less than 1000 Da. Recent reports of other efficient SSM BHJ solar cells have also tended towards larger molecules.<sup>1,7,45</sup> It may be that the larger size helps to maintain structural order and/or continuous hole transport pathways in the blend film. With that said, considering that larger, more complex materials generally require costlier synthetic procedures,<sup>46</sup> there exists compelling motivation to develop materials that are both easy to synthesize and able to perform well in SSM BHJ solar cells. Developing a deeper understanding of the factors that govern charge transport in blend films may help achieve that goal. This will be the subject of future research.

In conclusion, experimentally measured hole and electron mobilities and the corresponding solar cell *FFs* for a large variety of solution processable small molecule bulk heterojunction solar cell systems were analyzed. Altogether this data suggests that in order to achieve high *FF* (> 65%) in SSM BHJ solar cells, both hole and electron mobilities must be greater than  $10^{-4}$  cm<sup>2</sup>/Vs. Achieving such high mobilities was found to be more important to high *FF* than establishing hole and electron mobilities that were balanced but less than  $10^{-4}$  cm<sup>2</sup>/Vs. In most SSM BHJ devices with low *FF*, it was found that at least one carrier, most often the hole, had a relatively low mobility of less than  $10^{-4}$  cm<sup>2</sup>/Vs. In contrast to amorphous polymer systems, neat film hole mobility values for a given molecule were generally found to set the upper limit of blend film hole mobilities. Thus, neat film mobility measurements may prove a useful tool for screening potential materials intended for SSM solar cells. Though we focus here on molecular donors, these results may also have implications for the development of new polymers and electron accepting materials for organic photovoltaics. Based on these findings, we conclude that in addition to tuning the

optical absorption and energy levels, future design of materials for SSM BHJ solar cells should aim to establish charge carrier mobilities of at least  $10^{-4} \text{ cm}^2/\text{Vs}$ .

## **2. Experimental Section**

*Single Carrier Diodes:* Hole only devices were fabricated using a structure of ITO/PEDOT:PSS/active layer/Au for molecules **5-11**. For molecules **1-4** thermally evaporated MoOx was used instead of PEDOT:PSS in order to provide better energetic alignment with the HOMO energy level. Electron only devices were fabricated using a device of Al/active layer/Ca/Al unless otherwise specified in referenced work. The film processing conditions for the active layers are detailed in the Supporting Information.

## **3. Supporting Information**

Molecule	Blend Ratio	Solvent	Annealing Temp (°C)	Electron Mobility (cm <sup>2</sup> /Vs)	Hole Mobility (cm <sup>2</sup> /Vs)	FF (%)	Reference or SI Figure
1	1:0	CHCl <sub>3</sub>	-	-	1.6E-06	-	SI Fig 1A
1	3:2	CHCl <sub>3</sub>	-	1.7E-06	2.6E-06	35	Lin et al. <sup>19</sup>
2	1:0	CHCl <sub>3</sub>	-	-	5.0E-06	-	SI Fig 1B
3	1:0	CHCl <sub>3</sub>	-	-	2.2E-05	-	SI Fig 1C
3	3:2	CHCl <sub>3</sub>	80	1.3E-04	2.0E-05	49	Lin et al. <sup>19</sup>
4	1:0	CHCl <sub>3</sub>	80	-	2.7E-05	-	SI Fig 1D
4	1:4	CHCl <sub>3</sub>	80	5.8E-05	6.6E-06	30	Lin et al. <sup>19</sup>
5	1:0	CHCl <sub>3</sub>	100	-	3.4E-04	-	SI Fig 1E
5	3:2	CHCl <sub>3</sub>	110	8.0E-04	4.0E-04	50	Zalar et al. <sup>28</sup>
6	1:0	CHCl <sub>3</sub>	80	-	5.0E-04	-	SI Fig 1F
6	9:1	CHCl <sub>3</sub>	80	3.0E-07	1.4E-04	27	SI Fig 2A, 3A
6	4:1	CHCl <sub>3</sub>	80	8.1E-06	1.2E-04	36	SI Fig 2B, 3B
6	7:3	CHCl <sub>3</sub>	80	2.6E-04	6.8E-05	43	SI Fig 2C, 3C
6	3:2	CHCl <sub>3</sub>	80	3.6E-04	4.3E-05	45	SI Fig 2D, 3D
6	1:1	CHCl <sub>3</sub>	80	1.0E-03	2.0E-05	46	Proctor et al. <sup>9</sup>
6	2:3	CHCl <sub>3</sub>	80	1.0E-03*	2.4E-05	39	SI Fig 2E
6	3:7	CHCl <sub>3</sub>	80	1.0E-03	6.8E-06	33	SI Fig 2F, 3E
7	1:0	CHCl <sub>3</sub>	-	-	3.0E-03	-	Shin et al. <sup>21</sup>
7	1:1	CHCl <sub>3</sub>	140	1.0E-03	3.0E-05	54	Shin et al. <sup>21</sup>
8	1:0	CHCl <sub>3</sub>	80	-	2.5E-04	-	SI Fig 1G
8	5:4	CHCl <sub>3</sub> + 0.2 mg/mL PDMS	-	2.5E-04	3.0E-04	65	Zhou et al. <sup>22</sup>
9	1:0	CB	-	-	1.0E-03	-	Love et al. <sup>6</sup>
9	4:1	CB + 0.4% DIO	-	2.6E-04	8.0E-04	41	Love et al. <sup>6</sup>
9	3:2	CB + 0.4% DIO	-	1.6E-03	5.8E-04	64	Love et al. <sup>6</sup>
9	1:1	CB + 0.4% DIO	-	2.0E-03	4.5E-04	67	Love et al. <sup>6</sup>
9	3:7	CB + 0.4% DIO	-	2.0E-03*	4.2E-05	48	Love et al. <sup>6</sup>
9	1:4	CB + 0.4% DIO	-	2.0E-03*	1.2E-05	44	Love et al. <sup>6</sup>
9	4:21	CB + 0.4% DIO	-	2.0E-03*	9.7E-06	38	Love et al. <sup>6</sup>
9	3:22	CB + 0.4% DIO	-	2.0E-03*	2.1E-06	33	Love et al. <sup>6</sup>
9	2:23	CB + 0.4% DIO	-	2.0E-03*	4.2E-07	31	Love et al. <sup>6</sup>
10	1:0	CB	130	-	8.0E-04	-	Zalar et al. <sup>28</sup>
10	7:3	CB + 0.4% DIO	70	-	8.0E-04	61	SI Fig 4A
10	3:2	CB	130	7.0E-04	3.0E-04	58	Proctor et al. <sup>10</sup>
10	3:2	CB	-	5.0E-04	1.0E-05	41	Proctor et al. <sup>10</sup>
10	3:2	CB + 0.4% DIO	70	5.0E-04	4.7E-04	68	Proctor et al. <sup>10</sup>
10	1:1	CB + 0.4% DIO	70	-	6.7E-04	69	SI Fig 4B
10	2:3	CB + 0.4% DIO	70	-	4.9E-04	68	SI Fig 4C
10	3:7	CB + 0.4% DIO	70	-	4.2E-04	65	SI Fig 4D
11	1:0	CHCl <sub>3</sub>	-	-	6.0E-04	-	SI Fig 1H

Table S6.1: Breakdown of data included in Figures 2 and 3 including film processing conditions and blend weight ratio of donor molecule to PC<sub>71</sub>BM. CB stands for chlorobenzene.\*Indicates data extrapolated following the trend of mobility and blend ratio.

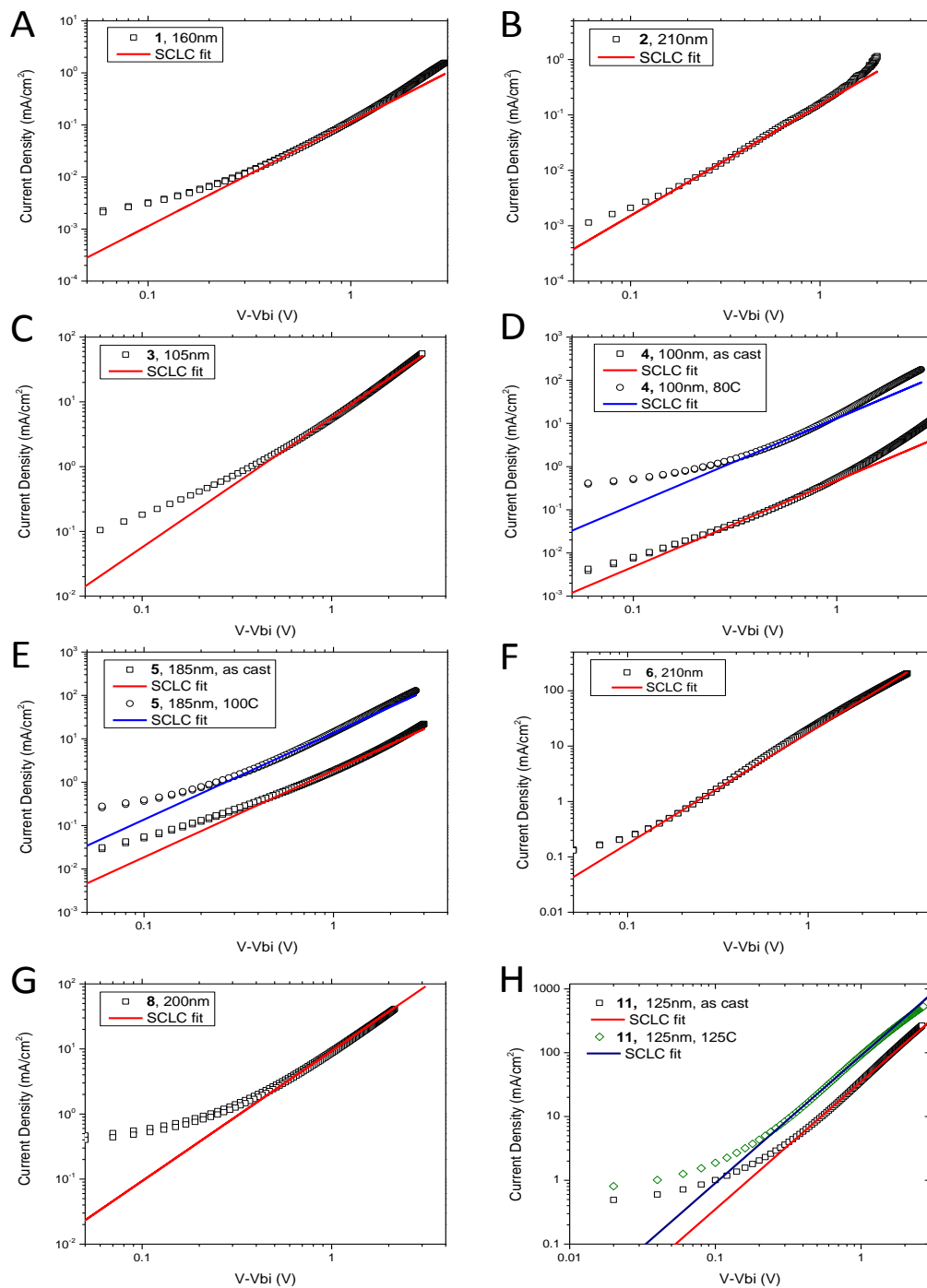


Figure S6.1: JV data (symbols) and fit lines to the Mott-Gurney Law for SCLC for neat film hole-only devices for molecules 1-6, 8 and 11 corresponding to A-H respectively. Film thicknesses are presented in the figure legends.

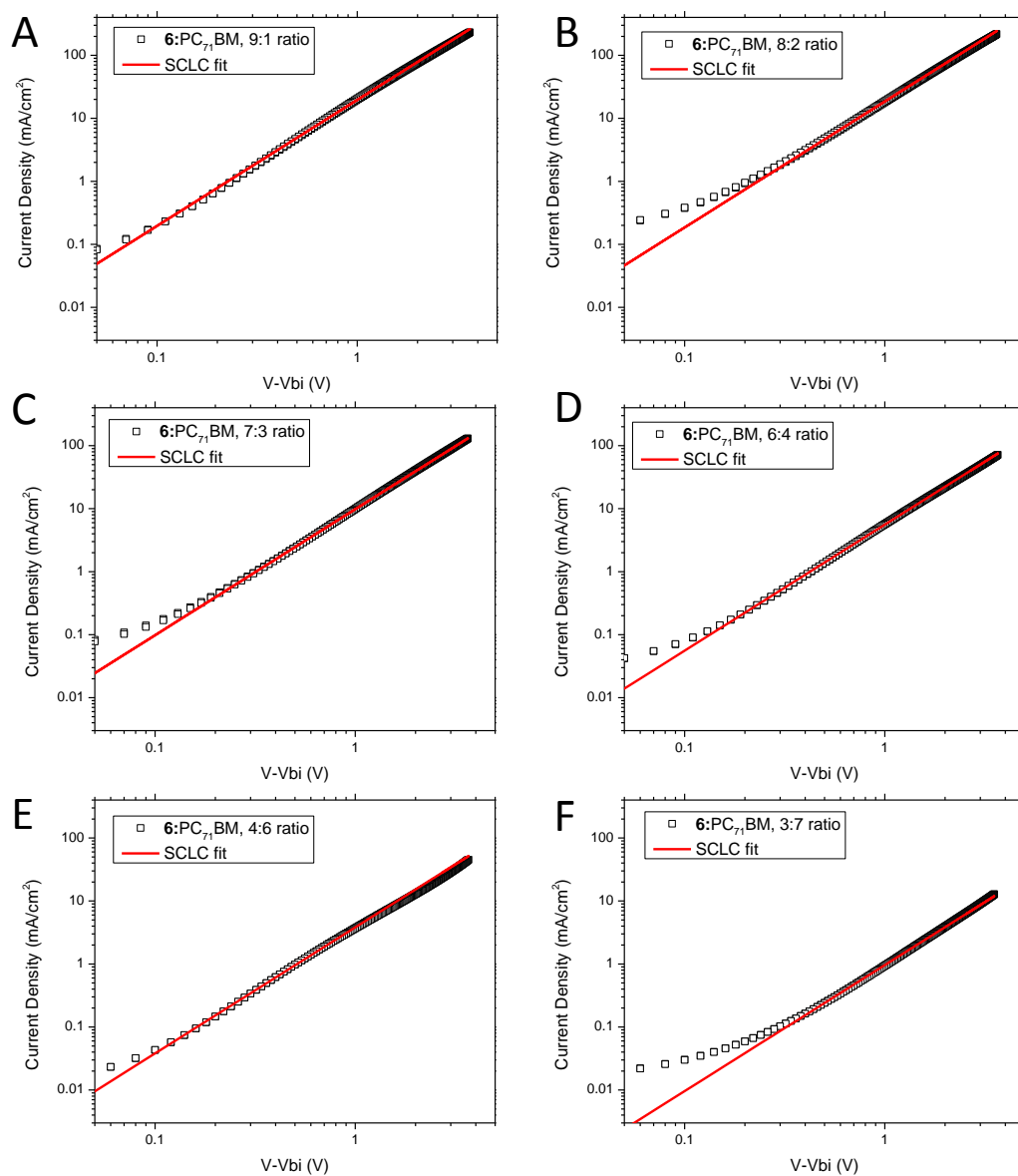


Figure S6.2: JV data (symbols) and fit lines to the Mott-Gurney Law for SCLC measured in hole-only devices with a structure of ITO/PEDOT:PSS/6:PC<sub>71</sub>BM/Au. Film thicknesses ranged from approximately 140-160 nm. Figure legends in A-F indicate the weight ratio of 6 to PC<sub>71</sub>BM for each device.

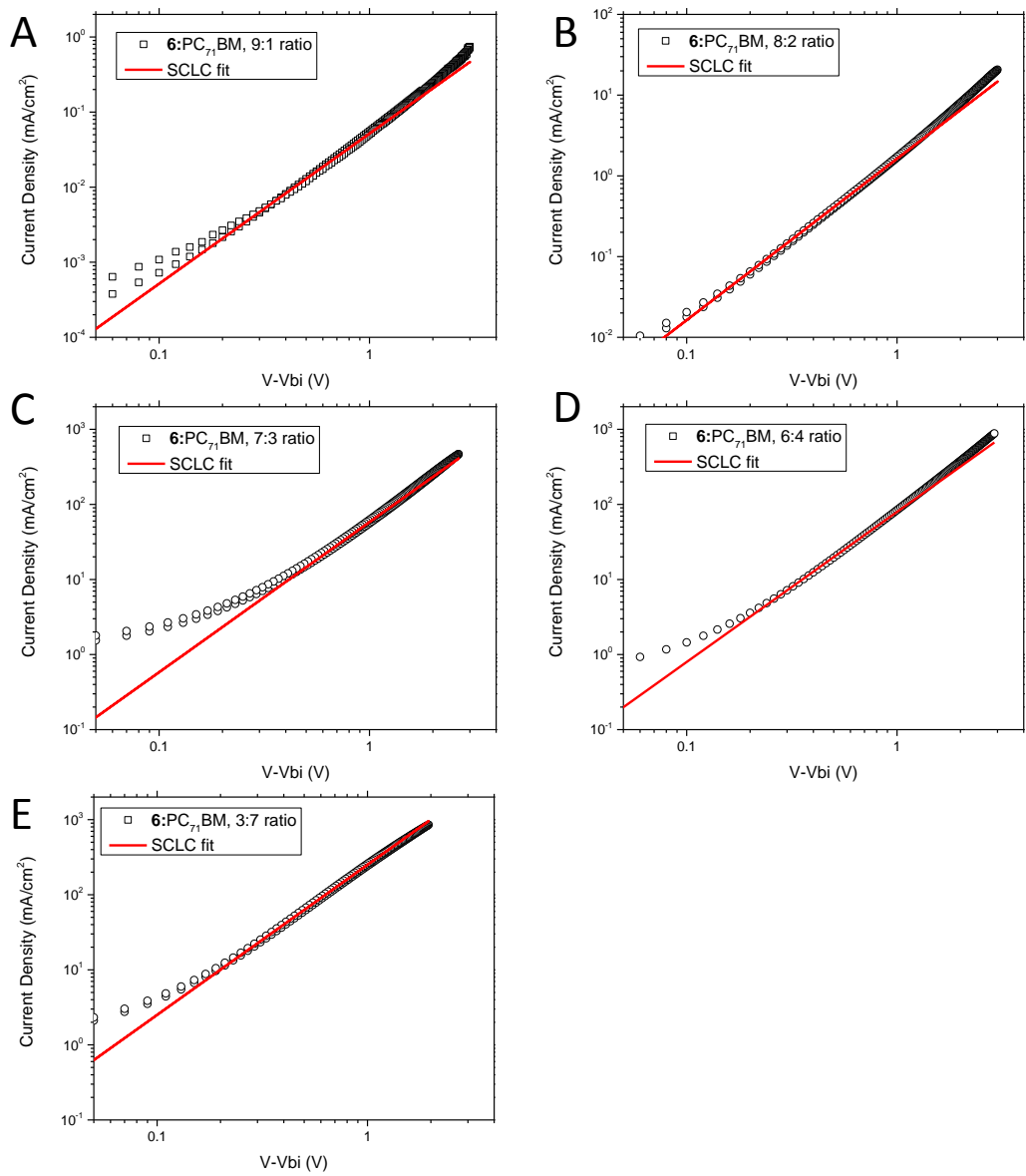


Figure S6.3: JV data (symbols) and fit lines to the Mott-Gurney Law for SCLC measured in electron-only devices with a structure of ITO/Al/6:PC<sub>71</sub>BM/Ca/Al. Film thicknesses ranged from approximately 130-150 nm. Figure legends in A-F indicate the weight ratio of 6 to PC<sub>71</sub>BM for each device.

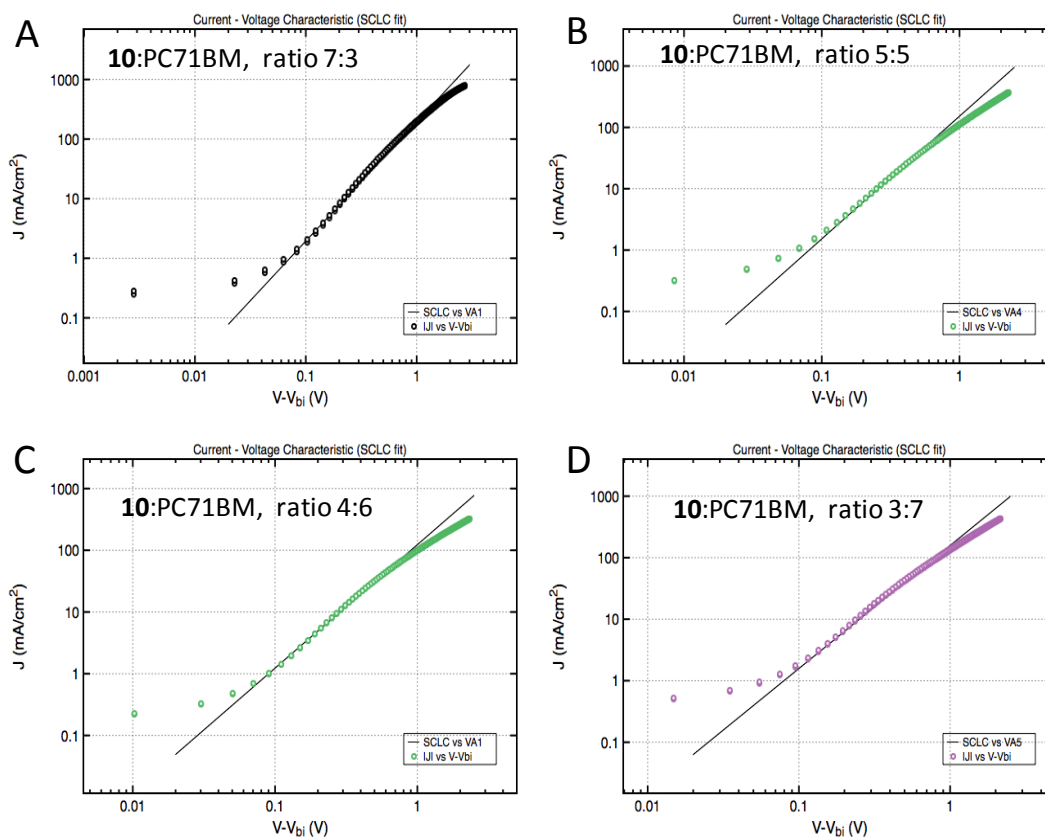


Figure S6.4: JV data (symbols) and fit lines to the Mott-Gurney Law for SCLC measured in hole-only devices with a structure of ITO/PEDOT:PSS/10:PC<sub>71</sub>BM/Au. Film thicknesses were approximately 100 nm. Figure legends in A-D indicate the weight ratio of 10 to PC<sub>71</sub>BM for each device.

#### 4. References

- [1] J. Zhou, Y. Zuo, X. Wan, G. Long, Q. Zhang, W. Ni, Y. Liu, Z. Li, G. He, C. Li, B. Kan, M. Li, Y. Chen, *J. Am. Chem. Soc.* **2013**, *135*, 8484–8487.
- [2] A. K. K. Kyaw, D. H. Wang, D. Wynands, J. Zhang, T.-Q. Nguyen, G. C. Bazan, A. J. Heeger, *Nano Lett.* **2013**, *13*, 3796–3801.
- [3] B. Walker, A. B. Tamayo, X. Dang, P. Zalar, J. H. Seo, A. Garcia, M. Tantiwiwat, T. Nguyen, *Adv. Funct. Mater.* **2009**, *19*, 3063–3069.
- [4] B. Walker, C. Kim, T.-Q. Nguyen, *Chem Mater* **2010**, *23*, 470–482.
- [5] B. Walker, J. Liu, C. Kim, G. C. Welch, J. K. Park, J. Lin, P. Zalar, C. M. Proctor, J. H. Seo, G. C. Bazan, T.-Q. Nguyen, *Energy Environ. Sci.* **2013**, *6*, 952–962.
- [6] J. A. Love, I. Nagao, Y. Huang, M. Kuik, V. Gupta, C. J. Takacs, J. E. Coughlin, L. Qi, T. S. van der Poll, E. J. Kramer, A. J. Heeger, T.-Q. Nguyen, G. C. Bazan, *J. Am. Chem. Soc.* **2014**, *136*, 3597–3606.

- [7] X. Liu, Y. Sun, B. B. Y. Hsu, A. Lorbach, L. Qi, A. J. Heeger, G. C. Bazan, *J. Am. Chem. Soc.* **2014**, DOI:10.1021/ja413144u.
- [8] T. S. Van der Poll, J. A. Love, T.-Q. Nguyen, G. C. Bazan, *Adv. Mater.* **2012**, *24*, 3646–3649.
- [9] C. M. Proctor, C. Kim, D. Neher, T.-Q. Nguyen, *Adv. Funct. Mater.* **2013**, *23*, 3584–3594.
- [10] C. M. Proctor, S. Albrecht, M. Kuik, D. Neher, T.-Q. Nguyen, *Adv. Energy Mater.* **2014**, DOI: 10.1002/aenm.201400230.
- [11] C. M. Proctor, M. Kuik, T.-Q. Nguyen, *Prog. Polym. Sci.* **2013**, *38*, 1941–1960.
- [12] G. Lakhwani, A. Rao, R. H. Friend, *Annu. Rev. Phys. Chem.* **2014**, *65*, 557–581.
- [13] A. Guerrero, S. Loser, G. Garcia-Belmonte, C. J. Bruns, J. Smith, H. Miyauchi, S. I. Stupp, J. Bisquert, T. J. Marks, *Phys. Chem. Chem. Phys.* **2013**, *15*, 16456–16462.
- [14] D. Credgington, F. C. Jamieson, B. Walker, T.-Q. Nguyen, J. R. Durrant, *Adv. Mater.* **2012**, *24*, 2135–2141.
- [15] V. D. Mihailetschi, J. Wildeman, P. W. M. Blom, *Phys. Rev. Lett.* **2005**, *94*, 126602.
- [16] A. Baumann, J. Lorrman, D. Rauh, C. Deibel, V. Dyakonov, *Adv. Mater.* **2012**, *24*, 4381–4386.
- [17] A. Wagenpfahl, C. Deibel, V. Dyakonov, *Sel. Top. Quantum Electron. IEEE J. Of* **2010**, *16*, 1759–1763.
- [18] C. Kim, J. Liu, J. Lin, A. B. Tamayo, B. Walker, G. Wu, T.-Q. Nguyen, *Chem. Mater.* **2012**, *24*, 1699–1709.
- [19] J. D. A. Lin, J. Liu, C. Kim, A. B. Tamayo, C. M. Proctor, T.-Q. T. Nguyen, *RSC Adv.* **2014**, 10.1039/C3RA45662E.
- [20] A. B. Tamayo, X.-D. Dang, B. Walker, J. Seo, T. Kent, T.-Q. Nguyen, *Appl. Phys. Lett.* **2009**, *94*, 103301–103301–3.
- [21] W. Shin, T. Yasuda, G. Watanabe, Y. S. Yang, C. Adachi, *Chem. Mater.* **2013**, *25*, 2549–2556.
- [22] J. Zhou, X. Wan, Y. Liu, Y. Zuo, Z. Li, G. He, G. Long, W. Ni, C. Li, X. Su, Y. Chen, *J. Am. Chem. Soc.* **2012**, *134*, 16345–16351.
- [23] Mott, N. F., Gurney, R. W., *Electronic Processes in Ionic Crystals*, Oxford University Press, **1940**.
- [24] J. C. Blakesley, F. A. Castro, W. Kylberg, G. F. A. Dibb, C. Arantes, R. Valaski, M. Cremona, J. S. Kim, J.-S. Kim, *Org. Electron.* 10.1016/j.orgel.2014.02.008.
- [25] W. Tress, K. Leo, M. Riede, *Phys. Rev. B* **2012**, *85*, 155201.
- [26] M. M. Mandoc, L. J. A. Koster, P. W. M. Blom, *Appl. Phys. Lett.* **2007**, *90*, 133504.
- [27] S. R. Cowan, R. A. Street, S. Cho, A. J. Heeger, *Phys. Rev. B* **2011**, *83*, 035205.
- [28] P. Zalar, M. Kuik, N.A. Ran, J.A. Love, T.Q. Nguyen, *Adv. Energy Mater.* DOI: 10.1002/aenm.201400438.
- [29] J. D. Kotlarski, P. W. M. Blom, *Appl. Phys. Lett.* **2012**, *100*, 013306.
- [30] J. D. Kotlarski, D. J. D. Moet, P. W. M. Blom, *J. Polym. Sci. Part B Polym. Phys.* **2011**, *49*, 708–711.
- [31] V. D. Mihailetschi, J. K. . van Duren, P. W. . Blom, J. C. Hummelen, R. A. . Janssen, J. M. Kroon, M. T. Rispens, W. J. . Verhees, M. M. Wienk, *Adv. Funct. Mater.* **2003**, *13*, 43–46.

- [32] S. M. Tuladhar, D. Poplavskyy, S. A. Choulis, J. R. Durrant, D. D. C. Bradley, J. Nelson, *Adv. Funct. Mater.* **2005**, *15*, 1171–1182.
- [33] A. Sharenko, M. Kuik, M. F. Toney, T.-Q. Nguyen, *Adv. Funct. Mater.* **2014**, DOI 10.1002/adfm.201304100.
- [34] N. C. Cates, R. Gysel, J. E. P. Dahl, A. Sellinger, M. D. McGehee, *Chem. Mater.* **2010**, *22*, 3543–3548.
- [35] K. G. Jespersen, F. Zhang, A. Gadisa, V. Sundström, A. Yartsev, O. Inganäs, *Org. Electron.* **2006**, *7*, 235–242.
- [36] K. R. Choudhury, J. Subbiah, S. Chen, P. M. Beaujuge, C. M. Amb, J. R. Reynolds, F. So, *Sol. Energy Mater. Sol. Cells* **2011**, *95*, 2502–2510.
- [37] P. Mark, W. Helfrich, *J. Appl. Phys.* **2004**, *33*, 205–215.
- [38] M. M. Mandoc, B. de Boer, G. Paasch, P. W. M. Blom, *Phys. Rev. B* **2007**, *75*, 193202.
- [39] R. Steyrlleuthner, M. Schubert, F. Jaiser, J. C. Blakesley, Z. Chen, A. Facchetti, D. Neher, *Adv. Mater.* **2010**, *22*, 2799–2803.
- [40] J. Liu, B. Walker, A. Tamayo, Y. Zhang, T.-Q. Nguyen, *Adv. Funct. Mater.* **2013**, *23*, 47–56.
- [41] J. A. Love, C. M. Proctor, J. Liu, C. J. Takacs, A. Sharenko, T. S. van der Poll, A. J. Heeger, G. C. Bazan, T.-Q. Nguyen, *Adv. Funct. Mater.* **2013**, *23*, 4990–4990.
- [42] O. P. Lee, A. T. Yiu, P. M. Beaujuge, C. H. Woo, T. W. Holcombe, J. E. Millstone, J. D. Douglas, M. S. Chen, J. M. J. Fréchet, *Adv. Mater.* **2011**, *23*, 5359–5363.
- [43] J. Zhou, X. Wan, Y. Liu, G. Long, F. Wang, Z. Li, Y. Zuo, C. Li, Y. Chen, *Chem Mater* **2011**, *23*, 4666–4668.
- [44] A. Sharenko, C. M. Proctor, T. S. van der Poll, Z. B. Henson, T.-Q. Nguyen, G. C. Bazan, *Adv. Mater.* **2013**, *25*, 4403–4406.
- [45] J. Liu, Y. Sun, P. Moonsin, M. Kuik, C. M. Proctor, J. Lin, B. B. Hsu, V. Promarak, A. J. Heeger, T.-Q. Nguyen, *Adv. Mater.* **2013**, *25*, 5898–5903.
- [46] T. P. Osedach, T. L. Andrew, V. Bulović, *Energy Environ. Sci.* **2013**, *6*, 711–718.

## Chapter VII

### Understanding Charge Transport in terms of Order and Percolation in Molecular Blend Films

#### 1. The story

Solution processed small molecule-based bulk heterojunction (SSM BHJ) solar cells have emerged as a promising technology with recent reports of power conversion efficiencies (PCEs) exceeding 9% for a variety of molecular architectures.<sup>1,2</sup> The steady rise in performance of SSM BHJ solar cells has been well documented and is known to largely be a result of improved charge carrier mobility<sup>3</sup>. Indeed, charge carrier mobility has been identified as one of the most critical parameters for continued improvement of both small molecule and polymer based solar cells<sup>4-7</sup>. Despite this progress, the underlying factors that limit the charge carrier mobility in SSM BHJ solar cells have not been explored in detail. Significant improvements in PCE may result from a deeper understanding of charge carrier transport in SSM BHJ solar cells.

Following decades of research into charge transport in organic semiconductors, it is generally understood that charge transport is most efficient when conducting domains are ordered and well connected<sup>8-12</sup>. To this end, multiple studies have qualitatively observed a positive correlation between increased structural order of donor molecules and hole mobility in SSM BHJ films<sup>1,2,13-15</sup>. However, the lack of a quantitative link between structural order and charge carrier mobility makes comparisons between material systems difficult and limits insights about how best to improve materials. A recent report also found that crystallization

of the donor material can drive phase separation in SSM BHJ films thereby enhancing the electron mobility as well - presumably due to enhanced connectivity of electron conducting domains<sup>16</sup>. This concomitant increase of structural order and phase separation complicates efforts to decouple the effects of order and domain connectivity on charge transport. For that reason as well as the difficulty of even qualitative measures of domain connectivity, it is generally unknown how much the connectivity of conductive domains, or lack thereof, limits the charge carrier mobility in SSM BHJ solar cells.

In this communication, we report on the factors limiting charge carrier mobility in blend films consisting of a range of molecular donor material systems (**Figure 7.1a**) using phenyl-C71-butyric acid methyl ester (PC<sub>71</sub>BM) as the electron acceptor. The donor materials considered in this study are 2,5-di-(2-ethylhexyl)-3,6-bis-(5'-n-hexyl-[2,2',5',2'']terthiophen-5-yl)-pyrrolo[3,4-c]pyrrole-1,4-dione (SM2), benzo[1,2-b:4,5-b']bis(4,4'-dihexyl-4H-silolo[3,2-b]thiophene-2,2'-diyl)bis(6-fluoro-4-(5'-hexyl-[2,2'-bithiophene]-5-yl)-benzo[c][1,2,5]thiadiazole (H1) and (7,7'-[4,4-bis(2-ethylhexyl)-4H-silolo[3,2-b:4,5-b']dithiophene-2,6-diyl]bis[6-fluoro-4-(5'-hexyl-[2,2'-bi-thiophene]-5-yl)benzo[c][1,2,5]thiadiazole]) (T1) each of which has been reported on previously with peak OPV power conversion efficiencies ranging from 3% to 7%<sup>17-19</sup>. Previous studies hinted that the charge transport properties of these material systems respond differently to the ratio of donor to acceptor in the blend film with a much greater dependence on donor content observed in SM2:PC<sub>71</sub>BM and H1:PC<sub>71</sub>BM than in T1:PC<sub>71</sub>BM films<sup>3,19</sup>. Here, we delineate the effects of order and domain connectivity on charge carrier mobility by incrementally varying the weight ratio of donor to acceptor. Hole and electron mobilities were determined from the current-voltage response of single-carrier diodes made using blend

films with zero to 100% donor content. As SSM BHJ films are highly sensitive to processing conditions, only the weight ratio of donor to acceptor was varied while the choice of solvent(s) and thermal processing was held constant in accordance with the previously reported recipes for optimal solar cell performance for each material system (see Experimental section). In all cases, the current-voltage response of the single carrier diodes was found to follow the Mott-Gurney law for trap-free space charge limited current allowing for direct assessment of the zero field charge carrier mobility. The measured electron mobilities as a function of donor content are shown in **Figure 7.1b**. All three systems show a similar trend with only modest decrease in electron mobility from 0 to 70% donor followed by a steep drop at higher donor content. This suggests that in the case of small molecule blend films using PC<sub>71</sub>BM as the electron acceptor, the threshold concentration of PC<sub>71</sub>BM for efficient electron transport is ca. 20-30%. This notion is consistent with the fact that virtually all soluble molecular donor materials blended with PC<sub>71</sub>BM to date have optimal solar cell performance at donor concentrations less than 80%<sup>1,2,20-23</sup>.

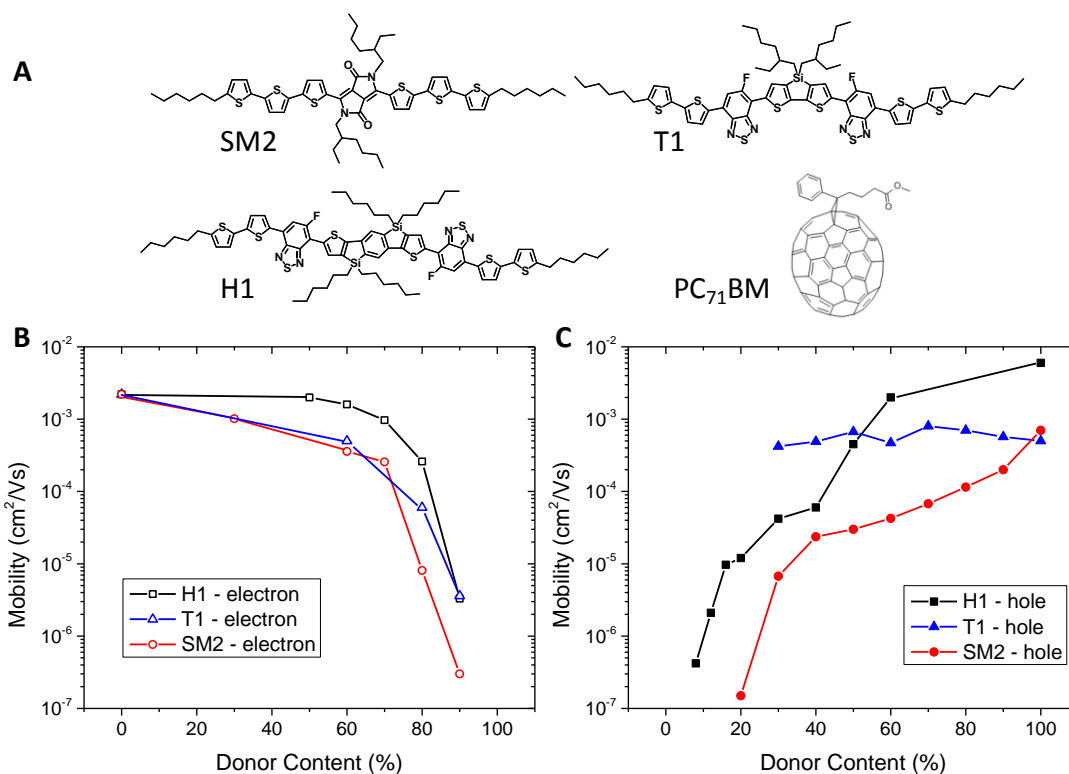


Figure 7.1: A) Chemical structures of materials studied. B) Electron mobility of films containing donor materials H1, T1, or SM2 blended with PC<sub>71</sub>BM as a function of donor content. C) Hole mobility of films containing donor materials H1, T1, or SM2 blended with PC<sub>71</sub>BM as a function of donor content.

The trends in hole mobility as a function of donor concentration, shown in **Figure 7.1c**, are notably different than that of the electron mobilities. In the case of T1:PC<sub>71</sub>BM, the hole mobility is remarkably stable across the entire measurable range of donor concentrations with a value of approximately  $8 \times 10^{-4} \text{ cm}^2/\text{Vs}$  (note: reliable hole-only diodes could not be fabricated for films with < 30% T1). The neat film hole mobility of SM2 is similar to that of T1, however, as PCBM is added, the hole mobility in SM2:PCBM films steadily decreases with the addition of more PCBM, dropping by nearly two orders of magnitude at 30% donor relative to 100% donor. The hole mobility of neat H1 in a neat film is found to be  $6 \times 10^{-3} \text{ cm}^2/\text{Vs}$  – among the highest reported to date for a solution processed

molecular donor. Note this is slightly higher than previously reported as the high series resistance of ITO was not accounted for in previous measurements<sup>19</sup>. Similar to the case of SM2:PCBM, the hole mobility in H1:PCBM films steadily decreases with the addition of more PCBM.

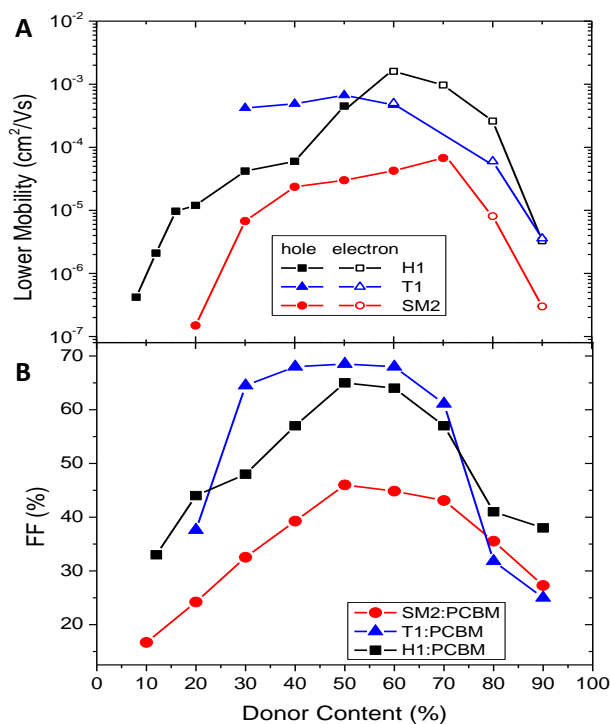


Figure 7.2: A) Slowest carrier mobility (holes closed symbols, electrons open symbols) in films containing donor materials H1, T1, or SM2 blended with PC<sub>71</sub>BM as a function of donor content. B) Solar cell fill factor in devices containing donor materials H1, T1, or SM2 blended with PC<sub>71</sub>BM as a function of donor content.

The influence of the charge transport properties on solar cell performance was explored by fabricating solar cells following the same active layer processing procedures as for the single carrier diodes. In an organic solar cell, the competition between extraction of charge carriers and nongeminate recombination is largely determined by the hole and electron mobilities. As the driving force for extraction reduces with an applied forward bias,

more and more charge carriers will recombine if either charge carrier mobility is too slow for efficient extraction. This loss is reflected in the solar cell fill factor (FF) and thus it is the FF that is expected to be most directly affected by the charge transport properties<sup>3,5</sup>. As shown in **Figure 7.2**, for all three systems the change in FF with donor content closely follows the trends of the slowest charge carrier mobility. This in turn shapes the PCE as a function of donor content (**Figure S7.1**). Note that the surprisingly stable hole mobility in T1:PCBM is reflected in the high and stable FF from 30-70% donor content while the drop in FF at 20% T1, suggests that the hole mobility in T1:PCBM likely also drops off in this concentration regime.

It is clear from Figure 7.2 that the hole is most often the slowest carrier as reported recently for a range of solution processed small molecule donor materials blended with fullerene acceptors<sup>3</sup>. Thus, the remainder of this article will focus on understanding the trends in hole mobility. Multiple reports have previously found a correlation between enhanced structural order of donor molecules and increased hole mobility when changing film processing conditions<sup>13,14,24</sup>. To explore the effects of structural order on charge transport in the materials systems studied here, grazing incidence wide angle x-ray scattering (GIWAX) measurements were performed on blend films across a range of donor concentrations for each system. Out of plane and in plane line cuts of the x-ray scattering data are shown for each system in **Figure S7.2** with shaded regions denoting the alkyl and  $\pi$ - $\pi$  stacking peaks. As reported previously, H1 crystallites are observed to take on a predominantly face-on orientation relative to the substrate with  $\pi$ - $\pi$  stacking in the out of plane direction<sup>19</sup> while T1 crystallites exhibit a predominantly edge-on orientation relative to the substrate with  $\pi$ - $\pi$  stacking in the in plane direction<sup>24</sup>. Similar to T1, SM2 crystallites

also exhibit  $\pi$ - $\pi$  stacking pre-dominantly in the in plane direction. The  $\pi$ - $\pi$  stacking peak for T1 and H1 are at  $q$  values of  $1.74 \text{ \AA}^{-1}$  and  $1.79 \text{ \AA}^{-1}$  corresponding to  $\pi$ - $\pi$  stacking distances of  $3.62 \text{ \AA}$  and  $3.52 \text{ \AA}$  respectively. The addition of PCBM is not observed to have significant impact on the position of the  $\pi$ - $\pi$  stacking peak for either H1 or T1. In contrast, the neat SM2 film has a  $\pi$ - $\pi$  stacking peak at  $q = 1.54 \text{ \AA}^{-1}$  and shifts to higher  $q$  value of  $1.68 \text{ \AA}^{-1}$  at PCBM concentrations  $\geq 20\%$  corresponding to  $\pi$ - $\pi$  stacking distances of  $4.08 \text{ \AA}$  and  $3.74 \text{ \AA}$  respectively. The SM2  $\pi$ - $\pi$  stacking peak in SM2:PCBM films is stable from 80%-30% SM2 and then increases to  $q = 1.76 \text{ \AA}^{-1}$  at 20% SM2 corresponding to a  $\pi$ - $\pi$  stacking distances of  $3.57 \text{ \AA}$ . The origin of the shift in  $\pi$ - $\pi$  stacking peaks is unclear though no concomitant shift in alkyl peaks was observed suggesting that aside from the closer  $\pi$ - $\pi$  stacking the crystal structure of SM2 does not significantly change upon addition of PCBM.

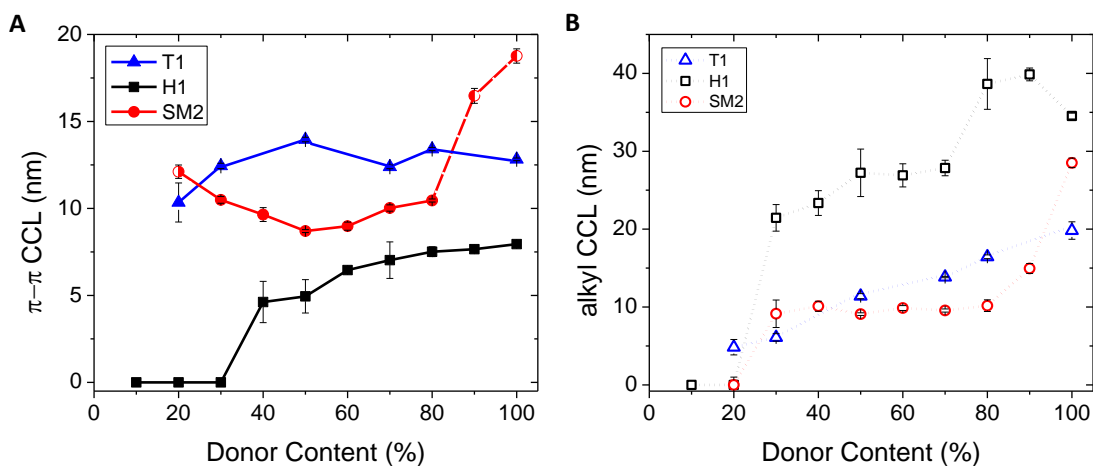


Figure 7.3: A)  $\pi$ - $\pi$  CCL as a function of donor content. The symbols for the SM2:PCBM are fully shaded ( $q = 1.68 \text{ \AA}^{-1}$ ) or half shaded (right:  $q = 1.76 \text{ \AA}^{-1}$ , left:  $q = 1.54 \text{ \AA}^{-1}$ ) to reflect the change in  $\pi$ - $\pi$  stacking distances. B) Alkyl chain CCL as a function of donor content.

For each system, the GIWAX data for the 1<sup>st</sup> order alkyl peaks and the  $\pi$ - $\pi$  stacking peaks in the dominant stacking direction (in plane or out of plane) were fit to a Pseudo-Voigt function. The full-width-at-half-maximum (FWHM) of the fits were used to calculate the

crystal correlation length according to Scherrer's equation ( $CCL = \frac{2\pi}{FWHM}$ ). The CCL is a measure of crystallite size and/or perfection and can be thought of as the average distance over which crystalline order is maintained<sup>25</sup>. We make no attempt here to discern between the effects of crystallite order and size on the CCL however it's worth noting that paracrystalline disorder in small molecules is generally small<sup>26</sup> and in the case of T1:PCBM, it was recently reported that the cumulative disorder in T1 crystallites is not large enough to affect the connection between the crystallite size and CCL. The CCLs for the donor  $\pi$ - $\pi$  stacking peak and alkyl stacking peaks are shown as a function of donor content in **Figure 7.3**. The symbols for the SM2:PCBM  $\pi$ - $\pi$  CCLs in Fig 3a are fully shaded ( $q = 1.68 \text{ \AA}^{-1}$ ) or half shaded (right:  $q = 1.76 \text{ \AA}^{-1}$ , left:  $q = 1.54 \text{ \AA}^{-1}$ ) to highlight the change in  $\pi$ - $\pi$  stacking distance. From this analysis, it is evident that in each system there is some degree of donor crystallinity over a wide range of donor concentrations. For each condition in which donor crystallinity was observed by GIWAX, evidence of phase separation was also observed in grazing incidence small angle x-ray scattering experiments (Figure S7.3) which is consistent with the notion that donor crystallization drives phase separation in SSM BHJs<sup>16</sup>.

Close inspection of the trends in CCL in the context of the mobility data reveals several interesting insights. For the case of H1, the  $\pi$ - $\pi$  CCL decreases steadily from  $\sim 8$  nm to 4.5 nm between 100% H1 and 40%. Below 40% H1, no scattering from  $\pi$ - $\pi$  stacking could be detected. The H1 alkyl CCLs show a similar trend but with much longer lengths scales from 35-40 nm at 80-100% H1 down to 21 nm at 30% H1 and no discernible alkyl scattering below 30% H1. Relative to the other two systems, the H1 system exhibits shorter  $\pi$ - $\pi$  CCLs but longer alkyl CCLs suggesting that while there is long scale coordination of H1

crystallites on the range of tens of nm's, the  $\pi$ - $\pi$  stacking is easily disrupted within these domains. Interestingly, the increase in  $\pi$ - $\pi$  CCL from 20% H1 to 40% H1 is much larger than the increase from 40% to 60% while the mobility change is much greater in the latter case. This suggests that the changes in mobility are likely not a result of the increased  $\pi$ - $\pi$  stacking alone and the connectivity between crystalline domains (driven in part by the trend towards larger crystallites) is also a significant factor governing the bulk hole transport.

For T1:PCBM, the  $\pi$ - $\pi$  CCL is higher than the other systems, fluctuating slightly between 12.4 and 14 nm from 100% T1 to 30% T1 and decreasing to 10.3 nm at 20% T1. In contrast, the alkyl CCL in T1:PCBM steadily decreases from a high of 20 nm in the neat T1 film down to 4.8 nm in the 20% T1 film. The relatively high and stable  $\pi$ - $\pi$  CCLs in T1:PCBM from 100% to 30% T1 seem consistent with the stable hole mobility over the same range. However it's interesting to note that in the high donor content (>80%) regime the hole mobility in T1:PCBM is less than that in H1:PCBM films despite the apparently superior ordering in the  $\pi$ - $\pi$  stacking direction.

For SM2:PCBM, the GIWAX data tells a different story than that of T1:PCBM and H1:PCBM. When going from 100% to 80% SM2, the  $\pi$ - $\pi$  CCL drops sharply from 18.8 nm to 10.5 nm while the alkyl CCL also decreases from 28.5 nm to 10.3 nm. Between 80% to 30% SM2 content, the alkyl CCL decreases only slightly to a low of 9.1 nm and then at 20% SM2 no peak is discernible. The  $\pi$ - $\pi$  CCL also decreases slightly from 10.3 nm at 80% SM2 down to 8.7 nm at 50% SM2 then rises to 10.5 nm at 30% SM2 and 12.1 nm at 20% SM2. All SM2:PCBM films in this study were annealed at 80 °C, thus the rise in  $\pi$ - $\pi$  CCL at lower donor content may be related to changes in the temperature for cold crystallization upon addition of PCBM as observed in other diketopyrrolopyrrole based systems<sup>16</sup>. Considering

the trends in  $\pi$ - $\pi$  CCL for SM2:PCBM in the context of the trends in hole mobility leads to the conclusion that structural order, or lack there-of, is not the limiting factor for hole transport in SM2:PCBM films. Rather it seems the distribution of donor crystallites in SM2:PCBM must stand in stark contrast to those in T1:PCBM crystallites in which donor crystallites appear to remain sufficiently connected to allow for efficient hole transport even at relatively low donor contents.

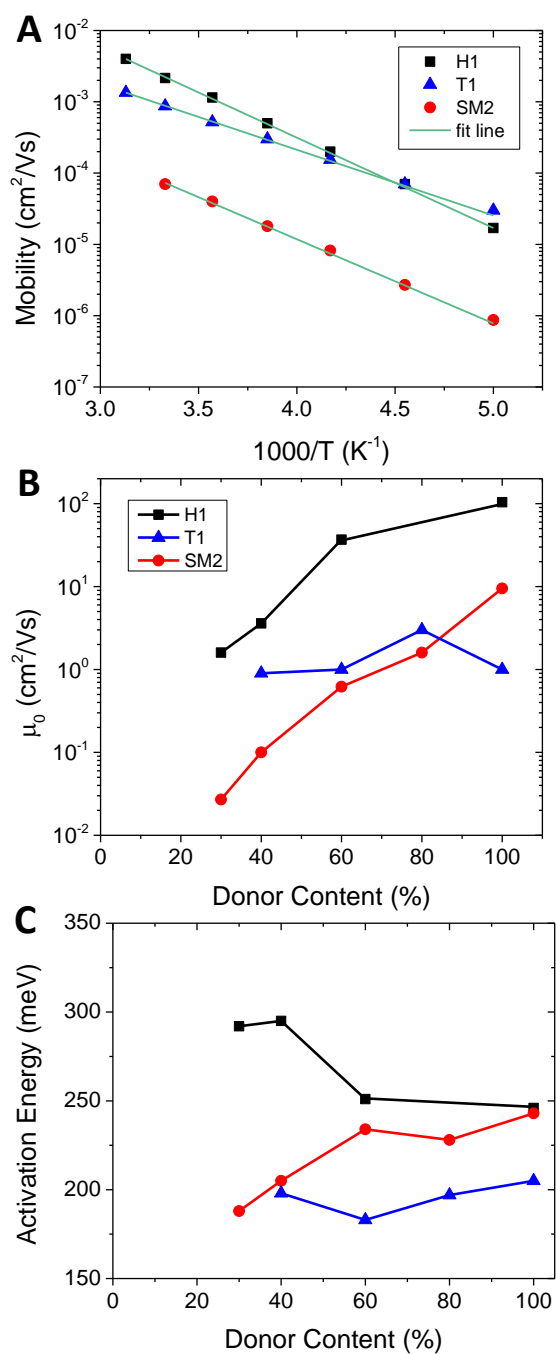


Figure 7.4: A) Hole mobility in blend films with 60% donor content by weight for as a function of inverse temperature. Lines are fits to Equation 1. B)  $\mu_0$  and C) activation energy as a function of donor content determined from temperature dependent hole mobility measurements in H1:PCBM, T1:PCBM and SM2 PCBM films.

In order to discern the effects of increased connectivity between ordered domains from changes in the efficiency of charge transport within ordered domains, temperature dependent mobility measurements were conducted for a range of donor concentrations in each system using the same single carrier diode structures as for the room temperature mobility measurements. The JV characteristics were measured at temperatures from 320K to 200K. Care was taken to ensure that the injecting contacts were ohmic and that device leakage currents were sufficiently low enough so as not to influence the low temperature data. It was found that in all cases, the mobilities follow an Arrhenius temperature dependence as has previously been reported for single carrier diode mobilities using neat polymers and small molecules<sup>27</sup>. The temperature dependent mobility data for blend films with 60% donor content by weight are shown in Figure 4a with the lines showing fits to the Arrhenius expression:

$$\mu = \mu_0 \exp\left(-\frac{\Delta}{kT}\right) \quad (1)$$

where  $\mu_0$  is the hole mobility at  $T \rightarrow \infty$ ,  $\Delta$  the activation energy,  $k$  Boltzmann's constant and  $T$  temperature. In organic semiconductors, the mobility pre-factor,  $\mu_0$ , has been described as a measure of electronic coupling between hopping sites in neat films<sup>27</sup> and has also been suggested to scale with the number of conductive pathways within a blend film<sup>28</sup>. At infinite temperature, charge carrier mobility in a blend film is not limited by energetic disorder but rather by the number of conductive pathways and how directly such conductive pathways allow charges to travel in the vertical direction across the film. As holes in a blend film are energetically confined to transport within domains with donor molecules,  $\mu_0$  can thus be interpreted as a measure of the connectivity of hole conducting domains. The activation

energy,  $\Delta$ , is related to energetic order with higher activation energy corresponding to higher disorder and thus lower charge carrier mobility at a given temperature<sup>27</sup>. The values for  $\mu_0$  and  $\Delta$  extracted from fits to Equation 1 are plotted as a function of donor content in Figures 4b and 4c respectively. The values for the  $\mu_0$  in the neat films of H1, SM2 and T1 range from 100 to 10 to 1  $\text{cm}^2/\text{Vs}$ . This huge variation in  $\mu_0$  for these highly crystalline small molecules is in contrast to the  $\mu_0$  values of 20-40  $\text{cm}^2/\text{Vs}$  that have been reported by Blom et al. for a large range of mostly amorphous conjugated polymers<sup>12,27</sup>. However, considering the notable differences in the average crystallite size, orientation, and  $\pi$ - $\pi$  stacking distance, in these three molecules it is perhaps not surprising to see a large variation in a parameter related to the amount of electronic overlap between hopping sites. With that in mind, the high  $\mu_0$  in H1 likely originates from a combination of the long range ordering of crystallites (evidenced by the long alkyl CCL and observed in transmission electron microscopy<sup>19</sup>), the small  $\pi$ - $\pi$  stacking distance and the face-on orientation relative to the substrate. The possibility of a H1 crystal structure that allows for multi-dimensional transport may also be contributing factor<sup>26</sup> and will be the subject of future research. Interestingly, the activation energy of neat H1 is found to be similar to that of SM2 with the activation of T1 being the lowest of the three materials. This suggests that decreasing the activation energy in H1 may be a viable route towards increasing the already high room temperature mobility to exceed  $10^{-2} \text{ cm}^2/\text{Vs}$ .

Looking at the donor content dependence of  $\mu_0$  and  $\Delta$ , reveals several interesting insights about the factors governing transport in blend films. As the donor content decreases in favor of more PCBM, the  $\mu_0$  values in H1:PCBM and SM2:PCBM decrease, while in T1:PCBM,  $\mu_0$  is relatively unchanged. In SM2:PCBM the decrease in  $\mu_0$  is fairly constant

across the concentration range considered whereas for H1:PCBM the slope noticeably steepens as the H1 content decreases below 60%. Thus it is evident that for each system the trend in  $\mu_0$  mirrors the trend in room temperature hole mobility. This suggest for H1:PCBM and SM2:PCBM blend films, below 60% and 100% donor content respectively, the hole transport is largely limited by the connectivity of hole conducting domains. This picture is consistent with the notion that in SM2:PCBM, the SM2 crystalline domains are not well connected and rather appear to be randomly distributed throughout the bulk film.

In contrast to  $\mu_0$  the  $\Delta$  in each system is reasonably constant from 100% down to 60% donor content. Below 60%, the  $\Delta$  in H1:PCBM increases while for SM2:PCBM a decrease in  $\Delta$  is observed. The decrease in activation for SM2:PCBM is especially surprising given that the mobility is actually decreasing. This finding can be reconciled by considering the trends in  $\pi$ - $\pi$  CCL. Comparing Fig 7.4c to Fig 7.3a, it can be seen that in the lower donor content regime for SM2:PCBM the  $\pi$ - $\pi$  CCL increases while  $\Delta$  decreases. The inverse is observed in H1:PCBM with the  $\pi$ - $\pi$  CCL decreasing while  $\Delta$  increases. For T1:PCBM, no significant changes in either  $\pi$ - $\pi$  CCL or  $\Delta$  are seen. To better illustrate this relation, in Figure 5 the activation energy is plotted versus the  $\pi$ - $\pi$  CCL measured in the same film. Acknowledging the scatter in the data, including one notable outlier for the neat SM2 film (which is likely related to its higher  $\pi$ - $\pi$  stacking distance), there appears to be a clear relation between  $\Delta$  and  $\pi$ - $\pi$  CCL with longer  $\pi$ - $\pi$  CCLs trending towards lower  $\Delta$ . This trend suggests that it is the superior ordering in the  $\pi$ - $\pi$  stacking direction that allows for a relatively small activation energy for hole transport in T1 films. This in combination with the range of  $\mu_0$  values, explains why the activation energies reported here differ from than what has been reported for neat amorphous polymers with similar room temperature

mobilities<sup>12,27</sup>. These findings strongly suggest that in molecular films holes are primarily transported through  $\pi$ -stacked domains rather than amorphous regions. Furthermore, it is the ordering within these domains that governs the activation energy for hole transport. Therefore increasing order in the  $\pi$ -stacking direction may be a viable route towards achieving higher charge carrier mobilities with SSMs. With that said, these results also show that  $\pi$ - $\pi$  stacking is not the only relevant parameter. The H1 system represents an important example in which the relatively high activation energy due to less order in the  $\pi$ -stacking direction can be overcome by maintaining superior connectivity between  $\pi$ -stacked domains thereby allowing for even higher hole mobility than observed in the systems with superior  $\pi$ - $\pi$  ordering. Thus, future molecular design should consider strategies to facilitate connectivity between ordered domains by for instance promoting long range order in the alkyl direction and fostering multi-dimensional electronic coupling between molecules and crystallites.

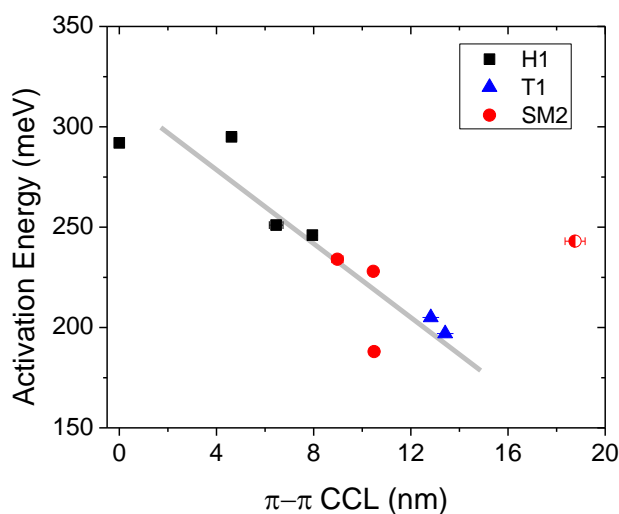


Figure 7.5: Charge transport activation energy versus  $\pi$ - $\pi$  CCL measured in films processed the same way. The half-shaded red circle represents the neat SM2 film. Line included as a guide for the eyes.

## 2. Summary and Conclusions

In summary, charge transport in solution processed molecular blend films was investigated with the aim of understanding the roles of order and the relative connectivity of conductive pathways. Using a combination of experimental probes, it was found that the limiting factors to charge carrier mobility in SSM BHJ solar cells vary between different material systems. In the case of H1:PCBM, it was found that from 100% to 60% donor, the hole transport is primarily limited by the relatively short range order in the  $\pi$ - $\pi$  stacking direction. At  $< 60\%$  H1, the hole transport drops sharply with increasing PCBM content due to a combination of increased disorder (ie. even shorter  $\pi$ - $\pi$  CCLs) and reduced connectivity between conductive domains. In the case of SM2:PCBM, it was found that the poor connectivity of SM2 crystalline domains limits the hole transport in spite of the relatively small activation energies enabled by the extended order in the  $\pi$ -stacking direction. In T1:PCBM, long range order in the  $\pi$ -stacking direction enables efficient hole transport through crystalline T1 domains which remain relatively well connected after the addition of PCBM thereby enabling relatively high hole mobility even in films with low donor content.

Looking across the three material systems considered, it was found that increased order in the  $\pi$ -stacking direction is correlated with lower activation energy for hole transport. Therefore increasing order in the  $\pi$ - $\pi$  stacking direction represents an important strategy for enabling higher charge carrier mobilities at room temperature. Furthermore, the connectivity of hole conducting domains was found to be of paramount importance to hole transport and is often the most limiting parameter to hole mobility in blend films. Based on these findings, we conclude that in order to increase the efficiency of small molecule solar cells, future

efforts should focus on designing molecules and processing techniques that facilitate better electrical connectivity between the  $\pi$ -stacked domains within blend films.

### 3. Experimental Section

*Single Carrier Diodes:* Hole only devices were fabricated using a structure of ITO/PEDOT:PSS/active layer/Au for molecules SM2 and T1. For H1, thermally evaporated MoOx/Al was used instead of Au in order to provide an ohmic contact. Electron only devices were fabricated using a device of Al/active layer/Ca/Al. For the active layers, H1:PCBM films were cast from solutions containing 40 mg/mL total weight in chlorobenzene with 0.4% DIO by volume. T1:PCBM films were cast from solutions containing 35 mg/mL total weight in chlorobenzene with 0.4% DIO by volume and a 70 °C annealing step was performed for 10 minutes following spin casting. SM2:PCBM films were cast from solutions containing 20-30 mg/mL total weight in chloroform and a 80 °C annealing step was performed for 10 minutes following the thermal deposition of the top electrode.

*Solar cells:* Solar cell devices were fabricated following the same active layer processing procedures as in the single carrier devices. The device structure was ITO/PEDOT:PSS/active layer/Ca/Al. All devices were tested under simulated AM1.5 illumination.

*GIWAXS:* All GIWAXS measurements were performed at Stanford Synchrotron Radiation Lightsource beamline 11-3 using a photon energy of 12.7 keV with a sample to detector distance of approximately 400 mm. Experiments were performed under a helium environment to minimize background scattering and sample damage from the x-ray beam. An incident angle of 0.12° (above the critical angle of the BHJ blend, but below the critical

angle of the substrate to ensure probing of the BHJ blend and not the substrate) was used in all cases. Images were collected with a MAR-345 2D image plate and processed with the software package WxDiff, provided by Dr. Stefan Mannsfeld.

#### 4. Supporting Information

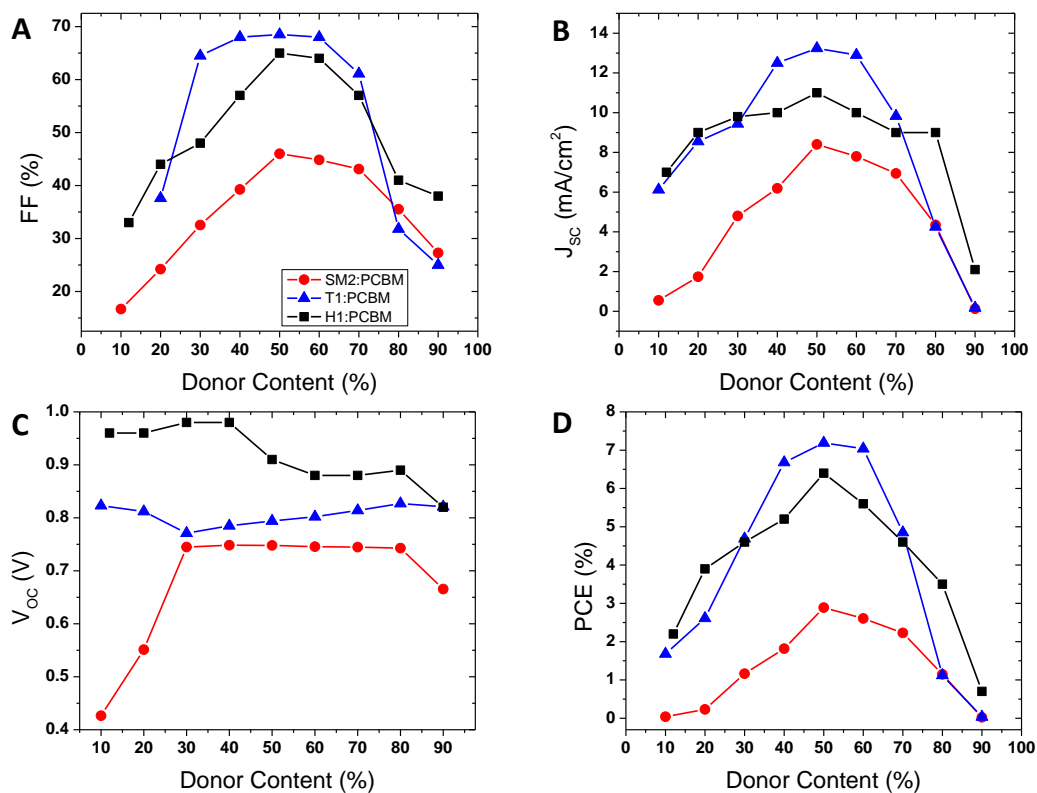


Figure S7.1: Fill Factor (A), short circuit current (B), open circuit voltage (C) and power conversion efficiency (D), in solar cell devices measured under AM1.5 illumination as a function of donor content.

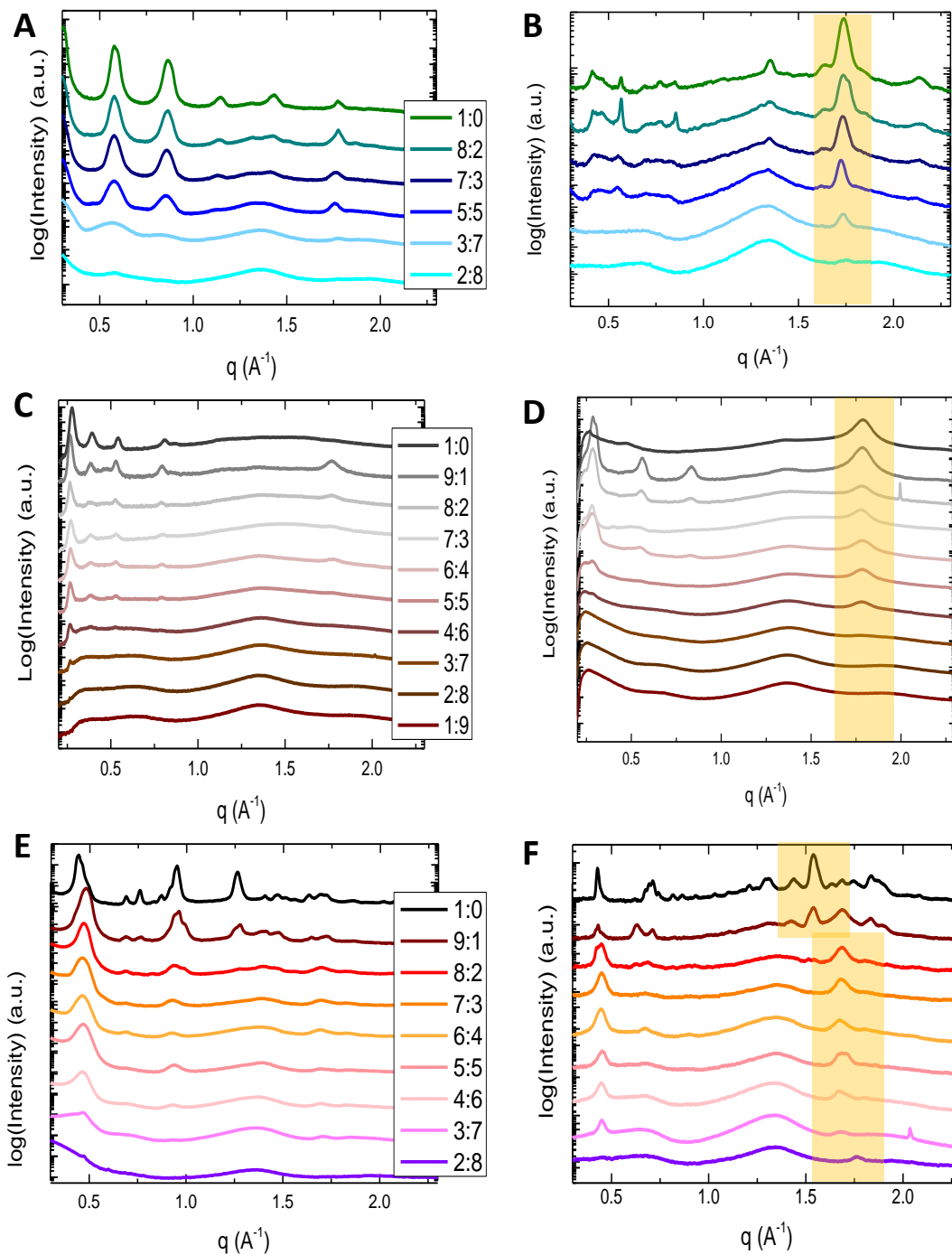


Figure S7.2: Line cuts from GIWAX measurements for blend films with T1:PCBM out of plane (A) and in plane (B), H1:PCBM in plane (C) and out of plane (D), and SM2:PCBM out of plane (E) and in plane (F). The yellow shaded regions highlight the  $\pi$ - $\pi$  stacking peaks.

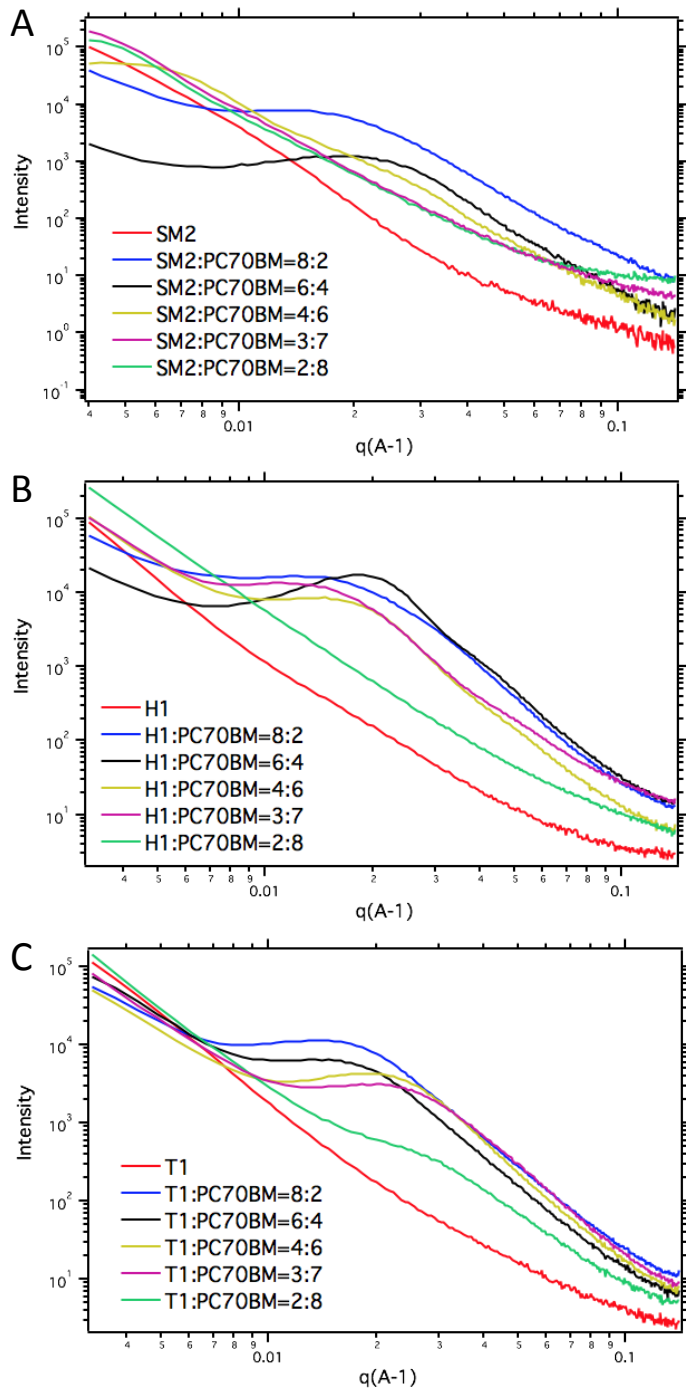


Figure S7.3: Grazing incidence small angle x-ray scattering of blend films containing PCBM blended with (A) SM2, (B) H1, and (C) T1. The donor:PCBM blend ratios are denoted in the figure legends.

## 5. References

- [1] Q. Zhang, B. Kan, F. Liu, G. Long, X. Wan, X. Chen, Y. Zuo, W. Ni, H. Zhang, M. Li, Z. Hu, F. Huang, Y. Cao, Z. Liang, M. Zhang, T. P. Russell, Y. Chen, *Nat. Photonics* **2014**, *advance online publication*.
- [2] B. Kan, Q. Zhang, M. Li, X. Wan, W. Ni, G. Long, Y. Wang, X. Yang, H. Feng, Y. Chen, *J. Am. Chem. Soc.* **2014**, *136*, 15529–15532.
- [3] C. M. Proctor, J. A. Love, T.-Q. Nguyen, *Adv. Mater.* **2014**, *26*, 5957–5961.
- [4] D. Bartesaghi, I. del C. Pérez, J. Kniepert, S. Roland, M. Turbiez, D. Neher, L. J. A. Koster, *Nat. Commun.* **2015**, *6*.
- [5] C. M. Proctor, M. Kuik, T.-Q. Nguyen, *Prog. Polym. Sci.* **2013**, *38*, 1941–1960.
- [6] C. M. Proctor, C. Kim, D. Neher, T.-Q. Nguyen, *Adv. Funct. Mater.* **2013**, *23*, 3584–3594.
- [7] W. Tress, K. Leo, M. Riede, *Phys. Rev. B* **2012**, *85*, 155201.
- [8] R. Noriega, J. Rivnay, K. Vandewal, F. P. V. Koch, N. Stingelin, P. Smith, M. F. Toney, A. Salleo, *Nat. Mater.* **2013**, *advance online publication*.
- [9] S. Holliday, J. E. Donaghey, I. McCulloch, *Chem. Mater.* **2013**.
- [10] V. Coropceanu, J. Cornil, D. A. da Silva Filho, Y. Olivier, R. Silbey, J.-L. Brédas, *Chem. Rev.* **2007**, *107*, 926–952.
- [11] L. J. A. Koster, *Phys. Rev. B* **2010**, *81*, 205318.
- [12] M. Kuik, G.-J. A. H. Wetzelaer, H. T. Nicolai, N. I. Craciun, D. M. De Leeuw, P. W. M. Blom, *Adv. Mater.* **2014**, *26*, 512–531.
- [13] B. Walker, A. B. Tamayo, X. Dang, P. Zalar, J. H. Seo, A. Garcia, M. Tantiwiwat, T. Nguyen, *Adv. Funct. Mater.* **2009**, *19*, 3063–3069.
- [14] S. Mukherjee, C. M. Proctor, J. R. Tumbleston, G. C. Bazan, T.-Q. Nguyen, H. Ade, *Adv. Mater.* **2015**, *27*, 1105–1111.
- [15] A. Sharenko, C. M. Proctor, T. S. van der Poll, Z. B. Henson, T.-Q. Nguyen, G. C. Bazan, *Adv. Mater.* **2013**, *25*, 4403–4406.
- [16] A. Sharenko, M. Kuik, M. F. Toney, T.-Q. Nguyen, *Adv. Funct. Mater.* **2014**, *24*, 3543–3550.
- [17] A. B. Tamayo, X.-D. Dang, B. Walker, J. Seo, T. Kent, T.-Q. Nguyen, *Appl. Phys. Lett.* **2009**, *94*, 103301–103301–3.
- [18] T. S. Van der Poll, J. A. Love, T.-Q. Nguyen, G. C. Bazan, *Adv. Mater.* **2012**, *24*, 3646–3649.
- [19] J. A. Love, I. Nagao, Y. Huang, M. Kuik, V. Gupta, C. J. Takacs, J. E. Coughlin, L. Qi, T. S. van der Poll, E. J. Kramer, A. J. Heeger, T.-Q. Nguyen, G. C. Bazan, *J. Am. Chem. Soc.* **2014**, *136*, 3597–3606.
- [20] Z. Li, G. He, X. Wan, Y. Liu, J. Zhou, G. Long, Y. Zuo, M. Zhang, Y. Chen, *Adv. Energy Mater.* **2012**, *2*, 74–77.
- [21] B. Walker, C. Kim, T.-Q. Nguyen, *Chem Mater* **2010**, *23*, 470–482.
- [22] X. Liu, Y. Sun, B. B. Y. Hsu, A. Lorbach, L. Qi, A. J. Heeger, G. C. Bazan, *J. Am. Chem. Soc.* **2014**, *136*, 5697–5708.
- [23] J. Liu, Y. Sun, P. Moonasin, M. Kuik, C. M. Proctor, J. Lin, B. B. Hsu, V. Promarak, A. J. Heeger, T.-Q. Nguyen, *Adv. Mater.* **2013**, *25*, 5898–5903.

- [24] J. A. Love, C. M. Proctor, J. Liu, C. J. Takacs, A. Sharenko, T. S. van der Poll, A. J. Heeger, G. C. Bazan, T.-Q. Nguyen, *Adv. Funct. Mater.* **2013**, *23*, 5019–5026.
- [25] Ryong-Joon Roe, *Methods of X-Ray and Neutron Scattering in Polymer Science*, Oxford University Press UK, **2000**.
- [26] I. Yavuz, B. N. Martin, J. Park, K. N. Houk, *J. Am. Chem. Soc.* **2015**, *137*, 2856–2866.
- [27] N. I. Craciun, J. Wildeman, P. W. M. Blom, *Phys. Rev. Lett.* **2008**, *100*, 056601.
- [28] K. Vakhshouri, D. R. Kozub, C. Wang, A. Salleo, E. D. Gomez, *Phys. Rev. Lett.* **2012**, *108*, 026601.

## Chapter VIII

### Effect of Leakage Current and Shunt Resistance on the Light Intensity Dependence of Organic Solar Cells

#### 1. The Story

Measuring the light intensity dependence of the current-density voltage ( $JV$ ) characteristics has proven to be a powerful tool for indentifying the primary recombination loss mechanisms in organic photovoltaic (OPV) devices.[1]–[3] Unlike other opto-electronic techniques for probing recombination mechanisms, light dependent  $JV$  studies do not require extensive experimental equipment or expertise. A solar testing setup (light source and  $JV$  measuring unit) and a series of neutral density filters or other means to attenuate the light intensity is all that is needed.

Nonetheless, as we demonstrate here, one must be very careful to use high quality devices when studying the light intensity dependence of solar cells as the light dependence can be strongly influenced by parasitic leakage currents. Such losses are well known to effect all types of solar cells;[4]–[7] however, many reports in the OPV literature have seemingly overlooked the influence of leakage currents when interpreting light dependent behavior.

Leakage current in a solar cell can be considered as undesirable current that is injected from the electrodes prior to the turn on voltage. Within the operating regime (0 V to open circuit voltage), leakage current flows opposite to the photocurrent and thereby reduces the light current. This phenomenon is typically described using a simple circuit model (see

Figure 8.1A) in which leakage (shunt) current can travel through the shunt resistor ( $R_{sh}$ ) that is in parallel to the photocurrent source and diode.[6] The magnitude of the leakage current is then determined by the magnitude of  $R_{sh}$  – the higher  $R_{sh}$ , the less current that runs through it. From this model it follows that:

$$J(I, V) = J_d(V) + J_{sh}(V) - J_{ph}(I, V) \quad (8.1)$$

where  $J$  is the net output current density,  $J_d$  diode current density,  $J_{ph}$  the photogenerated current density and  $J_{sh}$  the leakage current density that flows through  $R_{sh}$ . It is worth noting that  $J_d$  and  $J_{sh}$  depend only on voltage ( $V$ ) while  $J_{ph}$  scales with the incident light intensity ( $I$ ) as well and thus both  $J$  and  $J_{ph}$  are functions of  $V$  and  $I$ . Consequently, the relative influence of  $J_{sh}$  on  $J$  will increase at lower light intensities. In the event that  $J_{sh}$  is non-negligible this can lead to significant decreases in both open circuit voltage ( $V_{oc}$ ) and fill factor ( $FF$ ) at low light intensities. Following Ohm's law, the leakage current through  $R_{sh}$  can be expressed as

$$J_{sh} = \frac{V - JR_s}{R_{sh}} \quad (8.2)$$

where  $R_s$  is the series resistance. For an organic solar cell,  $R_s$  is typically taken to be the inverse slope of the dark current around  $J(0 \text{ mW/cm}^2, 1.5 \text{ V})$  and  $R_{sh}$  the inverse slope around  $J(0 \text{ mW/cm}^2, 0 \text{ V})$ .

Figure 8.1b shows the dark current of four different organic solar cells with varying magnitudes of leakage current. The  $R_s$  and  $R_{sh}$  for each device are shown in Table 8.1. The solar cell devices were prepared using the high performing solution processed small molecule system 7,7'-(4,4-bis(2-ethylhexyl)-4H-silolo[3,2-b:4,5-b']dithiophene-2,6-diyl)bis(6-fluoro-4-(5'-hexyl-[2,2'-bithiophen]-5-yl)benzo[c][1,2,5]thiadiazole), (*p*-DTS(FBTTh<sub>2</sub>)<sub>2</sub>) as the donor material and phenyl-C71-butyric acid methyl ester (PC<sub>71</sub>BM)

as the acceptor following the optimal procedures described by Van der Poll et al.[8] Though devices were prepared from identical solutions and procedures, a large variation can be seen in the dark current with device D1 exhibiting orders of magnitude higher current from 0 to 0.75 V as compared to device D4. From Figure 8.1B it is evident that D1 has the highest leakage current followed by D2, D3 and D4. This is also reflected in the  $R_{sh}$ , where D1 has the lowest  $R_{sh}$  followed by D2, D3 and D4. Such large variation in the leakage current of organic solar cells is not uncommon and is known to be affected by substrate cleaning procedures, film thickness, electrode interlayers and film deposition techniques.[5], [9], [10] In the case of the devices here, the range in  $R_{sh}$  is most likely a consequence of spin coating from a hot solution which led to variations in film thickness and film density which in turn affects the degree of cathode diffusion into the active layer.

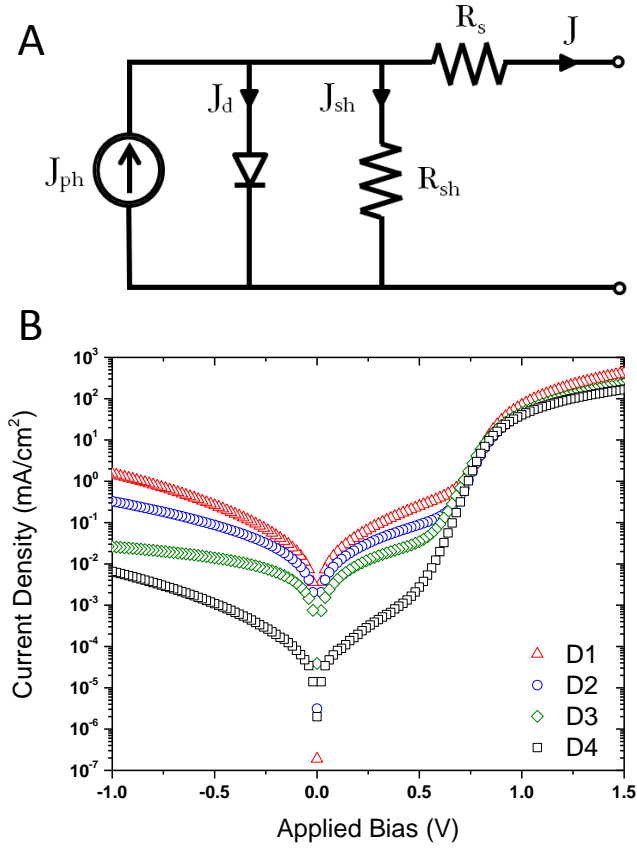


Figure 8.1. A) Simple circuit model showing current pathways and resistances in a typical solar cell. B) The current-voltage response measured in the dark of  $p$ -DTS(FBTTh<sub>2</sub>)<sub>2</sub>:PC<sub>71</sub>BM solar cell devices with leakage currents ranging from low to very high.

The effect of leakage current (ie. low  $R_{sh}$ ) at open circuit conditions is of particular interest as the light intensity dependence of the open circuit voltage is often used to understand the nature of charge carrier recombination. It has previously been shown by Koster et. al. that for an ideal system with only bimolecular recombination and negligible leakage current, the open circuit voltage can be expressed as

$$V_{oc} = \frac{E_{gap}}{q} - \frac{kT}{q} \ln \left( \frac{(1-P)\gamma N_c^2}{PG} \right) \quad (8.3)$$

where  $E_{gap}$  is the band gap,  $q$  is the elementary charge,  $k$  is Boltzmann's constant,  $T$  is temperature,  $P$  the dissociation probability of a bound electron-hole pair,  $\gamma$  the bimolecular recombination rate coefficient,  $N_c$  is the effective density of states, and  $G$  is the photogeneration rate [2]. As  $G$  is the only term in Equation 3 that depends on light intensity Koster et. al. predicted and confirmed that for a system with only bimolecular recombination the  $V_{oc}$  should have a logarithmic dependence on light intensity with a slope of  $kT/q$  [2]. Subsequently, it was shown that a system with trap-assisted recombination will have a slope greater than  $kT/q$  [11]. The light dependence of the  $V_{oc}$  has hence been used to distinguish bimolecular and trap assisted recombination in a variety of organic solar cell systems [1], [12], [13].

Equation 8.3 was derived by considering that for an ideal device with negligible leakage current, generation is cancelled about by recombination at open circuit. However, in the case of a non ideal device with low shunt resistance, the shunt current also contributes to cancelling out the photogenerated current such that at open circuit,

$$J_{ph} = J_{rec} + J_{sh}. \quad (8.4)$$

where  $J_{rec}$  is the recombination current. Following a previously described model for a metal-insulator-metal diode with only bimolecular recombination, the recombination current can be expressed as

$$J_{rec} = qL(1 - P)\gamma np \quad (8.5)$$

where  $L$  the active layer thickness,  $n$  the density of free electrons and  $p$  the density of free holes[2]. Likewise, when the photocurrent is measured under a strong reverse bias such that the photocurrent is saturated, the photocurrent can be expressed in terms of the generation rate  $G$ , as

$$J_{ph} = qLPG. \quad (8.6)$$

It should be noted that  $P$  may be voltage dependent as some organic solar cell systems have been shown to exhibit voltage dependent photogeneration[14], [15]. From Equation 8.2, it is evident that at open circuit  $J_{sh} = \frac{V_{oc}}{R_{sh}}$  and thus it follows from Equations 8.4-6 that

$$PG = (1 - P)\gamma np + \frac{V_{oc}}{qLR_{sh}}. \quad (8.7)$$

At open circuit, the quasi-Fermi levels across the device are approximately constant and their energy difference equal to the applied voltage, therefore

$$np = N_c^2 \exp\left(\frac{qV_{oc} - E_{gap}}{kT}\right). \quad (8.8)$$

Combining Equations 8.7 and 8.8, one can obtain an expression for  $V_{oc}$  similar to that of Equation 3 but now also considering the effect of shunt current, such that

$$V_{oc} = \frac{E_{gap}}{q} - \frac{kT}{q} \ln\left(\frac{(1-P)\gamma N_c^2}{PG - V_{oc}/qLR_{sh}}\right). \quad (8.9)$$

In the ideal case,  $R_{sh}$  is large such that even at low light intensities  $J_{sh}$  is negligible and Equation 8.9 simplifies to the expression in Equation 8.3. In the non ideal case,  $R_{sh}$  may be small such that the shunt current is non-negligible and thus the  $R_{sh}$  term in Equation 8.9 cannot be neglected. The effect of low  $R_{sh}$  will be to increase the  $V_{oc}$  light intensity slope

such that even a system with purely bimolecular recombination may appear to have a slope  $> kT/q$ . This is demonstrated in Figure 8.2a where the  $V_{oc}$  is plotted versus the incident light intensity for the four devices presented in Figure 8.1. The symbols represent data points and the lines are fits for a natural logarithmic dependence of  $V_{oc}$  on light intensity. While the low leakage device, D4, exhibits a slope of  $1.0 kT/q$  the slope steadily increases with increasing leakage current with D3, D2, and D1 exhibiting slopes of 1.2, 1.4 and  $2.0 kT/q$ , respectively. In contrast, when the effect of leakage current is accounted for by plotting  $V_{oc}$  versus  $PG - V_{oc}/qLR_{sh}$ , each device exhibits approximately the same slope of  $1.0 kT/q$  as predicted by Equation 8.9 (Figure 8.2B) for a system dominated by bimolecular recombination.

Device	$R_s$ [ $\Omega \text{ cm}^2$ ]	$R_{sh}$ [ $\Omega \text{ cm}^2$ ]	$V_{oc}$ slope [ $kT/q$ ]
D1	1.2	$2.2 \times 10^3$	2.0
D2	2.4	$5.7 \times 10^3$	1.4
D3	2.2	$2.7 \times 10^4$	1.2
D4	3.6	$1.2 \times 10^6$	1.0

**Table 8.1.** Series resistance and shunt resistance extracted from the dark current of solar cell devices D1, D2, D3 and D4 as well as the slope of the  $V_{oc}$  light intensity dependence of each device.

The effect of leakage current is also evident in the dependence of the device  $FF$  on incident light intensity as shown in Figure 8.2c. In the case of device D4 the  $FF$  appears steady at  $\sim 0.75$  from ca.  $2 \text{ mW/cm}^2$  to  $20 \text{ mW/cm}^2$  after which it decreases slightly with increasing light intensity to  $\sim 0.70$  at  $100 \text{ mW/cm}^2$ . The decrease of  $FF$  with increasing light

intensity has been reported to have two origins: series resistance and bimolecular recombination.[1], [5], [12], [16] The effects of bimolecular recombination have gained considerable attention in particular as bimolecular recombination is known to be a significant loss mechanism in most all organic solar cells.[1], [17], [18] Therefore, the  $FF$  dependence on light intensity has been used sporadically to infer differences in recombination dynamics across various organic solar cell systems which are often in turn then attributed to observed morphological changes. However, leakage currents can also influence the  $FF$  dependence on light intensity as illustrated by devices D1, D2, and D3 wherein the  $FF$  is observed to decrease at lower light intensities. The light intensity below which the  $FF$  decreases is determined by the shunt resistance. For instance, the  $FF$  of the lowest shunt resistance devices, D1, continuously decreases starting at intensities below  $100 \text{ mW/cm}^2$  where as the  $FF$  of D3 increases from  $100 \text{ mW/cm}^2$  to  $\sim 10 \text{ mW/cm}^2$  and then decreases at lower light intensities. As with the  $V_{oc}$ , the effect of leakage current on  $FF$  becomes increasingly prominent at lower intensities because the leakage current is independent of light intensity where as the magnitude of the photocurrent steadily decreases with decreasing light intensity.

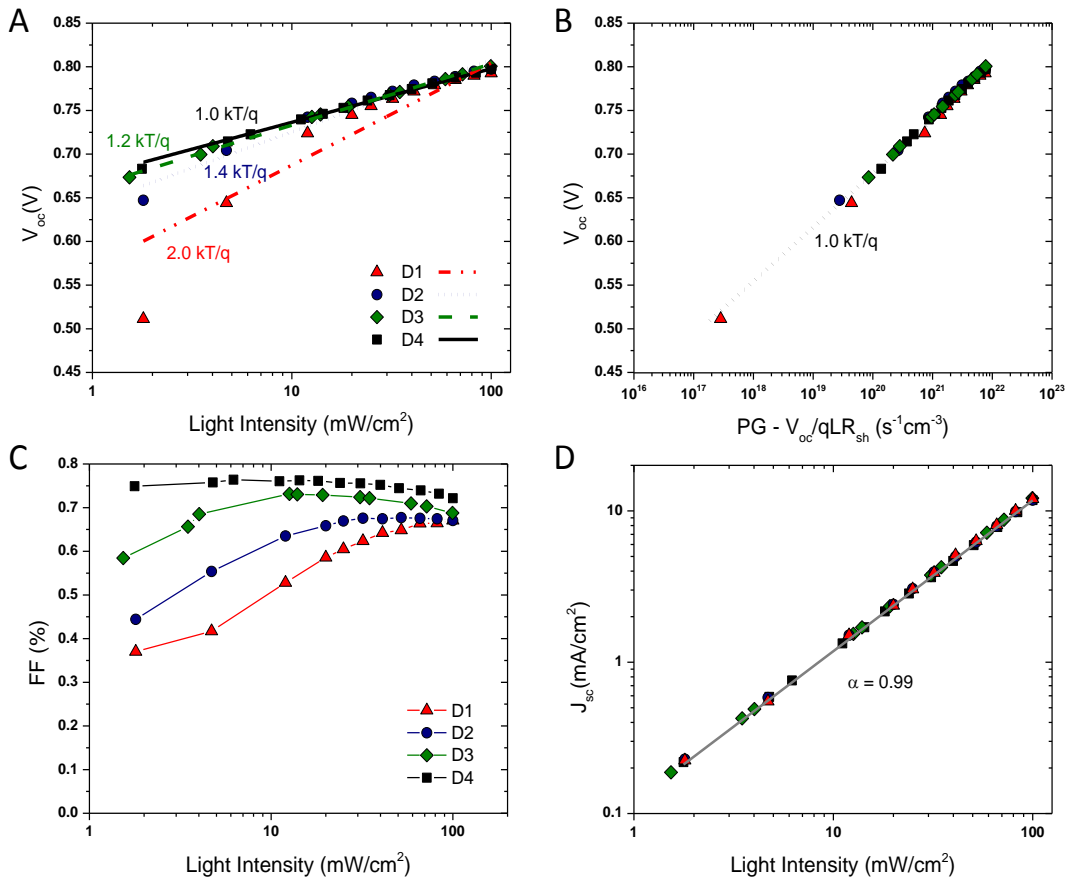


Figure 8.2: The light intensity dependence of the  $V_{oc}$  (A),  $FF$  (C), and  $J_{sc}$  (D) of devices D1, D2, D3 and D4. The solid and dashed lines in (A) are fits to the data using Equation 3. (B) Shows the  $V_{oc}$  of devices D1, D2, D3 and D4 plotted versus  $PG - V_{oc}/qLR_{sh}$  where the dashed line has a slope of  $kT/q$ .

It's worth noting that unlike the  $V_{oc}$  and  $FF$ , the dependence of the short circuit current ( $J_{sc}$ ) is *not* strongly influenced by leakage currents. This can be understood from Equation 1, which for the case of  $V = 0$  and  $JR_s \approx 0$ , reduces to  $J(I, 0) = J_{ph}(I, 0)$ . As shown in Figure 2d, the  $J_{sc}$  for all four devices here exhibits an identical dependence on light intensity which can be described with a power law fit to  $J_{sc} \propto I^\alpha$  with  $\alpha = 0.99$  which is a typical value for organic solar cells such as  $p$ -DTS(FBTTh<sub>2</sub>)<sub>2</sub>:PC<sub>71</sub>BM that have balanced

carrier mobilities and only modest bimolecular recombination losses at short circuit.[1], [15], [19]

Comparing Figure 8.2c with the light dependence of the solar cell power conversion efficiency (PCE) shown in Figure 8.3a, it is evident that the PCE light dependence is largely set by the trend in  $FF$  with the  $V_{oc}$  dependence also playing a role. At intensities close to one sun, the PCE of each device is similar as are the  $FF$ s however the difference is pronounced at lower light intensities where the leakage current competes favorably with the photocurrent. The origin of this is illustrated in Figure 8.3 which features the current voltage characteristics of D1 (Figure 8.3b) and D4 (Figure 8.3c) measured in the dark (black line) and at various illumination intensities ranging from 2-100 mW/cm<sup>2</sup> (color lines). As mentioned previously from 0 V to ~0.7 V, in both devices the dark current is dominated by the leakage current while the light current is dominated by the difference between photocurrent and leakage current. For device D1 the light current measured at 100 mw/cm<sup>2</sup> is over one order of magnitude higher than the leakage current across the operating regime and thus the  $FF$  and  $V_{oc}$  are not significantly decreased by the leakage current. However at lower light intensities, where the photo current is within one order of magnitude of the leakage current, the effect on the light current is pronounced resulting in steep drops in  $FF$  and  $V_{oc}$ . In contrast, as shown in Figure 8.3c, for device D4 with low leakage current, even at relatively low light intensities, the light current is orders of magnitude greater than the dark (leakage) current and thus the  $FF$  and  $V_{oc}$  can be measured independent of the leakage current across a wide range of light intensities.

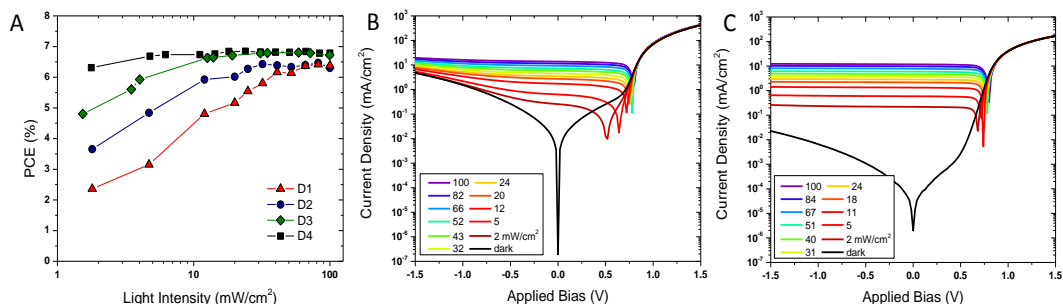


Figure 8.3: (A) The light intensity dependence of the PCE of devices D1, D2, D3 and D4. Current density as a function of applied bias for devices D1 (B) and D4 (C) measured in the dark and under illumination up to 100 mW/cm<sup>2</sup>.

In conclusion, the effect of leakage current and shunt resistance on the light intensity dependence of a model organic solar cell system has been demonstrated. In the case of solar cell devices with low shunt resistance ( $<10^6 \Omega \text{ cm}^2$ ), current-voltage measurements conducted at incident light intensities less than one sun may be significantly skewed by parasitic leakage current. In such devices, the effect of the leakage current will be to decrease the device  $FF$  and the  $V_{oc}$  increasingly more as the light intensity is decreased. The slope of the logarithmic dependence of the  $V_{oc}$  on light intensity is particularly sensitive to the effect of leakage currents with slopes ranging from 1 kT/q to 2 kT/q for the same material system depending on the shunt resistance. This effect may explain some discrepancies about the light intensity dependence of various OPV systems reported in the literature. Thus, we assert that care should be taken to ensure that parasitic leakage currents are minimized when measuring the light intensity dependence of organic solar cells.

## 2. References

- [1] C. M. Proctor, M. Kuik, T.-Q. Nguyen, *Prog. Polym. Sci.* **2013**, *38*, 1941–1960.
- [2] L. J. A. Koster, V. D. Mihailetschi, R. Ramaker, P. W. M. Blom, *Appl. Phys. Lett.* **2005**, *86*, 123509–123509–3.
- [3] R. Mauer, I. A. Howard, F. Laquai, *J Phys Chem Lett* **2010**, *1*, 3500–3505.
- [4] M. Wolf, H. Rauschenbach, *Adv. Energy Convers.* **1963**, *3*, 455–479.
- [5] Y. Zhou, T. M. Khan, J. W. Shim, A. Dindar, C. Fuentes-Hernandez, B. Kippelen, *J. Mater. Chem. A* **2014**, *2*, 3492–3497.
- [6] J. Nelson, *The Physics of Solar Cells*, Imperial College Press, **2003**.
- [7] M. A. Green, *Solid-State Electron.* **1981**, *24*, 788–789.
- [8] T. S. Van der Poll, J. A. Love, T.-Q. Nguyen, G. C. Bazan, *Adv. Mater.* **2012**, *24*, 3646–3649.
- [9] G. A. H. Wetzelaer, M. Kuik, M. Lenes, P. W. M. Blom, *Appl. Phys. Lett.* **2011**, *99*, 153506.
- [10] N. Li, B. E. Lassiter, R. R. Lunt, G. Wei, S. R. Forrest, *Appl. Phys. Lett.* **2009**, *94*, 023307–023307–3.
- [11] M. M. Mandoc, F. B. Kooistra, J. C. Hummelen, B. de Boer, P. W. M. Blom, *Appl. Phys. Lett.* **2007**, *91*, 263505.
- [12] C. M. Proctor, C. Kim, D. Neher, T.-Q. Nguyen, *Adv. Funct. Mater.* **2013**, *23*, 3584–3594.
- [13] S. R. Cowan, A. Roy, A. J. Heeger, *Phys. Rev. B* **2010**, *82*, 245207.
- [14] S. Albrecht, W. Schindler, J. Kurpiers, J. Kniepert, J. C. Blakesley, I. Dumsch, S. Allard, K. Fostiropoulos, U. Scherf, D. Neher, *J. Phys. Chem. Lett.* **2012**, *3*, 640–645.
- [15] C. M. Proctor, S. Albrecht, M. Kuik, D. Neher, T.-Q. Nguyen, *Adv. Energy Mater.* **2014**, DOI: 10.1002/aenm.201400230.
- [16] C. G. Shuttle, R. Hamilton, B. C. O'Regan, J. Nelson, J. R. Durrant, *Proc. Natl. Acad. Sci.* **2010**, *107*, 16448–16452.
- [17] G. Lakhwani, A. Rao, R. H. Friend, *Annu. Rev. Phys. Chem.* **2014**, *65*, 557–581.
- [18] S. Massip, P. M. Oberhumer, G. Tu, S. Albert-Seifried, W. T. S. Huck, R. H. Friend, N. C. Greenham, *J Phys Chem C* **2011**, *115*, 25046–25055.
- [19] S. R. Cowan, N. Banerji, W. L. Leong, A. J. Heeger, *Adv. Funct. Mater.* **2012**, *22*, 1116–1128.

## **Chapter IX**

### **Summary and Outlook**

#### **1. Summary**

This dissertation has focused on understanding loss mechanisms in solution processed small molecule solar cells. A particular emphasis was put on understanding the origin of voltage dependent losses as such losses were the biggest limitation to this technology at the onset of this research. It was found that such losses have two primary origins: field dependent generation and nongeminate recombination.

While field dependent generation may be a significant loss mechanism, it was shown that it can also be completely overcome by careful control of the blend film morphology. Reduced field dependent generation was found to be correlated with progressively purer and more order domains.

Once charge carriers are fully separated they must be extracted from the active layer before they recombine nongeminately. It was found that in all small molecule solar cells, there is some degree of nongeminate recombination – particularly at low fields close to open circuit. The nature of nongeminate recombination was found to be primarily bimolecular – meaning a free hole recombining with a free electron (as opposed to a trap mediated process). While there is some variation in the rate coefficient of bimolecular recombination between systems, it was shown that the charge carrier mobility is typically the most important determinant of the degree of voltage dependent nongeminate recombination losses. For a 100 nm solar cell, both holes and electron mobilities should be at least  $10^{-4}$

$\text{cm}^2/\text{Vs}$  in order to efficiently extract charge carriers before they recombine. In many cases it was found that the donor material was the limiting factor in the charge transport of blend films and the hole mobility measured in neat films sets the upper limit for blend films. Further investigation revealed that increased order along the  $\pi$ - $\pi$  stacking direction in donor molecules is correlated with lower activation energy for hole transport however even if donor crystallization is achieved the transport in blend films may still be limited by the number of conductive pathways.

## **2. Outlook**

After decades of research, much progress has been made on understanding of the underlying physics and improving the efficiency of organic solar cells to the current record of 10% PCE for a single junction cell. However several important challenges still remain. It is clear that future material design and device fabrication techniques must aim to maintain efficient charge transport properties while encouraging sufficient phase separation in the blend film. Multiple reports suggest that a charge carrier mobility of  $10^{-2} \text{ cm}^2/\text{Vs}$  for both holes and electrons is needed in order to maintain high fill factors in films thick enough to absorb all incident photons. Improvements in absorption coefficients and/or light management may enable complete absorption in thinner films thereby reducing the mobility requirements. A third approach would be to reduce the rate of bimolecular recombination which should also benefit the open circuit voltage. Looking ahead, if such improvements can be made then it stands to reason that single junction solar cells made from solution processed small molecules could well exceed power conversion efficiencies of 15%.